Hybrid Approaches to Quantum Information Using Ions, Atoms and Photons

by

Marko Cetina

B.S., California Institute of Technology (2004)

Submitted to the Department of Physics
in partial fulfillment of the requirements for the degree of

Doctor of Philosophy

at the

MASSACHUSETTS INSTITUTE OF TECHNOLOGY

May 2011

Author .....
Department of Physics
May, 19th, 2011

Certified by .....
Vladan Vuletić
Lester Wolfe Associate Professor of Physics
Thesis Supervisor

Accepted by .....
Krishna Rajagopal
Professor of Physics, Associate Head for Education, Physics

Hybrid Approaches to Quantum Information Using Ions, Atoms and Photons

by

Marko Cetina

Submitted to the Department of Physics
on May, 19th, 2011, in partial fulfillment of the
requirements for the degree of
Doctor of Philosophy

Abstract

This thesis presents two hybrid systems for quantum information processing - one joining cold ions and cold atoms and another coupling linear chains of atomic ions with photons via an optical resonator.

The first experimental realization of a hybrid cold-ion / cold-atom system is presented in the form of Yb atoms trapped in a magneto-optical trap overlapped with Yb^+ ions stored in a radio-frequency (RF) planar Paul trap. The overlap between the excited MOT atoms and the ion trap is used to obtain isotope-selective ion trap loading rates 10^4 times higher than previously achieved. The interaction between atoms and ions is measured by observing near-resonant charge-exchange collisions between Yb and Yb^+ with a collision rate matching the classical Langevin cross-section. Momentum transfer between cold atoms and cold ions is observed via collisions of Yb^+ ions with laser-cooled Rb atoms and a classical limit to the ion-atom collision energy in RF traps derived, with relevance to current ion experiments.

The second part of the thesis presents the first integration of a scalable, microfabricated surface ion trap chip with an optical resonator. This chip trap is used to produce a linear array of ion traps and load these traps with isotopically-selected chains of Yb^+ ions. The ion chains are overlapped with the mode of an optical resonator and the coupling of the individual ions to the resonator mode demonstrated by recording the frequency spectrum of the ions' near-resonance fluorescence. These measurements demonstrate the capability of the present system to store and process quantum information stored in short ion chains and to communicate this information via photons, with applications to large-scale trapped ion quantum information processing.

The strong-near resonant optical field available inside the optical resonator may also be used to produce a periodic optical potential for trapped ions, with applications to quantum simulation.

Thesis Supervisor: Vladan Vuletić
Title: Lester Wolfe Associate Professor of Physics

Acknowledgements

I would like to acknowledge the many people without whom this thesis would not have been possible.

First, I thank my parents for supporting and guiding me, especially with regard to people who, being very nonlinear, can be much more difficult to understand than atoms and light.

I thank the Sheehy family for welcoming me to the US and enabling my long academic journey here.

From my undergraduate days at Caltech, I would like to thank Prof. Thomas A. Tombrello for his unsurpassed mentorship and inspiration in choosing research problems.

At MIT, I worked with many capable people who directly enabled the results in this thesis. Andrew Grier's perserverence in balancing single ions against external electric fields was crucial to observing low-energy ion-atom collisions. Brendan Shields and Thaned Pruttivarasin helped with construction of the collision experiment. While building the collision experiment, Jonathan Campbell set an example of personal leadership that I can only hope to match.

Andrew Grier, Feđa Oručević, Chiara d'Errico and Markus Zwerger added cold Rb atoms to the ion-atom collision setup and observed the sympathetic heating of Yb^+ by cold Rb atoms.

With a mix of ion trapping, near-UV lasers, microfabrication, optical resonators and ultrahigh vacuum, the ion array experiment was truly a joint effort (evidenced by the four people it took to physically put it together!) Andrew Grier provided valuable suggestions for the design of the experiment and single-handedly performed the very fine task of aligning the optical resonator to the ion trap chip. Feđa Oručević assembled the vacuum pumping system and laid out the ion trap chip mask. Yufei Ge contributed invaluable experience, help and enthisiasm in fabricating the ion chip trap. The fabrication of a working 40 mm^2 trap with 7 μm features was enabled by Prof. Karl Berggren who gave us access to the MIT NSL class-10 cleanroom. Many thanks also go to Kurt Broderick for sharing his extensive knowledge of fabrication and inspiring a positive attitude towards this oftentimes frustrating and repetitive process.

Matthias Scholz gave a good example of the organizational skills needed to advance a complex experiment to a working stage. In this journey we were greatly helped by a number of undergraduate and visiting students - Renate Landig, Zhenkai Lu and

Jiwon Yune.

I am pleased to leave the ions and the resonator in the hands of a group of very talented and capable people - Dorian Gangloff, Kristi Beck, Alexei Bylinskii and Leon Karpa. I would like to especially acknowledge the new team for the first benchmark achievements - isotope-selective loading of the ion trap, controlled splitting of ion chains and measurement of ion coupling to the optical resonator.

For making the long nights in the lab not just bearable but fun, I thank Jit Kee Chin, Daniel Miller, Christian Sanner, Aviv Keshet and Edward Su from the BECII lab. Jit Kee, Dan, Aviv and Ed provided companionship in the late hours of the night interspersed with a thorough introduction to the technical details of quantum degenerate gasses and hours of German practice with Christian.

This work has been done in collaboration with Prof. Isaac Chuang's group. I thank Prof. Chuang both for crucial equipment and resources and for fresh intellectual perspectives on the engineering complex systems that inspired the ion array experiment.

Lacking dedicated external funding, the pioneering ion-atom collision experiment would not have been possible without prompt discretionary funding from the MIT-Harvard Center for Ultracold Atoms.

The work presented in this thesis was performed in the labs of Prof. Vladan Vuletić. I am indebted to Prof. Vuletić for his good taste in the choice of physical systems and for his long-term vision and audacity to address the truly important challenges in the field, no matter the technical obstacles.

Lastly, I would like to thank the whole Vuletić group and especially Haruka Tanji and Prof. Vuletić for their support during a health crisis during my time at MIT.

Contents

List of Figures

List of Tables

Chapter 1

Introduction

From its inception at the beginning of the 20th century, quantum mechanics has both altered our understanding of the universe and of the method of inquiry we use to approach it.

Even more visible are the practical applications of our newly gained understanding: the manipulation of nuclear processes, the development of semiconductors and the invention of lasers.

Despite these successes, our ability to control quantum systems remains limited compared to our mastery of the classical world. In most applications of quantum processes, we merely arrange the ingredients and passively observe the outcome: in microelectronic devices, the band structure of semiconductors is frozen long before the first bits flow; in accelerators and nuclear reactors, we are only spectators of processes taking place 6 orders of magnitude faster than the fastest present experimental controls.

Our gross mastery of nature, from chemical plants to satellites and computers, is a result of real-time control and manipulation of classical systems. This begs the question: what could we gain with similar real-time fine control of quantum systems. In other words, if thermodynamics could be used to engineer steam engines, what would come out of engineering quantum systems?

An insight into this question was given by Feynman [Fey82] who pointed to the massive parallelism inherent in quantum systems. A classical system of n objects each with k possible states is described by $n \log k$ integers. Meanwhile, the quantum state of a similar system requires $\sim k^n$ complex numbers to describe it. This complexity of describing even a relatively simple quantum objects lies behind our failure to understand and predict the behavior of many important systems, including molecules, phases of condensed matter and chemical reactions. Feynman asked if,

instead of representing and manipulating the state of a quantum system classically, the behavior of one quantum system could be simulated by another *quantum* system. In this way, rather than presenting an obstacle, the massive parallelism inherent in quantum systems could be used as a resource to make predictions about systems that hitherto remained unaccessible to systematic inquiry.

At the time of Feynman's proposal, it was not known what kind of physical systems could be simulated by a quantum system. In a classical setting, the question of simulating one system with another was addressed in a general form by Church [Chu36] and Turing [Tur36] who proved that any classical simulation or computation could be realized on any classical system satisfying a certain set of criteria (so-called Turing machine). A similar statement was proved for quantum simulation by Deutsch [Deu85] who proved that any quantum simulation could be performed on any *quantum* system satisfying a given set of criteria (so called universal quantum computer).

Paralleling classical information theory, Feynman's and Deutsch's work stimulated the new field of quantum information. A number of results that show the capabilities of quantum systems have been derived, including limits to capacities of quantum communication channels [SW98], methods for quantum error correction [Sho95, Ste96] and quantum algorithms for solving important problems with much lower asymptotic bounds on running time than their classical counterparts, including Fourier transforms [NC04], integer factoring [SLAH94] and database searches [Gro96].

Despite the fragility of quantum objects, the last two decades have also seen a dramatic improvement in our ability to manipulate and engineer them. Quantum superpositions of photons have been preserved over kilometer-scale distances, allowing long-distance quantum communication [UTSM+07, GT07] and practical quantum cryptography [BB84, Eke91]. Even before Feynman's proposal, the sensitivity of quantum states was employed to make atomic clocks and superconductor-based magnetic field sensors with superior accuracy and precision. In the past four years, clocks based on optical transitions in atoms [ATK08, LZC+08] and ions [RHS+08] have approached the sensitivity needed to test fundemental physics such as the time variation of the fine structure constant [LFDF09]. Ideas from quantum information have been used to make clocks using hitherto inaccessible atomic transitions [RSH+07] and to improve the precision of existing clocks [SSLV10]. At a more fundamental level, the control of increasingly large quantum systems has posed questions how to characterize entanglement between particles and understand the process of decoherence.

Our increasing ability to manipulate quantum objects has inspired hope that with sufficient effort, a practically useful quantum computer could indeed be built. A set

of requirements for realizing a quantum computer was spelled out by DiVincenzo in 1998 [DiV00]:

1. A scalable physical system with well-characterized quantum bits (qubits)
2. The ability to initialize the state of these qubits
3. Long decoherence times, much longer than the gate operation time
4. A universal set of quantum gates
5. A qubit-specific measurement capability

While realizing all of these requirements in a single system has so far proven elusive, realizing a subset of them may still lead to realizing quantum systems not fully amenable to classical simulation. With sufficiently many initialized qubits, a limited set of interqubit operations such as next neighbour interactions may be sufficient to realize a number of Hamiltonians relevant to modern condensed matter research [PC04b, PC04a].

On this road to quantum computation and simulation, a variety of systems have been proposed and demonstrated: superconducting circuits [CW08], atoms in optical lattices [Blo08], trapped ions, atom cavity QED [Kim08], linear optics, electronic quantum dots [PJT+05, LD98, KBT+06], nitrogen vacancy centers [CGT+06, DCJ+07], optical quantum dots [FEF+08], polar molecules [ADD+06], and others.

As could be expected when dealing with a difficult scientific and engineering goal, different systems afford different and complementary advantages:

- Superconducting circuits provide strong, long-distance interactions via superconducting resonators [WSB+04, BCK+08] and, being based on lithographic fabrication technology, are scalable to many qubits. However, they are limited by short coherence times [HKD+09, WHA+09].
- Atoms in optical lattices provide large numbers of qubits with good coherence times and, as of recently, single-atom addressing and high-fidelity initialization [WES+11, BPT+10]. However, interaction between separate qubits are limited to $\sim$ 1kHz by the rate of atom tunneling in optical potentials [WPGH05]. Rydberg excitations [GMW+09, UJH+09] promise faster gates but achieving high fidelities remains challenging.

- Ions offer unprecedented coherence times [BHIW91] and strong interactions enabling high-fidelity gates [BKRB08] and multi-particle entanglement [MSB+11]. However, as described in Section 2.3, scaling ion systems to hundreds of qubits presents significant challenges.

- Photons afford simple initialization and easy communication over long distances [GT07]. However, they interact so weakly that the dominant interactions are accomplished via projetive measurement. With the limited efficiency of detectors and brightness of available single-photon sources, the scaling of photonic systems is difficult.

Given the limitations of any one of these systems, it is very likely that any future large quantum information processor will be a hybrid system. In such a system, one physical implementation (such as polar molecules) could provide long coherence while another (for example, superconducting circuits) could provide interaction and communication [ADD+06].

1.1 Statement of Thesis Work

This thesis presents the first steps towards the realization of two hybrid quantum information processing systems.

In one approach, cold trapped ions, promising good coherence times and fast interactions, are combined with cold neutral atoms, promising scalability to many thousands of qubits.

In the second approach, cold ions are trapped on a microfabricated chip, and interfaced to photons via an optical resonator. The ion trap chip is made using scalable fabrication techniques compatible with solid-state quantum information approaches, such as superconducting circuits.

The work in thesis contains several scientific contributions:

1. the first demonstration of co-trapped cold atoms and ions [GCOV09, CGC+07]

2. the first investigation of ion-atom collisions in the cold regime via charge exchange [GCOV09]

3. a derivation of theoretical micromotion limits to the collision energy in cold ion-atom systems

4. the first integration of a medium-finesse optical cavity with a microfabricated ion trap

For realizing the above accomplishments a number of new technical developments were necessary, including:

1. development of external cavity diode lasers based on near-UV laser diodes for Yb^+ trapping and manipulation [KCCK06]

2. isotope-selective loading of ion traps from a magneto-optical cold atom trap [CGC+07]

3. fabrication of a scalable array of ion traps using lithographic techniques

1.2 Structure of Thesis

The thesis begins in Chapter 2 with a short overview of trapped ions as a theme common to both the presented hybrid approaches. The main body of the thesis is split into two parts addressing the two hybrid systems - ions combined with cold atoms and ions combined with an optical resonator.

Chapter 3 opens the first part of the thesis with an introduction to hybrid ion-atom systems for quantum information processing and the basic physics of ion-atom interactions governed by the r^{-4} polarization potential.

Chapter 4 presents the first experimental realization of a hybrid cold-ion / cold-atom system. The interaction of ions and atoms is investigated by observing inelastic charge exchange collisions between Yb^+ ions and laser-cooled Yb atoms trapped in a magneto-optical trap. Elastic momentum-transfer processes are investigated through collisions of Yb^+ ions with laser-cooled Rb atoms. Surprisingly, collisions of trapped ions with atoms at a lower temperature lead to heating of the ions.

The heating of trapped ions in collisions with cold neutral atoms is explained by the effect of trap-induced ion 'micromotion' in Chapter 5. While the micromotion effect can be reduced through a careful control of the ion trapping potential, a fundamental heating mechanism persists even at zero collision energy. Chapter 5

presents the first classical derivation of the temperature limits imposed by micromotion heating and explores the consequences of these limits on hybrid ion-atom systems.

The second part of the thesis begins in Chapter 6 with an introduction to photons as a vehicle for communicating quantum information at a distance. Realizing efficient coupling of ions to photons is difficult and Chapter 6 discusses three relevant approaches: high-NA imaging, use of optical resonators and collective coupling.

Chapter 7 presents a system for coupling ions to photons based on a fusion of ideas from Chapter 6: a collection of ions is placed inside a focused mode of an optical resonator. The chapter is split into three sections. Section 7.1 presents the design criteria for interfacing ions to photons and motivates the approach adopted in this thesis. Section 7.2 describes the design of a practical system, leaving the details of implementation for Section 7.3.

The operation of the ion-resonator system, including loading of isotopically-selected Yb^+ ions into the linear trap array and the coupling of individual ions to the optical resonator, is presented in Chapter 8.

Chapter 8 concludes the second part of the thesis with perspectives for future experiments using the ion array-resonator system, including collective coupling of ions to the mode of an optical resonator, probabilistic entanglement between ions and photon storage in ionic ensembles.

The thesis has four appendices:

Appendix A gives a formal theory of micromotion in ion traps, relevant to the derivation of the micromotion limits in Chapter 5.

Appendix B presents the technical details of the use of near-UV laser diodes for cooling and trapping of ions.

The work in on isotope-selective loading of a planar ion trap via a magneto-optical atom trap was published in [CGC+07] and is included as Appendix C.

The work on ion-atom charge exchange collisions was published in [GCOV09] and is included in Appendix D.

Several items presented in this thesis overlap with other MIT theses. Andrew Grier recorded most of the ion-atom collision data and assembled the optical resonator in the ion-photon experiment [Gri11]. Brendan Shields observed Yb^+ ions produced via ionization of atoms trapped in a magneto-optical trap [Shi06]. Jonathan Campbell helped record the first trapped ion signals using the Channeltron detector [Cam06].

Chapter 2

Quantum Information with Trapped Ions

Among the systems proposed for quantum information processing, as well as among physical systems in general, trapped ions have demonstrated the highest degree of control over quantum objects. Coherence times of a single ion qubit are measured in minutes [BHIW91] and 99.991 (1) % fidelities in the readout of the internal ion states has been demonstrated [MSW+08].

The long range electrostatic interaction between ions has been used to perform quantum gates as was first proposed by [CZ95] and realized by [SKHR+03]. Modern schemes such as [MlSr99] have achieved decreased sensitivity of gates to the residual motion of the ions, enabling gates with the highest fidelities of any system (99.3(1)%, [BKRB08]).

Control over small ion chains has been used to achieve entanglement between up to 14 particles [MSB+11] and a number of practical quantum algorithms have been demonstrated, including quantum error correction [CLS+04], quantum Fourier transforms [CBL+05] and Grover's search algorithm [BHL+05].

To motivate the coupling of ions to atoms and photons, this chapter presents a short introduction to trapped ions, their use for quantum information processing and the limitations to the scaling of ion traps to much larger numbers of qubits.

2.1 Radio-Frequency Ion Traps

The basic ingredient for manipulating trapping ions are traps that holds charged particles stably confined in vacuum. As first shown by Earnshaw in 1842 [Ear42], such trapping cannot be accomplished using static electric fields alone. A quick proof

is as follows:

Suppose that a charged particle is held stationary at point r_0 in vacuum. Then, electrostatic potential Φ must have a local extremum Φ_0 at this point. Now, consider a ball B of radius R about point r_0. If ϕ_0 is a local extremum then, for all sufficiently small $R < R_0$, the average value of ϕ on the surface S of B

$$\Phi_{avg}(r_0; R) = \frac{1}{4\pi R^2} \int_{S(R)} \Phi dA$$

must be either strictly smaller or strictly larger than ϕ_0. In free space the electrostatic potential satisfies Laplace's equation $\nabla^2 \phi = \nabla \cdot (\nabla \phi) = 0$ so, for $R < R_0$:

$$\begin{aligned}
\frac{d\Phi_{avg}(r_0;\ R)}{dR} &= -\frac{2}{4\pi R^3} \int_{S(R)} \Phi dA + \frac{1}{4\pi R^2} \int_{S(R)} \Phi \frac{\partial_r (4\pi R^2)}{4\pi R^2} dA \\
&+ \frac{1}{4\pi R^2} \int_{S(R)} \nabla \Phi \cdot dA \\
&= \frac{1}{4\pi R^2} \int_{B(R)} \nabla \cdot (\nabla \Phi)\, dV \\
&= 0
\end{aligned}$$

Since the electrostatic potential in free space is smooth, $\lim_{R \to 0} \Phi_{avg}(r_0;\ R) = \Phi_0$ so, for $R < R_0$ we conclude that $\Phi_{avg}(r_0;\ R) = \Phi_0$. Hence, r_0 cannot be an extremum point of the potential and a charged particle cannot be held in equilibrium in free space using only electric fields.

One way to sidestep Earnshaw's result has been to employ strong magnetic fields as is done in a Penning traps pioneered by Dehmelt [Deh68] . Another, more compact and flexible solution has been to use radio-frequency (RF) electric fields as first proposed by Wolfgang Paul in 1953 [PS53].

RF traps are based on inhomogeneous, sinusoidally varying electric fields of the form

$$E \equiv \mathrm{Re}\left(\tilde{E}(r)\, e^{i\Omega t}\right)$$

where Ω is the RF frequency and $\tilde{E}(r)$ is the complex vector describing the spatial variation of both amplitude and phase of the trapping field. At high RF frequencies, the spatial excursion of a particle with mass m_i and charge Q driven by the field E during one RF oscillation period will be small. Consequently, to first order, the

particle will see a homogeneous field $E(r_0)$ and, on a timescale of Ω^{-1}, its motion will be described by $r(t) \approx r_0 + r_{mm}(t)$ where

$$r_{mm}(t) = -\frac{QE}{m_i\Omega^2}$$

describes a fast 'micromotion' of the particle driven by the applied RF field. The micromotion $r_{mm}(t)$ allows the particle to sample the inhomogeneity of the electric field near r_0 which produces an additional force on the particle:

$$\begin{aligned} f(t) &= Q\left(E(r_0 + r_{mm}) - E(r_0)\right) \\ &\approx \left((r_{mm}\cdot\nabla)E\right)_{r=r_0} \\ &= -\frac{Q^2}{m_i\Omega^2}\left(\mathrm{Re}\, e^{i\Omega t}\tilde{E}\cdot\nabla\right)\left(\mathrm{Re}\,\tilde{E}e^{i\Omega t}\right) \end{aligned}$$

The quality of this micromotion approximation will correspond to the magnitude of f relative to the homogeneous field force $QE_r(r_0)$, commonly expressed in terms of the so-called Mathieu parameter[1]:

$$q = \frac{2Q\left|\nabla\tilde{E}\right|}{m_i\Omega^2} \tag{2.1}$$

For sufficiently large Ω, q will be small and the effect of the force f during one RF cycle will be small. However, the mean value of f over many RF periods

$$F_{sec}(t) = \langle f\rangle = \frac{\Omega}{2\pi}\int_0^{2\pi/\Omega} f(t)\,dt = -\frac{Q^2}{4m_i\Omega^2}\left\{\left(\tilde{E}\cdot\nabla\right)\tilde{\tilde{E}} + c.c.\right\}$$

will, in general, be nonzero and will add up to influence the overall ('secular') trajectory of the charged particle.

At RF frequencies commonly used for the trapping of charged particles, the radiation effects in the trap field can be neglected, corresponding to $\nabla\times\tilde{E} = 0$. The RF field can then be expressed as the gradient of a scalar RF potential as $\tilde{E} = -\nabla\Phi$, for which

[1] In quadrupole RF traps with no DC fields, the Mathieu parameter q is the only unitless parameter influencing the ion's motion. This is discussed in much more detail in Chapter A

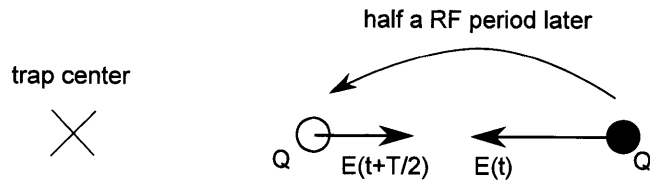

Figure 2-1: Operation of a Paul trap: a charged particle executes micromotion driven by an inhomogeneous RF electric field E increasing in magnitude away from the trap center; during the part of the RF cycle where the particle is farther away from the trap center, it feels a stronger restoring force, resulting in a net trapping effect.

$$\left(\tilde{E}\cdot\nabla\right)\bar{\tilde{E}}+c.c. \;=\; \left(\nabla\Phi\cdot\nabla\right)\nabla\bar{\Phi}+c.c.=\nabla\left|\Phi\right|^2$$

In this case, the secular force $F_{sec}(t)$ is conservative and itself the gradient of a corresponding potential effective 'secular' potential:

$$V_{sec}=\frac{Q^2\left|\tilde{E}\right|^2}{4m_i\Omega^2}=\frac{m_i}{2}\left\langle\dot{r}_{mm}^2\right\rangle \tag{2.2}$$

The effective secular potential derives from the RF driven micromotion of the ion and is precisely equal to the mean kinetic energy of this driven motion. Being proportional to the electric field power, it will tend to confine particles close the minima of the RF electric field. Fields with such minima can be easily created in vacuum, leading to a stable trapping of charged particles.

In 1D, this trapping mechanism has a simple explanation (Figure 2-1). As the particle's micromotion excursion and the driving RF field are out of phase, the particle will be farther away from the trap origin during the part of the RF cycle where it experiences an electric force directed towards the origin. For a field with a minimum near the origin, this restoring field will be larger than the counteracting field during the other half of the RF cycle, pushing the particle towards the trap center.

In practical ion traps, to avoid instability and parametric heating effects (Appendix A), the RF frequency is chosen to keep the maximal value of the Mathieu parameter

$$q_{max}=\frac{2Q\left|\nabla\tilde{E}\right|_{max}}{m_i\Omega^2}$$

below 0.3. This is almost always possible with a suitable RF drive to the trap. In this case, the secular potential can be expressed as:

$$V_{sec}\left(\vec{r}\right) = \frac{q_{max}Q\Phi_0}{4}\bar{V}_{sec}\left(\frac{\vec{r}}{L_0}\right) \tag{2.3}$$

where Φ_0 is the amplitude of the RF potential applied to the trap electrodes and

$$\bar{V}_{sec}\left(\vec{\rho}\right) = \frac{1}{2}\frac{\left|\tilde{E}\left(L\vec{\rho}\right)\right|^2}{\Phi_0\left|\nabla\tilde{E}\right|_{max}}$$

is a unitless 'reduced' trap potential expressed in coordinates scaled by the characteristic trap dimension L_0 given by the distance between the trap center and the nearest electrode.

For ions confined near the bottom of the trap at $r = 0$, the RF potential can be Taylor-expanded as

$$\Phi\left(\vec{r}\right) = \tilde{E}_0 + \frac{1}{2}\vec{r}\cdot\mathbf{g}\cdot\vec{r} + O\left(|r|^3\right)$$

where $g_{ij} = \partial_{ij}\Phi$ is the RF potential quadrupole matrix at $r = 0$.

The non-zero offset electric field $\tilde{E}_0$ at the trap center will introduce driven RF micromotion even for cold particles at the trap center. In addition to introducing Doppler shifts in optical addressing, this micromotion can drive nonlinear heating effects. In ion-atom hybrid systems, the residual RF field $\tilde{E}_0$ is even more damaging, setting a limit to the minimal system temperatures.

For low offset fields $\tilde{E}_0$, the secular potential near the trap center is dominated by the RF quadrupole term as:

$$V_{sec}\left(\vec{r}\right) = \frac{q_{max}Q\Phi_0}{8}\frac{E^2\left(\vec{r}\right)}{\Phi_0\left|g\right|_{max}} \tag{2.4}$$

corresponding to harmonic confinement of the particle with frequencies given by

$$\omega_i^2 = \frac{qQ\Phi_0}{4m_iL_0^2}\Upsilon_i \tag{2.5}$$

where

$$\Upsilon_i = \left(\partial_{ii}^2\bar{V}_{sec}\right)_{r=0} = \frac{L_0^2\left|g_{ii}\right|^2}{\Phi_0\left|g\right|_{max}}$$

are unitless, scale-free quantities that depend only on the trap shape along the eigendirections $\hat{x}_i$ of the trap quadrupole potential.

The trap electrodes that are most effective at producing confinement near the trap origin conform to the hyperbolic equipotential surfaces of $\vec{r} \cdot \mathbf{g} \cdot \vec{r}$. In this case, the RF field is a perfect quadrupole with the resulting trap depth of $U_{max} \sim 1$ and vibration frequencies given by $\Upsilon_i \sim 1$. In such quadrupole traps, the single particle equations of motion will also be fully linear, helping avoid parametric heating effects (Appendix A).

The planar traps presented in this thesis exhibit strong deviations from the quadrupole potential, decreasing the scaled trap depth from $U_{max} \approx 0.03$ to $U_{max} \approx 0.2$ (Section 7.2.2.3) and also introducing possible nonlinear heating effects (Chapter A). Even at these reduced depths, with typical RF potentials measured in the hundreds of volts, trap depths in excess of the thermal energy of room temperature ions are easily obtainable, surpassing the largest depths of neutral atom traps by more than three orders of magnitude.

In planar ion traps, the decreased value of Υ_i ($\Upsilon_i \approx 0.2$) is overcome by the the typical small small trap scale L, preserving the vibration frequencies in the 1-2 MHz range (Section 7.2.2).

2.2 Laser Cooling of Ions

The strong, deep confinement of ions in RF traps was instrumental in the early work on trapping and cooling of atoms. Predating the first laser cooling of neutral atoms [ABLM81] by three years, Doppler cooling of atomic ions was demonstrated by Wineland [WDW78] and, separately, by Dehmelt [NHTD78] in 1978.

To obtain sufficient light forces, the initial Doppler cooling of ions is usually performed on a strong atomic transition with linewidths $\Gamma/2\pi$ >100 kHz ($\Gamma = 2\pi \times 19.6$ MHz for the Yb^+ $S-P$ transition used in this thesis). In this regime, a semiclassical model of Doppler cooling applies, both in the free-particle regime for $\Gamma > \omega$ and in the resolved-sideband regime $\Gamma < \omega$ [Ste86]. In this picture, a trapped ion scatters the photons from the cooling beam at a rate:

$$\Gamma_{sc} = \frac{\Gamma}{2} \frac{s}{s + 1 + \left(\delta - \vec{v} \cdot \vec{k}\right)^2 / (\Gamma/2)^2} \tag{2.6}$$

where Γ the linewidth of the atomic excited state, s the saturation parameter scaling linearly with the laser intensity, $\delta < 0$ the laser detuning from the atomic resonance, and v is the ion's velocity. At typical laser detunings $\delta \sim \Gamma$ and temperatures achieved

by Doppler cooling of small samples of ions, $\vec{v} \cdot \vec{k} \ll \Gamma$ and

$$\begin{aligned} \Gamma_{sc} &\approx (\Gamma_{sc})_{v=0} - \beta \cdot v \\ \beta &= -\frac{\hbar k \Gamma}{2} \frac{s}{s+1} \frac{2\delta k / (\Gamma'/2)^2}{\left[1 + \delta^2 / (\Gamma'/2)^2\right]^2} \end{aligned}$$

with $\Gamma' = \sqrt{1+s}\Gamma$ the saturation-broadened atomic linewidth[2].

The scattering of photons with momentum $\hbar k$ out of the cooling beam causes a mean radiation pressure force $\Gamma_{sc}\hbar k$. The dependence of this force with the ions' velocity causes a viscous drag with friction coefficient β which dissipates the ions' kinetic energy at a mean rate

$$P_{cool} = \beta \langle v^2 \rangle$$

The radiation cooling force is composed of individual photon scattering events. After photon N scatterings, the fluctuations of the cooling force will lead to an increase in the variance of the ions momentum along the beam of $N(\hbar k)^2$. The scattering of photons into free space also causes random recoils. After N scatterings, the momentum variance acquired by the atom in this process will also be $N(\hbar k)^2$. Together, these two processes lead to a heating power

$$P_{heat} \approx 2 (\Gamma_{sc})_{v=0} (\hbar k)^2 / 2m$$

Equating the fixed cooling rate to the mean velocity-dependent cooling rate yields the ions' final mean kinetic energy:

$$\langle E_k \rangle = \frac{\hbar \Gamma'}{4} / \frac{2(-\delta)/(\Gamma'/2)}{1 + \delta^2/(\Gamma'/2)^2} \tag{2.7}$$

As discussed in the previous section, close to the bottom of the trap, the potential experienced by the ions will generally be harmonic, in which case, by the virial theorem, $\langle E_k \rangle = k_B T_D / 2$ with T_D - the ions' equilibrium temperature under Doppler cooling - reaching a minimum of $\hbar\Gamma'$ for $\delta = -\Gamma'/2$.

[2]Static electric fields displace ions away from the center of RF trap, leading to RF-driven micromotion. The associated Doppler shifts cause the optimal laser cooling detuning to be larger than Γ, with a corresponding increase in the achievable ion temperature.

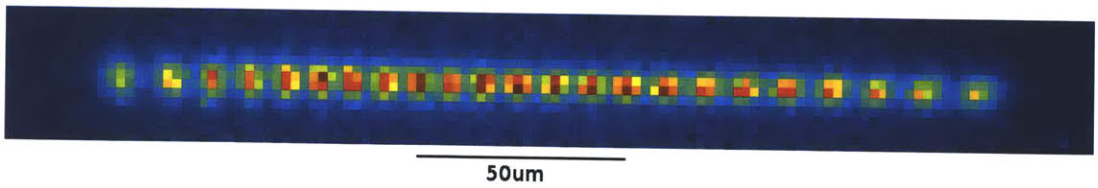

Figure 2-2: Linear chain of individual trapped $^{174}Yb^{+}$ ions produced in the setup from Section 7.1

2.2.1 Ion Coulomb Crystals

When cooled, clouds of trapped ions condense to form ordered crystals, with the ion-ion repulsion balanced by the trap confinement [WBI+87, DPC+87]. The balance of forces acting on a small part of the ion crystal then implies $\nabla V_{trap} = QE_{cry}$ with $V_{trap} = V_{sec} + V_{DC}$ the total trap potential including both the RF secular potential and any DC potential in energy units and E_{cry} the static electric field produced by the ion crystal E_{cry}.

In large crystals, the ions can be thought of as a charge fluid of density $n(r)$. Since E_{cry} satisfies the free-space Poisson equation, the ion density n is related to the trap potential as:

$$\nabla^2 V_{trap} = Q\nabla \cdot E_{cry} = 4\pi Q^2 n\Omega$$

By Laplace's equation, the divergence $\nabla^2 V_{DC}$ of the part of the trap potential due to static electric fields vanishes. When the frequency of the RF field is adjusted to keep the Mathieu stability parameter constant, this results in an ion density independent of the ions' mass m_i as:

$$n = \frac{\nabla^2 V_{trap}}{4\pi Q^2} = \frac{q\Phi_0}{16\pi QL^2}\nabla^2 \bar{V}_{sec} \tag{2.8}$$

The corresponding ion spacings in typical traps is between $2\mu m$ and $20\mu m$, allowing the addressing of individual ions using lasers, especially if the trap is relaxed in one direction, causing the ions to arrange in one-dimensional linear chains (Figure 2-2).

When excited, ion crystals oscillate in a series of normal modes at frequencies ω_k , starting with the center of mass mode where the whole crystal oscillates at the trap frequency. The k-th mode will correspond to oscillation of the j-th ion with amplitude U_{jk} where the matrix U_{jk} can be chosen to be orthonormal. In terms of the mode coordinates, the Hamiltonian for the ions' motion close to the equilibrium

position takes the form:

$$H = \sum_k \left(\frac{P_k^2}{2m_i} + \frac{m_i \omega_k^2 R_k^2}{2} \right)$$

where R_k and P_k are the coordinate and momentum of the k-th mode with the corresponding displacements $r_j = U_{jk} R_k$ and momenta $p_k = U_{ki} P_i$. For the center of mass mode, $U_{jk} = 1/\sqrt{N}$ with $r_j = R_k/\sqrt{N}$ and $p_j = P_k/\sqrt{N}$.

2.2.2 Quantization of Vibrational Modes of Ion Crystals

For small ion crystals in harmonic traps, both the the ions' interactions with the environment and the heating effects due to the trap RF fields are heavily suppressed, resulting in very high Q's of the individual modes. This low intrinsic decoherence allows laser cooling on narrow ion transitions to be used to reach very low temperatures. In this limit, the quantization of the ions' motional modes becomes important with each mode described by its creation and annihilation operators:

$$a_k = \sqrt{\frac{m_i \omega_k}{2\hbar}} \left(R_k + \frac{i}{m_i \omega_k} P_k \right)$$

with $R_k = \left(a_k + a_k^\dagger \right) a_{0,i}$ with $a_{0,k} = \sqrt{\hbar / 2 m_i \omega_k}$ the extent of the ground state wavefunction of mode k as measured by R_k.

2.2.3 Sub-Doppler Cooling

A cooling laser addressing an atomic dipole transition excites transitions between the eigenstates of a given vibrational mode via the dipole potential $V_d(t)$. In the Heisenberg picture, $V_d(t) = -\sum_{k,j} E_k^L U_{kj} d_j \cos(kr - \omega t)$ with $\vec{E}^L \cos(kr - \omega t)$ the laser electric field and $d_j = d \left(\sigma_j e^{-i\omega_0 t} + \sigma_j^\dagger e^{+i\omega_0 t} \right)$ the atomic dipole operators with ω_0 the atomic transition frequency. For a laser tuned close to the atomic resonance, terms oscillating at $\approx 2\omega_0$ can be neglected, yielding

$$V_d = -d \sum_j E_j^L \sigma_j \exp \left\{ i\delta t - i \sum_k \eta_{jk} \left(a_k e^{-i\omega_k t} + a_k^\dagger e^{+i\omega_k t} \right) \right\} + c.c.$$

with $\eta_{jk} = \vec{k} \cdot U_{jk} a_{0,k}$ the Lamb-Dicke parameter measuring the extent of the ground state wavefunction of the ion j due to mode k along the laser direction in units of the

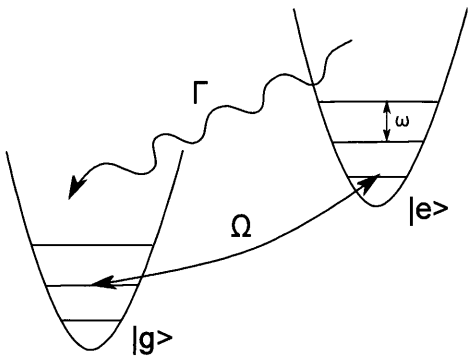

Figure 2-3: Sideband cooling for state initialization of trapped ions

light wavelength. For the cooling laser propagating along the oscillation direction of a center of mass mode, $\eta_{jk} = ka_{0,cm}$ with $a_{0,cm}\sqrt{\hbar/2M\omega_k}$ the real-space extent of the ground-state wavefunction of the center of mass of the entire crystal.

At small values of the Lamb-Dicke parameter,

$$V_d \approx -d\sum_j E_j^L \left[\sigma_j e^{i\delta t} - i\sum_k \eta_{jk} e^{i\delta t}\left(\sigma_j a_k e^{-i\omega_i t} + \sigma_j a_k^\dagger e^{+i\omega_i t}\right)\right] + c.c.$$

The cooling laser is seen to drive three types of atomic transitions: those which leave the number of vibrational quanta in the mode k unchanged, those that increase it by one and those that decrease it by one. The last type of transitions can be employed to cool the ions' motional modes below the Doppler limit (2.7) as shown on Figure 2-3.

Sub-Doppler cooling is usually accomplished via a variant of the resolved sideband cooling shown in Figure 2-3. Two of the ions' internal states, $|g\rangle$ and $|e\rangle$ are coupled via a laser beams resulting in an effective Rabi frequency Ω. With the decay rate Γ from $|e\rangle$ to $|g\rangle$ smaller than the mode vibration frequency ω, each of the two states splits into individual harmonic oscillator states corresponding to n motional quanta in the crystal's vibrational mode. With the minimum quantum number under cooling scaling as $(\omega/\Gamma)^2$ for $\eta_L \ll 1$, cooling of the vibrational modes of an ion chain to the quantum ground state becomes possible. This was realized by [DBIW89].

2.3 Scaling of Trapped Ions

With a growing number of ions in a trap, the number of vibrational modes of the ion crystal increases. Unlike in solid-state crystals, due to the long range of the Coulomb interaction, the spacing between the vibrational modes in an ion crystal remains largely independent of the number of ions [Ste97]. While at first sight, this allows spectral addressing of individual motional modes of the crystal for ion-ion gates, performing such gates on large crystals presents a number of obstacles as discussed by [WMI+97].

As the ion crystal grows, the coupling of a laser beam addressing an individual ion to the joint crystal mode decreases as $N^{-1/2}$, necessitating higher laser powers to drive multi-qubit gates. High laser powers lead to AC Stark shifts which both complicate the manipulation of individual ions and cause errors in single-ion addressing [GRL+03]. Additional problems arise from trap anharmonicities which couple crystal modes and lead to dissipation of excitations of a single mode. The coupling to other crystal modes also forces these to be cooled to the ground state, which presents significant difficulties in larger crystals.

[KMW02] proposed avoiding the problem of controlling large ion crystals by splitting the ions into a large number of independent 'processing zones'. Using < 10 ions, arbitrary quantum operations could be performed in each zone. The quantum information would be communicated between the individual trapping zones by physically moving ions. The operation of one trapping zone, including quantum error correction was demonstrated by [CLS+04]. Recently, ions have been moved between zones with minimal heating by [BOV+09].

Scaling the proposal from [KMW02] to thousands of ions presents considerable challenges, some of which were explored by [Cro05]. To accurately move many ions, very large numbers of control electrodes need to be driven with fast and accurate voltage pulses; laser light needs to be accurately delivered to each trapping zone; ion fluorescence needs to be efficiently collected to detect internal states.

A more fundamental problem arises from the heating of ions by fluctuating electric fields close to trap surfaces. The heating rates observed in traps so far are inversely proportional to the trap frequency and scale as d^{-4} with distance from the electrode surface [DOS+06]. With typical heating rates of 1 vibrational quantum/ms at ion-electrode distances of 100 μm, the anomalous heating presents a big obstacle to integration of multi-electrode registers at distance scales smaller than 50 μm .

The problem of anomalous heating has recently been partially addressed by cool-

ing of traps to crygenic temperatures. At distance scales of 75 μm, [LGA$^+$08] has demonstrated the reduction of the anomalous heating rate by two orders of magnitude relative to room-temperature traps.

Chapter 3

Hybrid Ion-Atom Systems

As described in Chapter 2, the long-range interaction between ions makes controlling their interactions in large ensembles difficult. Atoms trapped in optical lattices suffer from the opposite problem - the next-neighbor interactions in these systems are very weak ($\sim h\times 100$ Hz), limiting the operations that can be performed before the atoms are irreversibly lost.

A hybrid system combining cold atoms and cold ions could potentially address both of these problems. The ion-atom interaction potential is much stronger than the atomic van der Waals potential, allowing significantly faster gate speeds. [ICZ07] predicted that, by bringing the ion sufficiently close to the atom, the interaction potential can be made comparable to the trap potentials, resulting in gate speeds comparable to the 100kHz atom trapping frequencies.

Scaling as r^{-4} , the ion-atom potential also has a much shorter range than the Coulomb interaction between trapped ions, allowing for controlled local interactions between an ion and a low-entropy ensemble of trapped cold atoms (obtained, for example, as the Mott insulator state in an optical lattice). Based on this idea, [DIC10] envisioned a scalable system using an ion as a "read head" to controllably address a large number of cold atoms.

Hybrid ion-atom systems also show promise for quantum simulation. Ions placed in a Bose-Einstein condensate were postulated by [CKL02] to behave similar to charge impurity states in a superconductor, giving rise to a family of localized defect states. [CCR00] studied the transport of an ion in an ultracold gas of its parent species and predicted significant quantum corrections arising from coherent charge exchange processes.

In spite of this theoretical interest an experimental proposal by [SML05], at the

start of this thesis, no experiment had demonstrated trapping of cold atoms together with cold ions. Before presenting our first realization of a hybrid ion-atom system, this chapter presents an overview of ion-atom interaction in the relevant energy range.

3.1 Overview of Ion-Atom Collisions

Investigations of ion-atom scattering have a long history starting with Langevin's investigations of charge transport in gases [Lan05]. Here, the dominant long-range interaction arises from the polarization of the atom by the ion's electric field. As for any object polarizable object, the resulting interaction energy is $-d \cdot E_i/2$ where $d = C_4 E_i$ the dipole induced in the atom with polarizability C_4 by the ion's electric field $E_i = e/r^2$.

In a mixed sample of cold atoms and cold ions, the r^{-4} interaction will cause scattering of the otherwise unbound particles. The dynamics of this scattering can be described in the center of mass coordinates using a Hamiltonian

$$H = \frac{p^2}{2\mu} - \frac{1}{2}\frac{C_4}{r^4} \tag{3.1}$$

where $\mu = m_i m_a / (m_i + m_a)$ is the effective mass of the ion-atom system. For unbound scattering with center of mass energy E, this should be combined with the initial conditions at $t = 0$: $p(0) = -\sqrt{2\mu E}$, $r(0) \to +\infty$.

Since the total angular momentum L is conserved by the spherically symmetric r^{-4} polarization potential, and H can written in terms of an effective radial potential $V(r)$ as

$$\begin{aligned} H &= \frac{p_r^2}{2\mu r^2} + V(\vec{r}) \\ V(r) &= \frac{L^2}{2\mu r^2} - \frac{C_4}{4r^2} = E\frac{b^2}{r^2} - \frac{C_4}{4r^4} \end{aligned}$$

where $b = L/\sqrt{2\mu E}$ is the collision impact parameter.

To approach the region near $r \approx 0$ where the r^{-4} polarization potential dominates, the system needs conserve angular momentum. This results in an angular momentum barrier of $V_{max} = L^4/8C_4\mu^2 = E(b/r_L)^4$ with peak at $r_b = \sqrt{C_4\mu/L^2} = b/\sqrt{2}$.

The Hamiltonian (3.1) posses a natural length scale [Lan05]

$$r_L = \sqrt[4]{\frac{2C_4}{E}} \tag{3.2}$$

at which the polarization potential is comparable to the total center of mass energy E. After expressing distances in units of r_L, masses in units of μ and energy in units of E, the Hamiltonian (3.1) assumes a universal form:

$$H_e = \frac{p^2}{2} - \frac{1}{4r^4} = \frac{p_r^2}{2} + \frac{b^2}{r^2} - \frac{1}{4r^4} \tag{3.3}$$

After the same rescaling of units, the initial condition at the start of the collision proces becomes

$$\begin{aligned} p(0) &= -\sqrt{2} \\ r(0) &\to +\infty \end{aligned}$$

Since r_L, μ and E are the only classical length, mass and energy scales for the ion-atom scattering problem in the r^{-4} polarization potential, the dynamics in an arbitrary collision is reducible to a *single* universal scattering problem. A consequence of this is that *all* classical cross-sections governed only by the r^{-4} potential will scale as $\sigma(E) \sim \sigma_L$ where $\sigma_L = \pi r_L^2 \sim E^{-1/2}$ is the classical ion-atom interaction cross-section first derived by Langevin [Lan05] . An important property of cross-sections scaling as $E^{-1/2}$ is a reaction rate $R \sim v\sigma$ which is independent of energy. In the particular case of Langevin collisions, $R = n_{atom}K$ with n_{atom} the atom density and K the Langevin rate coefficient given by

$$K = \pi\sqrt{\frac{4C_4}{\mu}} \tag{3.4}$$

with $\mu = m_i m_a/(m_i + m_a)$ the reduced mass in the ion-atom collisions. The result (3.4) will be very important for interpreting the results of $Yb + Yb^+$ charge exchange experiments in Chapter 4.

In a quantum treatment, the commutation relation between r and p corresponds to $\hbar$ expressed in the new units: $[r, p] = i\bar{\hbar}$ with $\bar{\hbar} = \hbar/(2\mu^2 C_4 E)^{1/4}$. The magnitude of $\bar{\hbar}$ will determine the 'quantumness' of the collision: small values of $\bar{\hbar}$ will correspond to semiclassical collisions while for $\bar{\hbar} \sim 1$ quantum effects can be expected to be important. In terms of the typical angular momentum L_{max} in the Hamiltonian (3.1) $L_{max} = r_L\sqrt{2\mu E}$, $\bar{\hbar}$ can be expressed as $\bar{\hbar} = \sqrt{2}/(L_{max}/\hbar)$. Ion-atom collisions

will assume a strongly quantum character when the typical angular momentum in a collision becomes of order $\hbar$.

$\bar{\hbar} > 1$ in fact exactly corresponds to the quantum limit of scattering in a single partial wave. All partial waves except $l = 0$ will be exponentially suppressed if all the partial waves except $l = 0$ remain confined outside the angular momentum barrier of height

$$\begin{aligned} E_s &= \frac{L^4}{8C_4\mu^2} \\ &= \frac{l^2\,(l+1)^2\,\hbar^4}{8C_4\mu^2} \end{aligned}$$

which corresponds to

$$E < E_s = \frac{\hbar^4}{2C_4\mu^2} \tag{3.5}$$

or $\bar{\hbar} > 1$, as expected.

In summary, at collision energies higher than the s-wave limit E_s, ion-atom collisions can be expected to be well-described with the classical Langevin model. In this regime, the only relevant lengthscale for the collisions is the Langevin radius $r_L = (2C_4/E)^{1/4}$, corresponding to cross-sections scaling as $\sigma_L = \pi r_L^2$ and collision rates independent of the particle energy.

Compared to the r^{-6} potential responsible for collisions between neutral atoms, the r^{-4} polarization potential is stronger and has a longer range. Consequently, the angular momentum of collisions at the same center of mass energy is higher and lower energies E_s are needed to reach the quantum single partial-wave regime. For example, in the $^{174}Yb^{+}$-$^{172}Yb^{+}$ system presented in this thesis, using $C_4 = 143\,a_0^3$ [ZD07], $E_s = k_B \times 50$ nK.

The collision energies reached in this thesis [GCOV09] as well as in the recent ion-BEC experiments [ZPSK10, SHD10] are significantly higher than the s-wave scattering limit. Even if the present experimental problems are addressed, Chapter 5 presents fundamental limits to ion-atom collision energies in typical RF ion traps that are generally higher than the s-wave collision threshold E_s. Consequently, one may expect that in the ion-atom experiments performed the near future, most effects will be accurately described by a semiclassical model similar to the one given in this and the following sections.

3.2 Classical Ion-Atom Scattering

This section presents a short overview of the classical trajectories in an attractive r^{-4} potential and gives analytic expressions for the angular deflection $\Delta\theta$ as a function of the the impact parameter.

The deflection $\Delta\theta$ determines momentum transfer between ions and atoms which governs elastic ion-atom collisions investigated in the case of Yb^++Rb in Chapter 4 of this thesis. The limiting case $\Delta\theta \rightarrow 0$ is also relevant to atom loss as observed in recent ion-BEC experiments .

The character of classical ion-atom collision trajectories will be determined by the ratio of the center-of-mass energy and the angular momentum barrier height $V_{max} = E\left(b/r_L\right)^4$. Trajectories with impact parameter $b > r_L$ will remain outside the outer radial turning point defined by $V(r) = E$, located at $r_0 = r_L e^{\phi}/\sqrt{2}$ with $b^2 = r_L^2 \cosh(2\phi)$. Trajectories with impact parameter $b = r_L\sqrt{\cos(2\phi)} < r_L$ will terminate in a close-range ion-atom collision governed by the molecular collision potentials (Figure 3-1).

The shape of collision trajectories as well as the total angular deflection in the collision can be found by integrating the trajectory equation for $\theta(r)$ in polar coordinates. The radial velocity $r(t)$ of the colliding ion-atom system can be obtained from conservation of H_e:

$$\partial_t r = \pm\sqrt{2/\mu}\sqrt{E + V(r)} \tag{3.6}$$

with the $-$ sign corresponding to inward and the $+$ sign to the outward trajectories. The angular velocity can be obtained from conservation of angular momentum as

$$\mu r^2 \partial_t \theta = L = \sqrt{2\mu E} b \tag{3.7}$$

In the scaled coordinates (3.6) and (3.7) give:

$$\theta'(r) = \frac{\pm b}{r^2\sqrt{1 + V(r)}} = \frac{\pm b}{\sqrt{r^4 + \frac{1}{4} - b^2 r^2}} \tag{3.8}$$

The above integrals can be expressed in terms of elliptic functions. For ingoing trajectories with $b > 1$:

$$\theta(r) = \int_{\infty}^{r} \frac{b d\rho}{\sqrt{\rho^4 + \frac{1}{4} - b^2\rho^2}} = \frac{b}{r_0} F\left(\arcsin\left(\frac{r_0}{r}\right) \mid \frac{r_L^4}{4r_0^4}\right)$$

with $F(\phi|x) = \int_0^{\phi} \left(1 - x\sin^2\theta\right)^{-1/2} d\theta$ the incomplete elliptic integral of the first kind. The total angle change of the trajectory between $-\infty$ and ∞ is:

$$\Theta = \frac{2b}{r_0} K\left(\frac{r_L^4}{4r_0^4}\right) \tag{3.9}$$

with $K(x) = F\left(\frac{\pi}{2} \mid x\right)$ the complete elliptic integral of the first kind.

For large impact parameters, the distance of closest approach will be $r_0 \approx b$. Since, for small x, $K(x) \approx \pi/2 + \pi x/8$, at large impact parameters, total angle change of the trajectory will be:

$$\Theta \approx b\pi/r_0 \approx \pi + \frac{3\pi}{16}\left(\frac{r_L}{b}\right)^4 \tag{3.10}$$

As b approaches r_L, $r_0 \to r_L/\sqrt{2}$ and

$$\begin{aligned} \Theta &\approx 2\sqrt{2}K\left(1 - 4\sqrt{b/r_L - 1}\right) \\ &\approx -\log\left|b/r_L - 1\right|/\sqrt{2} \end{aligned}$$

As $r \to r_L$, the ion starts to orbit the atom for a progressively larger number of turns before eventually escaping back to infinity, corresponding to the divergence of the total deflection angle Θ (Figure 3-1).

For $b < r_L$, the integrand can be put into a standard form by a substitution

$$r \to \frac{1}{\sqrt{2}} \frac{1-v}{1+v}$$

as:

$$\begin{aligned} \theta(r) &= \frac{2b}{\sqrt{1-b^2}} \int_{-1}^{v_f} \frac{1}{\sqrt{\left(v^2 + \tan^2\frac{\phi}{2}\right)\left(v^2 + \cot^2\frac{\phi}{2}\right)}} dv \\ &= \frac{\sqrt{2\cos(2\phi)}}{\sin\phi}\left[\tan\left(\frac{\phi}{2}\right) F\left(\arctan\left(v\cot\left(\frac{\phi}{2}\right)\right), \sec^4\left(\frac{\phi}{2}\right)\cos\phi\right)\right]_{v=-1}^{v=v_f} \\ v_f &= \frac{1-\sqrt{2}r}{1+\sqrt{2}r} \end{aligned}$$

The total angular deflection of the trajectory between $r = \infty$ and the collision point at $r = 0$ is now

$$\Theta = 2\frac{\sqrt{2\cos(2\phi)}}{\sin\phi}\tan\left(\frac{\phi}{2}\right)F\left(\frac{\pi-\phi}{2}, \sec^4\left(\frac{\phi}{2}\right)\cos\phi\right) \tag{3.11}$$

with $\phi = \arccos\left(b^2/r_L^2\right)/2$.

For near head-on collisions corresponding to $b = 0$,

$$\Theta \approx \int_0^\infty \frac{bdr}{\sqrt{r^4+\frac{1}{4}}} = \frac{\Gamma(1/4)^2}{2\sqrt{2\pi}}b \approx 2.62b$$

For $b \to r_L$, $\phi \to 0$ and

$$\begin{aligned}\Theta &\approx \sqrt{2}F\left(\frac{\pi-\phi}{2}, 1\right) = \sqrt{2}\int_0^{(\pi-\phi)/2}\sec\theta\, d\theta \\ &\approx -\sqrt{2}\log|\phi| \approx -\log|1-b/r_L|/\sqrt{2}\end{aligned}$$

A plot of the total angular deflection Θ in the collision is shown on Figure 3-2.

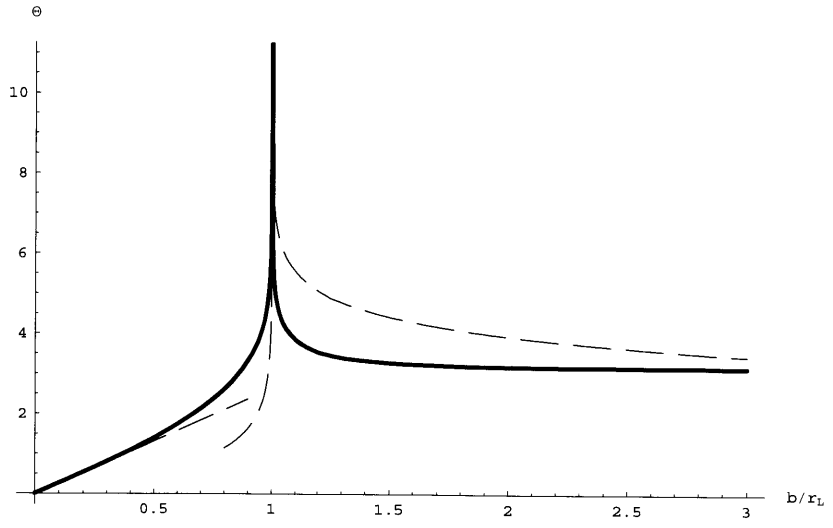

Figure 3-2: Solid line: total angular deflection Θ of the trajectories from Figure 3-1 as function of the impact parameter. Dashed lines: asymptotic approximations close to $b = 0$ and $b = r_L$.

In summary, at large impact parameters the ion's deflection in a collision scales as

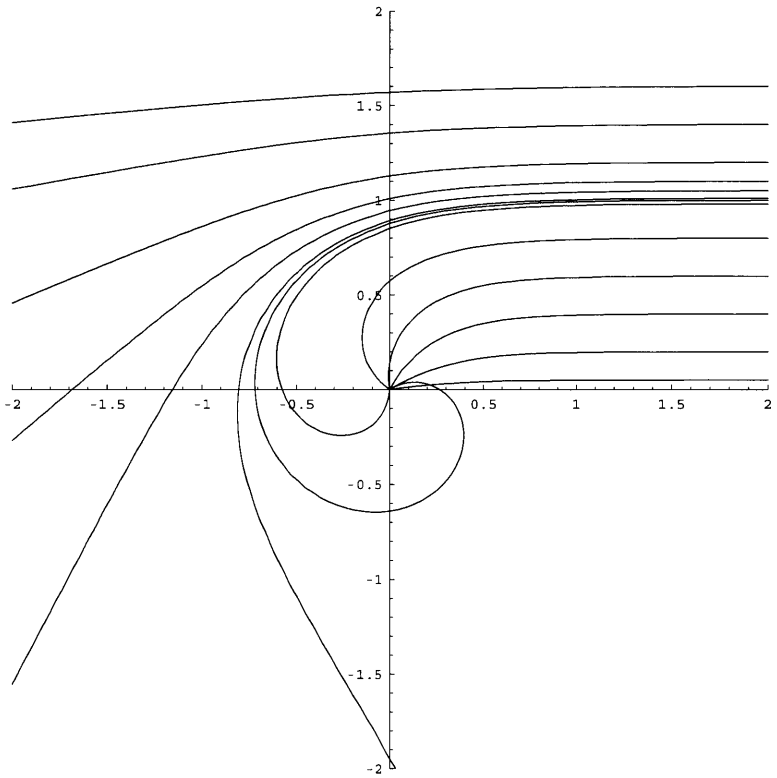

Figure 3-1: Center of mass trajectories in a r^{-4} attractive potential. The axes are scaled to the critical impact parameter $r_L = (2C_4/E)^{1/4}$.

$(r_L/b)^4$. As the impact approaches a critical impact parameter $b = r_L$, the ion and the atom start to circle each other before eventually escaping to infinity again with the number of full turns in the collision trajectory diverging as $-\log|1 - b/r_L|/2\pi\sqrt{2}$. At impact parameters smaller than r_L, the collision trajectory terminates in a hard impact at $r = 0$ along a straight line directed along $\Theta = 2.62b/r_L$.

3.3 Elastic Ion-Atom Scattering

For sympathetic cooling of ions with atoms or [MTMS92] or for considering the interactions of an single ions with an atom condensate [ZPSK10], the dominant effect is elastic ion-atom scattering. As argued in Chapter 5, this scattering typically takes place at energies higher than the s-wave scattering limit and can consequently be described by classical trajectories.

Classical elastic ion-atom collisions are fully described by the deflection $\delta(b/r_L)$. For non-hard core collisions, $\delta = \Theta - \pi$. For elastic close-range collisions, the incoming

and outgoing trajectories will have the same shape so in this case $\delta = 2\Theta - \pi$.

A generic elastic cross-section can then be expressed as:

$$\sigma(E) = 2\pi \int_0^{\pi} \left(\frac{d\sigma_i}{d\Omega} + \frac{d\sigma_o}{d\Omega} \right) f(E, \delta) \sin(\delta) \, d\delta$$

where f is a unitless quantity that depends on the collision energy. Since classical scattering processes that depend only on the r^{-4} potential do not have a natural energy scale, f for such processes cannot depend on E and, as expected, the corresponding elastic cross-section is proportional to the Langevin cross-section $\sigma_L = \pi r_L^2$.

One elastic process that depends only on the r^{-4} potential is the momentum transfer from the ion to the atom in a collision:

$$\Delta p = \mu [I - R(\Delta\theta)] v$$

where $v = p_i/m_i - p_a/m_a$ is the initial relative velocity between the ion and the atom and $R(\Delta\theta)$ a rotation in the plane perpendicular to the system's total angular momentum. The transferred Δp is the quantity of special interest for cooling dynamics of ions and neutral atoms or molecules. For an ion colliding with a cloud of atoms of density n_a, the rate of momentum transfer will be

$$\partial_t p_i = n_a v \pi \int_0^{\infty} b db \, \Delta p(b)$$

Averaging over different impact parameters, the momentum transfer in the direction perpendicular to the direction of the collision will be zero while the momentum transferred in the direction of the collision can be expressed in terms of an equivalent momentum transfer cross-section σ_p as:

$$\partial_t p_i = n_a v \, (\mu v) \, \sigma_p$$

with

$$\begin{aligned} \sigma_p &= 2\pi r_L^2 \int_0^{\infty} f(\Delta\theta) \, x dx \\ f(\Delta\theta) &= 1 - \cos \Delta\theta(x) \end{aligned}$$

σ_p corresponds to the cross-section for the ion to change its forward momentum by the relative center of mass momentum μv. As expected, it is proportional to the Langevin cross-section. The last integral can be done numerically

$$\int_0^1 \left[1+\cos\left(2\Theta\left(x\right)\right)\right] x dx + \int_1^\infty \left[1+\cos\Theta\left(x\right)\right] x dx \;\; = \;\; 0.370 + 0.104$$

to show that momentum transfer in an atom-ion collision is dominated by hard-core encounters with $\sigma_p = 0.95\sigma_L$.

More generally, we may be interested in the cross-section σ_c for the momentum transferred to exceed a certain value p_0. Since atom traps have depths V_0 much smaller than ion traps, such cross-sections σ_c with $p_0 = \sqrt{2m_a V_0} \ll \mu v$ are of interest for estimating atom loss in a a hybrid ion-atom system. In this case, the impact parameter b_c below which atom loss occurs will be much larger than r_L and

$$f\left(\Delta\theta\right) = \begin{cases} 0 & , \Delta\theta \approx \sin\Delta\theta < p_0/\mu v \\ 1 & , \Delta\theta > p_0/\mu v \end{cases}$$

Using the small angle approximation (3.10),

$$\Delta\theta \approx \frac{3\pi}{16}\left(\frac{r_L}{b}\right)^4$$

giving the atom loss cross-section of

$$\sigma_c = \sigma_L\sqrt{\frac{3\pi}{16}}\left(\frac{\mu E}{m_a V_0}\right)^{1/4}$$

The deviation from the Langevin cross-section is due to the appearance of an energy scale in the problem, namely the atom trap depth V_0.

In the quantum regime, the s-wave threshold E_s appears as another energy scale. Here, a scattering can be said to have occurred if it produces a measurable effect on the ion-atom wavefunction. For a collision at impact parameter b, this will be true if $|\Delta p|$ exceeds the Heisenberg-limited value of $p_0 = \hbar/b$. In the limit of many partial waves, the limiting case of $|\Delta p| \approx \hbar/b$ will occur for $b \gg r_L$, in which case

$$f(b, \Delta\theta) = \begin{cases} 1 & , \Delta\theta > \hbar/b \\ 0 & , \Delta\theta < \hbar/b \end{cases}$$

and $\sigma(E) = 2\pi b_c^2/2$ where the critical impact parameter $b_q \gg r_L$ is defined by:

$$b_q \Delta\theta(b_c) \approx \hbar/b_c$$

(3.10) then gives:

$$b_q \approx \left(\frac{\mu C_4^2}{E\hbar^2}\right)^{1/6}$$

corresponding to the quantum elastic scattering cross-section $\sigma_{el} \approx \pi b_q^2 \sim E^{-1/3}$. A full quantum derivation with many partial waves for a hard-core close range ion-atom potential in [CD00] gives

$$\sigma_{el} = \pi\left(1 + \frac{\pi^2}{16}\right) b_q^2 \tag{3.12}$$

As expected, $\sigma_{el} > \sigma_L$ with

$$\frac{\sigma_{el}}{\sigma_L} = \left(1 + \frac{\pi^2}{16}\right) 2^{-2/3} \left(\frac{E}{E_s}\right)^{1/6} = 1.02 \left(\frac{E}{E_s}\right)^{1/6}$$

approaching unity as the collision energy approaches the limit $E = E_s$ of a single partial wave.

Since a r^{-4} potential is of a sufficiently short range, the quantum s-wave scattering for $E < E_s$ the can be described by

$$\sigma_{el} = \frac{4\pi}{k^2} \sin^2(ka) \approx 4\pi a^2 \tag{3.13}$$

with a a finite scattering length. Approaching $E = E_s$ from both sides using (3.12) and (3.5) gives an estimate for the magnitude of typical ion-atom scattering length

$$a \approx \left(\frac{\mu C_4}{2\hbar^2}\right)^{1/2}$$

a also corresponds to the natural quantum length scale in the ion-atom Hamilto-

nian: the scale on which the kinetic energy is equal to the r^{-4} potential energy. In the $Yb^+ + Yb$ system presented in this thesis, $a \approx 4750a_0$ - much larger than the typical atom-atom scattering lengths due to the r^{-6} van der Waals potential ($a \approx 50a_0$). It is these large atom-ion scattering lengths that have been behind interest in controlled ion-atom collisions for quantum information processing [ICZ07, CKL02]. Unfortunately, such large scattering lengths come at a price of very low s-wave limiting energies. As will be shown in Chapter 5, reaching these energies with ions trapped in an RF trap can be expected to be challenging.

3.4 Inelastic Ion-Atom Collisions and Charge Exchange

3.4.1 Hard-Core Charge Exchange Collisions

Most inelastic processes in ion-atom collisions are due to interactions of the molecular potentials on the scale of $r \sim 10a_0$, which is smaller than the classical Langevin distance scale r_L (for the Yb-Yb^+ collisions at temperatures below $300K$ studied in this thesis, $r_L > 20a_0$). Classically, such collisions can occur only for $b < r_L$, resulting in classical ion-atom inelastic cross-sections of the form $\sigma = p\sigma_L$ where $p(E) < 1$ is the probability of the inelastic process in a close-range collision.

Inelastic processes such as charge exchange studied in the Chapter 4 of this thesis also involve a change in the electronic wavefunctions of the colliding species. In collisions between different species, the energy separation ΔE between the final $A'+B'$ and initial $A + B$ states will usually be on the scale of the electronic states (several eV). Since this is much larger than the collision energies between laser cooled atoms and ions ($E < 100$meV), the probability of the inelastic process can be expected to be independent of the collision energy. Barring strong coupling to a close collision channel, endothermic processes with $\Delta E > 0$ will be strongly suppressed by energy conservation ($p \ll 1$).

The exothermic inelastic processes are also suppressed by the large energy defect: in order to transfer electronic energy to the center of mass radial coordinate, the system also needs to transfer momentum. The electrons being much lighter than the nuclei, the electronic states carry much less momentum than the center-of-mass coordinate, suppressing the collision process. To conserve both energy and momentum, the system can emit a photon to remove the excess energy. However, due a short duration of the collision and poor Frank-Condon overlap, the probability for photon

emission will be low (e.g. $p < 10^{-7}$ for Na+Ca^+ [MCMS03]).

For the $^{172}Yb^+ + {}^{174}Yb^+ \longrightarrow {}^{172}Yb + {}^{174}Yb^+$ charge exchange process studied in this thesis, ΔE is equal to the difference in ionization energies E_{ion} of different Yb isotopes arising from a small difference in the effective mass of the valence electron. With m_n the nuclear mass and m_e the electron mass, in analogy with hydrogenic atoms,

$$\Delta E_{ion} \approx E_{ion} \Delta m_n \frac{\partial}{\partial m_n} \log\left(\frac{m_e m_n}{m_n + m_e}\right) \approx -h \times 60 \text{ MHz}$$

A more accurate measurement based on spectroscopy of high Rydberg states of Yb gives $\Delta E = -h \times 160$ MHz [Gri11], which is smaller than the lowest collision energies studied ($E > h \times 200$ MHz). Therefore, the molecular orbitals corresponding to the two collision channels are expected to be strongly mixed in a close-range collision. Since the collision energies studied are also much higher than the s-wave limit of Yb-Yb^+ scattering ($E_s \approx h \times 1$ kHz), this mixing will be averaged over many partial waves with the result of $p \approx 1/2$.

3.4.2 Charge Exchange by Tunneling

A quantum correction to the classical collision model arises at high collision energies, [Hol52]. During a grazing Langevin collision at $b > r_L$, charge exchange is inhibited by the potential barrier of height equal to the atom's ionization energy and thickness comparable to the impact parameter b. As the collision energy increases, the typical impact parameters decrease, allowing the tunneling of the atom's valence electron to the ion. Tunneling introduces a coupling between the two states $A^+ + B$ and $A + B^+$ of approximate strength $V(r) \sim E_{ion} t(r)$ where

$$\begin{aligned} t(r) &= \exp\{-\alpha r(t)\} \\ \alpha &= \sqrt{2 m_e E_{ion}/\hbar^2} \end{aligned}$$

is the WKB tunneling amplitude. In the case of near-resonant exchange between Yb isotopes, $V(r)$ will cause the valence electron to Rabi flop between the two nuclei at rate $\Omega_t = V(r)/\hbar$ with the total charge exchange probability $P = \sin^2(\phi/2)$ with the Rabi phase ϕ given by

$$\phi = \int_{-\infty}^{\infty} dt\, E_{ion} \exp\{-\alpha r(t)\}/\hbar$$

For small impact parameters $b < b_c$ corresponding to small $r(t)$, the total accumulated phase ϕ will vary rapidly with b, resulting in a change exchange probability that averages to 1/2, similar to the classical result above, while for $b > b_c$, ϕ will exponentially decay to zero. A correction to the Langevin cross-section arises when $b_c > r_L$, in which case the limiting trajectories will be nearly straight lines with $r(t) \approx \sqrt{b^2 + v^2 t^2}$. Since, even at room temperature, the collision time b/v will be much longer than than E_{ion}/h, at $b = b_c$, the exponent in the integrand will be large and the contribution to the integral will come mostly from $r(t) \approx b$, giving

$$\begin{aligned} \frac{\pi}{2} \approx \phi(b = b_c) &\approx \frac{E_{ion} b_c}{\hbar v} e^{-\alpha b_c} \int_{-\infty}^{\infty} e^{-\alpha b_c x^2/2} dx \\ &= \frac{E_{ion} \alpha b_c}{\hbar v \alpha} e^{-\alpha b_c} \sqrt{\frac{2\pi}{\alpha b_c}} \\ &\approx \frac{E_{ion}}{\hbar v \alpha} e^{-\alpha b_c} \sqrt{2\pi} \end{aligned}$$

or

$$b_c = \sqrt{\frac{\hbar^2}{8 m_e E_{ion}}} \log\left(\frac{2\mu E_{ion}}{\pi m_e E}\right) \tag{3.14}$$

corresponding to a tunneling contribution to the charge exchange cross-section of the form [DMW58]:

$$\sigma_{ex} = \pi b_c^2 = (a - b \log E)^2 \tag{3.15}$$

Due to a much weaker scaling with energy, the tunneling cross-section (3.15) will dominate at high collision energies. In the Yb-Yb^+ system studied in this thesis, the tunneling cross-section (3.15) becomes comparable to the Langevin cross-section at collision energies corresponding to temperatures $T \sim 50K$ i.e. collision energies $E \sim 5$meV.

A quantum calculation of charge exchange in the Yb-Yb^+ system was done by [ZDC09]. For certain values of the reduced mass in the collision frame, [ZDC09] show good agreement (within a factor of 2) with the resonant Langevin model, for collision energies between 10^{-11} eV (100 nK) and 10^{-3} eV (10K). For other values of the reduced mass, however, the predicted charge-exchange cross-section is significantly reduced, in contrast to the experimental results presented in Chapter 4 of this thesis.

In summary, cold ion-atom charge exchange collisions are expected to follow a Langevin cross-section of the form $\sigma = p\pi r_L^2$ with p the probability of charge exchange in the inner hard-core collision largely independent of the collision energy. In near-resonant collisions such as those between different isotopes of the same atom presented in Chapter 4 of this thesis, $p \approx 1/2$ due to strong mixing of molecular potentials during the close-range collision.

The collision rate $R = n_{atom} v \sigma$ resulting from Langevin cross-sections is independent of energy and can be written as $R = n_{atom} K$ with $K = \sqrt{C_4/\mu}$ the charge exchange rate coefficient expressed in terms of the atom's polarizability and the reduced mass of the ion-atom system.

Chapter 4

Co-Trapped Cold Atoms and Cold Ions

This chapter presents the first experimental results in a hybrid cold atom-cold ion system.

A surface RF Paul trap is loaded with Yb^+ ions produced by photoionization of atoms trapped in a magneto-optical trap (MOT). The collisions between Yb^+ ions trapped in the ion trap and the Yb atoms in the MOT are studied by observing inelastic charge exchange between the two species. The range of collision energies available in the experiment was 3 μeV - 4 meV, limited by the residual RF-driven micromotion of the ions in the trap.

Elastic collisions between cold atoms and cold ions are studied by trapping Rb atoms in a magneto-optical trap and observing the effects of Rb-Yb^+ collisions on the temperature of the trapped Yb^+ ions .

This chapter gives a general description of the experiments. More detail can be found in the MIT thesis of Andrew Grier [Gri11] as well as in the two papers enclosed in Appendix C and Appendix D.

4.1 Hybrid Ion-Atom Traps

At the start of this thesis, in spite of several proposals [SML05], co-trapping of cold atoms and ions - a fundamental requirements for any of the schemes in Section 3 - had not yet been demonstrated.

At first sight, trapping and laser cooling atoms and ions in the same spatial region entails significant technical complexity: atoms and ions need to be produced from separate effusive sources combined with electron-impact or photo-ionization; the RF

ion trap design needs to provide sufficient optical access for cooling of both species; two laser systems are needed to cool both atoms and ions.

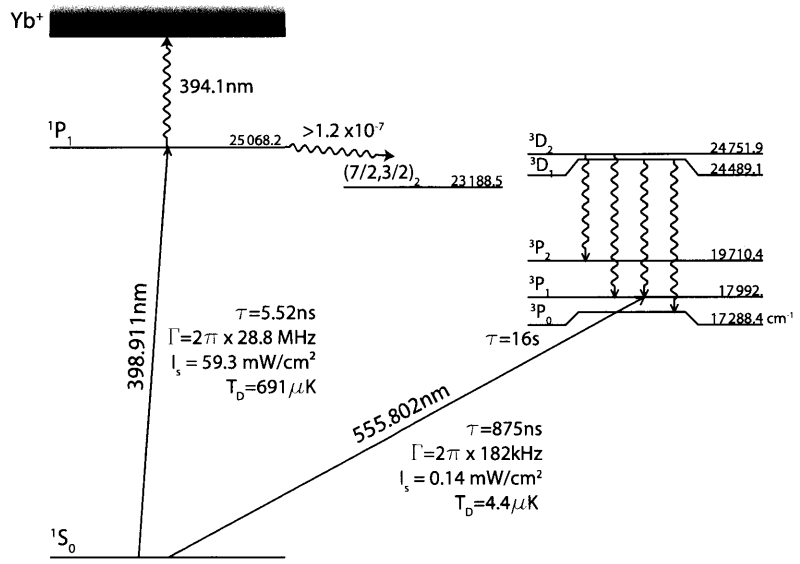

Figure 4-1: Levels relevant to laser cooling of Yb. All wavelengths are given in vacuum. The data for the $^1S_0$-$^1P_1$ transition is from [BRD+03] and for the $^1S_0$-$^3P_1$ transition from [KHTY99]. Unlike the narrow $^1S_0$-$^3P_1$ intercombination transition, the $^1S_0$-$^1P_1$ transition is not completely closed, with branching ratio $\geq 1.2 \times 10^{-7}$ to the remaining states [HTK+99]. The $\left(\frac{7}{2}, \frac{3}{2}\right)_2$ state is metastable while the triplet ^3D states experience allowed transitions to the metastable $^3P_2$ and $^3P_0$ states with lifetimes of >1s and 16 s, respectively [HBO+05].

These challenges become significantly less daunting if the same atomic species is employed as both atoms and ions. This is particularly true in the case of the Yb atoms adopted in this thesis. As demonstrated by [HTK+99], Yb atoms can be trapped in a magneto-optical trap (MOT) using a single light frequency close to the dominant $^1S_0 - ^1P_1$ transition at 399 nm. Up to 5×10^6 Yb atoms have been trapped in this manner [LBSM00], in spite of decays from the $^1P_1$ state to metastable D-states [KHTY99] (Figure 4-1),

Laser cooling and trapping of Yb atoms is further simplified by the availability of blue-violet diode lasers for driving the strong $^1S_0$-$^1P_1$ Doppler cooling transition (Appendix B). Following the first demonstration of a Yb MOT using 30 mW laser diodes by [PY03], the power output of these devices has continued to improve (cf. 120 mW NDV4313 from Nichia Corporation), promising a cheap and convenient replacement for frequency-doubled Ti:sapphire systems.

A Yb MOT also allows easy production of ions by photoionization from the $^1P_1$ state which is significantly populated during the operation of the atom trap. The frequency of the $^2S_{1/2} - ^2P_{1/2}$ Doppler cooling transition in Yb^+ is sufficiently high to ionize the $^1P_1$ state, further simplifying the laser system.

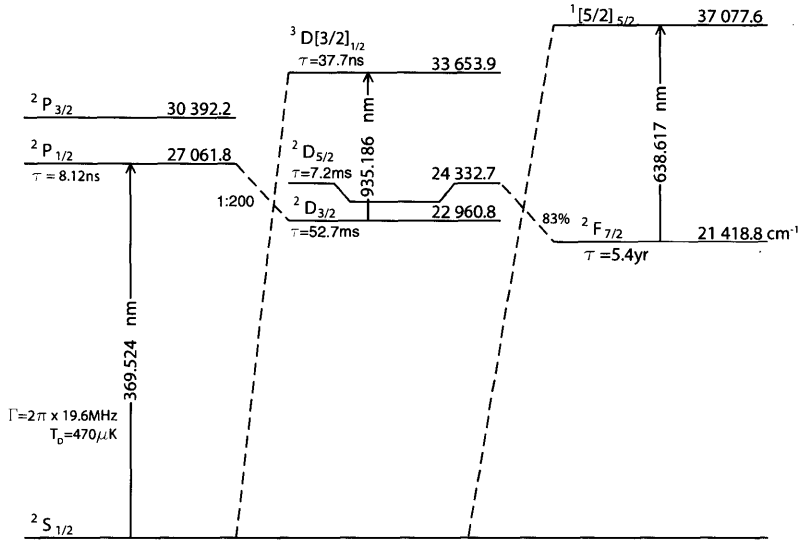

Figure 4-2: Levels relevant to laser cooling of Yb^+ using the scheme from [BGK+91]. All wavelengths are in vacuum. The lifetime of the $^2P_{1/2}$ state is from [OHM+09], of the $^2D_{3/2}$ state from [YM00], of the $^2D_{5/2}$ from [TRGK+97], of the $^3[3/2]_{1/2}$ state from [BPG93] and of the $^2F_{7/2}$ from [RTB+00]. The branching ratio of the $^2D_{5/2}$ state is from [TRGK+97]. The $^2P_{1/2}$ state decays with 1 : 200 branching ratio to a metastable $^2D_{3/2}$ state [OYM+07], from which it can be repumped via the $^3D[3/2]_{1/2}$ state. Occasionally, the ion may fall into the $^2F_{7/2}$ state from which it can be repumped with a 638.6 nm laser [LHLBH89].

As demonstrated in Appendix B of this thesis and summarized in [KCCK06], near-UV laser diodes also faciliate Doppler cooling Yb^+ ions. For cooling small samples of ions, much less power is needed than for cooling atoms, allowing a single laser to be used. The metastable $^2D_{3/2}$ state, populated during Doppler cooling of Yb^+ (Figure 4-2), can also be repumped using a readily-accessible diode laser operating at 935 nm.

4.2 Experimental Setup

4.2.1 Laser System

An all-diode laser system for trapping Yb atoms and ions is shown on Figure 4-5. A 399 nm laser diode (NDHV310ACAE1 from Nichia Corp., Japan) is operated in a an external Littrow grating cavity with $\approx 30\%$ grating diffraction efficiency and protected from spurious optical feedback with an optical isolator. For cooling Yb atoms, this 399 nm master laser is stabilized via a DAVLL lock [CLH+98] to Yb atoms in a hollow cathode lamp (He-backfilled L2783 Galvatron backfilled from Hamamatsu Photonics, Japan).

To obtain sufficient power for operating a Yb MOT, the 399 nm master laser is used to inject a a slave laser diode (also NDHV310ACAE1). After passing through a TeO_2 acousto-optical modulator (1206C-833-2 from Isomet Corp., VA) used for beam switching, the slave laser produces up to 8 mW of cooling and trapping light. Mindful of the high saturation intensity of the Yb $^1S_0 - ^1P_1$ transition, to conserve power, the 399 nm light is delivered to the experimental chamber in free space.

Light for laser cooling of Yb^+ ions is provided by a cooled grating laser (NDHUA110APAE2 from Nichia Corporation, Japan, Appendix B) stabilized via the Pound-Drever-Hall scheme [Bla98] relative to a temperature-stabilized Fabry-Perot optical resonator. After passing through a TeO_2 acousto-optical modulator (1206C-833-2 from Isomet Corp., VA), the 369.5 nm diode laser delivers up to 175μW of light in a single-mode polarization-maintaining fiber.

During laser cooling, Yb^+ ions decay from the excited $^2P_{1/2}$ state to the metastable $^2D_{3/2}$ state with a branching ratio of 1:200 [OYM+07]. Repumping from the $^2D_{3/2}$ state is accomplished with an antireflection-coated diode laser in a Littrow external grating cavity operating at 935nm. The repumping laser is protected from optical feedback with an optical isolator and stabilized relative to a temperature-stabilized Invar Fabry-Perot cavity using the Pound-Drever-Hall scheme. After passing through an acousto-optical modulator used for switching, the repumping laser delivers up to 3mW in a single-mode polarization-maintaining fiber.

4.2.2 Ion Trap

Optical access for simultaneous trapping of atoms and ions can be provided by using a surface electrode trap similar to the ones discussed for quantum information processing [CBBJ05]. A setup employing such a surface trap to overlap cold atoms and

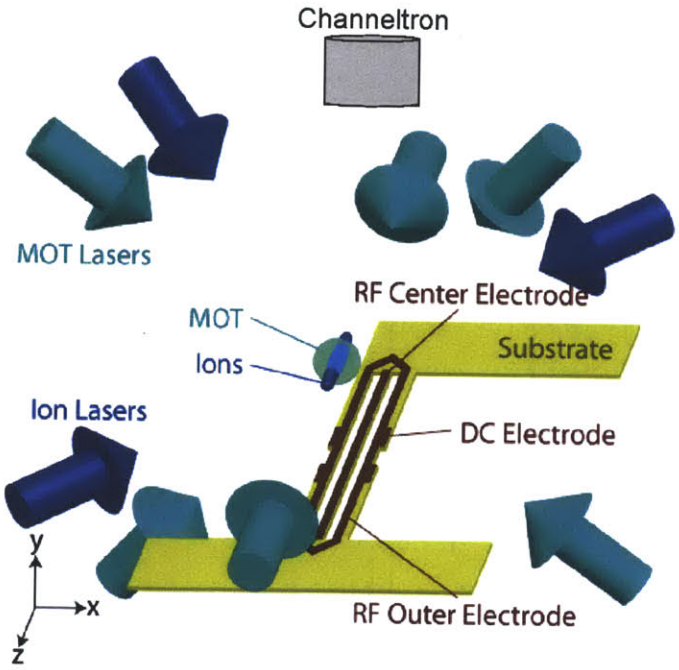

Figure 4-3: Experimental setup for trapping cold ions and cold atoms in the same spatial region

cold ions is shown on Figure 4-3.

The ion trap is made using commercial PCB technology by Hughes Circuits, Inc. on a UHV-compatible PCB substrate (Rogers 4350). The trapping potential is formed by applying RF voltages to two trap electrodes (center and outer), composed of three 1 mm-wide Cu-plated rods. Four additional 200 μm wide copper electrodes are used to cancel residual DC electric fields and provide confinement along the z-axis.

The location of the center of the RF ion trap can be adjusted by varying the ratio of the RF drive amplitudes of the center and the inner electrodes. To avoid ion micromotion, it is important that the voltages applied to all RF electrodes be either in-phase or 180° out-of-phase relative to each other.

For initial measurements of trap loading via photoionization of cold atoms, the ion trap was operated at 850kHz with 540 V drive amplitude on the outer electrode and -340 V drive amplitude on the center electrode, yielding secular trap potentials with depth of up to 0.16 eV and typical secular trap frequencies of $\omega = 2\pi \times 90$ kHz .

To overlap the ion trap with the atom MOT to study ion-atom interactions, the position of the ion trap needed to be adjusted, which was accomplished by varying the drive ratio between the center and outer electrodes. Real-time control of the drive voltages on both RF electrodes was accomplished using the dual RF resonator setup

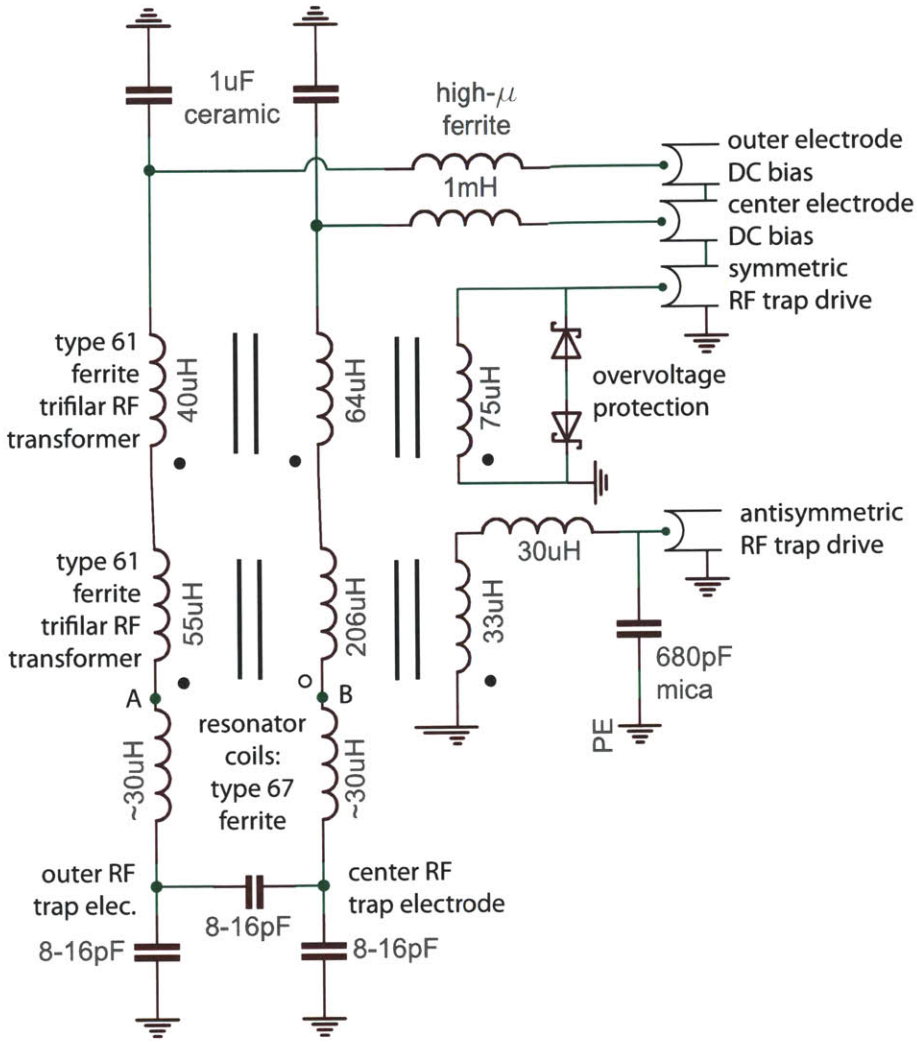

Figure 4-4: 50Ω impedance-matched two-channel RF ion trap drive

shown on 4-4.

The outer and central RF trap electrodes are driven using two series $L - C$ resonators employing ≈ 30 μH inductors hand-wound on toroidal type-67 ferrite cores (FT-240-67 2.4" OD × 1.4" ID × 0.5" H from Amidon Corp., CA). As the two circuits are tuned to resonance, the parasitic mutual capacitance between the trap electrodes (8-16 pF) leads to an avoided crossing of the resonator modes, resulting in coupled drive modes with symmetric i.e. antisymmetric excitations of the two electrodes. To drive the trap electrodes with an arbitrary ratio of RF voltages, individual *modes* are driven separately using two trifilar transformers wound on type-61 ferrite cores. Inductively coupling to one transformer core drives the symmetric oscillation mode of the two electrodes while the other core drives the antisymmetric mode. To compen-

sate for the difference in frequency between the symmetric and antisymmetric modes of $\approx$ 300 kHz, an additional $L-C$ network is placed behind the antisymmetric drive transformer. Additional DC bias can be supplied to the trap electrodes through the transformers via two $L-C$ bias tees.

The dual-channel resonator is tuned to operate at 1.472 MHz and the symmetric and antisymmetric modes driven separately using two 1W amplifiers (ZHL-32A from MiniCircuits, NY). With $<$ 1 W of RF power input to each of the two channels of the trap drive, during the ion-atom collision measurements, the secular oscillation frequencies of the trapped Yb^+ ions were $\omega = 2\pi \times 130$ - 160 kHz.

4.2.3 Magneto-Optical Trap

Yb atoms are produced in a resistively heated Ta-foil oven located 8 cm from the trapping region, described in more detail in Andrew Grier's thesis [Gri11]. Atoms leaving the oven are captured in a magneto-optical trap (MOT) formed by magnetic coils producing a quadrupole field with a gradient of 45 G/cm, together with three perpendicular pairs of circularly polarized 399 nm-beams. To conserve power, after passing through the vacuum chamber, the 399 nm beams are retroreflected through $\lambda/4$ waveplates. Using 1.7 mm-waist beams with a a total power of 10m W, we typically trap between 50×10^3 and 300×10^3 isotope-selected Yb atoms.

For experiments with Rb described in Section 4.5, a reactive Rb getter was added to the vacuum chamber. The MOT optics was also changed to accommodate both 399nm Yb MOT light and the 780nm Rb light.

A picture of the experimental setup, including the vacuum chamber, the ion trap, the MOT magnetic coils and the associated optics is shown on Figure 4-6.

4.2.4 Imaging System

The Yb atoms and ions trapped in the hybrid trap are imaged using the fluorescence gathering setup shown on Figure 4-7. Light emitted by the atoms is gathered by a molded-glass asphere placed inside the vacuum chamber. After passing through the 5.34mm-thick vacuum window at an angle of 36° relative to the optical axis, the light is re-imaged with $\approx 2:1$ magnification to a secondary focus. The light from the secondary image is collimated with precision-machined asphere, spectrally filtered and split between a CCD camera (AP260E from Apogee, Inc., CA) and a photon-counting photomultiplier detector.

The photomultiplier was H7360-02 from Hamamatsu, selected for $<$ 100/s dark

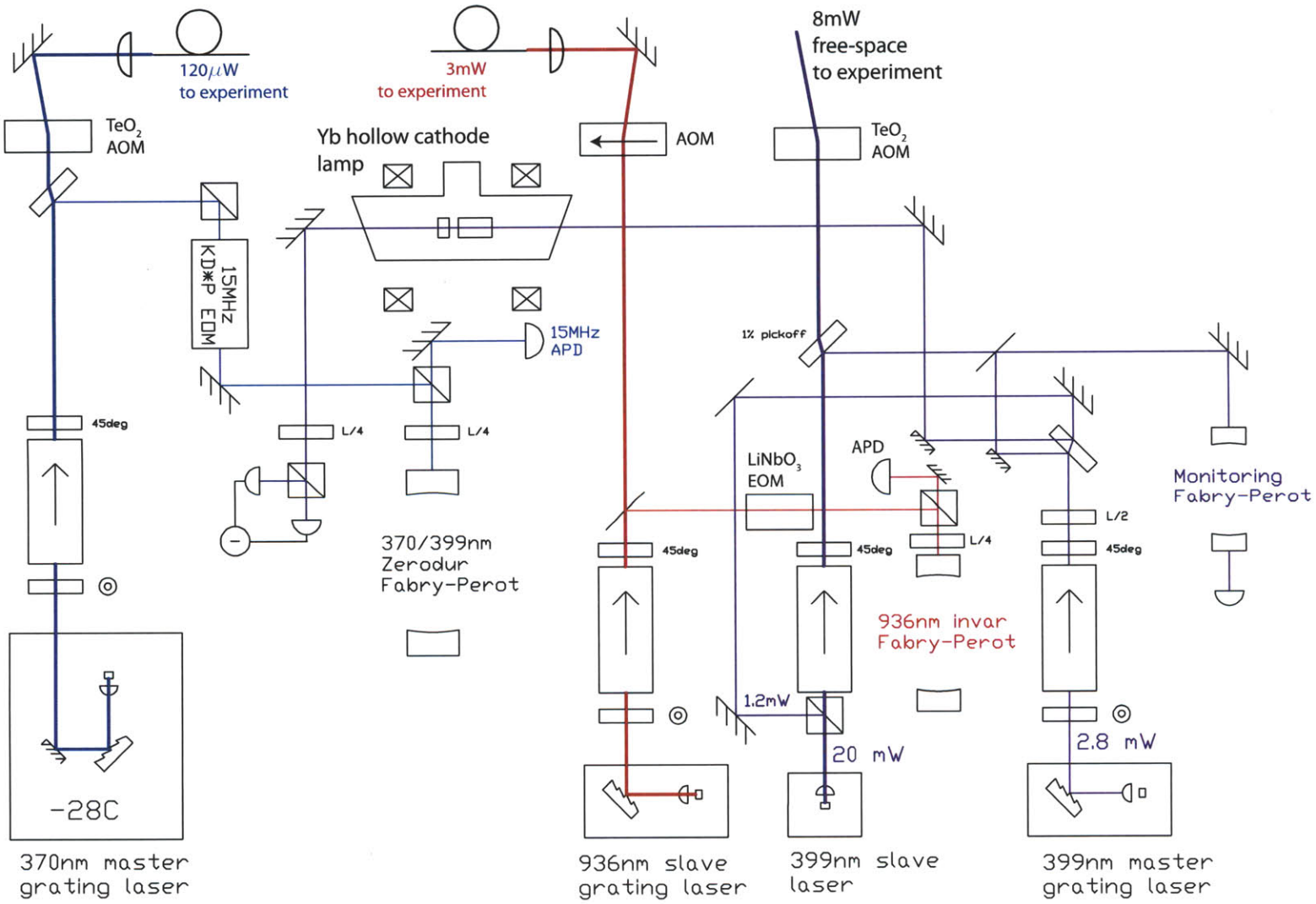

Figure 4-5: Optical setup employing stabilized laser diodes to produce light for cooling Yb atoms and ions

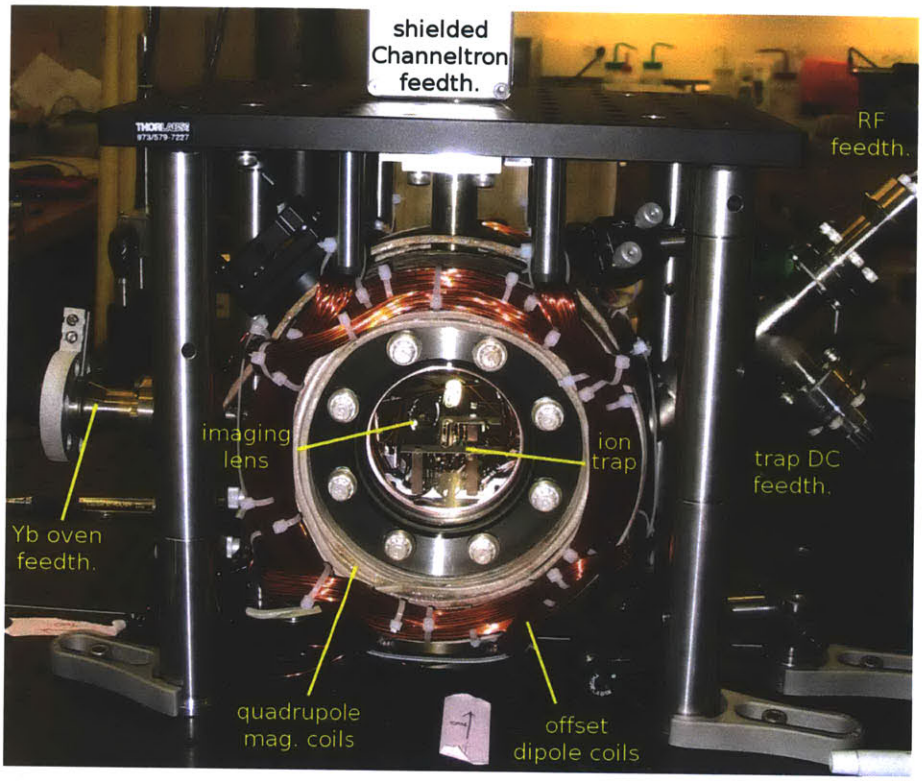

Figure 4-6: Image of the experimental setup for observing ion-atom collisions

count rate, with a specified quantum efficiency of 19% at 370 nm. The quantum efficiency of the full-frame CCD camera was measured at 370 nm as $(18 \pm 2)\%$ and at 399 nm as (35 ± 2) %.

4.2.5 Electronic Ion Detection

Ions trapped in the Paul trap can be detected electronically using a Channeltron ion detector (Magnum 5901 from Burle Corporation, PA) located (40 ± 3) mm from the ion trapping region. To detect the trapped ions, the Channeltron ion detector is rapidly turned on by applying -2 kV to its front electrode using a Pockels cell driver (model 835B from Analog Modules, FL). The resulting electric field pulls the trapped ions out of the trap and, after a flight time 3.25μs, causes them to be detected by the Channeltron in a time-resolved <125 ns-wide pulse.

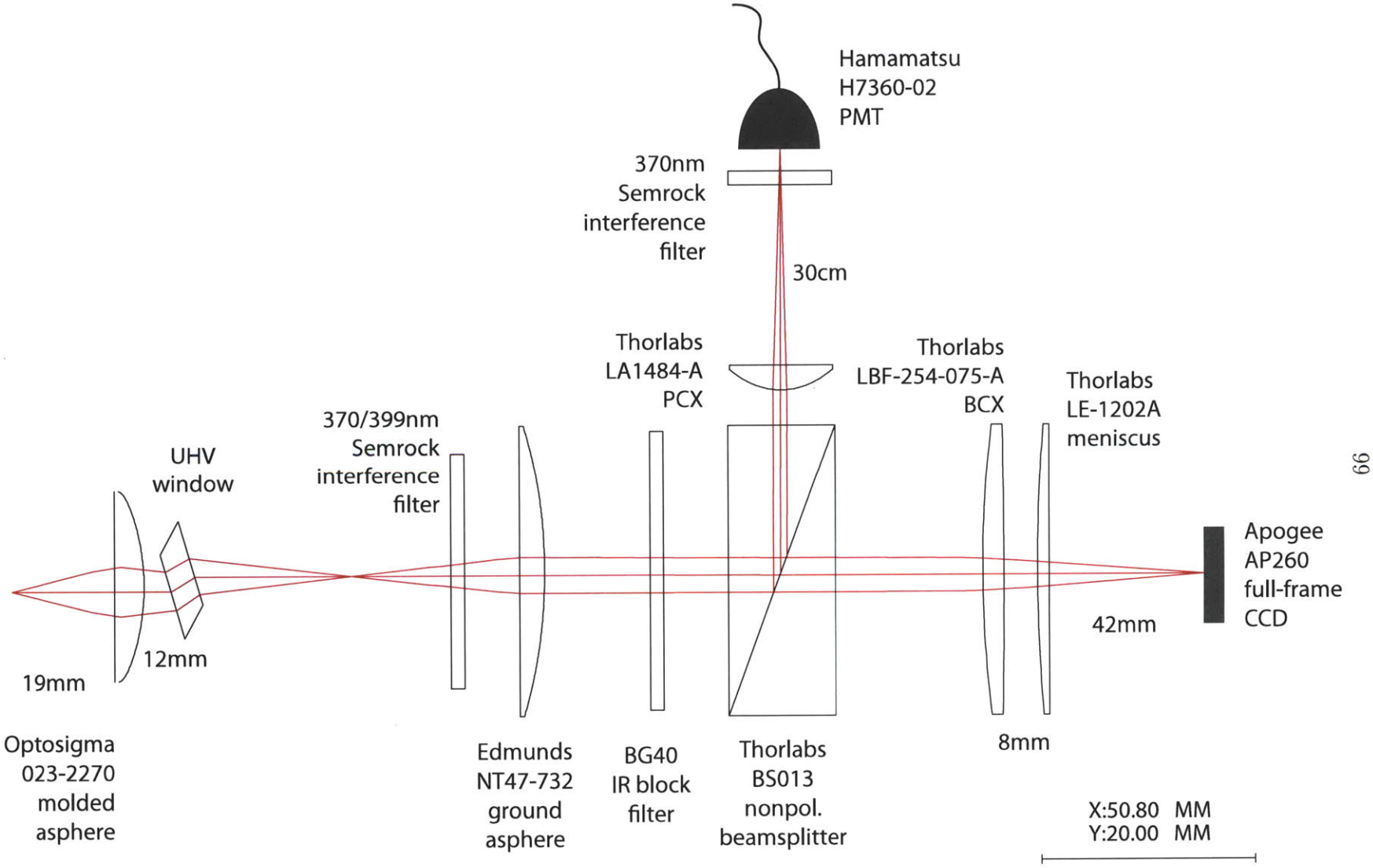

Figure 4-7: Setup for fluorescence imaging of the atoms and ions

4.3 Rapid, Isotope-Selective Loading of Surface Ion Trap

The presence of cold excited-state atoms in the atom trap close the ion trapping region allows highly efficient isotope-selective loading of the ion trap, as described in detail in Appendix C.

We use either a focused laser beam at 370 nm and power of 750μW or a focused UV LED centered at 385 nm with 8.7 mW output power to ionize the MOT atoms from the excited $^1P_1$ state and load the resulting ions into our planar ion trap. The response of the MOT to the ionizing light can be described as

$$\frac{dN_a}{dt} = -\left(\kappa + \kappa_i\right) N_a + L \tag{4.1}$$

where N_a is the number of trapped atoms, L the atom loading rate, κ the one-body atom loss rate without the ionizing light and κ_i is the ionization-induced loss rate. For $\kappa_i < \kappa$, (4.1) can be linearized about the equilibrium atom number N_0 to yield

$$\frac{d\left(\Delta N_a\right)}{dt} = -\kappa\left(\Delta N_a\right) - \kappa_i N_0$$

If the ion loss rate κ_i is modulated by turning the ionizing light on and off with a square wave with angular frequency ω faster than the MOT reloading rate κ, the MOT response will be described by

$$\frac{\Delta N_a}{N_0} \approx \frac{2\kappa_i}{\pi\omega}\cos\left(\omega t\right)$$

By comparing the modulation of the MOT fluorescence measured using the lock-in amplifier with the average MOT fluorescence, one can determine the MOT atom loss rate due to the ionizing beam. The results of this measurement are shown on Figure 4-8. The fit of the observed MOT loss rate to straight line indicates a one-photon loss process. We have also confirmed that the dominant loss proceeds from the excited $^1P_1$ state of Yb: when the 399nm MOT light and the 370nm photoionization laser are modulated out-of-phase such that the 370nm UV light interacts only with the ground state atoms, the MOT loss rate is decreased 13-fold.

During photoionization, the emitted electron causes the Yb^+ ion to recoil with energy

$$E_{recoil} = (E_\gamma - E_i)\, m_e/m_i$$

where $E_i = hc/394$ nm is the Yb ionization energy, $E_\gamma = hc/370$ nm is the energy of the ionizing photon, m_e the electron mass and m_i the mass of the Yb^+ ion. Since the resulting recoil energy of 640 neV is much smaller than the depth of the ion trap, the energy of the ions produced close to the center of the RF trap will be given by the effective of the RF at the ionization location. Consequently, a large fraction of the ions produced inside the trapping volume can be expected to be captured by the ion trap.

To verify the loading of the ions produced by photoionization of the MOT atoms into the RF trap, the Channeltron detector is pulsed using a Pockels cell driver after varying loading times and the height of the time-resolved peak corresponding to trapped ions is measured [Gri11]. To calibrate the Channeltron detector, we measure a small number of trapped ions so that on average, the Channeltron receives less than one ion. The charge produced in the Channeltron detector from the impact of an ion is exponentially distributed with a mean significantly above the background, allowing us to easily distinguish one-ion events from zero-ion backgrounds and average them to calibrate the Channeltron detector.

The results of the ion loading measurements are shown on Figure 4-9. The maximal obtained loading rate of 4×10^5 Yb^+ ions/s is three orders of magnitude higher than what is achieved in other experiments by photoionization of a thermal atomic beam. The top curve shows the loading of the ion trap using a focused 750 μW laser beam at 370 nm. The middle curve shows loading with a UV LED centered at 385nm with intensity of 125 mW/cm^2. Loading from the atomic beam is shown as the bottom curve bottom curve, with the loading rate magnified 100×. To record the bottom curve, the MOT light is detuned to the blue of atomic resonance to remove the trapping and cooling effect of the MOT while preserving excitation of the hot atomic beam. Since the cold MOT operates only on atoms near-resonant with the laser light, the trapped atoms can be expected to be isotopically pure. The ratio of the corresponding MOT- and beam- loading rates implies> 400 isotope selectivity of the MOT-assisted ion trap loading scheme.

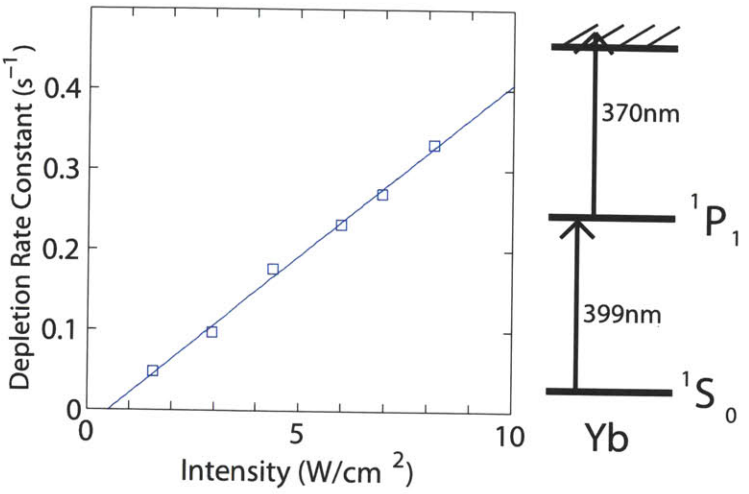

Figure 4-8: Depletion of the Yb magneto-optical trap due to ionization by a focused 370 nm laser

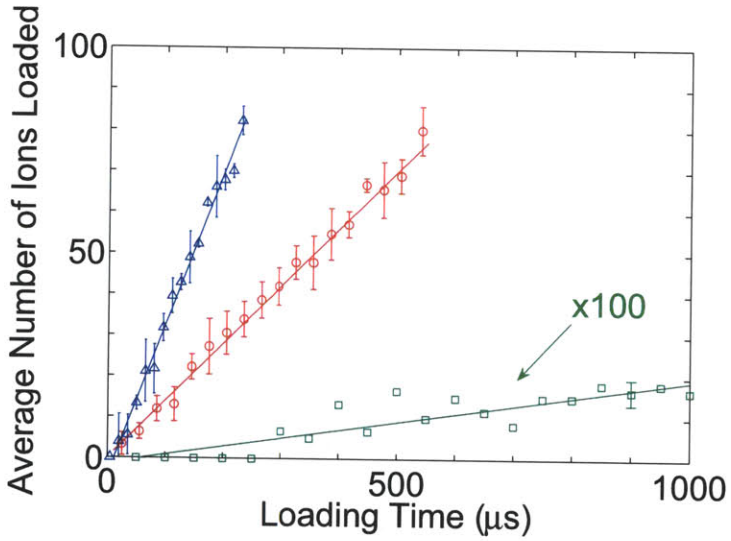

Figure 4-9: Loading of a planar RF trap with Yb^+ ions produced by photoionization of Yb atoms in a MOT using 750 μW of focused 370 nm laser light (top curve) and 8.7 mW of light from a UV LED (125 mW/cm^2 intensity) emitting at (385 ± 10) nm (middle curve). The bottom green curve (scaled 100×) shows the loading using the UV LED from thermal atoms obtained by detuning the MOT laser to the blue of the atomic resonance.

4.4 Ion-Atom Charge Exchange Collisions

Having realized a system combining trapped laser-cooled ions with trapped laser-cooled atoms, an intuitive way to observe the interactions between them would be to look for the effects of momentum and energy transfer. Observing such elastic collisions is made difficult by the presence of much stronger heating and cooling effects, especially the RF-induced heating (Section 5.1) and laser cooling.

Inelastic processes provide an effective method for singling-out ion-atom collisions. In the Yb-Yb^+ system, charge exchange collisions between different Yb isotopes are further enhanced by being nearly resonant (Section 3.4), making them a good first candidate for observing ion-atom interactions.

4.4.1 Observation of Charge Exchange

To observe charge-exchange collisions between Yb atoms and ions, $^{172}Yb^+$ or $^{174}Yb^+$ ions are produced by photoionizing the corresponding atoms trapped in the MOT using the same 369.5 nm laser light that is used for cooling of the produced ions. Doppler-cooling is accomplished using two 369.5 nm laser beams focused to 140 μm-waists at the ions' location. To ensure cooling of all three of the ions' degrees of freedom, the cooling beams are angled relative to the ion trap axes by $> 20°$.

To spatially overlap the atoms with the ions, the fluorescence emitted during Doppler cooling of both species is imaged using the system described in Section 4.2.4 An additional camera is used to verify the overlap from a different angle.

In principle, ion-atom overlap could be achieved by shifting the center of the MOT using a dipole magnetic field. However, the range of available MOT displacements in our system was limited by the clipping of the laser cooling beams by the ion trap electrodes. To preserve the number of trapped Yb atoms, the ion trap was instead displaced away from the trap surface by applying a RF voltage to the central trap electrode in anti-phase with the main trap drive. A relative drive amplitude of the inner electrode between -0.63 and -0.70 places the center of the RF trap at a point 3.5 mm above the trap surface, allowing for overlap with the atom MOT.

To avoid loading new ions by ionizing the excited MOT atoms, the 370 nm ion cooling light and the 399 nm MOT light are cycled out-of-phase at 53kHz (slower cycling frequency caused increased MOT atom loss). The 399 nm light is operated at 76% duty cycle while the phase and duty cycle of the 370 nm light were alternated between two configurations. In one configuration, the 370 nm beam is cycled with

20% duty cycle and out of phase with the MOT light, preventing further ionization of MOT atoms. To load the ion trap, the cycling pattern of the 370 nm beam is switched to ~70% duty cycle, in phase with the MOT light.

The experimental procedure for observing charge exchange is as follows:

1. trap Yb atoms of a desired isotope in the MOT

2. cycle the 370 nm and 399 nm beams in-phase to ionize the MOT atoms

3. load small crystals of $^{172}Yb^+$ or $^{174}Yb^+$ ions into the ion trap

4. switch the 370 nm / 399 nm beam cycling to be out-of-phase

5. wait several seconds for the ion population to stabilize

6. trap Yb atoms of a different Yb isotope (^{172}Yb, ^{174}Yb or ^{171}Yb)

7. record the fluorescence emitted by the ions using the photomultiplier

The observed ion fluorescence as a function of time is shown on a log-linear plot on Figure 4-10. The background rate of fluorescence decrease was obtained by detuning the 399 nm laser < 500 MHz to the blue of the MOT resonance. The remaining two curves were obtained at different ion-atom overlaps, obtained by applying a magnetic field of <5 G.

Good linear fits to the dependence of the logarithm of the ions' fluorescence on time indicate a single-ion process, consistent with charge exchange. Here, the exchange of an electron between a trapped Yb^+ ion and an atom of a different Yb isotope causes the trapped Yb^+ ion to be replaced by an ion of a different isotope. Since the new isotope is not resonant with the cooling laser, the observed fluorescence from the ion cloud during laser cooling decreases.

The interpretation of the decrease of the ions' fluorescence as being due to charge exchange is further supported by the variation of the observed rate of fluorescence decrease with the atoms' position i.e. the drop in the rate of fluorescence decrease when the 399 nm MOT beams (which are non-resonant with the ions), are detuned.

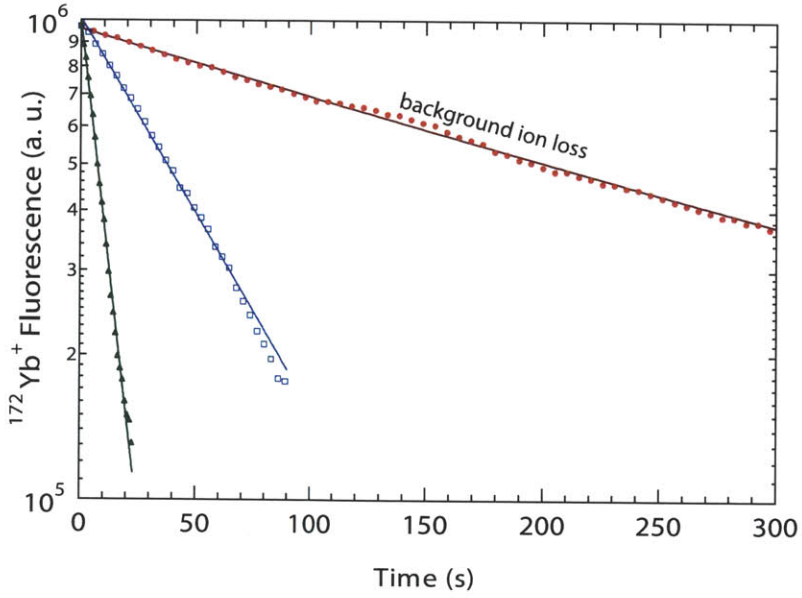

Figure 4-10: Decrease of the fluorescence emitted by samples of trapped, laser-cooled $^{172}Yb^+$ ions due to charge-exchange collisions with ^{174}Yb atoms as a function of time. The squares and the triangles correspond to different overlaps between the ions and the atoms in the MOT. The circles show the rate of fluorescence decrease in the absence of MOT atoms.

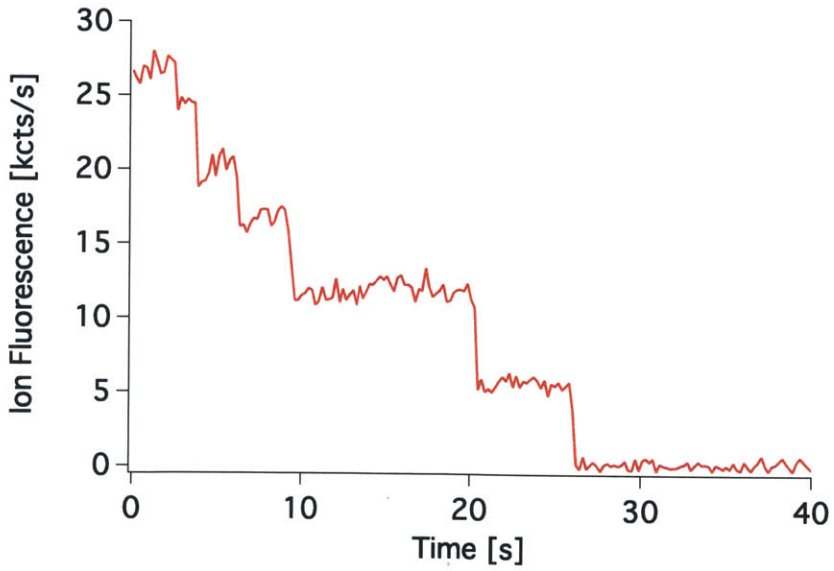

Figure 4-11: Decrease of fluorescence from individual Yb^+ ions due to charge-exchange with laser-cooled Yb atoms.

The same atom-induced fluorescence decrease can be observed at the level of individual Yb^+ ions, as shown on Figure 4-11.

4.4.2 Measurement of Charge Exchange Cross-Section

To relate the decrease in the sd on Figure 4-10 to the microscopic Yb-Yb^+ charge exchange cross-section, the atom density at the ion's location and the collision energy both need to be known.

The density of Yb atoms encountered by the ions was calibrated by comparing the fluorescence pictures of the trapped Yb^+ ions with the pictures of the Yb atoms trapped in the MOT (Figure 4-12). Using the known quantum efficiency of the photomultiplier and the known scattering rate of Yb^+ ions at the given detuning and laser power, the observed photomultiplier count rate of 5000 counts / ion was used to calibrate the light gathering of the imaging system. Using this calibration, and the information about the ion-atom overlap from the fluorescence pictures, the effective Yb atom density seen by the trapped ions could be calculated, with peak predicted atom densities on the order of $2 \times 10^8/\mathrm{cm}^3$.

As described in Section 5.1, the dominant energy in ion-atom collisions arises from the motion of the ions. This motion can be detected by observing the Doppler broadening of the ion resonance line as the Doppler cooling laser is swept towards the ion resonance (Figure 4-13). The kinks in the fluorescence profile have been shown by [DPC+87] to correspond to onset of ion crystallization.

The two curves on Figure 4-13 correspond to different values of the applied DC electric field which, by displacing the ions from the center of the trap, introduces RF-driven micromotion. As discussed in the next section and also in [Gri11], such micromotion forms the dominant contribution to the ion-atom collision energy in our measurements. The amount of micromotion can be measured by observing the correlation of the fluorescence emitted by the ions with the trap RF drive [BMB+98]. The use of this 'correlator' method for measuring the ion-atom collision energy is described in detail in [Gri11].

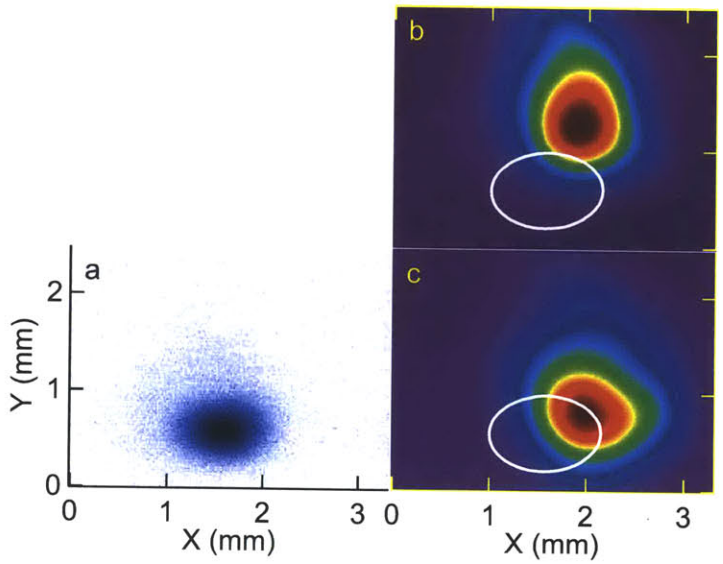

Figure 4-12: Images of ion cloud (left) and MOT atoms (right) used to overlap the ion and the atom traps and calculate the average atom density encountered by the trapped ions

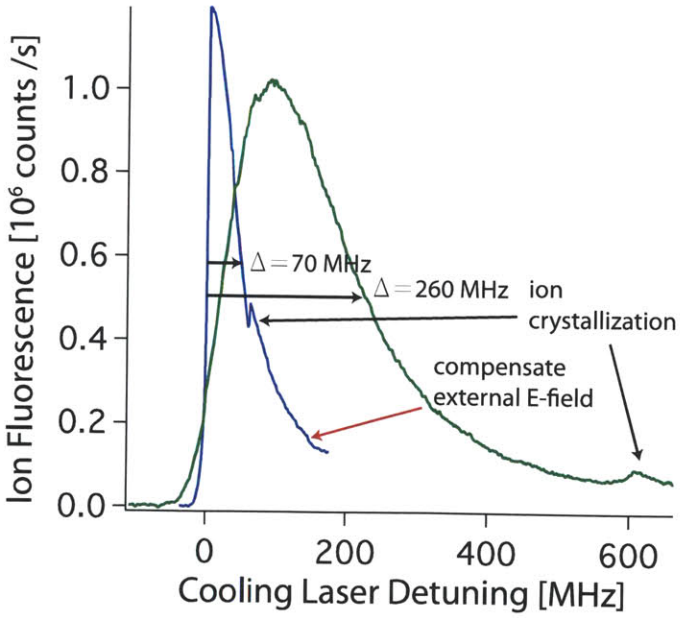

Figure 4-13: Dependence of fluorescence emitted by Yb^+ ions on the detuning of the Doppler cooling laser. The linewidth of the ions' fluorescence decreases with the DC electric field felt by the ions, indicating influence of micromotion on the ions' velocity.

Figure 4-14 shows the measured charge exchange rate, expressed in terms of the rate coefficient K (eq. 3.2). The data is shown as a function of the micromotion-dominated ion-atom collision energy. The collision energy can be varied across several orders of magnitude by applying an external electric field. To reach the lowest collision energy corresponding to $\sim$ 23 mK, the measurements were taken with single ions localized close to the center of the RF trap.

In the range of collision energies between 10^{-5} eV and 10^{-3} eV, the experiment shows good agreement with the Langevin cross-section model with 50% charge exchange probability. The deviation of the highest- energy point, at a collision energy equivalent to 40 K, may indicate an onset of the tunneling charge exchange process described in Section 3.4.2.

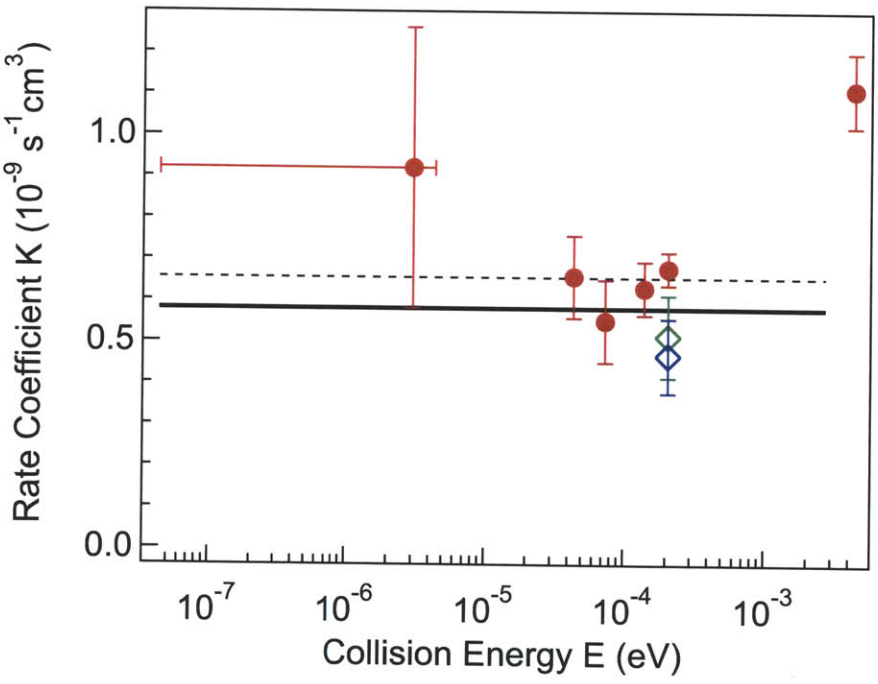

Figure 4-14: Rate coefficient for charge exchange in collisions of Yb^+ with Yb. Different isotope combinations are shown: $^{172}Yb^+ + {}^{174}Yb$ (red circles), $^{174}Yb^+ + {}^{172}Yb$ (blue diamond), $^{172}Yb^+ + {}^{171}Yb$ (green diamond). The solid black line shows the predicted Langevin rate coefficient with only the Yb ground state polarizability; the dashed line includes the $^1P_1$ polarizability of the excited MOT atoms.

4.5 Momentum-Transfer Collisions

Although inelastic charge-exchange collisions provided a convenient avenue for observing ion-atom interactions, in a viable hybrid ion-atom system, they would likely be undesirable.

To remove the masking influence of strong resonant charge exchange collisions, the colliding Yb atoms were replaced by Rb, as described in detail in [Gri11]. Although $Rb-Yb^+$ charge exchange is energetically favorable, it is heavily supressed by the poor momentum overlap of the two colliding states ([MCMS03]). Recent results on an ion in a BEC by [ZPSK10] put $Rb-Yb^+$ charge exchange rate 5 orders of magnitude lower than the elastic processes.

To investigate elastic ion-atom collisions, a small Rb atom MOT is produced close to the location of the trapped ions. The MOT size and atom number are estimated by imaging its fluorescence with a dedicated setup. Typically, 7.5×10^3 Rb atoms are trapped in a cloud with $1/e^2$ radius of 30 μm.

By adjusting the MOT quadrupole magnetic field, the trapped Rb atoms are introduced into the cloud of Yb^+ ions. Typically, the ion cloud has a $1/e^2$ radius of 50 μm. The ion cloud is centered relative to the null of the RF trap by looking for correlation between the RF trap drive and the scattering rate of photons during laser cooling [BMB^+98].

Surprisingly, although the sub-Doppler cooled Rb MOT atoms were at lower temperature than the RF-heated clouds of Yb atoms, the dominant effect of Rb atoms on the trapped Yb^+ ions was heating.

The atom-induced heating is characterized in Figure 4-15 by observing the change in the width Δ of the ion fluorescence spectrum during laser cooling as the Rb atoms are moved through the center of the ion cloud. To account for a variation in the number of Rb atoms as the Rb MOT is displaced, the measured width Δ is normalized to the absolute Rb MOT fluorescence. Clipping of Rb MOT laser beams inside the vacuum chamber led to a decrease in the number of Rb atoms in the left part of the figure, resulting in a larger deviation in the measured normalized width Δ.

An explanation for the heating of Yb^+ ions based on the interruption of their RF-driven micromotion will be given in the next chapter. As the amount of micromotion increases away from the trap center, the heating due to Rb atoms increases as the Rb MOT is moved away from the center of the ion trap.

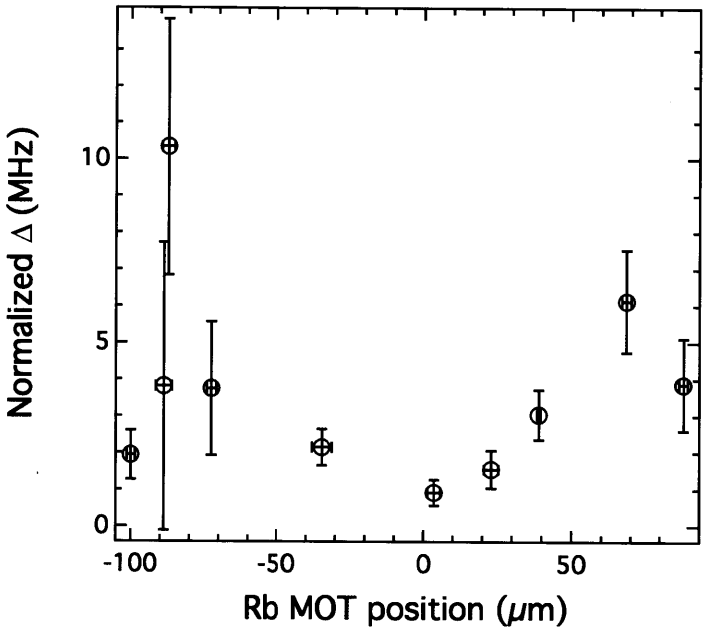

Figure 4-15: Heating of Yb^+ ions by collisions with laser-cooled Rb atoms measured by a relative increase of the width Δ of the ions' Doppler cooling profile as a function of the distance between the center of the MOT and the center of the ion cloud.

Chapter 5

Classical Limits to Ion-Atom Collisions

The heating of the Yb^+ ions in collisions with cold Rb atoms observed in the previous chapter can be explained by taking into account the effects of the RF trapping potential. This chapter presents an analysis of these heating effects and their implications for future hybrid ion-atom systems.

Section 5.1 introduces the process of RF-induced heating in ion-atom collisions in Paul traps, as first described by [MD68]. This model predicts a limit to energies achievable in ion-atom collisions that depends on the residual RF-driven motion of the trapped ion.

The gros RF-driven micromotion can in principle be compensated by sensitively controlling the electric fields of the ion trap to keep the ion at the node of the RF trapping potential. During an ion-atom collisions, however, the ion experiences an additional field produced by the colliding polarized atom. The interaction of the trapped ion with this electric field is explored in Section 5.2. A new result derived in Section 5.2 is a fundamental classical limit to the ion-atom collision energies achievable in RF traps.

For the ion-atom systems studied in the present experiments [GCOV09, ZPSK10, SHD10], the classical energy limit derived in Section 5.2 is higher than the energy at which quantum effects are expected to dominate ion-atom collisions. To enter the quantum regime, Section 5.3 suggests using light atoms such as Li or avoiding RF effects by confining the ions in a dipole trap.

5.1 Sympathetic Cooling of Ions

As described in detail in Appendix A, when viewed at times separated by an integer number of RF periods, the motion of an ion close to the bottom of a harmonic RF trap is described by a conserved effective Hamiltonian $\mathcal{H}$. With $V_{DC}(r)$ the DC electric potential experienced by the ion, $\mathcal{H}$ can be written in the form:

$$\mathcal{H}(p,r) = \frac{p_{sec}^2}{2m_i^{eff}} + V_{sec}(r) + V_{DC}(r)$$

where $V_{sec}(r)$ is the effective secular potential of the ion trap, m_{eff} the ion's effective mass and $\vec{p}_{sec} = \vec{p} - m_i\vec{v}_{mm}$ the ion's secular momentum, differing from the ion's real momentum $\vec{p}$ due to position- and time-dependent micromotion with velocity $\vec{v}_{mm}(r,\, t)$.

The Hamiltonian $\mathcal{H}$ describes the evolution of the ion's trajectory separated in time by an integer number of RF periods. Along this coarse-grained 'secular' trajectory, $\mathcal{H}$ represents a conserved energy, expressable as the sum of the trap potential $V_{sec}(r) + V_{DC}(r)$ and the secular kinetic energy

$$E_k = m_i^{eff} v_{sec}^2/2$$

where $\vec{v}_{sec} = \vec{p}_{sec}/m_i^{eff}$ is the ion's secular velocity.

Assuming that an ion-atom collision takes place on a spatial scale much smaller than the trap trajectory and a timescale fast relative to the trap dynamics, the secular velocity after the ion-atom collision will be:

$$\vec{v}'_{sec} = \frac{m_i\left(\vec{v}_{sec} + \vec{v}_{mm}\right)}{m_i + m_a} + \frac{m_a}{m_i + m_a} R_L(\theta)\left(\vec{v}_{sec} + \vec{v}_{mm}\right) - \vec{v}_{mm}$$

where $R_L(\theta)$ is a rotation matrix by the collisional deflection about the relative ion-atom angular momentum vector L. The change in the ion's secular kinetic energy after the collision will be

$$\begin{aligned} E'_k - E_k &= \frac{m_i^2 m_a\left(1-\cos\theta\right)}{m_i^{eff}\left(m_i+m_a\right)^2}\left(-m_i v_{sec}^2 + m_a v_{mm}^2\right) \\ &- \frac{m_i m_a}{m_i^{eff}\left(m_i+m_a\right)}\vec{v}_{sec}\cdot\left(m_i - m_a + m_a R_L^T - m_i R_L\right)\vec{v}_{mm} \end{aligned} \tag{5.1}$$

As the shape of Langevin trajectories depends only on the ratio of the impact parameter to the Langevin radius, the distribution of the collisional deflections θ will

not depend on the collision energy. Since in a harmonic trap (i.e. close to the trap origin), v_{sec}^2, v_{mm}^2 and $v_{sec}v_{mm}$ are all proportional to the ion's energy, the change in the ion's secular kinetic energy will then be proportional to the secular energy as $E_k - E_k' = fE$ with f a random variable dependant on the trap shape, the time of the collision in the RF cycle and the phase of the secular motions but not on the energy of the ion.

If the trap frequencies are sufficiently incommensurate, the ion's trajectories will be randomized in the subspace $\mathcal{H} = E_k$ between the individual collisions. In this case, a sequence of ion-atom collisions can be viewed as a Markov process in $\log E$ described by

$$\log E^{(n+1)} = \log E^{(n)} + \log f$$

where $\log f$ are identical random variables with distributions that depends on the trap parameters and the ion/atom mass ratio but is independent of the ion's current energy $E^{(n)}$.

By the central limit theorem, the distribution of the *logarithm* of the ion's energy after $n \gg 1$ collisions will then be Gaussian with mean $\log E_0 + n \langle \log f \rangle$ and standard deviation $\sqrt{n}\sigma_0$ where σ_0 is its standard deviation of $\log f$. In terms of the ion's energy, the resulting distribution will have significantly larger fluctuations and longer tails at both high and low energies than a thermal sample. As discussed by [DeV09], these non-thermal tails persist even for collisions with neutral atoms at a finite temperature.

For small changes of the ion energy in a collision, $\log f$ is approximately equal to $(E_k' - E_k)/E$. When averaged over one RF cycle and over the whole trap volume, the secular velocity and the micromotion will be uncorrelated. Therefore,

$$\langle E_k' - E_k \rangle \approx \frac{m_i^2 m_a (1 - \cos\theta)}{m_i^{eff} (m_i + m_a)^2} \left(-m_i \langle v_{sec}^2 \rangle + m_a \langle v_{mm}^2 \rangle \right) \tag{5.2}$$

This expression for the mean change in the ion's energy after a collision with a cold neutral atom was first derived by Major and Dehmelt in the context of sympathetic cooling of ions using a buffer gas [MD68].

The first term in (5.2) represents the decrease in the ion's secular kinetic energy due to the collision with the neutral atom and takes the same form as for buffer gas cooling in free space.

The second, heating, term arises due to the fact that in an RF trap, the secular motion is defined relative to changing action-angle variables of $\mathcal{H}$. As the secular momentum p_{sec} of $\mathcal{H}$ is related to the physical momentum by a micromotion shift

$m_i v_{mm}$, by damping the physical momentum, a collision will *add* to the secular momentum, increasing the secular energy. In the case where the ion starts with zero secular momentum, and the collision removes the ion's entire physical momentum, the secular momentum added by the collision will be equal to the full micromotion shift $m_i v_{mm}$. In this case, after the collision which stops it, the ion will have *gained* secular energy $\Delta E_{sec} = (m_i v_{mm})^2 / 2m_i^{eff}$.

The measurement of ion heating or cooling using the secular rather than the real Hamiltonian may seem surprising. The puzzle is resolved when one remembers that the choice of energy as the quantity to measure is a consequence of its conservation in an isolated system, itself a consequence of time-translation symmetry of such systems. Since the RF trap only possess discrete time-translation symmetry, the only meaningful conserved quantity to use (and minimize) becomes $\mathcal{H}$.

If close-range collisions with neutral atoms are allowed without any further control, to preserve control over the system, the removal of the secular energy by the atoms will have to be larger than the heating due to interruption of micromotion, corresponding to $\langle \log f \rangle < 0$. Otherwise, close range collisions will have to be avoided e.g. by holding the ions and the atoms in separate traps (Section 5.3).

At high RF frequencies, the mean kinetic energy of micromotion is equal to the secular potential (Section 2.1) and, also $m_i^{eff} \approx m_i$ (Appendix A). This allows (5.2) to be rewritten in terms of the mean energies of the ion as:

$$\langle E_k' - E_k \rangle = \frac{2 m_i m_a (1 - \cos\theta)}{(m_i + m_a)^2} \left(- \langle E_k \rangle + \frac{m_a}{m_i} \langle V_{sec} \rangle \right) \tag{5.3}$$

The sign of (5.3) will depend on the relative magnitude of the mean secular potential and kinetic energy in the trap. For initially thermalized ions, by the virial theorem in the overall harmonic secular potential, $\langle E_k \rangle = \langle V_{DC} + V_{sec} - V_0 \rangle$ where V_0 is the potential at the bottom of the trap at $r = r_0$. In a field-compensated trap $V_{\mathrm{sec}}(r_0) = 0$, so the condition for cooling becomes:

$$\frac{m_a}{m_i} < 1 + \frac{\langle V_{DC} \rangle}{\langle V_{sec} \rangle} \tag{5.4}$$

In a pure RF trap, this is equivalent to $m_a < m_i$. Close to the limit $m_a \approx m_i$, the change in the ion's energy in an individual collision is no longer small and the distribution of $\log f$ deviates from the distribution of $\Delta E_k / E$. A Monte-Carlo simulation for 2D RF confinement gives an improved limit $m_a < 2.17\, m_i$ [ZRSK11].

The atom mass limit becomes more stringent in the presence of nonzero DC potentials. Here, the ions will cluster in the regions of a the deconfining DC potential,

leading to $\langle V_{DC} \rangle < 0$, by (5.4), a decreased upper limit to m_a. Intuitively, in the deconfining directions of the DC potential, the ions can travel to larger distances from the trap center, leading to larger micromotion and consequent heating in collisions with atoms. In the limit of equally strong confining RF and deconfining DC potentials, the ions move very far from the trap origin, $\langle V_{DC} \rangle \approx - \langle V_{RF} \rangle$ and $m_a \ll m_i$ is required in order to preserve cooling.

In the presence of offset dipole DC electric fields, the ion will be displaced from the center of the RF potential until further displacement is limited by the mean secular force during the ion's micromotion with nonzero velocity $\vec{v}_{mm}$. As before, the mean energy of this micromotion will correspond to the mean secular potential at the bottom of the trap at $\vec{r} = \vec{r}_0$. By (5.3), $V_{sec}(\vec{r}_0) > 0$ will lead to constant ion heating under collisions with cold atoms and sympathetic cooling of an ion with neutral atoms in close-range collisions will then only be possible down to kinetic energies comparable to the energy of the offset micromotion $V_{sec}(\vec{r}_0)$:

$$E_k \sim V_{sec}(\vec{r}_0) = \frac{e^2 E_{DC}^2}{2m\omega^2} \tag{5.5}$$

The effect of displacing the *atoms* away from the center of the ion trap is similar to the effect of an external electric field. Again, the collisions happen in a region of nonzero RF field which drives the ions' micromotion. The interruption of micromotion at the collision point $\vec{r}_0$ leads the ion to gain energy on the order of the trap potential $V_{sec}(\vec{r}_0)$ at this point. This effect qualitatively explains the heating observed on Figure 4-15.

In summary, at energies higher than $\sim$ 100 nK, close-range ion-atom collisions follow clasical Langevin physics. The interruption of RF micromotion in these collisions contributes to ion heating. For $m_a \gtrsim m_i$, this heating overcomes the sympathetic cooling by cold atoms, leading to runaway increase in the ion's energy. For $m_a < m_i$, in traps away from stability limits, the ultimate energy reached in close-range ion-atom collisions is limited by the enrgy of the ion's micromotion at the collision point.

5.2 Classical Micromotion Energy Limit

By using an appropriate trap design and possibly measuring the residual ion's micromotion, it may be possible to decrease external offset electric fields and bring the energy limit (5.5) below a single ion motional quantum, opening the door to ion-atom gates via close-range ion-atom collisions [ICZ07].

In addition to the external fields, however, a different, hard to compensate, source of offset electric field exists: the field produced by the atomic dipole itself during the collision. By tugging on the ion, the atom displaces the ion from the trap origin, introducing micromotion. This micromotion is interrupted by the hard ion-atom collision, leading to heating.

A new result of this thesis, presented in this section, is a classical calculation of the limit imposed by this heating process. For most ion, atom and trap parameters, the obtained limit is higher than both the energy of a single motional quantum in the ion trap and the s-wave limit for ion-atom collisions (Section 3.1), justifying the classical approach. The obtained results indicate that for a hybrid quantum system to be viable, the ions and the atoms will likely need to be confined to separate traps preventing close-range collisions and the associated heating.

For a free atom and an ion confined to a trap, the classical Hamiltonian can be written as:

$$H = \frac{p_a^2}{2m_a} + \frac{p_i^2}{2m_i} + \frac{1}{2}\frac{C_4}{|r_a - r_i|^4} + \frac{1}{2}m_i r_i^T \omega^2 r_i$$

As the atom approaches from infinity at low energy, the ion will initially be held tightly by the trap and the collision can be approximated by a Langevin Hamiltonian of the form:

$$H_L = \frac{p_a^2}{2m_a} + \frac{C_4}{2\,|r_a|^4}$$

At low collision energies, the trajectory of this Hamiltonian takes the form of a partial spiral with the greatest angular deflection occuring close to the Langevin radius i.e. at $r_a \approx |r_a - r_i| \approx r_L = (2C_4/E)^{1/4}$. For $r \ll r_L$, this spiral will asymptote to a head-on collision, as described in Section 3.2.

As the atom approaches the ion, the ion will be displaced from the trap center by the attractive ion-atom potential by $|\Delta r_i| \approx 2C_4/m_i\omega^2\,|r_a|^5$. This displacement will start affecting the collision trajectory when $|\Delta r_i| \sim |r_a|$ or at $|r_a| \sim |r_i| \sim r_T = \left(C_4/m_i\,|\omega|^2\right)^{1/6}$. r_T sets the natural length scale for the effects of the trap

on the collision. For low energy collisions, it is in fact the only classical energy scale. The associated momentum, energy and time scale are $p_T = \left(C_4 m_i^5 |\omega|^4\right)^{1/6}$, $E_T = \left(C_4 m_i^2 |\omega|^4\right)^{1/3}$ and $t_T = 1/|\omega|$. Interestingly, the collision dynamics happens at the secular frequency of the ion trap.

At low collision energies, the characteristic lengthscale r_T for the interaction of the ion-atom system with the ion trap will be much smaller than the ion-atom Langevin radius r_L. In this case, the effects of the trap on the collision trajectory will be felt only in domain of low angular deflection corresponding to r_i, $r_a \ll r_L$. In other words, when considering the trap effects on the collision trajectory at low energies, it is sufficient to only consider head-on collisions. After rescaling $t \to t_T t$, $\vec{r} \to r_T \vec{r}$, $\vec{p} \to p_T \vec{p}$, the original Hamiltonian then takes the unitless form:

$$H_{eff} = -\frac{1}{2}\frac{1}{(r_i - r_a)^4} + \frac{1}{2}\vec{r}_i \cdot \bar{\omega}^2 \cdot \vec{r}_i + \frac{p_a^2}{2\bar{m}_a} + \frac{p_i^2}{2}$$

with $\bar{m}_a = m_a/m_i$ and $\bar{\omega}^2 = \omega^2/|\omega|^2$ and the initial condition $r_i^0 = 0$, $r_a^0 = \infty$, $E = 0$, $L = 0$.

For near isotropic traps, $\bar{\omega}^2 \approx I$, yielding a universal 1D radial problem of the form

$$H_{eff}^1 = -\frac{1}{2}\frac{1}{(r_i - r_a)^4} + \frac{1}{2}r_i^2 + \frac{p_a^2}{2\bar{m}_a} + \frac{p_i^2}{2} \tag{5.6}$$

Intially, the atom approaches the ion held fixed by the trap along the low-energy trajectory given by

$$r_a^3 = 3\left(t_{coll} - t\right)/\sqrt{\bar{m}_a} \tag{5.7}$$

with t_{coll} the time of the close-range collision. In this regime, the atom will displace the ion from the trap center until the r^{-4} potential overcomes harmonic confinement. This will coincide with the potential minimum near $r_i = 0$ becoming degenerate, which in H_{eff}^1 happens at:

$$\begin{aligned} r_i &= 0.294 = R_i \\ r_a &= 1.761 = R_a \end{aligned}$$

This model is valid as long as the adiabaticity condition $|d \log V/dt| \ll 1$ i.e.

$r_a \gg \bar{m}_a^{-1/6}$, is satisfied. For $m_a \geq m_i$ this will extends to $r_{i,a} \sim 1$. Once the atom's attraction overcomes the ion's trap confinement, the radial separation of the ion-atom system will evolve in the center of mass frame with only a small effect of the trap, leading to a collision at radius $r = r_c$. The collision radius r_c will range between R_i and R_a depending on the mass ratio: for $m_a \gg m_i$, the ion will be pulled to the initial atom's location at $r_a = R_a$ while for $m_a \approx m_i$, the collision takes place at roughly the half-way point $r_i = r_a \approx 1$.

The displacement of the ion away from the trap origin will transfer a part of the atom's energy on the order of $E_c = m_i \omega^2 r_c^2/2$ to the joint ion-atom motion inside the trap, binding the atom to the trap. Since the r^{-4} polarization potential does not have stable orbits, the joint atom/ion system can then be expected to undergo repeated hard-core collisions at $r_i \sim r_c$.

As described in the previous section, in the presence of the trap potential, hard-core collisions can add to the system an energy on the order of the ion's micromotion energy. In a compensated RF trap, the mean micromotion energy will be equal to the secular potential of the ion trap. After several hard-core collisions at radius $r = r_c$, the system will therefore gain enough energy to eject the atom to infinity, leaving the ion with energy $E_i \sim E_c$. For $m_i \approx m_a$, E_c and E_i will be proportional to E_T as the sole energy scale in the classical problem.

For $^{174}\mathrm{Yb}^+ + ^{87}\mathrm{Rb}$, using the Rb polarizability of $C_4 = 319 a_0^3$, the collisional energy gain is predicted to be on the order of $E_{\mathrm{gain}} \sim k_B \times 40\ \mu\mathrm{K}$, even in a relatively weak 100kHz ion trap. This is significantly higher than both the vibrational quantum of the ion trap ($k_B \times 5\ \mu\mathrm{K}$) and the ion-atom s-wave scattering limit ($E_s = \hbar^4/2C_4\mu^2 \sim 50$ nK).

In collisions with heavy atoms, the atom's intertia may delay it in escaping to infinity, allowing even more heating collisions to take place and further increasing the ion's ultimate energy. Conversely, the added micromotion energy may be decreased by using a lighter atom. In this case, the atom can be attracted quickly enough to the ion that the later doesn't have enough time to be significantly displaced from the trap center. For $m_a \ll m_i$, the ion displacement will remain small and the atom can be assumed to follow the unperturbed trajectory (5.7). The force on the ion due to the atom is then:

$$F_a(t) \approx 2r_a^{-5} = \frac{2}{3^{5/3}} \left(\frac{m_a}{m_i}\right)^{5/6} (t_{coll} - t)^{-5/3}$$

The ion's equations of motion can be integrated to find the ion's displacement at the time of the collision $t = t_{coll}$:

$$r_c = r_i(t_{coll}) = \int_{-\infty}^{t_{coll}} \sin(t_{coll} - \tau) F(\tau) d\tau \approx 1.12 \left(\frac{m_a}{m_i}\right)^{5/6}$$

By the same argument as before, the atom will stay bound to the ion until micro-motion heating causes it to be ejected, leaving the ion with energy on the order of $m_i \omega^2 r_c^2/2$ i.e.

$$E_i \sim E_T' = E_T \left(\frac{m_a}{m_i}\right)^{5/3} = \left(\frac{C_4 |\omega|^4 m_a^5}{m_i^3}\right)^{1/3} \tag{5.8}$$

The expression (5.8) has been checked by performing numerical simulations of cold classical ion-atom collisions in a realistic quadrupole RF trap. The simulation is performed in the natural classical units of m_i, r_T, t_T and E_T.

The trap confinement in the $x-y$ plane is due to a RF quadrupole field producing an axially symmetric harmonic secular potential with $\omega_x = \omega_y = 1.02$. The RF frequency was chosen as $\Omega = 9.43$, for a Mathieau stability parameter of $q = 0.20$. Axial confinement is produced using an axially symmetric quadrupole DC field, resulting in axial trap frequency of $\omega_z = 0.29$. To break the trap symmetry and aid in laser cooling, additional quadrupole DC fields of the form $m_i \omega_{xx}^2 (x^2 - y^2)/2$ and $m_i \omega_{xy}^2 xy$ are applied with $\omega_{xx} = 0.40$ and $\omega_{xy} = 0.38$.

An ion of mass $m_i = 1$ is confined to the center of the trap and an atom of mass $\bar{m}_a$ is allowed to approach it head-on from a random direction along the low-energy trajectory for $r_T \ll R_L$ (5.7). The simulation is started at a random RF phase and at a large ion-atom distance of $r_0 > 5$, ensuring that any deviations from the ideal cold-atom trajectory correspond to an energy scale ($\sim r_0^{-4}$) much less than the energies involved in the collision.

The ion and the atom trajectories are evolved using the Dormand-Prince explicit Runge-Kutta method with integral step control. The singularity in the r^{-4} potential is avoided by detecting the collision using the conditions

$$\begin{aligned} (r_i - r_a) \cdot (\dot{r}_i - \dot{r}_a) &< 0 \\ |r_i - r_a| &< \epsilon \\ \frac{L^2}{2\mu} &< \frac{\epsilon}{2|r_i - r_a|^2} \end{aligned}$$

where L is the center of mass ion-atom angular momentum and μ the reduced mass of the ion-atom system. $\epsilon \approx 0.1$ is typically chosen, ensuring that the collision cutoff happens at an energy scale three orders of magnitude higher than the typical simulation scale. The last condition ensures that the collision cutoff happens well inside the Langevin radius, leading to a 1D head-on collision. The hard-core collision is then simply executed by reversing the ion's and the atom's momenta in the center of mass frame.

A sample ion-atom trajectory for $\bar{m}_a = 87/174$ corresponding to the Yb^+ / Rb system similar to the one from [ZPSK10] is shown on Figure 5-1. After the initial collision, the atom remains bound until the third collision knocks it out of the trap.

As described before, the proper quantity to use to measure ion heating in atom collisions is the secular energy $\mathcal{H}$. In a quadrupole trap such as the one described above, $\mathcal{H}$ has a quadratic form that can be calculated using the period-advance map phase space $U_{2\pi}$ as described in detail in Appendix I. In the absence of the atom, $\mathcal{H}$ will be conserved throughout the ion's motion. The magnitude of the secular energy $\mathcal{H}$ for the trajectories from Figure 5-1 is shown as the black diamonds on Figure 5-2. For ease of calculation, $\mathcal{H}$ is computed only at times of maximal RF field where it takes the form of a fixed quadratic form.

To quantify heating of the whole system, the atom's kinetic energy and the ion-atom potential can be added to $\mathcal{H}$. The resulting quantity, displayed as stars on Figure 5-2, is conserved as long as the relative motion of the atom and the ion is slow relative to the trap RF drive and changes abruptly in the hard-core collisions.

The distribution of the ion's energy gain during 600 collisions with random initial atom directions and at random RF phases for $m_i/m_a = 87/174$ is shown on Figure 5-3. The distribution of energies is bimodal with a separation between the ion-atom encounters that involve only one hard-core collision ($E_i < 2E'_T$) and those that lead to the formation of a bound ion-atom cluster. In the former case, the energy gain is bounded by the maximal micromotion energy at the collision location $r_i = r_a = r_c$. In the latter case, a long enough chain of repeated close-range ion-atom collisions can impart large energies to the ion before the atom is finally ejected.

Figure 5-4 shows the mean energy gained by an initially cold $^{174}Yb^+$ ion in collisions with atoms of varying mass. Each point is obtained by averaging over 600 random collisions.

As most ion-atom encounters involve few close-range encounters, the mean energy gain is very closely approximated by $E'_T = \left(C_4 |\omega|^4 m_a^5/m_i^3\right)^{1/3}$, following the simple analytic model described above.

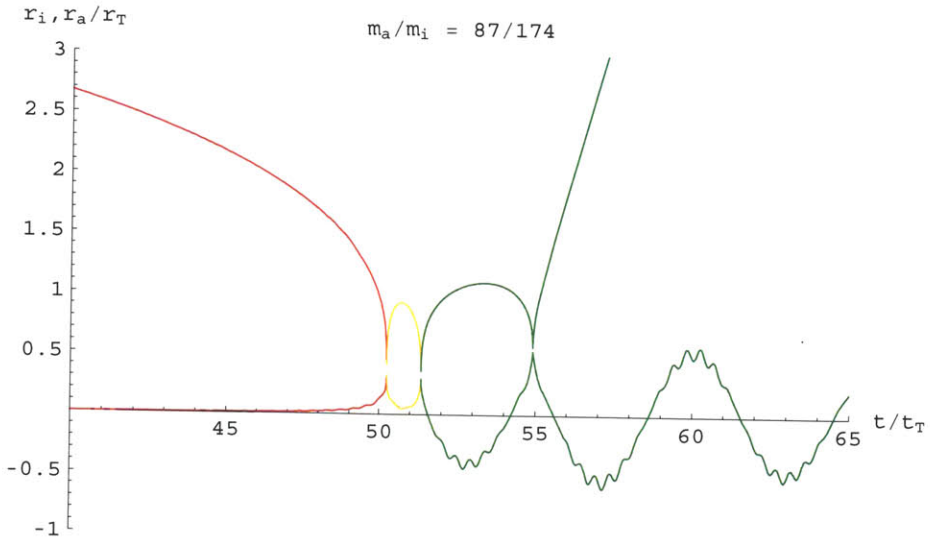

Figure 5-1: Projection of sample ion and atom collision trajectories for $\bar{m}_a = 87/174$ onto the trap x-axis. The trajectories following successive ion-atom collisions are colored sequentially. The beating in the ion's oscillations after the collision is due to mixing between different trap axes by the additional DC potential.

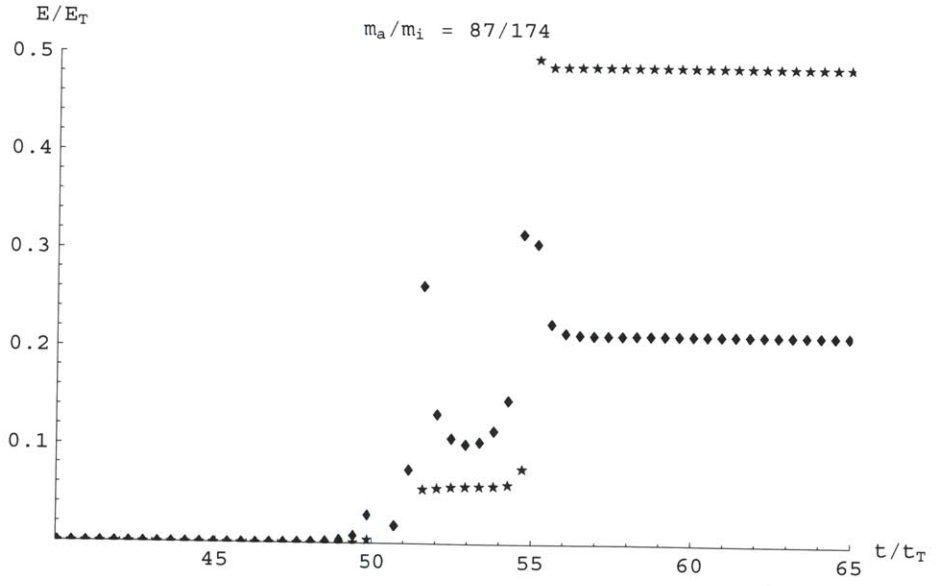

Figure 5-2: Ion secular energy ($\mathcal{H}$, diamonds) and the total system secular energy (stars) during the collision from Figure 5-1.

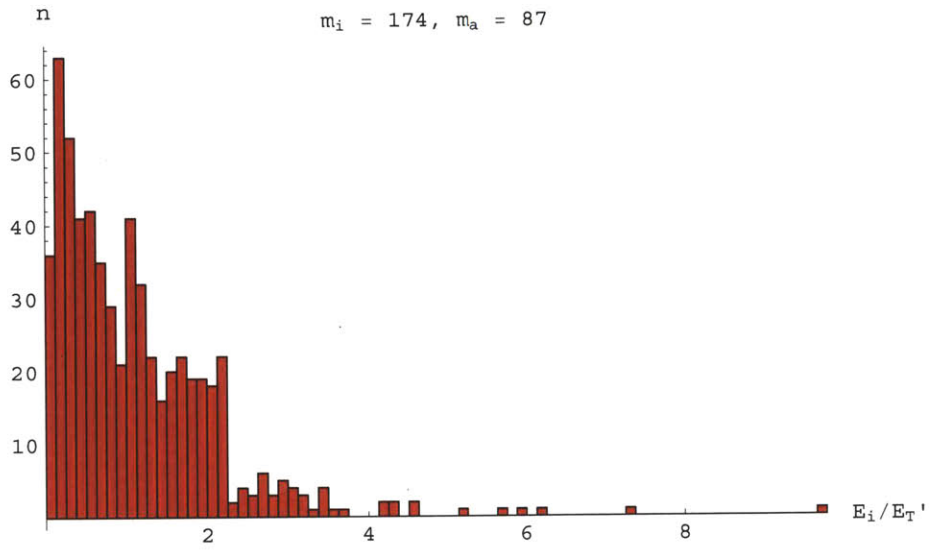

Figure 5-3: Distribution of the energies gained by a ^{174}Yb ion initially at rest in the center of an RF trap in 600 collisions with cold ^{87}Rb atoms, in units of $E_T' = \left(C_4 \left|\omega\right|^4 m_a^5/m_i^3\right)^{1/3}$.

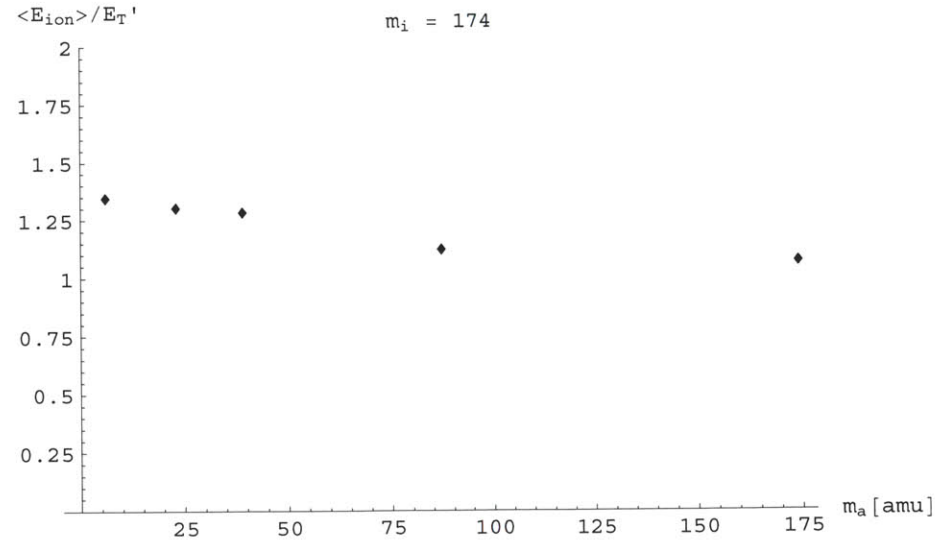

Figure 5-4: Mean energy gained by a ^{174}Yb ion initially at rest in the center of an RF trap in 600 collisions with cold atoms, in units of $E_T' = \left(C_4 \left|\omega\right|^4 m_a^5/m_i^3\right)^{1/3}$, as function of the atom mass.

5.3 Perspectives

In the past two years, two experiments [ZPSK10, Den09] have placed trapped ions inside a Bose-Einstein condensate of cold atoms with the long-term goal promise of observing coherent interactions between the ion and the condensate. The collisional heating derived in the previous section places significant constraints on this program.

Table 5.1 shows the approximate energies gained in hard-core collisions of $^{174}Yb^+$ with different cold atoms. This micromotion energy limit is expressed in temperature units as well as in the units of the ion trap vibrational quanta and the ion-atom s-wave collision energy. Also shown are the stray electric fields that would induce ion micromotion with energy on the order of E'_T.

Collisions with Yb^+ ions are considered as Yb is the heaviest ion species that is commonly trapped and E'_T is inversely proportional to the ion mass. Atoms with masses more than one half of the ion mass are not considered as collisions with them are expected to heat the ion as described in Section 5.1.

The last two lines of Table 5.1 correspond to the ion-BEC systems realized by [ZPSK10] and [SHD10], respectively.

atom/ion	$E'_T/k_B\,[\mu K]$	$E'_T/\hbar\omega$	E'_T/E_s	E_{DC} [V/m]
^{7}Li / $^{174}Yb^+$	$3 \times f^{4/3}$	$0.07 \times f^{1/3}$	$0.5 \times f^{4/3}$	$0.2\, f^{5/3}$
^{23}Na / $^{174}Yb^+$	$20 \times f^{4/3}$	$0.5 \times f^{1/3}$	$30 \times f^{4/3}$	$0.5\, f^{5/3}$
^{41}K / $^{174}Yb^+$	$70 \times f^{4/3}$	$1.5 \times f^{1/3}$	$500 \times f^{4/3}$	$0.9\, f^{5/3}$
^{87}Rb / $^{174}Yb^+$	$300 \times f^{4/3}$	$6 \times f^{1/3}$	$6000 \times f^{4/3}$	$1.9\, f^{5/3}$
^{87}Rb / $^{138}Ba^+$	$350 \times f^{4/3}$	$7 \times f^{1/3}$	$6200 \times f^{4/3}$	$1.8\, f^{5/3}$

Table 5.1: Classical ion-atom collision energy limits due to trap micromotion for collisions of $^{174}Yb^+$. f is the secular frequency of the ion trap in MHz.

The ratio of the classical micromotion energy scale E'_T to both the energy of the ion trap motional quantum and the fixed s-wave scattering limit decreases with a decrease in the ion trap confinement. Still, even in an ion trap with secular frequencies on the order of 10 kHz (comparable to atom traps), in both of the realized ion-BEC systems, the classical micromotion energy limit is comparable to the energy of one trap motional quantum while and many times greater than the ion-atom s-wave scattering limit. At the same time, to achieve these energies, the stray DC electric fields in the trap would need to be controlled at the level of 1 mV/m - three orders of magnitude better than the best control currently achieved in ion traps

[SHD10, ZPR+10, GCOV09].

The true quantum regime of s-wave atoms colliding with an ion in the ground trap state could be accessible using a light atom such as ^{7}Li together with a heavy ion such as Yb^+. In a 1 MHz ion trap, the classical micromotion limit is lowered below both the s-wave scattering threshold and the energy scale of trap vibrational excitation. Classical heating effects may be further reduced in this regime by the quantization of the ion's motion.

At the same time, the field sensitivity would remain at the level of 200 mV/m - in principle detectable by spectroscopy on a narrow ionic transition. At an RF trap frequency of 10 MHz, the ion micromotion due to DC fields on the order of 200 mV/m would give rise to RF sidebands at the 20 ppm level which could be detected by quantum jump spectroscopy on a <50 kHz wide transition.

The micromotion-induced heating could also be eliminated by trapping the ion in a static optical lattice trap as has been recently accomplished by [SEHS10]. The lattice needs to be deep enough to counter any residual electric fields; with these fields at the level of 200 mV/m, a lattice depth on the order of 200 atomic recoils (1.5 MHz) would be needed for Yb^+, corresponding to a lattice vibration frequency of 170 kHz. Since the s-wave energy limit E_s is proportional to μ^{-2} with μ being the reduced mass in the collision frame, a light atom is again advantageous. In the case of Yb^+ and Li, $E_s \sim 130$ kHz. Given the difficulties of cooling atoms in optical lattices to the ground vibrational state, a shallower lattice would likely have to be used to reach the s-wave collision limit with a proportionately larger electric field sensitivity.

A different approach would be to prevent close-range ion-atom collisions by spatially separating the ion and atom traps as proposed by [ICZ07]. To preserve the strong interaction between the ion and atoms, this spatial separation would have to remain small - on the order of 100nm. Control of independent traps on this scale could be achieved by interferometric control of an atom dipole trap relative to the ion trap electrodes.

Chapter 6

Ions and Photons

To implement any of the presently known quantum algorithms such as [SLAH94] or [Gro96] in a regime not accessible to classical computers, many thousands of qubits will be required. When the almost certain need for quantum error correction is taken into account, this number increases to tens or even hundreds of thousands of physical qubits with millions of needed controlled interactions. While the requirements for quantum simulation are less demanding, many interesting Hamiltonians would benefit from at least hundreds of ions [PC04b]. The ion approaches based on the CCD idea described in Section 2.3 may be scalable up to $\sim$ 1000 ions across mm-scale areas; however, the constraints imposed by physically moving ions make further scaling unlikely.

Communication over long distances between many sites with low losses and high connectivity is already achieved in classical switched fiber-optic telecommunication systems. A *typical* optical fiber has loss of 0.2 dB/km, which translates into 95% fidelity for the transmission of a quantum bit encoded in an optical photon over 1 km - far higher than any mechanism not involving light. The low decoherence afforded by light has already been used to create entanglement over 144 km [UTSM+07] and to implement commercial quantum cryptography systems [Eke91].

On the other side, light is already used to manipulate quantum information stored in ions and provide readout of the quantum states. If the ions' interaction with light could be extended to efficiently *transfer* the ions' quantum information to single photons, a low-decoherence reconfigurable quantum interface between remote ions would become possible. Significant steps towards such an interface have been taken in atomic systems - both with single atoms [BBM+07] and with atomic ensembles [ST07, CDLK08].

With an efficient ion-photon interface, one may envision wiring up individual

CCD-style trapped ion quantum information processors with optical fibers multiplexed using high-efficiency optical switches. With each processor possessing sufficient resources to implement high fidelity gates and error correction to overcome decoherence due to photon losses in the optical interconnects, scaling to thousands of processors and millions of ions could be possible.

Unfortunately, efficient coupling of atoms to light is a difficult goal that has stimulated research for a number of decades. To give context to the design of the ion-photon system presented in Section 7.1 of this thesis, a number of methods, including high-NA optics, optical resonators and collective enhancement, relevant for coupling ions to photons, will be given in the next sections.

6.1 Coupling of Atoms to Photons: An Introduction

To say that an atom (or an ion) is efficiently coupled to a single optical mode for transmission of quantum information implies that the coupling to this mode is faster than all other processes leading to leakage of information from the system. Specifically, the coupling needs to be faster than the intrinsic decoherence of the internal atomic states used as a qubit as well as the coupling to any other electromagnetic modes which carry information away from the atom. The later case invariably arises due to spontaneous emission arising from the coupling of an emitting atom to all the empty electromagnetic modes at its transition frequency.

For describing the coupling to the desired mode, it is then useful to introduce a parameter η, often called the single-atom cooperativity, quantifying the ratio of coupling to the desired mode to the spontaneous emission into the empty modes. In terms of η, the efficiency of collecting information into the desired mode is

$$p_{coupling} = \frac{\eta}{1+\eta} \tag{6.1}$$

Since internal atomic decoherence is usually slower than photon emission from excited states, most excited atoms are already strongly coupled to one particular optical mode - that corresponding to their free-space spontaneous emission pattern. For making such coupling useful, however, the free-space emission needs to be channeled into a mode that can be easily transmitted over a distance. Needless to say, spanning a significant portion of 4π steradians, the spontaneous emission pattern itself is ill-suited for the task.

In principle, using suitable high-numerical aperture optics, up to one half of the atom's emission pattern could be collected into a single Gaussian mode compatible with fiber transmission. Such collection has been demonstrated in atoms [TCA+08] and ions [SHG+10], achieving 9.8% and 1.35% coupling efficiencies to the single mode of an optical fiber . Diffractive collection optics for collection of light emitted by ions was recently demonstrated by [SNJ+11], promising single-mode coupling efficiencies of up to 20% . Still, none of these approaches promise to collect most of ion's emitted radiation and achieve a truly efficient ion-photon interface.

If collecting the full spontaneous emission pattern is difficult, one may ask if this pattern can be modified to fit a convenient mode. The road to engineering the emission of an emitter was opened by Purcell in 1946 with a suggestion that the rate of an atom's spontaneous emission can be increased by coupling it to a high-Q resonator [Pur46].

An application of Purcell's idea to trapped ions is the guiding idea behind the work presented in this half of the thesis. Before proceeding, it is worth noting its main features - specifically the effect of the resonator quality factor Q and the mode volume.

6.2 Resonant Enhancement

The physics of an atom's emission of electromagnetic field is captured by the coupling of the emitter and the various modes of the electromagnetic field. Inside a volume V, the electric and magnetic fields can be decomposed into individual modes as:

$$\vec{E} = \sum_{\lambda} e_{\lambda}(t)\,\vec{E}_{\lambda} \quad , \quad \vec{H} = \sum_{\lambda} h_{\lambda}(t)\,\vec{H}_{\lambda}$$

with the modal fields $(E_\lambda,\, H_\lambda)$ satisfying:

$$\begin{aligned} \nabla \times \vec{H}_{\lambda} &= \frac{\epsilon}{c}\omega_{\lambda}\vec{E}_{\lambda} \\ \nabla \times \vec{E}_{\lambda} &= \frac{\mu}{c}\omega_{\lambda}\vec{H}_{\lambda} \end{aligned}$$

Although the modes $(E_\lambda,\, H_\lambda)$ will usually not be losses, loss can be modeled as leakage into radiating modes. By enclosing the whole system in a sufficiently large box of volume V, radiation modes can then be explicitly included, resulting in a

net lossless system in which all modes posses real frequencies ω_λ with electric and magnetic fields satisfying orthogonality relations

$$\begin{aligned} \int_V \vec{E}_\lambda \cdot \vec{E}_{\lambda'} dV &\sim \delta_{\lambda,\lambda'} \\ \int_V \vec{H}_\lambda \cdot \vec{H}_{\lambda'} dV &\sim \delta_{\lambda,\lambda'} \end{aligned} \tag{6.2}$$

together with conservation of electric and magnetic energies:

$$\frac{1}{8\pi} \int \vec{E}_\lambda \cdot \epsilon \vec{E}_\lambda dV = \frac{1}{8\pi} \int \vec{H}_\lambda \cdot \mu \vec{H}_\lambda dV = \frac{\mathcal{E}_\lambda^m}{2} \tag{6.3}$$

By choosing an appropriate normalization, the modal energy $\mathcal{E}_\lambda^m$ can be made equal for all modes as $\mathcal{E}_\lambda^m = \mathcal{E}$.

Using mode orthogonality and the normalization (6.3), Maxwell's equations inside the volume V containing an emitting atomic polarization density P can be decomposed into the individual modes as:

$$\begin{aligned} h_\lambda \omega_\lambda &= \partial_t e_\lambda + \frac{1}{\mathcal{E}} \int_V d^3 r \, \vec{E}_\lambda (r) \cdot \partial_t \vec{P} \\ e_\lambda \omega_\lambda &= -\partial_t h_\lambda \end{aligned} \tag{6.4}$$

When driven by one point atomic dipole d at location r_0, the electric field amplitude e_λ in each mode will oscillate harmonically as:

$$\partial_{tt} e_\lambda + \omega_\lambda^2 e_\lambda = -\frac{1}{\mathcal{E}} \vec{E}_\lambda (r_0) \cdot \partial_t \vec{d} \tag{6.5}$$

Coupling to multipole emitters proceeds similarly with $E_\lambda (r)$ replaced by higher derivatives and d replaced by the emitter's multipole strength.

Using (6.3), the total energy can be expressed as a sum of energies $\mathcal{E}_\lambda$ in each mode:

$$\mathcal{E}_\lambda = \mathcal{E} \left[\frac{e_\lambda^2 (t)}{2} + \frac{h_\lambda^2 (t)}{2} \right]$$

Since, within each cycle, the average electric ($\mathcal{E} \langle e_\lambda^2 \rangle_t / 2$) and magnetic ($\mathcal{E} \langle h_\lambda^2 \rangle_t / 2$) energies are equal, $\mathcal{E}_\lambda = \mathcal{E} \langle e_\lambda^2 \rangle_t$.

To maintain the normalization (6.3), the mode amplitude $\vec{E}_\lambda$ must scale as $E_\lambda \sim \sqrt{4\pi\mathcal{E}/V_{eff}}$ where

$$V_{eff} = \int \vec{E}_\lambda \cdot \epsilon \vec{E}_\lambda \, dV / E_\lambda (r_0)^2 \tag{6.6}$$

is the effective volume of the mode λ as seen by the dipole. For modes localized around the emitter, V_{eff} will be significantly smaller than the total box volume V, reflecting the enhancement of the coupling of the emitter to photons localized in its vicinity.

When a dipole oscillating at frequency ω_0 is introduced into the volume V at time $t = 0$, the excitation of a mode of frequency ω_λ at time t will be:

$$e_\lambda (t) \approx \sqrt{\frac{4\pi}{V_{eff}\mathcal{E}} d\omega_0^2} \times \frac{\sin\left(\left(\omega_\lambda - \omega_0\right) t/2\right)}{\left(\omega_\lambda - \omega_0\right)/2} \frac{\sin\left(\left(\omega_\lambda + \omega_0\right) t/2\right)}{\omega_\lambda + \omega_0} \tag{6.7}$$

For coupling to modes near ω_0, the second term in (6.7) will rapidly oscillate at frequency $\approx \omega_0$. Then, similar to the rotating wave approximation in quantum optics,

$$\left\langle \left[\frac{\sin\left(\left(\omega_\lambda + \omega_0\right) t/2\right)}{\omega_\lambda + \omega_0} \right]^2 \right\rangle_t \approx \frac{1}{8\omega_0^2}$$

and the total energy in all continuum modes will be

$$\mathcal{E}_{cont} (t) \approx \frac{4\pi d^2 \omega_0^2}{8 V_{eff}} \sum_\lambda \frac{\sin^2\left(\left(\omega_\lambda - \omega_0\right) t/2\right)}{\left[\left(\omega_\lambda - \omega_0\right)/2\right]^2}$$

At times t longer than the timescale of the separation of modes, the above sum can be turned into an integral $\int \rho_\lambda (\omega) \, d\omega$, where ρ_λ is the density of electromagnetic modes in the volume V. In exact analogy to the derivation of Fermi's golden rule in quantum mechanics, the summand can then be substituted with $2\pi t \delta (x)$, resulting in a constant power emitted into the continuum of electromagnetic modes

$$\partial_t \mathcal{E}_{cont} = P_{cont} \approx \pi^2 d^2 \omega_0^2 \rho_\lambda (\omega_0) / V_{eff} \tag{6.8}$$

(6.8) hints at methods for improving the coupling of an atom or ion to a photonic link: either decrease the density of unwanted electromagnetic modes or increase the density of modes of shape coinciding with the desired spatial mode. To decrease the density of optical modes, one would have to modify the medium through which

light propagates on the scale of a wavelength, as suggested by Yablanovitch [Yab87]. This would inevitably bring the atom close to a material surface. While this has been accomplished for atoms [ADW+06], bringing ions very close to surfaces presents significant challenges, as described in the next section.

To increase the density of desired optical modes, the emitter can be placed inside a resonant structure, as suggested by Purcell. A resonator of finite linewidth κ and volume V_c can be modelled as coupling to modes which extend beyond the resonator to fill the whole radiation box V, converting the single resonant mode at frequency ω_c to a near-continuum of hybrid resonator-box modes. In this picture, resonator decay can be thought as being due to interference between the neighbouring hybrid modes with spacing $\Delta \sim \kappa$. An exact calculation [WW30] predicts a spacing of $\Delta = \pi\kappa/2$, corresponding to an overall mode density of $\rho = 2/(\pi\kappa)$.

For $\kappa \ll \omega_c$, the near-continuum modes will remain localized to the resonator volume. For a resonator tuned to resonance with the atom, the power emitted into the resonator (6.8) is

$$P_{cav} \approx 2\pi d^2 \omega_0 \frac{Q}{V_{eff}} \tag{6.9}$$

where $Q = \omega_c/\kappa$ is the Q-factor of the resonator.

(6.9) can also be derived directly from (6.5) by including resonator loss as a damping term:

$$\partial_{tt} e_c + \kappa \partial_t e_c + \omega_c^2 e_c \;=\; -\sqrt{4\pi/V_{eff}\mathcal{E}}\,\partial_{tt} d$$

On-resonance, the radiated power is equal to the power lost from the oscillator:

$$P_{cav} \;=\; \kappa \mathcal{E}_c = \kappa \mathcal{E} \left\langle e_c^2 \right\rangle_t$$

Using $Q = \omega_c/\kappa$, the power lost from the oscillator on-resonance is given by (6.9), as expected.

For emission into free space, $V = V_{eff}$ and the density of electromagnetic modes of both polarizations is $\rho_\lambda = 8\pi c^{-3}\omega^2 V/(2\pi)^3$. The coupling of each mode to a dipole emitter oriented along the $\hat{z}$-axis will scale as $E_\lambda \cdot d \sim \hat{z} \cdot E_\lambda$. Averaging this over all directions of emission and both polarizations, the effective emission dipole becomes $d/\sqrt{3}$ yielding free-space emission power

$$P_{cont} = \frac{d^2\omega_0^4}{3c^3} \tag{6.10}$$

in agreement with the power radiated by a classical dipole.

Relative to stray emission into free space, the power emitted into the resonator is:

$$\eta = \frac{P_{cav}}{P_{cont}} = \frac{3}{4\pi^2}\left(\frac{2\pi c}{\omega_0}\right)^3 \frac{Q}{V_{eff}} \tag{6.11}$$

This relation, derived by Purcell in [Pur46], fundamentally characterizes the coupling of an atom to a resonator mode. Since the physics of coupling to the resonator and the continuum modes is fundamentally the same, η remains independent of the details of the emitter.

Relation (6.11) also remains true in the quantum case for a driven two-level atom in the limit of low saturation. In this case, the oscillation of the quantum-mechanical dipole remains largely sinusoidal. Since Maxwell's equations are linear, the relations (6.10) and (6.9) remain true with d and P replaced by quantum operators in the Heisenberg picture. Taking the ratio, one then gets back (6.11). Since in multi-level atoms, free-space emission can also take place on other transitions, the cooperativity is simply modified as $\eta' = r\eta/(1+r)$ with r being the branching ratio for the desired transition.

As pointed out by Purcell, the same result is also obtained for spontaneous emission. While the state of the system corresponding to one photon in this case is highly non-classical, the Heisenberg equations of motion for the electromagnetic field operators remain identical obtaining the same ratio of the emissions into the resonator and into free space. In the limit of $\eta \ll 1$, the expressions (6.9) and (6.10) for the power emitted into the cavity and into free space have simple quantum analogies: $P_{cont} = \Gamma\hbar\omega$ with Γ the atomic free-space spontaneous photon emission rate and $P_{cav} = \hbar\omega\kappa\left(g_R/\kappa\right)^2$ where g_R/κ is the excitation of the cavity when driven by the single-photon atom-cavity coupling g corresponding to Rabi frequency $g_R = 2g$. Together, this leads to an expression for the single-atom cooperativity η in terms of the single-photon parameters of the form:

$$\eta = \frac{g_R^2}{\kappa\Gamma} = \frac{4g^2}{\kappa\Gamma} \tag{6.12}$$

6.2.1 Coupling of Ions to Optical Resonators

(6.11) suggests two approaches to increasing emission into a resonator mode: increasing the quality factor of the resonator and decreasing its effective mode volume.

In the case of ions, the minimal achievable resonator volumes are limited by the effects of charges on the resonator's surfaces. The presence of even 10 stray electrons $D = 10\ \mu$m away from an ion would lead to an ion displacement of $\Delta r > 1\ \mu$m, even for a heavy ion such as Yb^+ in a strong trap ($\omega \approx 2\pi \times 5$ MHz). Surface charging of this magnitude would be easily encountered on dielectric resonator surface under vacuum, especially when illuminated by blue/near-UV light necessary for Doppler-cooling of ions ([HBHB10]). Being comparable to the scale of the optical resonator, a micron-scale displacement would cause a significant change in the ion's coupling to the resonator.

An additional problem arises in the temporal domain due to micromotion induced by the nonzero trap RF field at the displaced ion's location with amplitude $x_{mm} = \sqrt{2}\Delta r\,\omega/\Omega$. As first observed by , the induced micromotion causes frequency modulation of the ion's coupling to the resonator. For resonator modes narrower than the trap RF frequency Ω, the effective coupling of the ion to the resonator is reduced to the carrier transition with relative strength given by $J_0^2\left(2\pi x_{mm}/\lambda\right)$ where $J_0\left(x\right)$ is the Bessel function of the first kind of 0-th order. With the trap operating at a typical RF frequency of $\Omega = 2\pi\times 40$ MHz, this corresponds to a tenfold reduction in the effective ion-photon cooperativity η.

More fundamentally, as described in Section 2.3, charge fluctuations on surfaces lead to heating of ions which have been observed in many different traps to scale as D^{-4} [DOS+06]. At 4 K, 75 μm away from a surface, the resulting field noise has been measured on the scale of 10^{-12} $V^2/m^2/Hz$ at 1MHz [Lab08]. 10 μm from a surface, the expected heating would be at least 10^5 quanta per second, even at cryogenic temperatures. With motion-mediated ion gates limited by the trap frequency (Chapter 2), such heating would be expected to introduce significant decoherence into operation of a quantum register interfaced to a small optical resonator.

6.2.2 Fabry-Perot Resonators

Among optical resonators with vacuum volumes larger than $(10\,\mu\text{m})^3$, the highest Q factors have been achieved in Fabry-Perot cavities consisting of two curved spherical, highly reflecting mirrors separated by a distance much larger than an optical wavelength. The modes of such a cavity will be equivalent to an equal superposition of

two counterpropagating free-space modes. The forward energy flux

$$\Phi = \frac{c}{4\pi}\int_{\pi} E_{\lambda;1,2} \times H_{\lambda;1,2} dA$$

of each of these free-space modes through any plane π perpendicular to the resonator axis will be constant. The energy stored in each free-space mode is then simply the flux over the cavity transit time:

$$\mathcal{E}_{\lambda;1,2} = \Phi L/c$$

where L is the cavity length.

The coupling will be maximized if the emitter is placed at the anti-node of the interference pattern formed by the two counter-propagating modes, near a plane π_0 where the resonator mode achieves its minimal cross-section. At this location, the wavefronts of the two free-space modes will be nearly planar, with $H_{\lambda;1,2} \approx \hat{z} \times E_{\lambda;1,2}$. Since the electric and magnetic energies in a free-space mode are equal, the total energy in each free-space mode can be written as:

$$\mathcal{E}_{\lambda;1,2} = \frac{1}{4\pi}\int_{V} E^2_{\lambda;1,2} dV = \frac{L}{4\pi}\int_{\pi_0} E^2_{\lambda;1,2} dA$$

The effective volume of the resonator mode is then

$$V_{eff} = \int E^2_{\lambda} dV \,/ E_{\lambda}(r_0)^2 = 2L\int_{\pi_0} E^2_{\lambda;1} dA \,/ 4E_{\lambda;1}(r_0)^2$$

For nearly-Gaussian transverse mode profiles of Fabry-Perot resonators, $E_{\lambda;1} \sim e^{-r^2/w^2}$, yielding

$$V_{eff} = L\pi w^2/4 \tag{6.13}$$

When placed under vacuum, the losses in Fabry-Perot resonators will occur only at the mirror surfaces, causing the resonator Q to scale with the mirror separation L as

$$Q = L\omega_c \mathcal{F}/\pi c \tag{6.14}$$

where $\mathcal{F} = \pi\sqrt{1-l}/l$ is the so-called resonator finesse expressed in terms of the fractional power loss l at each mirror. The finesse $\mathcal{F}$ is equal to the ratio of the

separation $\Delta_{FSR} = \pi c/L$ between the neighboring longitudinal modes of the resonator and the linewidth κ of each resonator mode.

Since both the resonator volume and its Q factor are proportional to its length, the maximum resonator cooperativity can be expressed only in terms of the finesse and the mode cross-section πw^2 at the emitter's location as

$$\eta = \frac{24\mathcal{F}}{\pi w^2 k^2} \tag{6.15}$$

where $k = 2\pi\omega_c/c$ is the free-space wavevector. (6.11) can also be expressed as $\eta = \mathcal{F} \times 2\,(\eta_1 + \eta_2)$ where

$$\eta_{1,2} = \frac{\Delta\Omega}{4\pi} \Big/ \frac{2}{3}$$

are the cooperativities for emission of a photon into either of the two counterpropagating free-space modes. Here, $\Delta\Omega = (2/kw)^2$ is the total solid angle subtended by the two free-space modes. The factor of $2/3$ is due to polarization averaging during emission into all free-space modes as described in Section 6.1.

The enhancement of the emission into the cavity relative to free space by the cavity finesse can be thought of as being due to the redistribution in frequency space of the free space modes along the cavity axis. The cavity concentrates the modes to a width κ around each longitudinal cavity resonance separated by Δ_{FSR}, resulting in an enhancement of the density of modes near the cavity resonance by a factor of $\mathcal{F}$. An additional factor of 2 arises from the positive interference between the two counterpropagating modes for emission near anti-nodes of the cavity field.

Following the initial demonstration of ion-cavity interaction by [GKH$^+$01], the Purcell enhancement for emission of a photon from an ion into an optical resonator was first observed by [KLH$^+$04], employing $\mathcal{F} = 15,600$ Fabry-Perot cavity to reach $\eta = 1.7$ on a the open $^2D_{3/2} - ^2P_{1/2}$ transition in Ca^+. Recently, [DRB$^+$10] used a finesse-70,000 cavity operating on the same transition to reach $\eta = 6.2$, corresponding to maximal photon-coupling efficiency of 86% .

6.3 Collective Enhancement

A different method of enhancing coupling emitters to a particular electromagnetic mode comes from (6.4). If, instead of one emitter, we consider an emitting dipole

density P, the excitation of a given mode will be proportional to the overlap of the modal electric field E_λ with P [1]. If the emitters are distributed so that their dipole density exactly reproduces one mode, by mode orthogonality (6.2), the *entire* radiation will go into the desired mode with complete suppression of coupling to stray modes.

This effect can be thought of as arising due to interference between the coherent emissions of the individual emitters: for emission into one mode, the individual emitters add constructively while for the other modes, their emissions cancel. With a finite number N of emitters, each carrying a dipole d_Σ/N, the emission into the desired mode will scale as the coherent sum $(Nd_\Sigma/N)^2$ while for the emission into the other modes, the individual emitters will be randomly phased with the total radiated power proportional to the incoherent sum $N\,(d_\Sigma/N)^2$. The single-mode cooperativity of the system will then scale with the number of emitters as $\eta_N \sim (Nd_\Sigma/N)^2 \,/\, (Nd_\Sigma/N)^2 \sim N$. As $N \to \infty$, the entire emission is beamed into one mode.

In a classical setting, this phenomenon of superradiance is commonly employed. By properly choosing the phases of an array of N antennas, their emission pattern can be directed into one direction (one free-space mode) with power gain N relative to an incoherent array of emitters [Mai].

This phased-array emission enhancement persists into the quantum regime, even for the emission of a single photon, as first described by [Dic54]. If out of N atoms equally coupled to a resonator mode, only the i-th is excited, corresponding to the total system wavefunction of the form $|\downarrow .. \uparrow ... \downarrow\rangle$, the probabilities p_c and p_f for the emission of a single photon into a given mode and into free space will have the single-particle ratio (6.11).

If, however, one starts with an entangled N-atom of the form

$$|\psi\rangle = \frac{1}{\sqrt{N}} \{|\uparrow\downarrow ... \downarrow\rangle + |\downarrow\uparrow\downarrow ... \downarrow\rangle + ... + |\downarrow ... \downarrow\uparrow\rangle\} \tag{6.16}$$

the quantum mechanical amplitudes $A_{c;i} = A_c$ for the photon to be emitted into the given mode from each of the components of the entangled state will add coherently with the total amplitude $A'_c = \sum_i A_{c;i}/\sqrt{N} = \sqrt{N}A$, corresponding to an enhancement of the single-photon Rabi frequency g' by a factor of $\sqrt{N}$. By the measurement postulate, $|A_c|^2 = p_c$ and the probability for the entangled state (6.16) to emit a

[1] in the case of multipole atomic emission, the overlap will be between derivatives of E_λ and the multipole distribution

photon into the single mode will be $p_c' = |A'|^2 = \left|\sqrt{N}A\right|^2 = Np_c$. This represents N-fold enhancement relative to the case when only one atom is excited.

Since the individual amplitudes A_f for emission into free space will have random phases ϕ_i, the probability of emission into free space will be

$$\left|A_f'\right|^2 = \sum_{ij} \left|A_f/\sqrt{N}\right|^2 \left\langle e^{i(\phi_i - \phi_j)} \right\rangle = |A_f|^2$$

which is the same result as for uncorrelated emitters.

Atomic states of the form (6.16) have been used to generate single photons in a well-defined optical mode [ST07]. The collective enhancement the coupling of atoms to an optical cavity has also been used to produce squeezed clock states for metrology [SSLV10] and to observe a phase transition in the coupled system [BGBE10].

6.4 Ion-Photon Coupling: Summary

As shown in this chapter, the coupling of ions to photons can be enhanced by using tightly focused photon modes, placing the ions inside Fabry-Perot optical resonators or employing collective ion states of the form 6.16. By placing a large collection of ions into an optical resonator with low mirror losses, ion-photon cooperativity parameters $\eta > 100$ could be achieved, allowing efficient coupling ($p_{coupling} > 98\%$) between single photons and the collection of ions.

Resonator-enhanced collective coupling of trapped ions to an optical mode was recently realized by [HDM+09] using a bulk 3D Coulomb crystal. Using ~ 500 ions in a 3000-finesse resonator, [HDM+09] demonstrated collective ion-resonator coupling equivalent to $\eta \approx 8$.

However, for performing controlled quantum operations and achieving a truly scalable ion-photon interface, this approach has severe limitations. The irregular structure of 3D crystals makes optical addressing of individual ions difficult. As discussed in Section 2.3, trap anharmonicities cause coupling between the motional modes of the crystal, making the addressing of individual modes for performing quantum gates difficult. Furthermore, in bulk crystals, most of the ions are located away from the node of the RF field and experience strong RF-driven micromotion. This motion, inhomogenously broadened among the ions in the crystal, will affect any scheme involving scattering of photons from an external spatial mode into the resonator, decreasing

the maximal obtainable ion-photon cooperativity. As described in Appendix A, in large crystals the driven micromotion also causes ion heating which will significantly affect the coherence of any procedure involving the ions' motion.

Many of the problems presented by bulk Coulomb crystals would be avoided if the ions are placed in a linear chain placed inside the mode of an optical resonator and directed along the nodal line of the RF field of an ion trap. A system of this type is described in the following chapters of this thesis.

Chapter 7

Ion Trap Array in an Optical Cavity

The previous chapter outlined a number of approaches to achieving an efficient interface between ions and photons together with the limitations of each approach. Free-space systems suffer from low coupling efficiency, optical resonators are limited by the deleterious effects of dielectric surfaces on trapped ions, while collective interfaces based on bulk Coulomb crystals are incompatible with trapped-ion quantum logic.

To avoid the limitations of each individual approach and achieve a useful and efficient interface, it is likely that several of these systems will need to be combined. Following this hybrid idea, the present chapter introduces a system for interfacing a collection of trapped ions with an optical resonator in way compatible with trapped-ion quantum logic.

The chapter is split into three sections. Section 7.1 introduces the overall approach based on an array of linear ion chains placed inside the mode of an optical resonator. Section 7.2 discusses the design criteria for the resonator and the ion trap, leaving the experimental implementation, including detailed schematics and initial characterization of the various sub-systems, for Section 7.3.

7.1 Ion Trap Array in an Optical Cavity: Concept

To be useful for quantum information and quantum simulation, an ion-photon interface of this kind should posses:

1. good coherence of the ions' internal and motional states

2. precise control over the ions' internal states

3. control of motional modes of multiple ions for generating effective interactions and performing quantum gates

4. scalable architecture compatible with modern fabrication techniques

5. efficient conversion of quantum information stored in ions to photons

In light of the recent successes in solid-state approaches to QIP and their inherent scalability, an ideal system would also allow integration with solid-state and microfabricated systems.

In the context of these requirements, the recent work with trapped ions points to a number of constraints:

1. Addressing individual ions and their motional modes in bulk Coulomb crystals containing more than 20 ions is difficult, especially for three-dimensional conformations of ions (Section 2.3). To address many ions with high fidelity a segmented trap architecture with < 20 ions in each trap, will likely be needed [WMI+97].

2. The ions in different segments need to efficiently communicate with each other. Between close-lying segments, this can be accomplished by physically moving ions [BOV+09, AUW+10]. On a larger scale, coupling to photons will likely be needed.

3. For efficient coupling to photons, Fabry-Perot optical resonators, collective enhancement via dozens of ions, or both, will be required (Section 6.1)

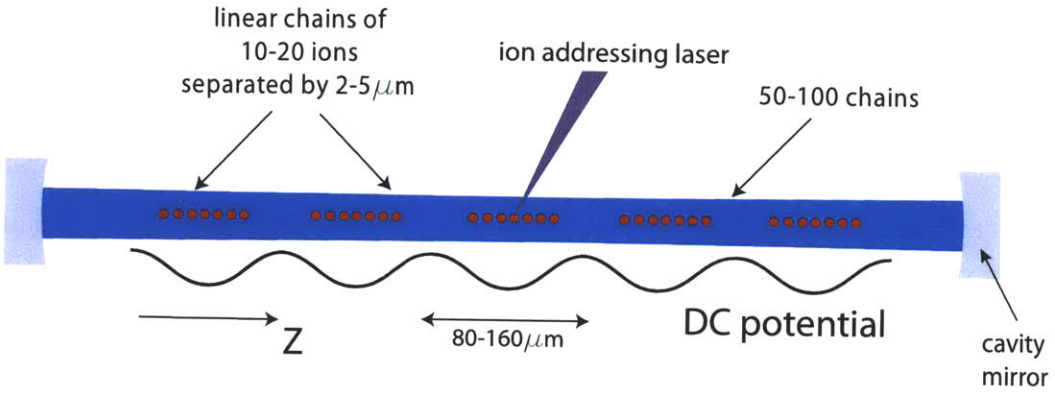

Figure 7-1: Linear array of ion traps inside an optical resonator

To meet these challenges, this thesis presents the design shown on Figure 7-1. 50 to 100 linear chains, each consisting of 10-20 ions, are placed inside the mode of a Fabry-Perot optical resonator and confined in the transverse plane by a linear RF Paul trap coaxial with the resonator mode. To avoid heating and degradation of coupling to the resonator due to RF-driven ion micromotion (Section 6.2.1), the ions are trapped close to the node of the trap's RF electric field and split into linear chains using a DC potential.

With ion trap frequencies on the order of 1 MHz, the spacing of ions in each chains is 2-5 μm, allowing for single-ion optical addressing using focused near-UV light resonant with the ions' strong $S-P$ transition. In addition to optical addressing of individual ions, the limited number of ions in each chain enables accurate spectral addressing of the chains' vibrational modes. Taken together, these capabilities allow each chain to be used as a general-purpose quantum register similar to the one used by [MSB+11] to entangle up to 16 ions.

While our system preserves a degree of motional coupling between the individual chains (Section 7.2.3) together with the the ability to move ions between from one chain to the next, the main coupling between spatially separated ion chains is achieved via the shared optical resonator mode. The coupling of each chain to the resonator mode, characterized by the cooperativity parameter η, is enhanced both by the Q-factor of the resonator ($\eta \sim Q$, Section 6.1) and by the collective coupling of all ions in each chain ($\eta \sim N$, Section 6.3).

7.1.1 Interfacing Collective Excitations to Single Yb^+ Ions

The use of collective coupling for quantum information with ions presents a challenge: in most schemes, the qubits used correspond to individual ions and not collective states of the form 6.16. This problem can be solved by taking advantage of the single-ion addressability afforded by our system. This section describes a variant of the the scheme proposed by [LLC+11] adapted to the of Yb^+ ions used in this thesis.

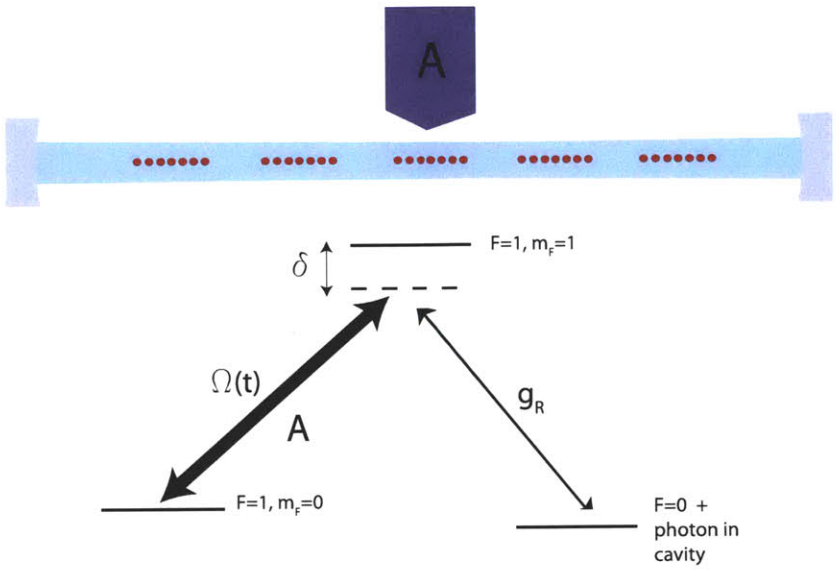

Figure 7-2: Proposed transfer of a photon into the ionic ensemble via STIRAP

In $^{171}Yb^+$ ions, quantum information can be stored with > 10 s coherences times [BHIW91] in the first-order magnetic-field insensitive $F = 0$ ($|\downarrow\rangle$) and $F = 1$, $m_F = 0$ $|\uparrow\rangle$ states. The ions can be initialized into the $|\downarrow\rangle$ state by optical pumping out of the $|\uparrow\rangle$ state on the $^2S_1$ - $^2P_1$, $F = 0$ - $F = 1$ transition. To write a photonic excitation into a particular ion chain, a stimulated Raman adiabatic passage process (STIRAP) can be used as shown on Figure 7-2, with the probability of success scaling as the collective cooperativity $N\eta$ of the ionic ensemble.

Initially, the ion chain that the photon is to be written into is illuminated from the side with beam A coupling the $F = 1$, $m_F = 0$ ground state to the excited $F = 1$, $m_F = 1$ state with Rabi frequency $\Omega_A(0)$ and a detuning δ chosen so as to match the detuning of the photon to be written. The ions in the chosen chain are coupled to the excited $F = 1$ state via two processes - the coupling via the side laser $\Omega_A(t)$ and the absorption of the photon by each atom with Rabi frequency $g_R(z_j)$ where z_j is the location of the j-th atom in the chosen chain. Assuming a constant

cross-section of the resonator mode, due to the standing wave nature of the resonator field, g_R will depend on the ion location as $g_R(z_j) \sim \cos(kz_j)$.

At the suitably chosen detuning δ, the two excitation processes will lead to the formation of a long-lived state that does not couple to the excited $F = 1$ state in any of the participating ions. The condition for the system to be in the dark state can be written as

$$\alpha_j \Omega_A(t) + \beta g_R(z_j) = 0,\ j = 1..N \tag{7.1}$$

where α_j is the amplitude of excitation of the j-th ion into the $|\uparrow\rangle$ state and β is the amplitude for the system to remain in the initial unexcited state. (7.1) corresponds to the formation of an N-ion W-state of the form

$$|\varphi_0\rangle \sim \sum_j \left[g_R(z_j)\,|\downarrow .. \uparrow_j .. \downarrow\rangle - \Omega_A(t)\,|\downarrow ... \downarrow\rangle\right]$$

For $\Omega_A(0) \gg g_R$, the initial state of the system with all ions in the $|\downarrow\rangle$ state, will be the dark state of the system. If the intensity of beam A is decreased adiabatically, the system will stay in the dark state which, as the beam A is attenuated, will transition to the collective state in which one atom has made the transition:

$$|\varphi_1\rangle \sim \sum_j g_R(z_j)\,|\downarrow .. \uparrow_j .. \downarrow\rangle \tag{7.2}$$

The next step is to transfer the stored excitation into a single ion. This can be accomplished by performing another STIRAP operation driven by a beam B counterpropagating to beam A together with beam C illuminating the ions through the resonator mode. The Rabi frequency $\Omega_1(t)$ for interaction of beam B with the ions can be assumed to be uniform across the addressed ions while the beam C will induce a Rabi that varies between the ions as $\gamma_R(z_j,\, t) = \gamma_R^0(t)\cos(kz_j)$.

If the detunings of the two lasers are adjusted to match the frequency of oscillation of the center of mass mode of the ion chain in the trap, the stored excitation can be coupled to the motion of the ion chain. Setting $\gamma_R(0) \gg \Omega_1(0)$, the initial collective ion state (7.2) will match the dark state of the new STIRAP process. As beam C is attenuated and the power of the coupling beam B increased, the original excitation will be transferred to the center-of-mass motion of the given chain of ions.

Finally, the excitation of the center-of-mass mode of the ion chain can be transferred to a particular ion using a π pulse performed with a focused pair of Raman

beams coupling the $|\downarrow, n = 1\rangle$ and $|\uparrow, n = 1\rangle$ states of the given ion via the excited $F = 1$ state, similar to the operation performed in [MMK+95].

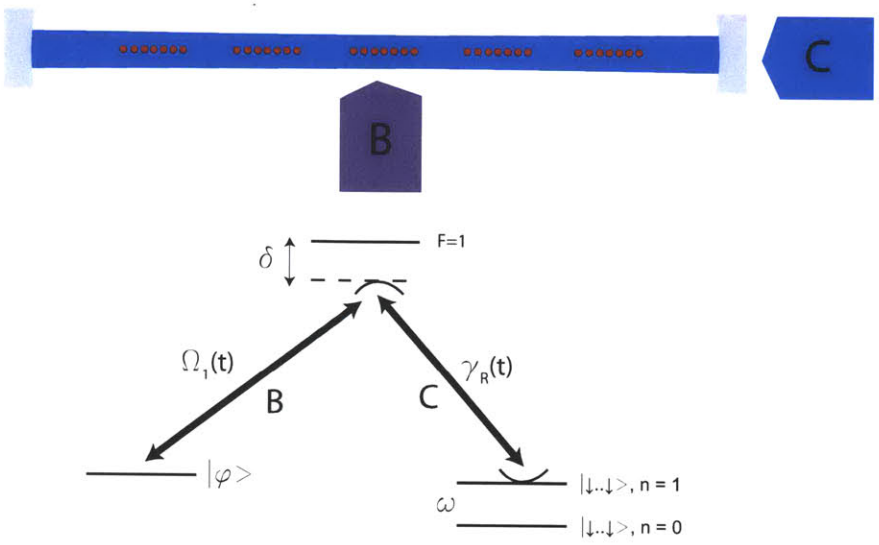

Figure 7-3: Transfer via cavity STIRAP of a collective ion excitation into the motional mode of an ion chain

7.2 Ion Trap Array in an Optical Cavity: Design

7.2.1 Optical Resonator

As described in Section 6.2.2 of Chapter 6, to achieve efficient coupling of ions to photons, it is desirable to use a Fabry-Perot resonator with a high mirror reflectivity and a mode tightly focused around the ions.

The highest mirror reflectivities are available in the near-IR optical range, away from the strong blue and UV dipole transitions in atomic ions. Since the choice of the atomic states enters into the ion-resonator coupling expressed by the cooperativity parameter η only through the branching ratio of the excited ion state (Section 6.2), the narrow, closed quadrupole $^2S_{1/2}$ - $^2D_{3/2}$ or $^2S_{1/2}$ - $^2D_{5/2}$ transitions in Ca^+, Sr^+ or Ba^+ can be used to achieve high coupling, as was done by [MKB+02]. However, with lifetimes of the metastable ^2D states in excess of 300 ms ([LWGS05, MLN+99]), the photon retrieval rate in such a system is prohibitevely low, even relative to the long coherence times available in ions.

When employing the excited ion ^2P states, a choice has to be made between a cavity operating on the strong, nearly-closed, short-wavelength ^2S - ^2P ion transition and and a cavity operating on the weaker near-IR open ^2D - ^2P transition available in Ca^+, Sr^+ and Ba^+. Recently, the open near-IR ^2D - ^2P transition has been used by [DRB+10] for coupling a Ca^+ ion to a finesse-70,000 cavity, achieving $\eta \approx 6.2$. While cavities with even lower losses have been used in atom-cavity experiments (e.g., [MNB+05]), integrating such high-finesse resonators with trapped ions has been challenging as evidenced by the gradual progress in improving the ion-resonator cooperativity since the pioneering work by [KLH+04].

The cavity coupling on an open ^2D - ^2P transition is degraded by the branching ratio of the excited ^2P state which, in Ca^+ and Sr^+, is below 1:12 [LWGS05, MLN+99]. Consequently, a cavity with 12× lower finesse resonant with the blue or near-UV ^2S - ^2P ion transition should reach comparable photon coupling. Cavities with finesse>10,000 in the blue and near-UV ranges have been demonstrated (see e.g., Section 7.3.2 and [Lei09]), allowing coupling of other ions as well as increased photon scattering rates.

For the work in this thesis, the Yb^+ion was chosen for its magnetic field-insensitive long-lived $F = 0$ - $F = 1$ ground-state hyperfine qubit states allowing simple initialization. Additionally, simple diode lasers were available for Doppler cooling and ion/cavity manipulation on the strong $^2S_{1/2}$ - $^2P_{1/2}$ transition.

An attractive alternative ion for coupling to optical resonators is Ba^+ whose

long-wavelength strong $^2S_{1/2}$ - $^2P_{1/2}$transition at 493.5nm promises decreased mirror losses. The $^2D_{3/2}$ - $^2P_{1/2}$ 650nm trasition in Ba^+ with its favorable 1:3 branching ratio presents another alternative .

To consider the effect of the geometry of a single-mode Fabry-Perot resonator on ion-photon coupling, it is useful to express its cooperativity parameter as

$$\eta = \frac{6\mathcal{F}}{\pi^2}\frac{\lambda}{R}\frac{1}{\sqrt{\chi\,(1-\chi)}} \tag{7.3}$$

where λ is the light wavelength and $\chi = L/2R$ the ratio of the resonator length L to the mirrors' diameter of curvature. To increase η, one can decrease the mirrors' radius of curvature R, decrease the length L of the resonator or bring the resonator to the near-concentric configuration $L \approx 2R$. The last option leads to nearly-unstable resonators that are difficult to align and maintain under vacuum.

At present, the shortest commercially available radius of curvature on mirrors polished to sufficienly low surface roughness to allow finesses above $10,000$ in the near-UV range is 25 mm. Mirrors with this curvature were chosen for the experimental setup presented in the next chapter. Fabry-Perot cavities with shorter radii of curvature have been demonstrated using the CO_2 laser ablation technique [SCH+06]; the integration of such microfabricated cavities with ions is currently being explored in Prof. Chuang's group at MIT as well as at the University of Innsbruck (Austria) and at the University of Sussex (UK).

The last option for increasing ion-resonator coupling is to decrease the resonator length L. In the regime of $L < R \approx 25$ mm, the mirror surfaces are brought within a Rayleigh range of the resonator mode waist, causing the ion-resonator coupling to scale only weakly with the resonator length L as $\eta \sim L^{-1/2}$. At the same time, the length of the resonator is bounded from below by the need to fit ~ 50 traps separated by $\sim 100\ \mu$m into its mode. For the work presented in this thesis, $L \approx 23.7$ mm allows matching of the resonator modes to the 12.643 GHz-hyperfine splitting in $^{171}Yb^+$ for collective ion-photon coupling schemes such as the one presented in Section 9.3.

7.2.2 Ion Trap

To realize the system from Figure 7-1 as a part of a scalable quantum information architecture, fine control over many hundreds of ions across >100 chains will be needed, requiring hundreds of individual electrodes, together with the associated control circuitry. The individual traps and electrodes should also be kept as small as possible

so as to maximize the ion density on a chip and reduce the effect of spatial inhomogeneities on ion coherence and control [WMI+97]. With $10 - 20$ ions per chain and typical ion spacing of $2 - 5$ μm, this implies trap array periods between 50 μm and 160 μm.

Since the periodic potential of the DC trap array satisfies Laplace's equation in free space, it will decay exponentially away with distance h from its source as $\exp\{-2\pi h/d\}$ where d is the array period. The minimal depth of the individual DC wells is set by stray electric fields acting on the ions, typically on the order of 10 V/m. With array trap spacing of 100 μm and DC voltages limited by field emission to less than ~500 V the ion-DC source distance is bounded from above as $h < 300$ μm. On the opposite end, until the problem of anomalous heating is addressed, with typical ion gate times of $(1 - 10)$ μs, the ion-electrode distance will have to be kept above 50 μm at room temperature and 10 μm at cryogenic temperatures (Section 2.3 of Chapter 2).

7.2.2.1 Trap Fabrication Technologies

For fabricating electrode structures with ~ 100 μm pitch, microelectronic techniques present several attractive approaches that have already been used to make working ion traps. Broadly, these traps can be divided into two groups: 3D and 2D.

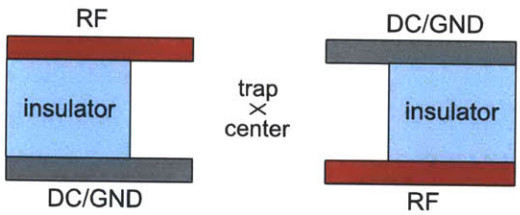

Figure 7-4: 3D microfabricated RF ion trap geometry: two conductive electrode layers are separated by an insulating layer resulting in an efficient approximation of the quadrupole RF potential

In 3D traps (Figure 7-4), the RF electrodes are arranged in two layers separated by an insulating layer, emulating the ideal quadrupole configuration (Section 2.1) and producing high trap depths and ion vibrational frequencies. The high field efficiency of 3D traps comes at the price of difficult fabrication, largely because of the need to remove large amounts (~mm^3) of the insulating substrate. In Si or (Al)GaAs this can be accomplished by wet chemical etching or dry reactive ion etching. However, the relatively low resistivity of semiconductors at room temperature ($\rho < 1$ kΩ·cm for commercially available intrinsic Si) leads to high trap heating and relatively low

breakdown voltages. Dielectrics (SiO_2, Al_2O_3) can be used but require more chemically complex or less directional etches.

The only monolithically microfabricated 3D structure which has trapped ions so far [SHO+05], was based on GaAs with AlGaAs insulating layers and experienced breakdown with only $10V$ applied to the RF electrodes. The low trap depths ($k_B \times 900$ K) resulted in 10min mean ion lifetimes, even in the presence of Doppler cooling. The observed ion heating power was also larger than for other traps of similar size ($50\times$ larger than for ions 40 μm above the gold surface of a 2D trap [SCR+06]).

The fabrication difficulties inherent in fabricating 3D structures can be sidestepped by assembling the trap from separate planar pieces. The technique of joining alumina wafers with electrodes defined by excimer laser micro-machining followed by multi-directional evaporation has been especially successful and is currently used by many groups [RBKD+02, SPZSK08, HOS+06, BOV+09, TKL+00]. In contrast to microelectronic techniques that are either self-aligning or for which accurate standard alignment methods exist, the joining of 3D trap layers has so far been done by hand. While the accuracy of hand assembly could be enhanced i.e. by introducing alignment holes into each wafer and then using Si microfabricated guides to join them, the scalability of this approach remains questionable.

Since the first proposal by [CBBJ05], surface electrode (2D) ion traps (Figure 7-5) have attracted considerable interest as they can be easily made using standard scalable microfabrication techniques. Since the first experimental demonstration [SCR+06], complex traps with hundreds of electrodes, many zones, electrical vias and through-wafer holes for ion loading have been demonstrated, making efficient use of standard fabrication facilities [AUW+10].

A more serious problem is the exposure of the insulating substrate to the ions (Figure 7-5a). Under vacuum, the exposed dielectric will gather surface charges, leading to a displacement of the ions with an obvious negative effect on laser-beam addressing. Less obvious but even more serious are the resulting changes in the frequencies of the normal modes of ion chains as were encountered in the recent work by [BOC+11]. Fortunately, the problem of exposed dielectric can be addressed by using an electroplating process similar to the one used in this thesis to define thick electrodes with small gaps. Further reduction in dielectric area exposed to the ions can be obtained by using a wet etch (i.e., H_2O:HF solution) to isotropically undercut the insulator under the electrodes. Recently, gap to electrode thickness ratios of 50:1 have been obtained in commercial SOI wafers by deep reactive ion etching [BLB+09].

Owing to its ease and scalability to many electrodes, a planar surface-electrode

architecture similar to [LGL+08] was chosen for the work in this thesis.

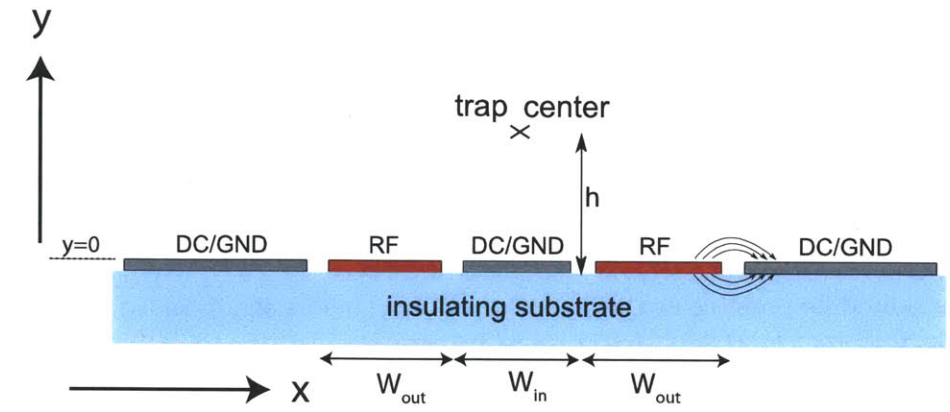

(a)

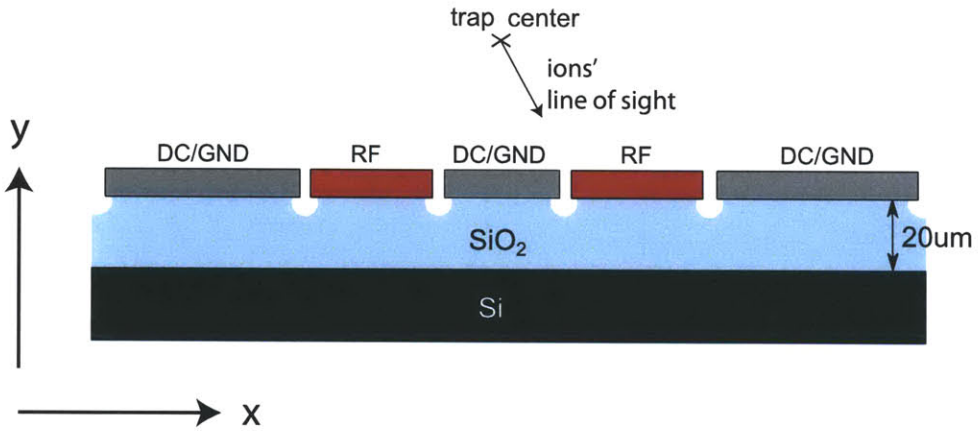

(b)

Figure 7-5: (a) Basic 2D lithographic RF ion trap geometry: insulating wafer is patterned with metal electrodes to produce a quadrupole field at height h above the chip surface (b) Advanced 2D lithographic trap: thick, closely spaced electrodes are used together with an undercut in the insulating layer to shield the ion from charges trapped on the surface of the dielectric; the insulating layer can be located on top of native Si, allowing integration with other devices

7.2.2.2 Anomalous Heating and Trap-Electrode Distance

As described at the start of this section as well as in Section 2.3, close to trap surfaces, ions are affected by fluctuating surface charges. In a trap fabricated using a Au electroplating procedure similar to the one used in this thesis, for ions located 75 μm above the trap surface, [Lei09] measured an anomalous ion heating rate of (5.4 ± 0.4)

vibrational quanta per ms in a room-temperature trap with 773 kHz ion secular frequency.

As a compromise between the ability to form controlled periodic potentials and the anomalous heating, for the work in this thesis, an ion-surface distance of $h = 134$ μm was chosen. Assuming a d^{-4} dependence of heating rates with electrode distance (Section 2.3), heating rates < 1 quantum/ms should be obtainable for a Yb^+ ions trapped in a 1 MHz-trap. As modern gates are first-order insensitive to heating happening on a timescale slower than gate operation, given this heating rate, hundreds of gates should be possible at this ion-trap distance before significant decoherence due to anomalous heating becomes a limiting factor, even for a trap operating at room temperature.

7.2.2.3 RF potential

To produce smooth ion chains overlapped with the node of the RF field, it is advantageous to employ a design of RF electrodes with maximum symmetry. For a planar trap, this implies translational symmetry along the axis of the trap array together with reflection symmetry about a plane perpendicular to the chip and passing through the line of ions.

The simplest design satisfying the above conditions is the 5-electrode design proposed by [CBBJ05] and shown on Figure 7-5a. Intuitively, a 3D four-rod quadrupole trap is tilted 45° and three of its rods (two RF and one DC) projected onto a plane. The fourth DC rod is split into two and laid on the two sides of the structure, forming the leftmost and the rightmost DC electrodes.

Since the electrostatic RF potential above a translationally symmetric structure satisfies the 2D Laplace equation, it can be expressed as the real part of a complex meromorphic function with argument $\tilde{z} = x + iy$.

To shield the ions from the effects of exposed dielectric surfaces described in Section 7.2.2, the electrodes in planar traps are brought closely together, minimizing insulating gaps. In this case, the RF potential takes a simple form derived by [Wes08]:

$$\Phi_{RF} = V_{RF,o}\,\mathrm{Re}\left[-\frac{1}{\pi i}\log\left(\frac{\tilde{z}-r_1}{\tilde{z}+r_1}\Big/\frac{\tilde{z}-r_2}{\tilde{z}+r_2}\right)\right]$$

where $x = \pm r_1$ and $x = \pm r_2$ are the midpoints between the RF and DC trap electrodes and $V_{RF,o}$ is the amplitude of the RF voltage applied to the two outer RF electrodes. In terms of the widths W_{out} of the RF electrodes and W_{in} of the central electrode as defined on Figure 7-5, $r_1 = W_{in}/2$ and $r_2 = W_{in}/2 + W_{out}$.

The trap center is defined by the zero of the RF electric field and is located at $\vec{r}_0 = (x_0, y_0)$ with

$$x_0 = 0 \quad , \quad y_0 = h = \sqrt{r_1 r_2}$$

Close to the trap center, the RF trap confinement is due to the quadrupole electric produced by the applied RF potential. Due to axial and reflection symmetries of the trap geometry, when expressed in the (x, y, z) coordinate system, the quadrupole strength $\mathbf{g}$ of the RF potential takes the simple diagonal form

$$\begin{aligned} \mathbf{g} &= \begin{pmatrix} g_{xx} & 0 & 0 \\ 0 & g_{yy} & 0 \\ 0 & 0 & 0 \end{pmatrix} \\ g_{xx} = -g_{yy} = g &= \frac{4 V_{RF,o}\, W_{out}}{\pi h \left(W_{in} + W_{out}\right)^2} \end{aligned}$$

resulting in equal trap secular frequencies along the $x-$ and $y-$ axes given by (2.5) as:

$$\omega^2 = \frac{qeg}{4m_i}$$

where $q = 2eg/m_i\Omega^2$ is the Mathieu stability parameter of the surface ion trap expressed in terms of the angular frequency of the RF trap drive Ω.

Using (2.4) from Chapter 2, one can also obtain an analytic expression for the secular potential:

$$\begin{aligned} V_{sec} &= \frac{qeV_{RF,o}}{8} \frac{h\, W_{out} \left(W_{in} + W_{out}\right)^2 \left(h^4 + r^4 + 2h^2\left(x^2 - y^2\right)\right)}{\pi \left(r^4 + r_1^2\left(r_1^2 - 2x^2 + 2y^2\right)\right)\left(r^4 + r_2^2\left(r_2^2 - 2x^2 + 2y^2\right)\right)} \\ V_{sec,\, x=0} &= \frac{qeV_{RF,o}}{8} \frac{h\, W_{out} \left(W_{in} + W_{out}\right)^2 \left(h^2 - y^2\right)^2}{\pi \left(r_1^2 + y^2\right)^2 \left(r_2^2 + y^2\right)^2} \end{aligned}$$

The dominant escape direction from the above secular potential is along the vertical $\hat{y}$-axis with the neck of the potential located at:

$$\begin{aligned} x_{neck} &= 0 \\ y_{neck} &= \sqrt{h\left(h + r_1 + r_2\right)} \end{aligned}$$

corresponding to the total depth of the RF secular potential

$$V_{sec-max} = \frac{qeV_{RF,o}}{8} \times \frac{h^3 W_{out}}{\pi (h + r_1)^2 (h + r_2)^2}$$

The parameters chosen for the trap used for experiments described in this thesis are shown in Table 7.1. To preserve trap stability and limit nonlinear RF-induced heating effects, the Mathieu stability parameter was limited to $q \leq 0.3$. Strong ion confinement is realized by maximizing the quadrupole strength g and the depth of the secular potential $V_{sec-max}$. At a fixed RF drive voltage, the chosen geometry maintains 95% of the maximal achievable quadrupole strength and 75% of the trap depth at the given ion height h.

The RF drive voltage is limited by electrical breakdown caused by Fowler-Nordheim electron tunneling from electrode surfaces facing the narrow gaps between the RF and DC trap electrodes. Planar traps with comparable interelectrode gaps of $(6 - 10)$ μm , fabricated using a Au-plating procedure similar to the one used for the work in this thesis, have been shown by [Lab08] to experience electrical breakdown at RF drive amplitudes on the order of 400 V. To provide a margin of safety, the design RF voltage is limited as $V_{RF,o} \leq 300$ V.

parameter	**symbol**	**value**
ion - surface distance	h	134μm
gaps between RF electrodes	G	9 μm
width of outer RF electrodes	$W_{out} - G$	190μm
with of central electrode	$W_{in} - G$	127 μm
RF voltage on outer RF electrodes (max.)	$V_{RF,o}$	300V
quadrupole strength of RF potential	g	0.304 $V_{RF,o}/h^2$
Mathieu stability parameter	q	0.3
RF drive frequency (max.)	Ω	$2\pi \times$ 21.7 MHz
ion secular frequency (max.)	ω	$2\pi \times$2.3 MHz
depth of secular potential (max.)	$V_{sec-max}$	260 meV
secular potential neck	(x_{neck}, y_{neck})	(0, 1.87 h)

Table 7.1: Design parameters of the planar RF trap used for the work in this thesis.

7.2.2.4 Adjusting Trap Height

In case of vertical misalignment with the resonator mode, the ions can be translated by driving the central electrode with an RF potential of amplitude $V_{RF,i}$. To avoid RF-induced micromotion, it is important that the potential $V_{RF,i}$ be applied either in-phase or 180° out-of-phase with the drive of the outer electrodes.

Using the analytic model from [Wes08], the RF potential produced by the inner electrodes is:

$$\Phi_{RF-inner} = V_{RF,i} \times \mathrm{Re}\left[-\frac{1}{\pi i}\log\left(\frac{z+r_1}{z-r_1}\right)\right]$$

Adding $\Phi_{RF-inner}$ in-phase with the potential Φ_{RF} produced by the outer electrodes yields the new location of the trap above the surface of $(x, y) = (0, H)$ with the new trap height H given by:

$$H^2 = \frac{r_2 - r_1 - rr_2}{r_2 - r_1 + rr_1}h^2$$

To achieve a given trap height H, the drive ratio $r = V_{RF\,i}/V_{RF,o}$ needs to be

$$r = -\frac{H^2 - h^2}{H^2 r_1 + h^2 r_2}W_{out}$$

at which point the trap quadrupole strength becomes

$$g = \frac{4r_2\left(r_2^2 - r_1^2\right)H}{\pi\left(r_1^2 + H^2\right)\left(r_2^2 + H^2\right)^2}$$

The trap neck is now located at

$$y_{max}^2 = H^2 + \sqrt{\left(H^2 + r_1^2\right)\left(H^2 + r_2^2\right)}$$

corresponding to the RF trap depth of

$$V_{sec-max} = \frac{qeV_{RF,o}}{8} \times \frac{r_2\left(r_2^2 - r_1^2\right)\left(H^2 + r_1^2\right)}{\pi H\left(\sqrt{H^2 + r_2^2} + \sqrt{H^2 + r_1^2}\right)^4}$$

Increasing the trap height from 134 μm to 155 μm would require driving the inner RF electrodes to -0.180 of the outer electrode drive amplitude. If the drive frequency

is kept the same, the trap depth would decrease by 32%. If the drive frequency is lowered to keep the Mathieu stability parameter q the same, the trap depth would decrease by 15%.

7.2.2.5 Increasing Trap Depth

The dominant escape direction from the surface trap described in the previous sections is along the positive y-axis while the secular potential barriers in the lateral x-direction are significantly higher.

Trap depth can be increased by redistributing the available confinement using a DC potential Φ_Q. To prevent micromotion, the applied DC electric field $E_Q = -\nabla\Phi_Q$ needs to vanish at the trap center, which can be easily accomplished by applying DC voltages to the trap electrodes proportional to the RF voltages. If a negative voltage V_Q is applied to the outer RF electrodes, the trap will be compressed in the vertical direction, preventing the ions from escaping in the $+\hat{y}$ direction.

The vertical compression of the trap corresponds to an increase in the vertical trap frequency ω_y. Using (2.5), one can show that:

$$\omega_y^2 = \omega^2 \left(1 + \frac{4V_Q}{qV_{RF,o}}\right) \tag{7.4}$$

Since the DC potential is divergenceless, the horizontal trap frequency ω_x will be lowered as:

$$\omega_x^2 = \omega^2 \left(1 - \frac{4V_Q}{qV_{RF,o}}\right) \tag{7.5}$$

For $V_Q > qV_{RF,o}/4$, the trap will bifurcate along the x-axis, displacing the ions from the RF node and introducing RF-driven micromotion. At RF drive amplitude of 350 V, this limit corresponds to , V_Q <22 V. To preserve the horizontal confinement, it is desirable to keep $V_Q < qV_{RF,o}/8$. The minimal depth of the secular potential in this case can be calculated as:

$$V'_{sec-max} = \frac{qeV_{RF,o}}{8} \times \begin{cases} .4 & , H = 3h/4 \\ .3 & , H = h \\ .1 & , H = 2h \end{cases}$$

At the previously chosen trap parameters ($V_{RF,o}$ =300 V, $\Omega = 2\pi \times 21.7$ MHz) and the design trap height of 134 μm, the maximal obtained trap depth is $V'_{sec-max} = 3.4$ eV, which is comparable to 3D quadrupole traps.

7.2.3 Ion Trap Array

To produce the linear array of ion traps, the central electrode in the 5-electrode trap shown on Figure 7-5 can be split into three sub-electrodes patterned with period d as shown in a top-down view on Figure 7-6. Applying a negative potential V_c to the central sub-electrode and a positive potential V_i to the other two sub-electrodes results in a periodic DC potential V_{array} which subdivides the RF trap into a periodic array of individual sub-traps.

For the traps used in the work presented in this thesis, the period d of the trap array was constrained by the limitations of our fabrication process, primarily the ~ 7 μm minimal interelectrode spacing imposed by electrical breakdown. With fixed interelectrode gaps, as d is decreased, an increasing area of the unshielded quartz substrate is exposed underneath the trapped ions, affecting the ions' position, introducing micromotion and altering the ions' secular frequencies ([HBHB10]).

To limit the exposed quartz area, three trap designs were made and fabricated, with $d = 125$ μm, $d = 140$ μm and $d = 160$ μm. After most 140 μm-period traps proved unviable, a conservative decision was made to use a 160 μm-period trap.

The symmetry of the design on Figure 7-5 ensures that the transverse electric field due to the trap array potential vanishes at the center of each sub-trap, minimizing the lateral micromotion of ions. The vertical field will vanish at the same point for a particular ratio V_c/V_i of the potentials applied to the sub-electrodes. For the 160 μm-period trap used in the experiments presented in this thesis, this occurs for $V_c = -1.0V_i$, accurate to within 5% as confirmed by comparison of a boundary-element simulation and an analytic calculation based on [Wes08].

Being periodic with period d, the axial potential produced by the trap array electrodes can be written as a Fourier sum of the form

$$(V_{array})_{x=0} = \sum_{j=0}^{\infty} A_j \cos\left(\frac{2\pi z}{d}\right)$$

The higher-order Fourier components will quickly decay with distance y away from the trap surface as $\exp(-2\pi y/d)$, causing the potential seen by the ions to be dominated by the first-order Fourier component V^1_{array}. For the design used in this

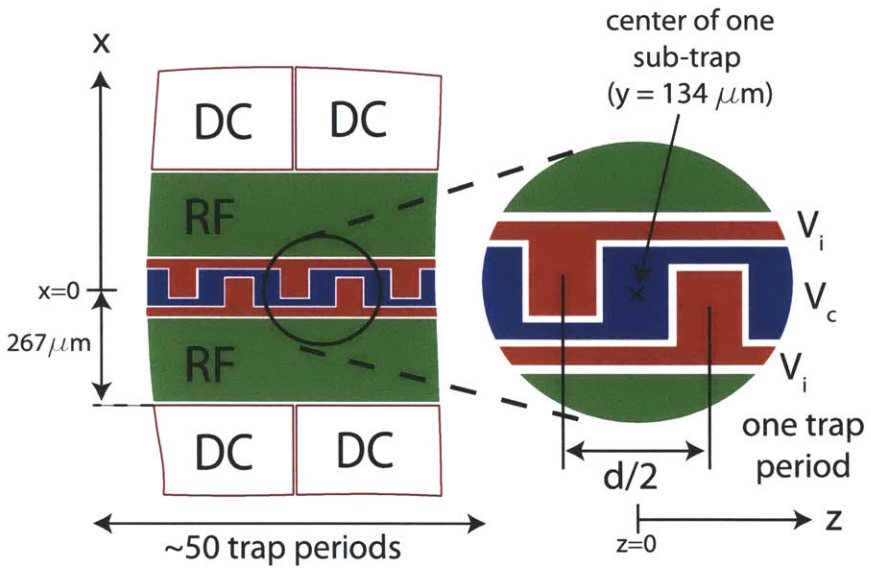

Figure 7-6: Short axial segment of the DC electrodes used to produce a linear array of ion traps 134 μm above the trap chip surface.

thesis, with $V_c = -V_i$, the axial array period is well approximated by

$$V_{array}(x = 0,\, y,\, z) = -(1.1 \pm 0.2)\, V_c \exp\left(-\frac{2\pi y}{d}\right) \cos\left(\frac{2\pi z}{d}\right) \tag{7.6}$$

Due to ion-ion repulsion, to contain an increasing number of ions in a single sub-trap, the array potential needs to be increased. However, the maximal axial confinement of an ion chain is limited by the onset of the structural zig-zag transition [Dub93] where ion-ion repulsion overcomes the radial RF trap confinement.

At the maximal trap frequency of 2.3 MHz from Table 7.1, a numerical model predicts a maximal of $N = 30 \pm 3$ Yb^+ ions in a single trapping site, reached for $V_i = -V_c = 1$ V, corresponding to axial ion vibration frequency of 350 kHz. Due to repulsion of ions at different sites, the maximal number of ions in the trap array would be somewhat lower i.e. $N \approx 25$.

7.3 Ion Trap Array in an Optical Cavity: Setup

7.3.1 Ion Trap Fabrication

The surface trap was fabricated using a modified version of the protocol from the previous work in prof. Chuang's group [LGL+08].

The fabrication was done by Yufei Ge and Marko Cetina in MIT's Research Laboratory of Electronics, in collaboration with prof. Isaac Chuang and prof. Karl Berggren's groups.

The facilities used were:

- Microsystems Technology Laboratory / Exploratory Materials Laboratory (EML) class >10,000 cleanroom for initial wafer cleaning, electroplating, wet etching and wirebonding
- The Chuang group chemical lab (Chuang wet lab) : electron beam evaporation
- Nanostructures Laboratory (NSL) : class 10 cleanroom for final wafer cleaning and photolithography
- Microsystems Technology Laboratory / Technology Research Laboratory (TRL) class >10,000 cleanroom foyer for die-saw cutting

Compared with the work in [LGL+08], the trap array had a larger substrate area (16.14 mm×2.35 mm) patterned with small (7 μm) features, resulting in much higher susceptibility to contamination (Figure 7-7a). Especially critical were the three DC array electrodes (Figure 7-6) as defects larger than 10 μm anywhere in this 14 mm×127 μm region would disconnect the electrodes and prevent ion trapping in all or part of the structure. The resolution of the lithography in the original process was also poor (Figure 7-7b), probably due to photoresist edge bead on the edges of the small 3 cm × 3 cm substrates.

To address these problems, a new process was developed using seed-free single-crystal Z-cut, 76.2 mm-diameter, 500 μm-thick, single-side optically polished quartz wafers from Hoffman Materials, Inc. (Carlisle, PA). The most contamination-sensitive parts of the process - final wafer cleaning and lithography were also moved to the class-10 NSL cleanroom.

The process starts with a thourough mechanical and chemical clean of the quartz substrate wafers. The bulk of the gold electrodes is formed by electroplating bulk Au from a of Au-sulfite electrolyte. To provide an electrical contact for the plating process, a Ag metal contact layer is deposited on the quartz wafer by electron-beam

evaporation using a Ti adhesion layer. The electrodes are patterned by using a positive photoresist to define the gaps between the electrodes and serve as a barrier to gold plating.

Following the gold plating process, the newly plated gold electrodes are still connected to the underlying silver layer. To produce the trap, the photoresist, Ag and Ti between the electrodes are chemically removed.

The final wafer is cut into individual 16.14 mm $\times$ 2.35 mm traps using a wafer die saw in two steps - one rough step designed to preserve as many traps as possible and another, fine step, to obtain accurate trap dimensions. After mounting to a steel chip holder, the finished trap is bonded with gold wires to printed circuit boards to provide in-vacuum electrical connections to the individual electrodes.

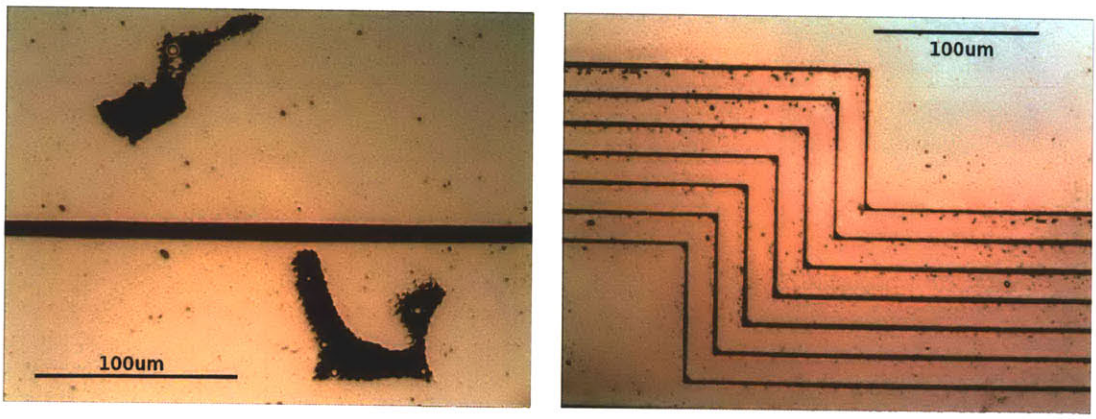

(a) (b)

Figure 7-7: Trap fabrication defects: (a) holes in electroplated gold layer due to contamination (b) non-uniform features in hard-contact lithography, probably due to photoresist edge bead.

7.3.1.1 Wafer Cleaning

Although the wafer supplier indicated that the wafers were to be 'cleanroom-cleaned', following a >15 min. "Pirranha clean" ($3:1$ H_2SO_4:H_2O_2) in EML and a 20 min. "RCA clean" ($4:1:1$ H_2O:NH_4OH:H_2O_2 at $65°C$) in the class-10 NSL cleanroom, dark field microscopy of the wafer still revealed dozens of white particles larger than $5\ \mu m$.

The chemical resistance of this residual contamination together with its white color are consistant with quartz dust from the wafer cutting and polishing process.

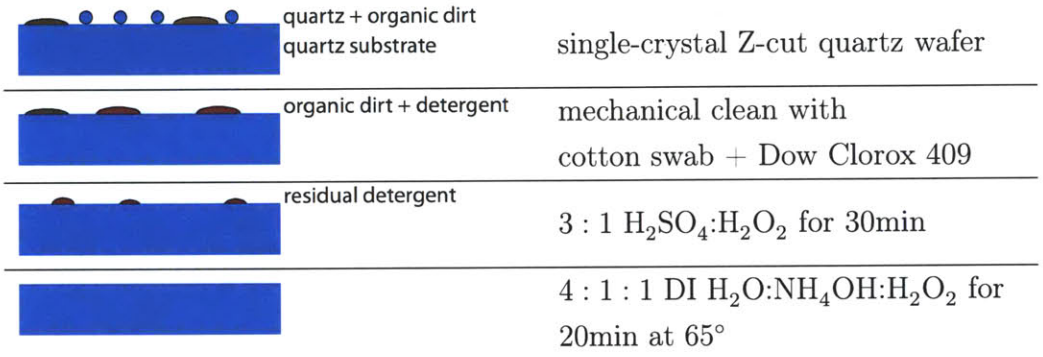

Figure 7-8: Trap fabrication: wafer cleaning procedure.

Wafer contamination was eliminated in the final version of the process as shown on Figure 7-8. Quartz dust is removed by spinning the wafer on a photoresist spinner while spraying with a surfactant (Dow Clorox 409 formula) and sweeping with a cotton swab.

Followed by a rinse with deionized water, cotton fibers and surfactant residue are removed by immersing the wafer in unheated $3:1$ H_2SO_4:H_2O_2 solution for 30 min. Skipping this step resulted in streaks on the wafer visible later in the processing.

Any remaining surfactant residue is removed by immersing the wafer in $4:1:1$ H_2O:NH_4OH:H_2O_2 solution heated to 65°C for 20 min. This step is performed in the NSL class-10 cleanroom to ensure wafer cleanliness prior to lithography.

7.3.1.2 Contact Layer Evaporation

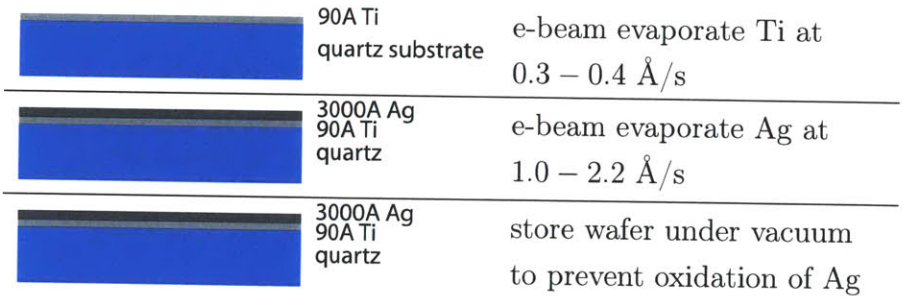

Figure 7-9: Trap fabrication: evaporation procedure.

After cleaning, the wafer is evaporated with a thin 10ÅTi layer to promote adhesion of the conductive evaporated Ag layer to quartz (Figure 7-9). The Ag layer will later act as the contact layer for electroplating 1-2μm thick Au electrodes.

To minimize wafer contamination, an attempt at electron-beam evaporation was made at NSL. The evaporation shutter was opened early, exposing the wafer to silver flux before the temperature of the silver target had equilibrated. Before reaching equilibrium, evaporation target materials are known to eject (spit) droplets, a number of which were seen on our wafer (Figure 7-10).

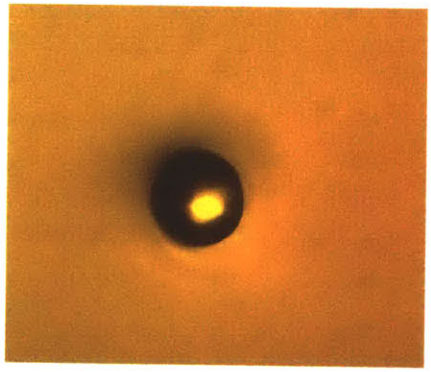

Figure 7-10: Ag droplet ($> 5\mu$m) deposited on the wafer during evaporation from a crucible out of thermal equilibrium. Yellow image tone is due to lack of blue illumination in the photolithography-compatible NSL cleanroom.

To avoid spitting, the final evaporation was performed on the MDC evaporator (MDC e-Vap 1000-1015 and e-Vap 4000-1015) in the Chuang wet lab.

Since the Chuang wet lab is not built to cleanroom standards, to minimize wafer contamination, after the final RCA clean in NSL, the sealed wafer cassette was opened and the wafer loaded *inside* the evaporator chamber.

Ti evaporation was performed at $\leq 4 \times 10^{-7}$ torr with growth rate of $0.3 - 0.4$ Å/s. A 8.86 kV electron beam was swept in a spiral pattern across a 1.4"-diameter crucible containing Ti pellets with 1.7 A (amplitude) applied to the electron beam sweep coils. To avoid spitting, the beam current was ramped up to the operating point of $158 - 165$ mA at 1 mA/s. For the first 4min of evaporation, the wafer was blocked by a shutter, allowing thermal equilibration of the crucible.

Ag evaporation was performed at $\leq 2 \times 10^{-8}$ torr with growth rate of $1.5 - 2.2$ Å/s. A 10 kV electron beam was swept in a spiral pattern across a 1.4" diameter crucible containing Ag pellets with 2.0 A (amplitude) applied to the beam sweep coils. To avoid spitting, the beam current was ramped up to the operating point of 42 mA at 1 mA/s and the wafer shutter was closed for the first 4.5 min. of evaporation.

To prevent oxidation of the exposed silver which can negatively affect the adhesion of the electroplated Au electrodes, the wafer was stored in a low-vacuum chamber ($p < 100$ mTorr).

7.3.1.3 Photolithography

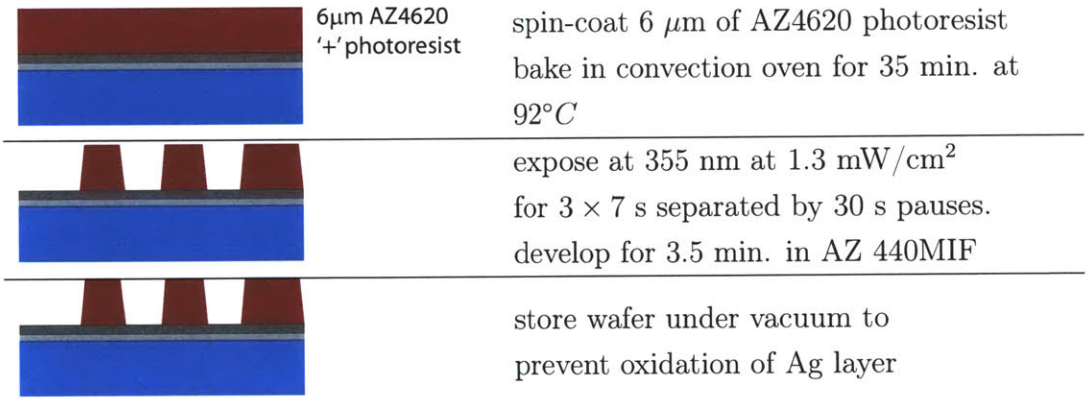

Figure 7-11: Trap fabrication: photolithography procedure.

To avoid contamination, photo lithography was performed in the class-10 NSL clean-room (Figure 7-11).

A process using a positive photoresist was chosen due to good availability of thick positive resists. The second advantage of a positive process is the resulting convex shape of the photoresist features (Figure 7-11), leading to concave gold-plated electrodes. With small interelectrode gaps, concave electrodes can hide the exposed substrate dielectric (Figure 7-5).

The wafer was pre-heated on a hotplate set to 110°C for 5 min. A 6 μm-layer

of the Hoechst Celanese AZ4620 positive photoresist was formed by spin-coating the wafer at 1500rpm for 10s, followed by 3500rpm for 60s. The photoresist edge bead was removed with a lint-free cue-tip wetted with acetone. The photoresist was hardened by baking in a convection oven at $92°C$ for 35 min.

A chrome-on-borofloat glass photolithography mask was ordered from Advance Reproductions Corp. (North Andover, MA). The mask was rested on the wafer by gravity (soft contact). The photoresist was exposed under a collimated 350 nm floodlight for 3×7 s with intervening 30 s pauses to avoid overheating the photoresist. The photoresist was developed in the AZ Electronic Materials 440MIF developer until the exposed areas were clean of photoresist ($\approx$ 3.5 min.).

The final results of the litography for the traps used in the experiment are shown on Figure 7-12. The developed photoresist features are convex with $\approx 15°$ sidewalls, caused by increased light exposure of the top positive photoresist layer. If the gold electroplating process was improved to produce thicker electrodes, the concave shape of the resulting gold electrodes could be used to shield the ions from any charges built up on the quartz substrate. With the current $(1.5 - 2.5)$ μm-thick gold plating process and $(7 - 9)$ μm electrode gaps, this shielding effect is unfortunately minimal.

To avoid oxidation of the exposed Ag layer, following lithography the wafer was stored under vacuum ($p < 100$ mTorr).

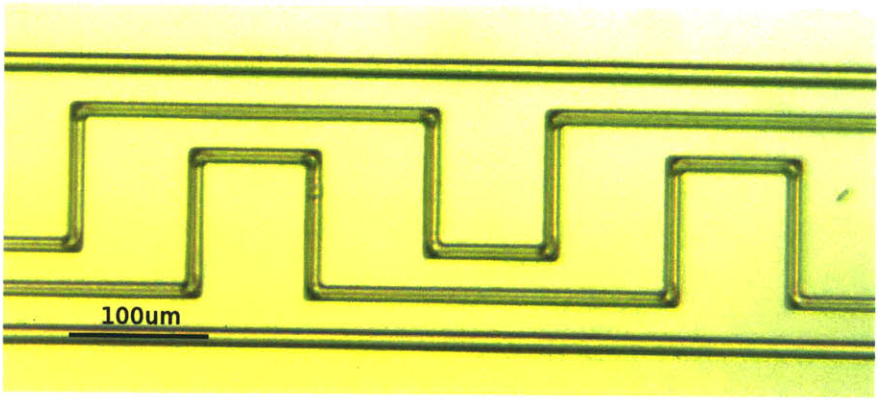

Figure 7-12: Trap features after lithography. The pattern on the central $7\mu m$-wide features is due to a sidewall slope of approximately 15°.

7.3.1.4 Electroplating and Wet Etching

To provide a low resistance to the high currents necessary for driving the RF electrodes to hundreds of volts (Section 7.2.2), a gold electroplating process similar to the one in [LGA+08] was used to grow thick Au electrodes. The electrodes were grown on top

of the Ag seed layer with the photoresist acting as an interelectrode barrier (Figure 7-18).

Compared to liftoff or dry etching, for fabrication of ion trap electrodes gold plating has the advantage of naturally rounding off sharp features, increasing the minimum interelectrode voltage at which field emission and electrical breakdown occur. The rounding arises from a local increase in the plating rate near sharp features: the electric field in vacuum during trap operation and in the electrolyte during plating both satisfy Laplace's equation; since, by Ohm's law, the plating current density and deposition rate are proportional to the local electric field, sharp features on electrodes experience increased plating rates.

To ensure uniform plating across the wafer surface, it is important to ensure a uniform plating electric field. Since this was difficult to do with the existing setup composed using a $1cm^2$ anode, a new plating setup was developed following [SJF00] (Figure 7-17). To minimize contamination while allowing flexibility in the instrument setup, the plating was performed in the EML cleanroom.

To avoid chemical contamination of the plating solution, the only materials submerged into the solution are glass, PTFE, gold and platinum. The gold plating solution is held in a ϕ6" $\times$ 3" Pyrex crystallization dish heated on a hotplate and stirred with a 3" long PTFE-coated magnetic bar (VWR USA) while its temperature is measured with a glass thermometer (Figure 7-17a).

The wafer is mounted onto a PTFE chuck via two PTFE screw-supported retainer clips (Figure 7-17b). The cathode connection to an exposed Ag area on the wafer is made via a bent gold wire with its tip pressed into a flat. The cathode wire is threaded under one of the wafer retainer clips and also held in place by a PTFE cathode retainer (Figure 7-17a). The anode is formed by a cylindrical ϕ5" $\times$ 2" platinized Ti mesh (type-N, from Uyemura USA Technical Center, Southington, CT) surrounding the wafer chuck.

Following [LGA+08], the TSG-250 gold sulfite plating solution from Transene Corporation (Danvers, MA) was used. Compared to cyanide gold plating solutions, the sulfite chemistry has low toxicity and good stability in storage.

The plating solution was pre-heated to $49°C-54°C$ and operated in single polarity using a high-stability constant-current supply (laser diode current controller).

During an initial plating run, a Cu wire was used instead of the Pt-Ir alloy to connect the cathode wire to the current controller. Although the Cu wire was kept out of solution, the heated solution evaporated and condensed on the Cu wire, allowing Cu^{2+} ions to pass into the plating solution, as evidenced by the blue color of the

contaminated solution (Figure 7-13, left). The contamination resulted in a porous, brown-colored gold film (Figure 7-14), parts of which were easily removable in an ultrasonic bath. Similar poor results were obtained for a range of plating currents (0.2-2 mA/cm^2) and stirring speeds (200-400 rpm). Lacking a chemical process to remove the Cu^{+2} ions, the contaminated solution was deemed unusable and a new batch of TSG-250 was obtained from the supplier (Figure 7-13, right).

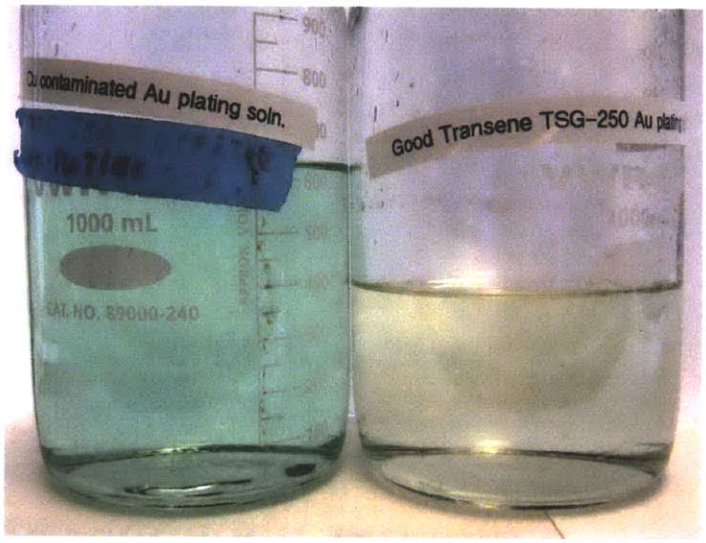

Figure 7-13: Cu^{2+} contaminated TSG-250 gold plating solution (left) and uncontaminated solution (right).

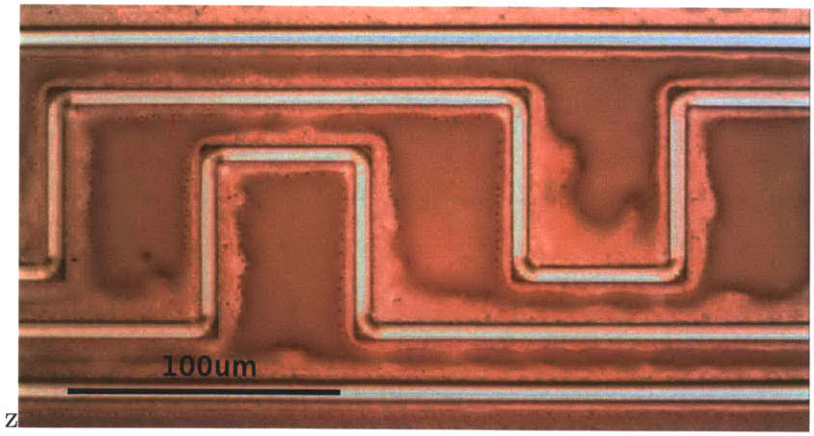

Figure 7-14: Gold layer plated out of the contaminated TSG-250 solution. The deposited gold is porous, friable and non-uniform.

The plating was calibrated using a trial wafer containing 47 traps with total

exposed cathode area (including Au cathode wire) of $(22 \pm 2)\ cm^2$. After pre-heating the solution to $49°C - 54°C$ and turning the magnetic stirrer at 230rpm, the trial wafer was attached to the holder chuck and submerged into the solution. The plating was performed at $16mA$ of cathode current ($0.65 - 0.8$ mA/cm^2) for 55min. After plating, deionized water was added to the plating solution to reconstitute the initial 500 ml solution volume.

The thickness of the trial gold film was estimated using Faraday's law as 2.3 μm - 2.8 μm. At this thickness, roughening of the gold film on a $\sim$ 1 μm scale is easily visible (Figure 7-15a).

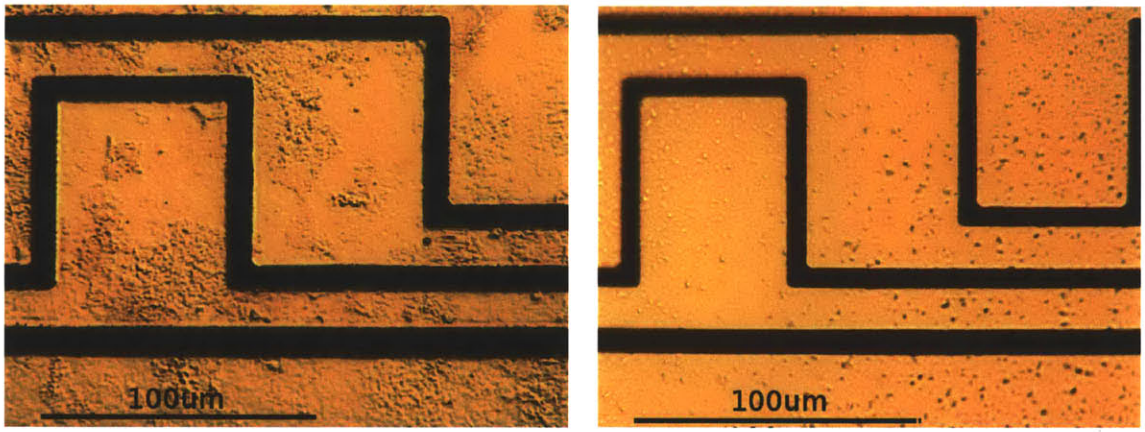

(a) (b)

Figure 7-15: (a) Trial wafer plated with $(2.3 - 2.8)$ μm-thick gold film out of the Transene TSG-250 gold-sulfite solution. Picture taken after etching the Ag and Ti layers. (b) Final trap wafer plated with $(1.6 - 1.9)$ μm-thick gold film plated out of the Transene TSG-250 gold-sulfite. Picture taken after etching the Ag and Ti layers and protecting the wafer with the NR9-3000P negative photoresist.

For plating the final wafer, after recording the solution volume, the plating solution was pre-heated to $49°C - 54°C$ and stirred via the magnetic stirrer at 230rpm. To minimize contamination, the wafer was wetted with deionized water immediately upon removal from the class-10 cleanroom container, allowing water surface tension to capture dust before it adheres to the trap structures. The wafer was then quickly attached to the holder chuck and submerged into the plating solution.

To decrease surface roughness, the final wafer was plated at $14.7mA$ of cathode current distributed over a total exposed area (including Au cathode wire) of $(20 \pm 2)\ cm^2$, resulting in average plating current density of $0.7 - 0.8\ mA/cm^2$. The plating time was 31 min for an estimated gold thickness of $(1.3 - 1.6)\ \mu m$ (Figure 7-15b).

The electrode thickness was checked by measuring the resistance of the RF electrodes on one of the finished devices. Similar to an electrolyte solution, the electrostatic potential inside an electrode satisfies Poisson's equation. Since for thin electrodes the current flow will be mostly tangential to the electrode surface, the electric potential ϕ inside the electrode is well-approximated by the solution to the 2D Poisson equation

$$\nabla_{\parallel} \cdot \left(\rho_{Au} \nabla_{\parallel} \phi\right) = I\delta\left(r - A\right) - I\delta\left(r - B\right)$$

with I the total current through the electrode and A and B the source and sink points, respectively.

In terms of the unitless solution ϕ_0 to $\nabla^2 \phi_0 = \delta\left(r - A\right) - \delta\left(r - B\right)$, the resistance of a given electrode will be $R = \rho_{Au} \Delta\phi_0 / h$ with ρ_{Au} the gold resistivity, h the electrode thickness and $\Delta\phi_0 = \phi_0\left(B\right) - \phi_0\left(A\right)$. A plot of the measured resistances vs. $\Delta\phi_0$ is shown on Figure 7-16.

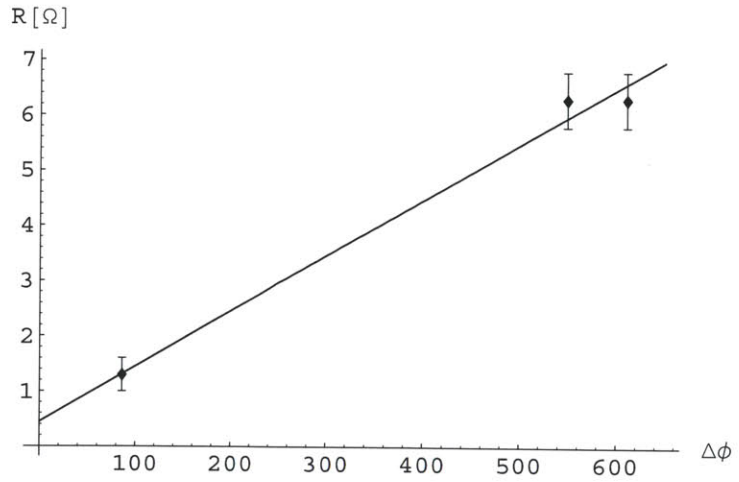

Figure 7-16: Measured electrode resistances for a trap from the final wafer as a function of the electrode shape factor determined using a linear finite element method. With gold resistivity $\rho_{Au} \approx 2.5 \times 10^{-10}$ Ω·cm, the fitted slope predicts $h = (2.4 \pm 0.2)$ μm.

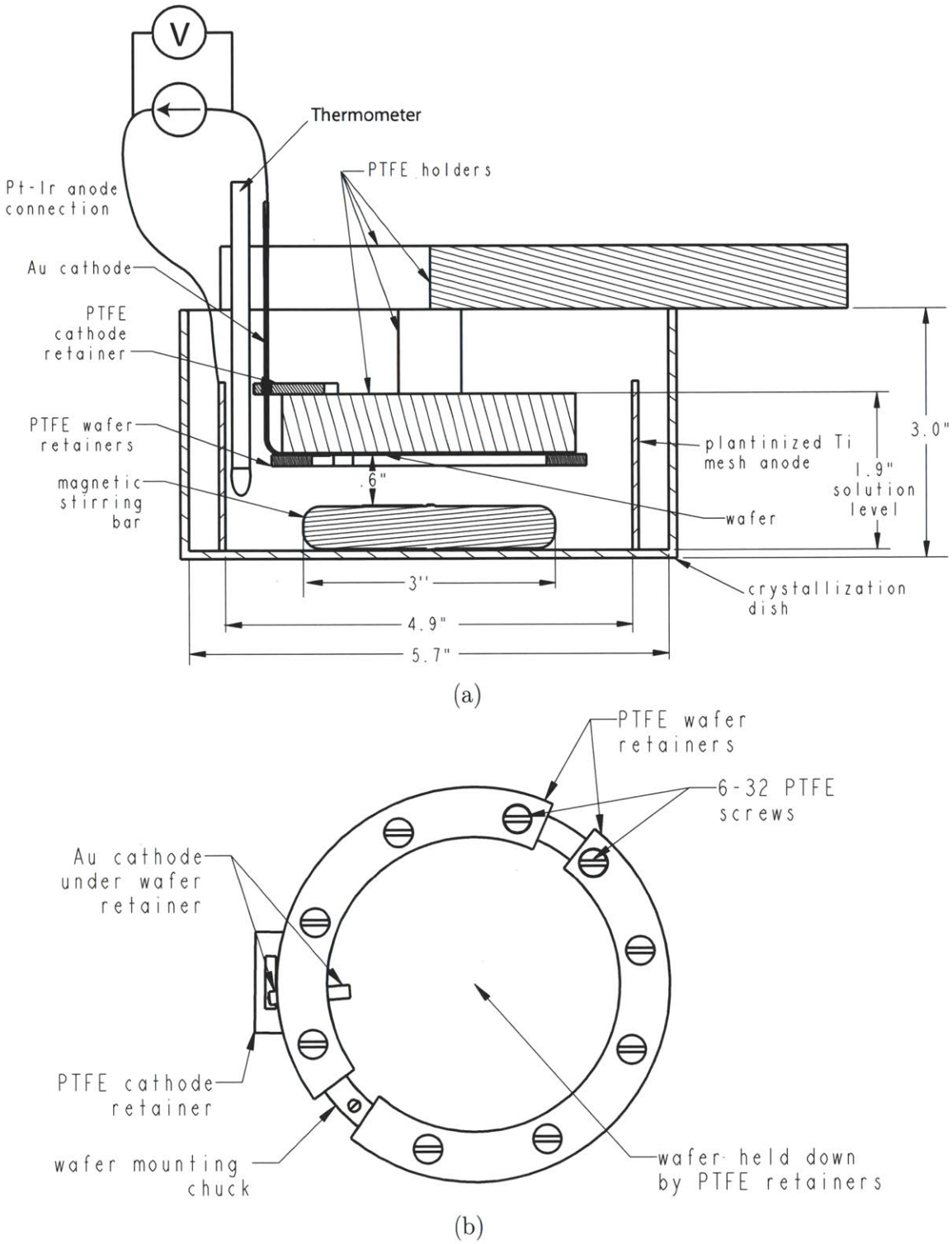

Figure 7-17: (a) Side cross-section view of the setup used for electroplating of 3" quartz wafers

(b) bottom view of the wafer holding chuck

7.3.1.5 Wet Etching

	wafer after electroplating with Transene TSG-250 gold-sulfite solution
	remove photoresist with acetone rinse with isopropy alcohol, blow-dry
	wet etch Ag with unheated $4:1:1$ DI H_2O:NH_4OH:H_2O_2 for $10-20$ s
	wet etch Ti with unheated $1:4$ HF:H_2O for $5-10$ s
	passivate with $1-2$ μm of NR9-3000P negative photoresist bake for 1min on hotplate set to $150°C$

Figure 7-18: Trap fabrication: electroplating and wet etching process.

Following electroplating, the trap electrodes are shorted via the Ag seed and the Ti adhesion layers. These layers are removed by a chemical wet etch in the EML acid hood as shown on Figure 7-18. Successful silver removal is indicated by the clear areas on the wafer turning from reflective silver to dimmed neutral gray. Successful removal of the Ti adhesion layer turns the wafer transparent with transmission losses dominated by the surface reflections due to index mismatch. The residual wafer reflectivity after the etch is a helpful indicator as contaminated regions of the wafer (e.g. wafer edges on Figure 7-21) will fail to etch completely while excessive etch duration, especially during the HF step, can cause normal electrodes to peal off.

To protect the wafer from contamination and prepare it for cutting, several microns of NR9-3000P photoresist are spin-coated onto the wafer, followed by a 1min bake on a $150°C$ hotplate.

Given the low standard of the EML cleanroom, to avoid contamination, the final wafer was not inspected under a microscope between the above steps. Figure 7-19 shows a wafer plated with the Cu-contaminated gold plating solution during the wet etching steps.

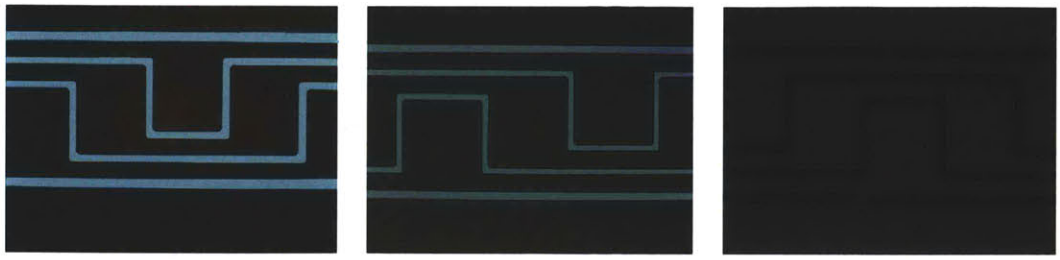

(a) (b) (c)

Figure 7-19: Wafer plated with Cu-contaminated Au plating solution during the wet etching process: (a) before Ag etch, (b) after Ag etch, (c) after Ti etch. The images were recorded under equivalent illumination, showing a marked decrease in the wafer reflectivity as the metal layers are removed.

7.3.1.6 Wafer Dicing

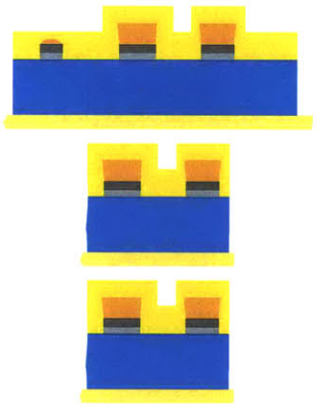

Figure 7-20: Trap fabrication: initial wafer cutting procedure.

To allow access to the trap electrodes for wirebonding as well as to accomodate the resonator mirrors and the MOT beams (Section 7.3.5.2), the trap wafer needs to be cut individual traps.

The cutting of the photoresist-passivated wafer was performed in TRL on a Disco Abrasive System Model DAD-2H/6T wafer dicing saw, using a 240 μm-thick, 2" diameter SiC blade.

Crystalline quartz is difficult to cut as the wafer easily develops long cracks along crystal planes. Cracks are intiated by localized stresses during cutting that are especially likely to appear if the wafer is not properly fixtured with its whole surface to distribute the cutting stresses. Cracking was decreased by replacing the standard UV-release wafer cutting adhesive (Ultron Systems Inc. P/N 1064) with the stronger

acetone-soluble Crystalbond Wafer-Mount 559 tape. In addition, each cut was performed in three passes with cut depths of 210 μm, 100 μm and 100 μm, leaving the remaining $\sim$ 90 μm of the substrate uncut.

As only one successful wafer was available at this stage of fabrication, to decrease the chance of catastrophic cutting failure, the cutting was performed in two steps. First, 11 cuts are made to separate the wafer into smaller segments with 2 traps on each segment (Figure 7-21). This was fortunate as after $\sim$ 8 cuts, subjected to cooling water and the cutting forces, the wafer started to peel off the adhesive; work with other quartz wafers showed that cracking is strongly aggravated by poor adhesion.

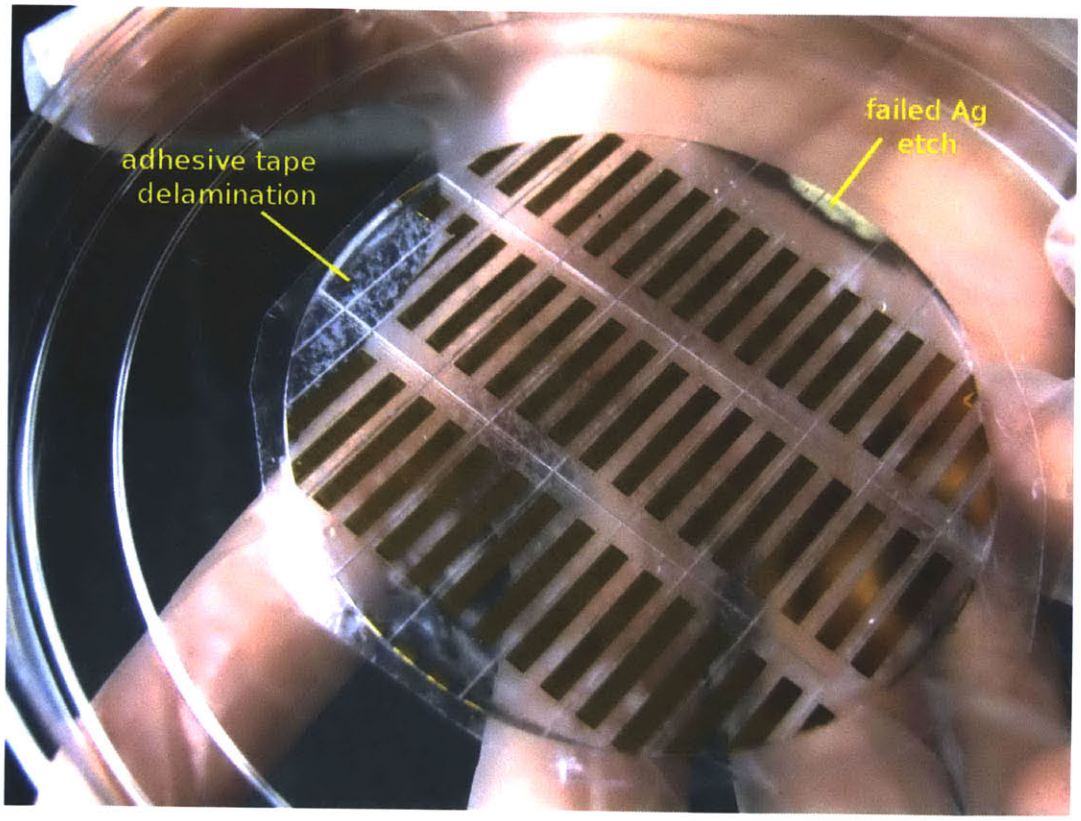

Figure 7-21: Wafer with traps used to trap ions in this thesis after first cutting. Ag residue is visible in the upper right corner. In the upper left corner, the adhesive tape has started to delaminate from the wafer due to cutting stresses.

After the first cutting step, the photoresist was removed and resistivity between neighbouring electrodes tested at low voltage in one 2-trap segment, yielding $R > 100$ MΩ.

The remaining traps were stored in atmosphere and at room temperature for 6 months. After removing the photoresist, these traps were found to exhibit resistances

between neighbouring electrodes as low as 2 kΩ. The contamination, probably due to photoresist, could be removed by the RCA base organic cleaning as shown on (Figure 7-23), yielding resistances between all electrodes on a test trap > 1 GΩ.

To minimize contamination of the exposed wafer, all the steps shown on Figure 7-23 were performed in NSL except the last cutting step which was done on the Disco die-saw in TRL.

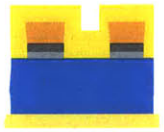	Separate one 2-trap segment from wafer by cracking the remaining 90 μm of quartz and cutting the adhesive with a razor blade
	Dissolve Wafer-Mount and photoresist in acetone Rinse with isopropyl alcohol Inspect for defects under microscope
	clean photoresist residue with $4:1:1$ H_2O:NH_4OH:H_2O_2 for 10 s followed by $1:4$ HF:H_2O for 5 s at room temp. rinse with DI water, blow-dry

Figure 7-22: Trap fabrication: photoresist removal and cleaning procedure.

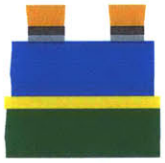	Rinse 4" Si wafer with acetone+isopropyl alcohol Spin NR9-3000P onto Si wafer at 800rpm for 40s Press quartz trap segments onto Si wafer Bake on hotplate set to 110°C for 40 min.
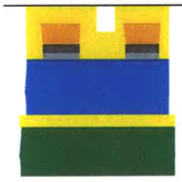	Spin NR9-3000P onto traps at 3000 rpm for 40 s Bake on hotplate set to 110°C for 3 min.
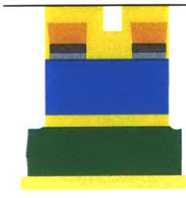	Attach the Si wafer to UV-release cutting tape After a test cut to calibrate the blade position, cut out individual traps to within 30 μm of the electrodes

Figure 7-23: Trap fabrication: final trap cutting.

Due to a small contact area (16mm × 2.3mm), delamination of the individual traps from the fixturing substrate during cutting was a significant problem. Delamination can probably be ameliorated by performing *fewer* saw passes per cut than what was here (3 cuts of 155 μm, 200 μm and 200 μm).

7.3.1.7 Trap Mounting

As we did not have access to a wire bonding machine in a higher-class cleanroom, the final trap assembly and bonding was done in EML using the Kulicke & Soffa 4124 wire bonder.

Before bonding, the protective NR9-3000P photoresist is washed away with acetone, followed by an isopropyl alcohol rinse and blow-drying. With trap storage times under new photoresist of less than one week, no degradation of dielectric strength between the trap electrodes was observed.

The wire bonder heating chuck is used to pre-heat the UHV-cleaned 316 stainless steel chip holder to $100°C - 120°C$. A single drop of mixed Epotek ND353 epoxy outgassed as per the procedure in Section 7.3.3.11 is applied to the chip chip holder and the trap chip lowered on top of it. During the approximately 3 minutes it takes the epoxy to cure, the trap is centered on the chip holder by gently pushing with carbon-tipped tweezers while observing the trap alignment using the wirebonder's long-working distance microscope (Leica). The epoxy cure is finished by leaving the chip holder on the heater, covered with Al foil (to protect the trap from dust) for another 5-10 minutes.

With the trap firmly attached to chip holder, the previously UHV-cleaned and prepared breakout/filtering PCBs assembly (Section 7.3.3) is attached to the holder using 0-80 screws. For ease of manipulation, the whole assembly is attached to a UHV-clean aluminum mount (Figure 7-24) that is removed prior to insertion into the vacuum chamber. To match the wire bonder's expected workpiece height, two additional UHV-cleaned shim pieces are used (not shown).

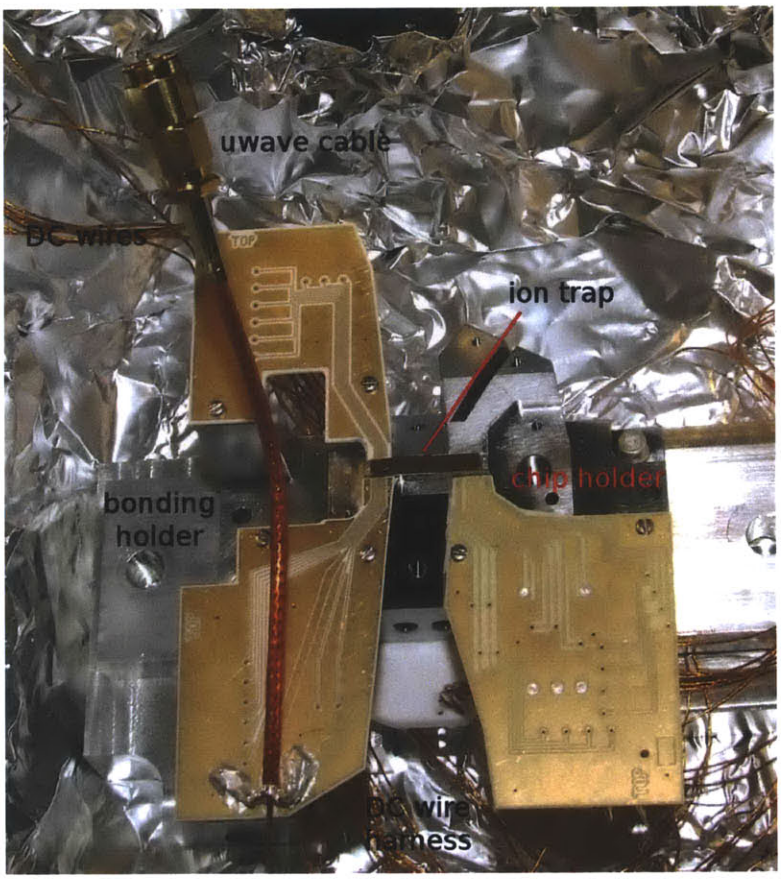

Figure 7-24: Trap assembly prior to wirebonding: the trap is epoxied to the chip holder which is then lowered into the prepared PCB assembly. To match the wirebonder's expected workpiece height, two additonal shim blocks are used.

The wire bonding was performed using 25 μm-diameter Au wire by Yufei Ge according to the diagram in Figure 7-25. For most DC electrodes, the trap mask provided only a 150 μm-wide bond pad with enough room for only one wire bond - in retrospect, a poor decision. In addition to decreased reliability, the lack of space prevents new bonds to be made if any of the existing bonds fail: placing a second bond on a test trap caused the ball end of the first bond to move and wedge itself between electrodes, resulting in a short. Additional bonds were made where space allowed as for several RF electrodes, the ground and the mirowave connections.

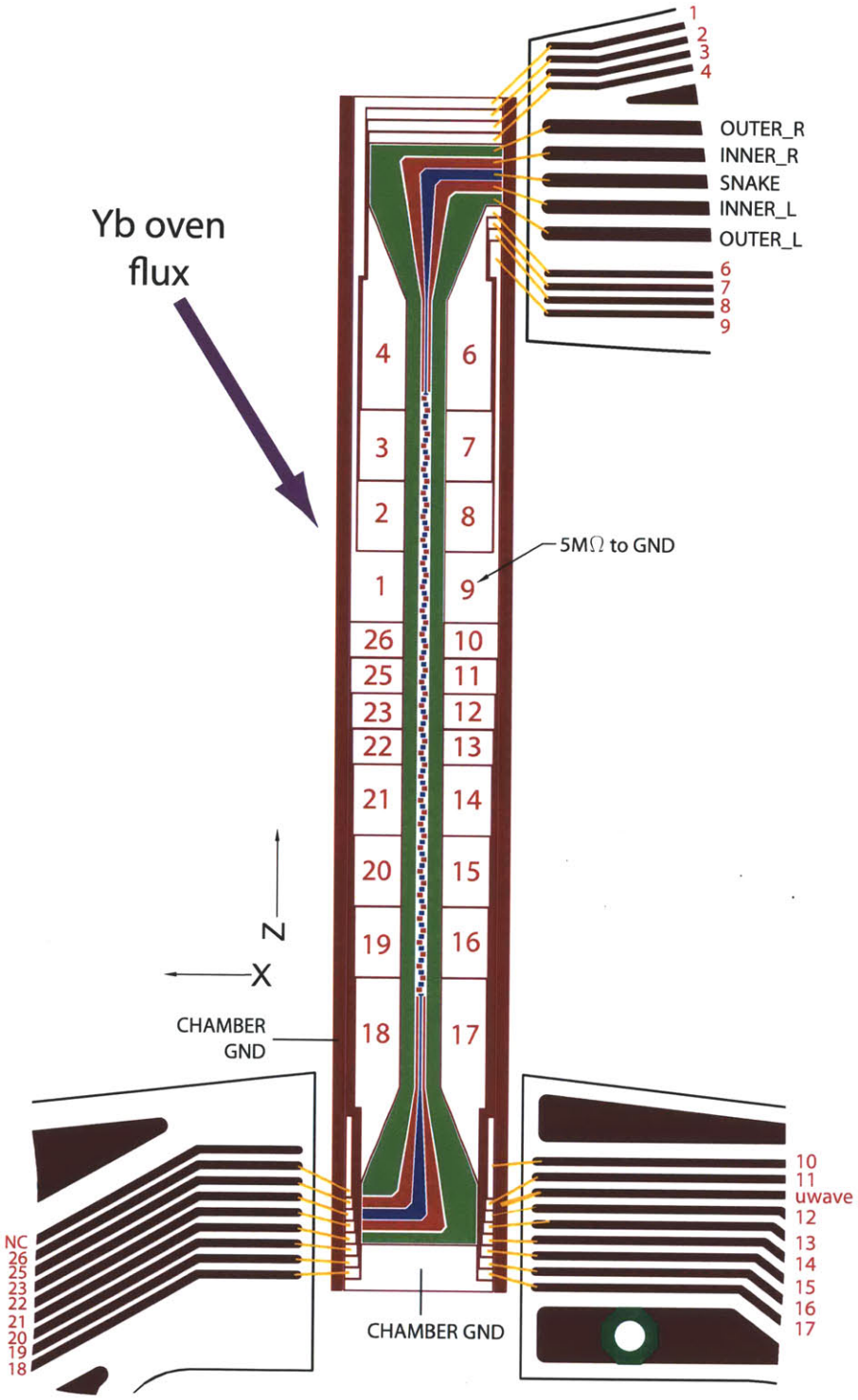

Figure 7-25: Schematics for wirebonding the ion trap array to the electrical breakout printed circuit boards.

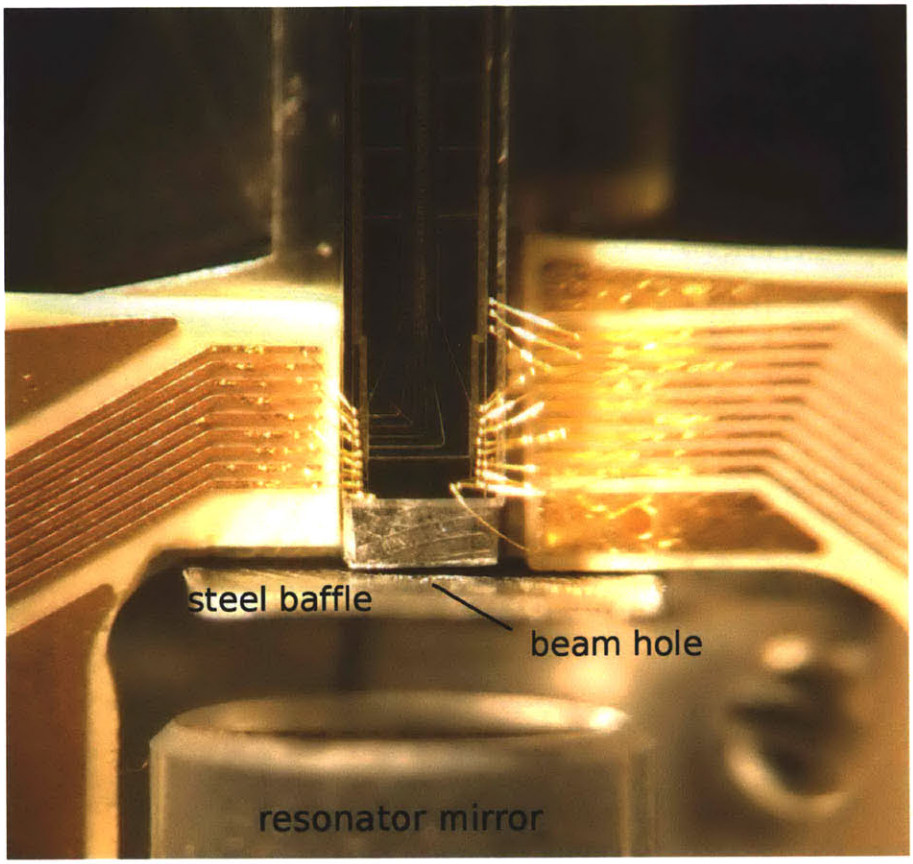

Figure 7-26: Actual trap after wirebonding. Also visible is one of the resonator mirrors as well as the steel baffle used to shield this mirror from the stray Yb oven flux.

7.3.2 Optical Resonator

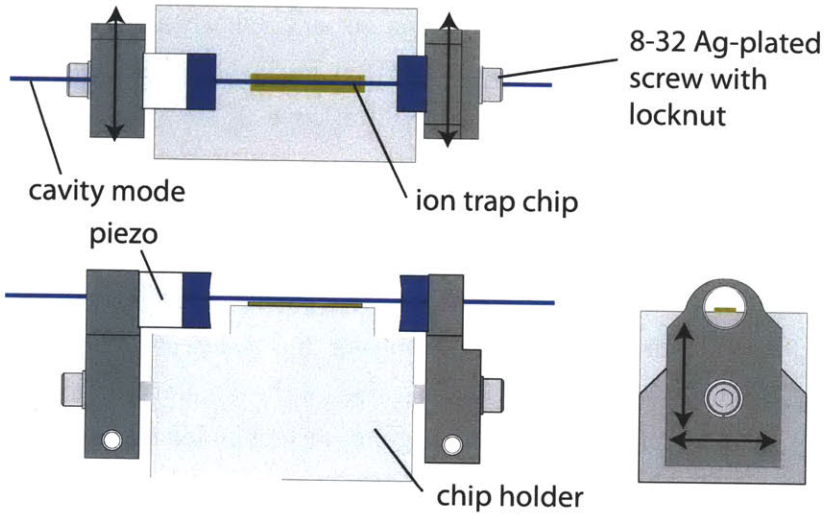

Figure 7-27: Degrees of freedom for alignment of the Fabry-Perot resonator to the ion trap array.

The assembly, alignment and testing of the optical resonator for the linear ion trap array is described in detail in Andrew Grier's thesis [Gri11].

8 mm-diameter, 25 mm-radius-of-curvature concave fused silica substrates with edge thickness of 4 mm were super-polished by Research Electro-Optics, Inc. (Boulder, CO). The substrates were coated by Advanced Thin Films (Boulder, CO) with a high-density electron-beam evaporated SiO_2-Ta_2O_5 dielectric stack. To decrease absorption in Ta_2O_5, the bulk material ratio between SiO_2 and Ta_2O_5 was $2:1$ with a Ta_2O_5 top (air-facing) layer. The transmission data supplied by AT Films indicates transmission of $(170-190)$ ppm at the target wavelength of 370 nm (Yb^+ D2 line), corresponding to a maximal finesse $\mathcal{F} = (16.5-18.5)\times 10^3$.

To allow tuning of the cavity, on of the two mirrors is attached to a single-layer piezoelectric transducer (Ferroperm, Denmark) using previously vacuum-outgassed ND353 epoxy. Prior to assembly, the piezo transducer is vacuum-cleaned in acetone, followed by isopropyl alcohol without using the ultrasonic tub. The piezo transducer and the second mirror are attached via the same epoxy to 316 stainless steel alignment blocks (Figure 7-27) which are connected to the chip holder via two silver-plated steel 8-32 screws. The screw connection between the alignment blocks and the chip holder allows the four degrees of freedom necessary to align the cavity mode to the ion trap array (Figure 7-27). The resonator alignment procedure is described in detail in Andrew Grier's PhD thesis [Gri11]. In the final assembly, the resonator

mode was measured to be nearly parallel to the trap axis with its center shifted by (± 5 μm, $+13 \pm 5$ μm) relative to the designed center of the ion trap [Gri11].

The length of the resonator was chosen so as to nearly match the 12.643 GHz-ground state hyperfine splitting in Yb^+ (Section 7.2.1). After assembly, the resonator length was measured using a modulated 370 nm laser. If the transmission of the laser through the resonator is observed while the resonator length is scanned so that its modes shift in frequency by Δ_{FSR}, the laser modulation will manifest as additional pairs of peaks in the transmission trace. As the laser modulation frequency is brought close to $\Delta_{FSR}/2$ where $\Delta_{FSR} = c/2L$ is the frequency spacing of the resonator's TEM_{00} modes, the pairs of transmission peaks due to laser modulation will merge, allowing one to determine the free spectral range of the resonator. Using this sideband spectroscopy method, the free spectral range of the assembled experimental cavity was determined to be $\Delta_{FSR} = (6,361.0 \pm 1.5)$ MHz, corresponding to the resonator length of $L = (23,565 \pm 5.5)$ μm and the waist of the TEM_{00} mode at the design wavelength of 369.525 nm of $w = 38.3$ μm.

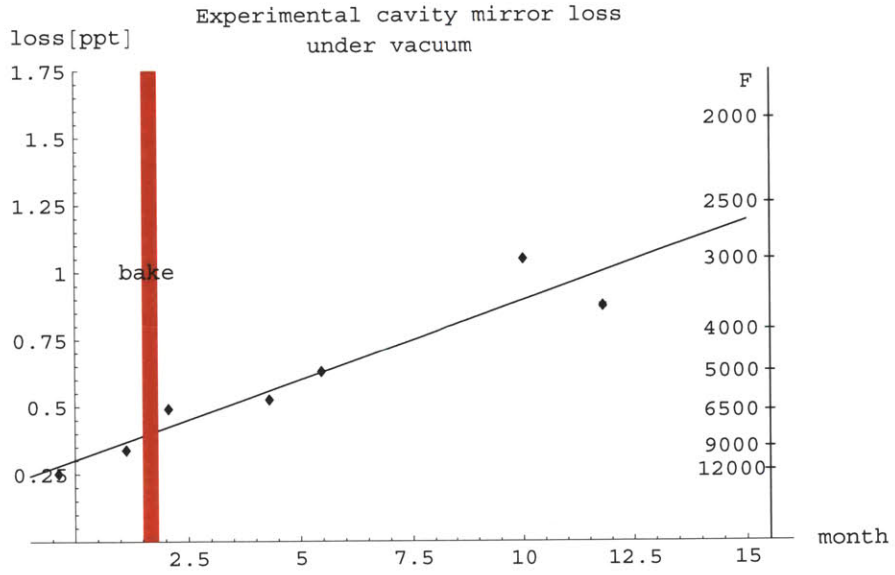

Figure 7-28: Finesse of the optical resonator as a function of time since the initial vacuum pumpdown. A linear fit gives the cavity mirror loss as a function of time equal to 60 ppm/month.

After the initial alignment of the resonator, the mirror finesse was monitored using the ringdown method [Gri11], obtaining the results shown on Figure 7-28.

The observed degradation of the mirror reflectivity is consistent with a linear increase in loss as a function of time, as would occur due to oxygen desorption from

the mirror surface under exposure to high vacuum. Due to a continous decay of cavity finesse from the maximal value of $\mathcal{F}_{original} = 12,500$ obtained right befor the resonator assembly to the present value of $\mathcal{F} = 3,600 \pm 300$, the the maximal achievable resonator cooperativity at the design wavelengh decreased from $\eta = 22.5\%$ to

$$\eta = \frac{24\mathcal{F}}{\pi k^2 w^2} = 6.5\% \tag{7.7}$$

7.3.3 Electrical Breakout

Providing connections to 30 trap electrodes under ultrahigh vacuum while supressing electronic field noise experienced by the ions below the level of 10^{-12} $V^2/m^2/Hz$ set by the expected surface charge fluctuations in our ion trap [LGL+08], presents a considerable challenge.

In the past, this problem has been addressed in a scalable fashion by mounting planar ion trap chips onto modular Ceramic Pin Grid Array Carriers (CPGAs) used in the microelectronic industry [LLC+09]. CPGA carriers allows scaling to hundreds of electrodes, reuse of chamber electrical designs [MNS+11] as well as easy exchange of traps.

The use of CPGAs in the present ion-chip-resonator system presents several obstacles. As the CPGA-pin mating tolerances are insufficient to ensure repeatable or even constant alignment of the ion trap to the optical resonator when subjected to the high-temperatures necessary to achieve ultrahigh vacuum, the resonator assembly and the ion trap would both need to be rigidly attached to the CPGA. Although the scalability of such a system would be preserved with a self-aligning optical resonator / trap assembly, a system of this type has not yet been demonstrated. Without a self-aligning system, the difficulty of resonator alignment easily exceeds that of replacing the ion trap chip on a fixed mount, negating the time savings from using a 'pluggable' CPGA.

Because of these difficulties, a CPGA was not used in the system presented in this thesis. Nonetheless, the CPGA idea motivated a custom breakout design that accommodates the oven flux and the MOT while being reusable between different traps (Figure 7-29). By employing standard microelectronic and hybrid techniques, including printed circuit boards, SMD components, conductive epoxies and wire crimping with standard gages, this design allows straightforward scaling to more than 100 DC electrodes.

In the following, the electrical breakout design is presented in the order of assembly.

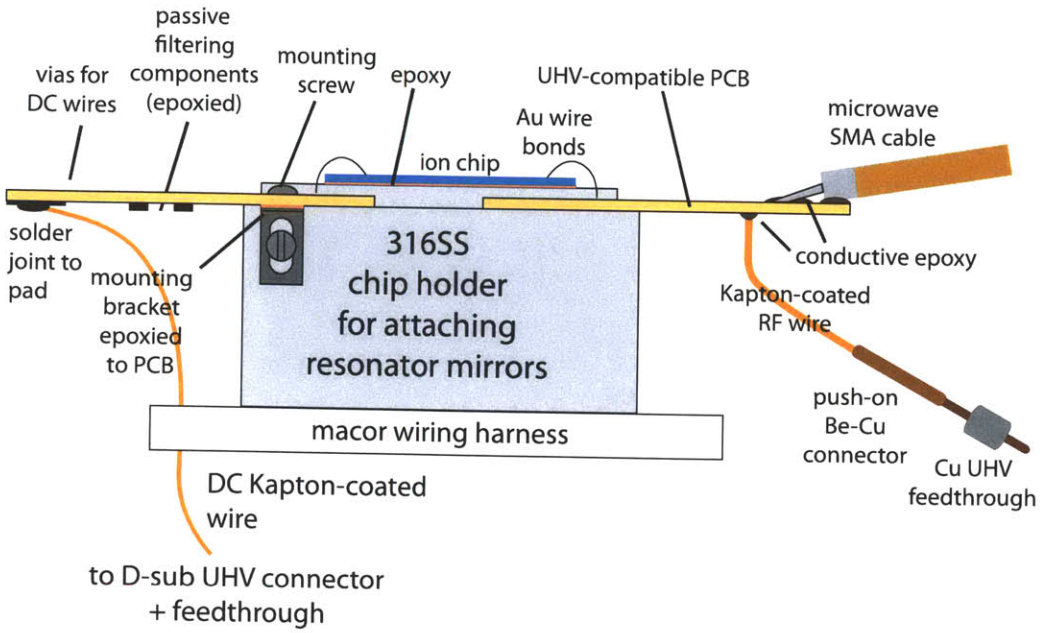

Figure 7-29: Electrical breakout of the ion-chip / resonator system.

7.3.3.1 Breakout Circuit Boards

The core of the electrical breakout is formed by three printed circuit boards (PCBs) made by Hughes Circuits, Inc. (San Marcos, CA). The boards are made on the ultrahigh vacuum-compatible Rogers 4350 glass-woven epoxy substrate which we previously demonstrated to be ultrahigh vacuum-compatible (Section 4.1). To slow down oxidation which could interfere with wire bonding, Hughes Circuits was asked to electroplate the Cu PCB electrodes with an Au layer. Contrary to the standard practice, *no* Ni barrier layer was used before Au plating. While the lack of Ni barrier layer will allow Cu to slowly diffuse through the Au layer and oxidize if exposed to air, the avoidance of Ni was thought to avoid the bigger problem of exposing magnetically-sensitive ions to inhomogeneous and hysteretic fields produced by this ferromagnetic material.

Prior to assembly, the PCBs were ultrasonically cleaned for 20 minutes in acetone followed by a 10-minute ultrasonic rinse with isopropyl alcohol and blow-drying. Ultrasonic cleaning in dichlormethane was attempted but abandoned as within 5 minutes, delimination of the copper electrodes was observed.

7.3.3.2 RF Grounding and Passive Filtering

The circuits implemented on the breakout PCBs are shown on (Figure 7-32).

The ground reference is provided by the chip holder which is electrically connected to both the vacuum chamber and the ground planes of the printed circuit boards.

The DC trap electrodes are tied to ground at RF frequencies via 10 nF 1206-size Ag:Pd ultrahigh vacuum-compatible surface-mount (SMD) shorting capacitors (1206B103K501P from Novacap, Inc.). To minimize inductive effects, the shorting capacitors are placed within 3 cm of the trap electrodes - a distance comparable to the size of the trap chip.

External noise on DC electrodes is filtered using 10 kΩ 1206-size Ag:Pd ultrahigh vacuum-compatible SMD resistors (RP1206BA-1002JN-91 from Barry Industries) inserted between the trap electrodes and the outside connections.

To minimize the ion micromotion due to phase-quadrature imbalance between the RF trap electrodes, two parallel 47 pF Ag:Pd SMD capacitors (1206N470M501P from Novacap, Inc.) are used to connect the two outer electrodes (OUTER_L and OUTER_R) at RF frequencies. The limited size of these capacitors still allows small out-of-phase voltages to be applied to adjust the radial position of the trap axis as discussed in Section 7.2.2.4.

Since no use of differential RF voltages on the trap array electrodes (INNER_L, SNAKE and INNER_R) could be envisioned, 10 nF capacitors (1206B103K501P from Novacap, Inc.) were used to closely tie these electrodes at RF frequencies.

Prior to assembly, the SMD resistors and capacitors were ultrasonically cleaned for 30 minutes in acetone followed by a 10-minute ultrasonic rinse in isopropyl alcohol and blow-drying.

To avoid blocking optical access to the ions, all passive components are attached to the bottom side of the PCBs, making extensive use of PCB vias. To ensure good contacts the passive components were epoxied to the PCBs using the H20E ultrahigh vacuum-compatible silver-conductive epoxy (Epotek, Billerica, MA). Soldering was not employed as ensuring reliable connections to SMD components would require the use of fluxes which are not ultrahigh vacuum compatible and would need to be fully removed using organic solvents - a difficult task given the many variously-shaped components on the PCBs.

The epoxying of the passive components was performed by Andrew Grier and is described in detail in [Gri11]. Briefly, Epotek H20E epoxy is mixed and then outgassed under low vacuum so as to eliminate trapped gas bubbles and decrease outgassing under ultrahigh vacuum. The cleaned PCBs are then put onto a hotplate covered with clean aluminum foil set to $150°C$ and the individual SMD components epoxied to it.

7.3.3.3 RF Connections

To minimize phase shifts between different RF electrodes, the RF connections between the breakout PCB and the outside of the vacuum system are made via short (< 1.5" long) $0.6mm$ Kapton-coated multi-stranded wires (311-KAPM-060 from Allectra Limited, East Sussex, UK). The specific RF wire lengths are given on Figure 7-31 and need to be accurate to within 0.2" to ensure a good connection to the vacuum feedthrough without exerting stress on the fragile PCB connections.

Before assembly, the Kapton-coated wires were cleaned by immersing into acetone for *at most 30 s,* followed by a 1-minute rinse in isopropyl alcohol, both *without sonication.* Longer soaking in acetone caused the Kapton film to unwrap from the wires, especially if sonication was performed at the same time.

After cleaning, the RF wires were attached to the vias on the breakout PCB boards using the Epotek H20E epoxy via the two step procedure described in Andrew Grier's thesis [Gri11].

The opposite ends of the RF wires were crimped to FTAPC032 Bu-Cu inline connectors (Kurt J. Lesker, Inc., Pittsburgh, PA) which plug onto the individual Cu pins of the EFT0083032 $500V$ vacuum feedthrough (Kurt J. Lesker). To accommodate the short RF wires, the vacuum-side feedthrough pins were shortened to the lengths given in Figure 7-30. To prevent breaking the ceramic-metal vacuum seals, the pins were stress-relieved by pliers while cutting them with wire cutters. To allow the Be-Cu connectors to slip easily onto the shortened pins, the ends of the cut pins can be rounded with a file.

FTAPC032 inline connectors are also used on the atmosphere side to connect tinned Cu wires to the RF feedthrough. To stress-relieve the connections and prevent damaging the fragile ceramic-to-metal seals on the feedthrough, the Cu wires are glued using cyanoacrylate glue to an insulating PCB attached (also via cyanoacrylate glue) to an Al cup fixed via screws to the steel feedthrough flange. Since the RF connections are not filtered relative to ground inside the chamber, to avoid noise pickup near the 1 MHz secular frequencies of the trapped ions, a Faraday shield consisting of a fine copper mesh is attached via a work clamp to the Al cup (Figure 7-30).

The RF electrodes are resonantly driven at 16.260 MHz via a helical resonator. The resonator is driven by capacitivly coupling to its output the signal from a 1 W RF amplifier (ZHL-32A from MiniCircuits, NY). The low voltage side of the resonator coil is shorted to ground via a 8.2 nF mica capacitor, allowing the RF electrodes to be biased at DC.

To protect against damage to the trap from over-voltage, the RF electrodes are

protected via low-capacitance (< 2 pF) vacuum spark gaps (MLH-0230 from Teledyne Reynolds, CA). The sparkgaps were tested by connecting them in parallel with a 100× voltage probe to the output of a helical resonator operating at 15.620 MHz. Under a gradual increase in the RF voltage, the spark gaps were seen to fire at RF amplitudes <240 V, limiting the output voltage to <200 V. Under a further increase in the RF drive amplitude, the voltage across the sparkgap gradually increases, not exceeding $250V$ at RF drive amplitudes of up to twice that corresponding to the gap firing threshold.

The RF electrodes that are not driven in a given trap configuration (so far, INNER_L, SNAKE and INNER_R) are shorted to the Faraday shield via $10nF$ capacitors and biased via $50k\Omega$ resistors as shown on Figure 7-32.

7.3.3.4 Mechanical Connection

The breakout PCBs are attached to the stainless steel block holding the trap chip using removable 0-80 steel mounting screws. Additional support to the PCBs is provided by 316 stainless steel brackets attached to the PCBs using the ND353 epoxy. After mixing the two epoxy components but prior to application, to decrease outgassing under ultrahigh vacuum, trapped bubbles in the epoxy were removed by placing it under low vacuum as described in Section 7.3.3.11.

7.3.3.5 Microwave Connection

One of the electrical breakout boards provides a $\approx 50\Omega$ microwave coplanar waveguide line that can be used to deliver 12.6 GHz radiation to the ion trap chip for addressing the ground-state hyperfine transition in $^{171}Yb^{+}$. The microwave signal is supplied via a ultrahigh vacuum-compatible Kapton SMA microwave cable (311-KAP50 from Allectra Limited, UK). As we were not aware of any vacuum-compatible microwave connectors compatible with our target bakeout temperatures of $\approx$ 200 °C, the SMA cable was epoxied directly to the breakout PCB using outgassed H20E conductive epoxy as described in [Gri11]. Prior to epoxying, the SMA cable was cut to length and cleaned using the same procedure as the RF wires.

To pass the microwave signal to atmosphere, the SMA connector at the opposite end of the cable is mated to a high-frequency ultrahigh vacuum feedthrough (IFDCG012011 from Kurt J. Lesker). The transmission loss of the feedthrough was measured as 1.9dB at 12.6 GHz using a calibrated 40 GHz network analyzer with the corresponding voltage-standing wave ratio of 3.6.

7.3.3.6 DC Connections

Connections to the DC trap electrodes are made using 0.35mm-diameter Kapton-coated multi-stranded wires (311-KAPM-060 from Allectra Limited, East Sussex, UK). To avoid ground loops, two additional ground sense wires are provided - one for each side of the chip holder.

While DC wires are more flexible and significantly longer than the RF wires, to ease their fitting into connectors, it was helpful to cut them to the specific lengths listed on Figure 7-31.

Prior to assembly, the DC wires were cleaned using the same procedure as for the RF wires. After cleaning, the DC wires are connected to the soldering pads on the bottom side of the PCBs via eutectic (80:20) $Au : Sn$ solder (Indium Corporation, Utica, IL) using an ultrasonic soldering iron (Sunbonder IV from Sanwa Components). To relieve stress on the solder joints, all DC wires are passed through holes made in a 1/8" thick Macor wiring harness using a water jet cutter as shown on Figure 7-31.

The opposite ends of the DC wires are connectorized with two ultrahigh vacuum-compatible 25-pin ceramic D-sub connectors (FTADD25C from Kurt J. Lesker, Inc., Pittsburgh, PA) following the pinout on Figure 7-31. After threading the DC wires through the back side of the FTADD25C connector, the wires were crimped to the FTADPEEK-10 Au-plated contacts (Lesker, PA) using a degreased crimping tool (100190 from Accuglass Products, Inc., San Fernando, CA) [1]. Due to a design error by Lesker, when mated to the 4.5" CF dual IFDGG251056X feedthrough from the same company, the assembled FTADD25C connectors did not fit through the standard 4.5" CF flange opening. This problem was resolved by filing the corners of the FTADD25C connectors using steel files, which did not affect the integrity of the connector.

On the air side, the DC trap wires are routed together with the two ground sense wires via a shielded D-sub connector to a buffered, differential-output, 100 kS/s, 16-bit DACs converter based on the Maxim MAX5734 16-bit 32-channel digital-to-analog converter (DAC). The digital input lines to the DAC (signal and ground) are filtered using an inductively coupled digital isolator (Analog Devices ADUM5400).

7.3.3.7 Chip Holder

The electrical breakout described so far is independent of both the trap chip and the optical cavity assembly and is fully reusable.

[1] The 100190 crimping tool was dissasembled and cleaned in an ultrasonic bath using the Branson IS industrial degreaser. Although this cleaning step will likely impact the long-term reliability of the tool, no mechanical problems were observed after $\sim$ 80 crimpings.

The mechanical connection between the trap chip, optical resonator and the break-out PCBs is provided by a stainless steel chip holder (Figure 7-29). The chip holder was made by the MIT Central Machine Shop from a single piece of 316 stainless steel (Industeel Group Arcelor, plates nr. 578426/1, heat #18301). A second copy of the holder was made in aluminum for testing purposes.

Prior to assembly, the steel chip holder is aggressively cleaned using the standard ultrahigh vacuum cleaning procedure employed on other all-metal vacuum parts.

7.3.3.8 Residual Magnetization in the Chip Holder

To avoid influencing the magnetic-field sensitive states of trapped ions, the main experimental chamber was made using nominally non-magnetic materials, including type-304 and 316 stainless steels. However, machining operations on stainless steel are known to cause transformations into ferromagnetic phases. Due to its proximity to the ions, the magnetic response of the milled chip holder was of special concern.

The magnetic response of the chip holder was tested by placing it in a field of (1200 ± 80) G , resulting in residual magnetization near the surface facing the trap of 4 G in the direction of the applied field. Based on this and assuming a linear magnetization response, the 45 G/cm MOT quadrupole field would then produce a maximum of 70 mG of residual magnetization near the holder surfaces.

Following the test and prior to assembly, the chip holder was demagnetized using a commercial demagnetizer producing a maximum field amplitude of 1.4 kG at 60 Hz. The residual magnetization after this procedure was less than 200 mG at all surfaces of the holder. Unfortunately, one of the regions of highest magnetization was the chip mounting surface, reflecting the increased deformation caused by machining to tolerances the fine features of the holder.

7.3.3.9 Temperature Control

The temperature of the ion trap / optical resonator assembly is regulated in-vacuum using a heater wire together with a temperature sensor (Figure 7-33). To avoid catastrophic vacuum failure and contamination of the optical resonator mirrors by decomposition of epoxy at high temperature, the heater design avoids the use of epoxies. Instead, a 0.010"-diameter Chromel wire is threaded through two 1" long steatite insulators (BC-CER-INS from Accuglass Products, Inc.) which are then inserted into holes provided in the chip holder. The heater has a total wire length of ≈ 5" and a total resistance of $(4 \pm 1)\,\Omega$.

The temperature of the resonator assembly is sensed with a DT-670 Si sensor (Lakeshore Cryotronics, Westerville, OH). Although a Si diode has a lower temperature sensitivity than a negative temperature coefficient resistor, this was the only available ultrahigh vacuum-compatible bakeable sensor. The temperature sensor (Tsense1,2) is connected via 311-KAPM-035 wires cut to the lengths specified on Figure 7-31 using the Epotek H20E conductive epoxy.

To provide good thermal contact the Si temperature sensor is attached to the ultrahigh vacuum-cleaned steel chip holder using outgassed Epotek ND353 epoxy. This was conveniently done just before epoxying the ion trap chip onto the chip holder as described in the next subsection.

7.3.3.10 Trap Integration

The ion trap is mounted to the chip holder just prior to wire bonding, making use of the wire bonder's heating chuck.

Epotek ND353 epoxy is first outgassed using the procedure described in Section 7.3.3.11. The outgassed epoxy, electrical breakout assembly, DT670 temperature sensor with Kapton wires attached, the chip holder and a finished trap were packaged in two cleanroom-compatible 6" photolithography mask carrier boxes and taken to the wire bonder in the MIT Exploratory Materials Laboratory.

As described in Section 7.3.1.7, the wire bonder heating chuck was used to preheat the chip holder to 100°C - 120 °C, at which point the temperature sensor is attached to it, followed by the trap chip.

With the trap firmly attached to chip holder, the holder was lowered onto the previously ultrahigh vacuum-cleaned and prepared breakout assembly while threading the temperature sensor wires through the holes in the Macor harness as shown on Figure 7-31.

Care is important at this stage as the unmounted PCBs can easily hit the trap chip.

The breakout printed circuit boards are attached to the chip holder from the top using 0-80 screws and from underneath using 4-40 screws passing through the stainless steel brackets previously attached to the circuit boards.

The trap is wirebonded to three printed circuit boards (PCBs) providing electrical breakout as described in Section 7.3.1.7.

In case of failure, the trap can be removed from the PCBs by physically tearing off the wire bonds. The trap can be non-destructively removed from the chip holder by heating the holder under vacuum above the ND353 decomposition temperature

(300 °C). A quicker, destructive method is to mount the chip holder to a mill stage and use a blank carbide endmill to shear the quartz trap sideways off the chip holder. Any residual epoxy can then be scraped off with a razor blade, leaving the chip holder intact. Both procedures can also be used to remove the DT-670 sensor which, with its Kapton wires, is incompatible with high temperatures or chemical degreasing.

7.3.3.11 Epoxy Outgassing Procedure

1. Set up a vacuum pump to pump down the 6" diam. Kurt Lesker O-ring hinged door vacuum chamber in prof. Chuang's lab. If using oil pump, make sure you use an oil filter and the oil filter is clean.

2. Clean microscope glass slides using the same procedures as for optics.

3. Put slides on 0.25" thick aluminum tray (looks just like a ping-pong paddle). The tray serves as a heat buffer to keep the epoxy warm and at low viscosity to allow rapid outgassing when vacuum is applied.

4. Put paddle on hotplate and set to 65°C.

5. After 10min, mix the two components in the mixing plastic bag. Squeeze mixed epoxy onto the glass slides with the slides still on the hotplate.

6. Transfer the Al paddle and the glass slides to the vacuum oven. Start pumping immediately.

7. Leave slides under vacuum for 2-4 h.

8. The epoxy is now ready to be applied. If the epoxy is too viscous, you can gently heat it up by putting the paddle back on a hotplate set to 50 °C for 5 min.

7.3.4 Channeltron Detector

Having shown its usefulness in the ion-atom collision experiments, a Channeltron ion detector (Magnum 5901 from Burle, Inc., PA) was included in the design of the trap array system.

The Channeltron is positioned with its front (22 ± 2) mm from the center of the ion trap chip and held using a MACOR clamp. With the front of the detector biased to -2 kV, the flight time of a Yb^+ ion between the trap and the detector was calculated using a 3D finite-element model as 1.9 μs.

Separate high-voltage connections are made to the front ring and the body of the Channeltron using insulated Kapton wire (311-KAPM-035 from Allectra Limited, UK), as described in [Gri11]. To allow better control over the ions' trajectories close to the Channeltron, an additional connection is made using the same wire to the front Ag surface of the ion imaging mirror, located within 5 mm of the Channeltron aperture. All three DC wires are passed through a 4-pin high-voltage 1.33" CF UHV feedthrough. To avoid RF interference, the feedthrough is Faraday-shielded on the air side using soldered-joined Cu wire mesh clamped via a steel worm C-clamp to the feedthrough flange.

To oprate the Channeltron as an ion detector, the front ring is biased to -2 kV with the Channeltron body and the imaging mirror held at ground potential.

To avoid inductive effects, the high-impedance output of the Channeltron's electron collecting cup was connected via a BeCu barrel connector (FTAIBC058 from Kurt J. Lesker, PA) to the central conductor of a UHV-compatible Kapton 50 Ω cable (311-KAP50 from Allectra Limited, UK). The other end of the 50 Ω was provided with a SMA connector and mated to a high-frequency SMA UHV feedthrough (IFDCG012011 from Kurt J. Lesker, PA). The ground shield of the 50 Ω cable was left ungrounded at the Channeltron end.

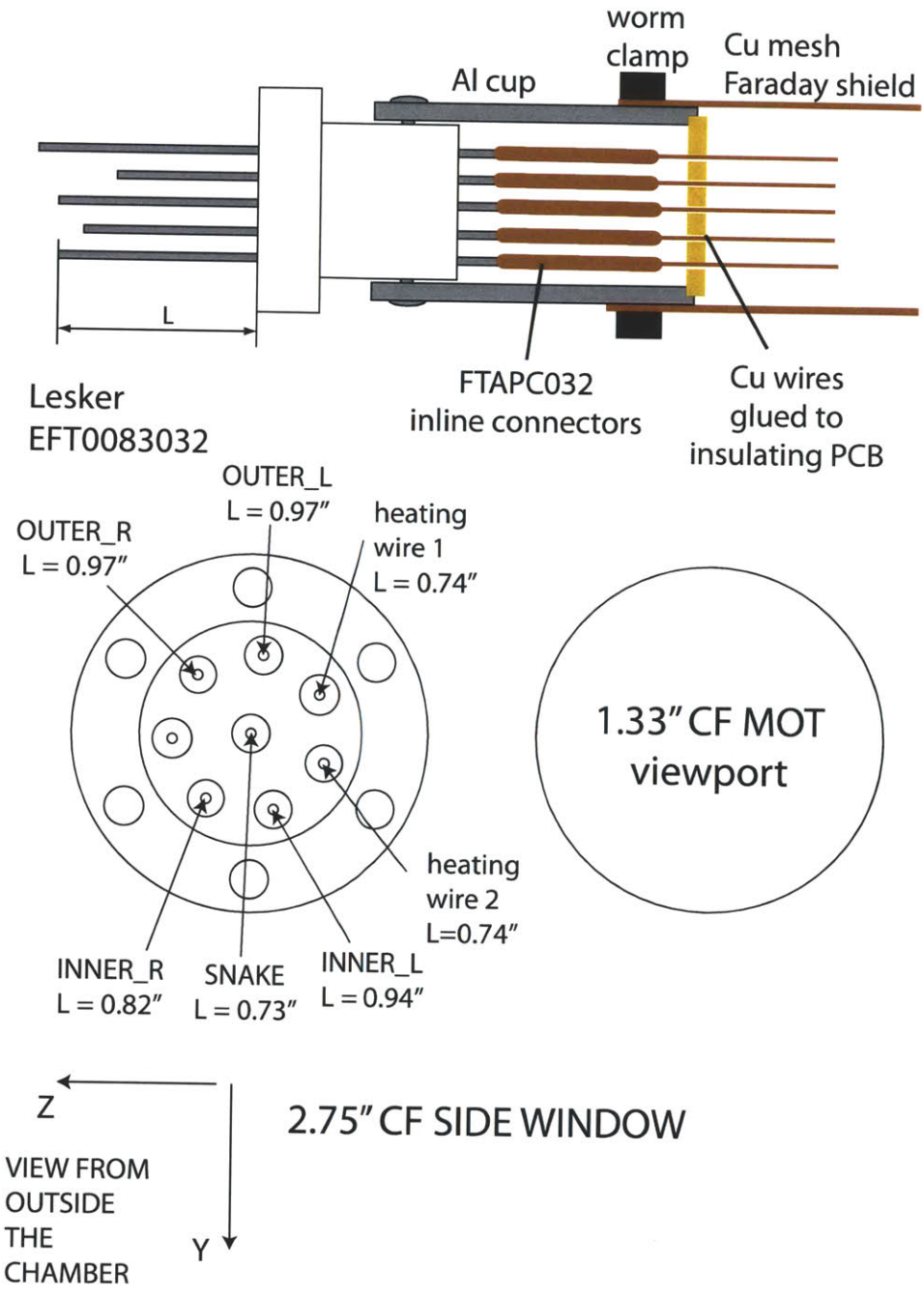

Figure 7-30: Pinout of the RF vacuum feedthrough.

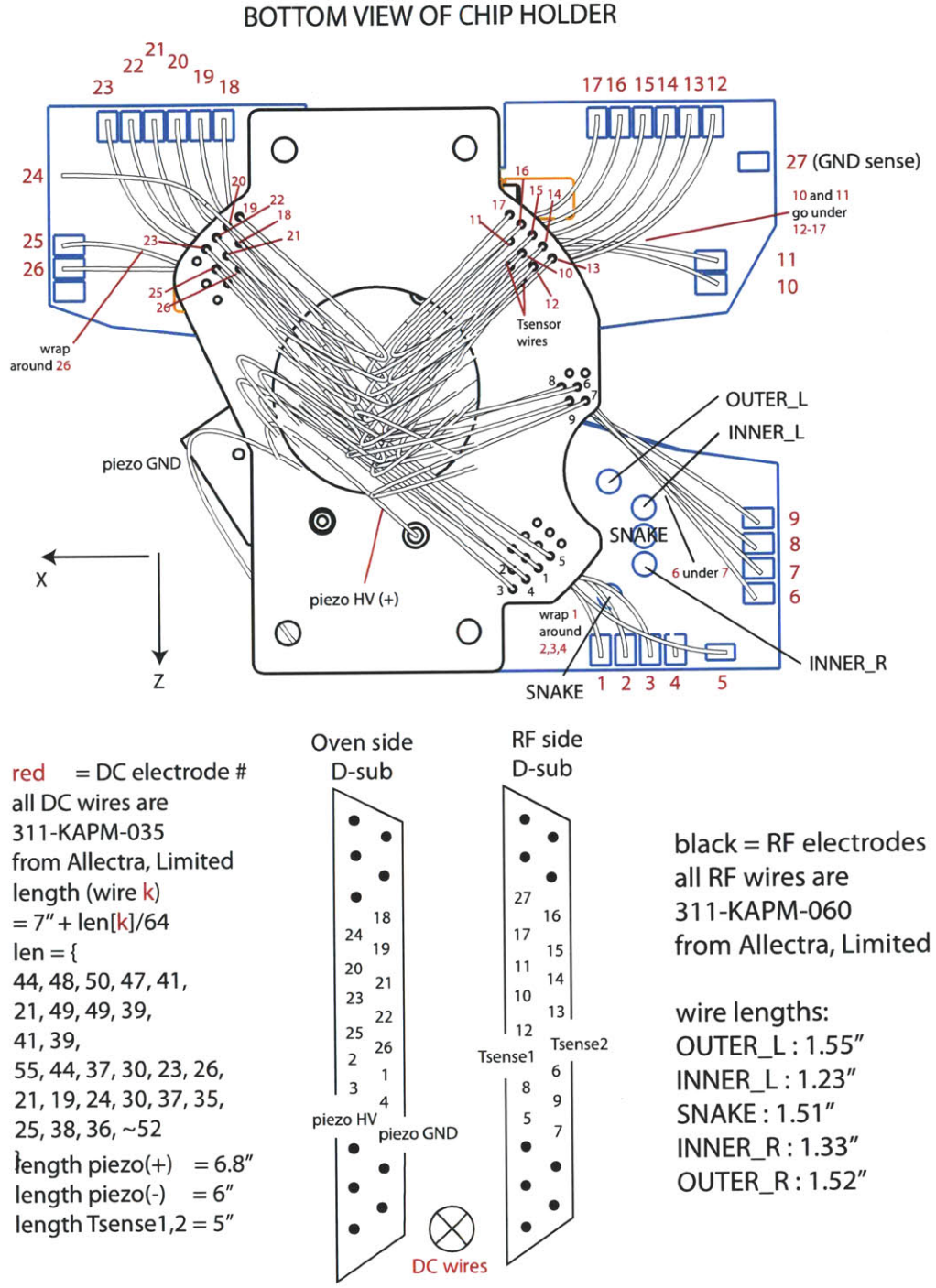

Figure 7-31: Pinout of the DC feedthrough. The D-sub connectors are shown as viewed from the plug side i.e. with the DC wires going into the plane of the drawing.

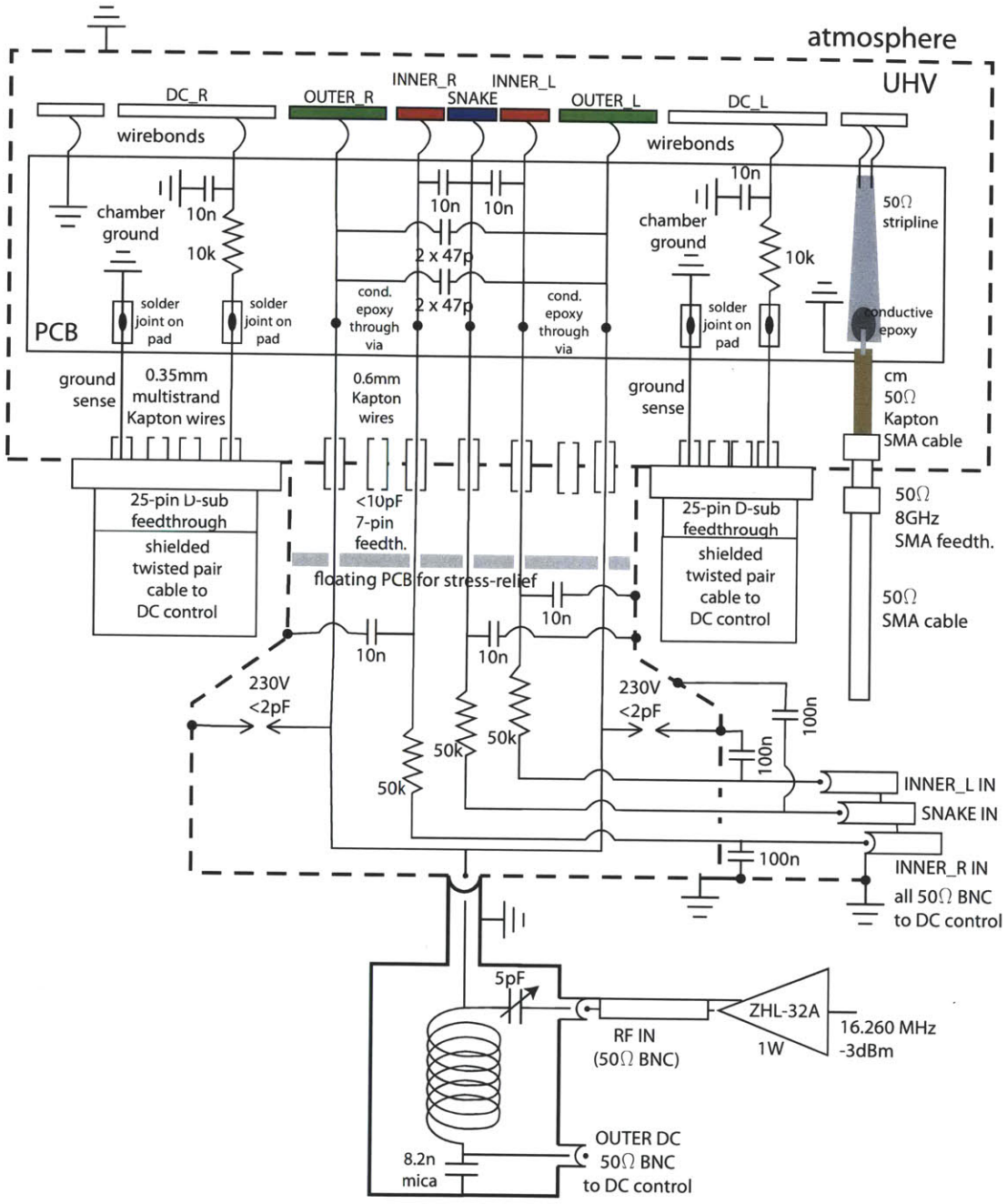

Figure 7-32: Electrical schematic of the ion trap array system.

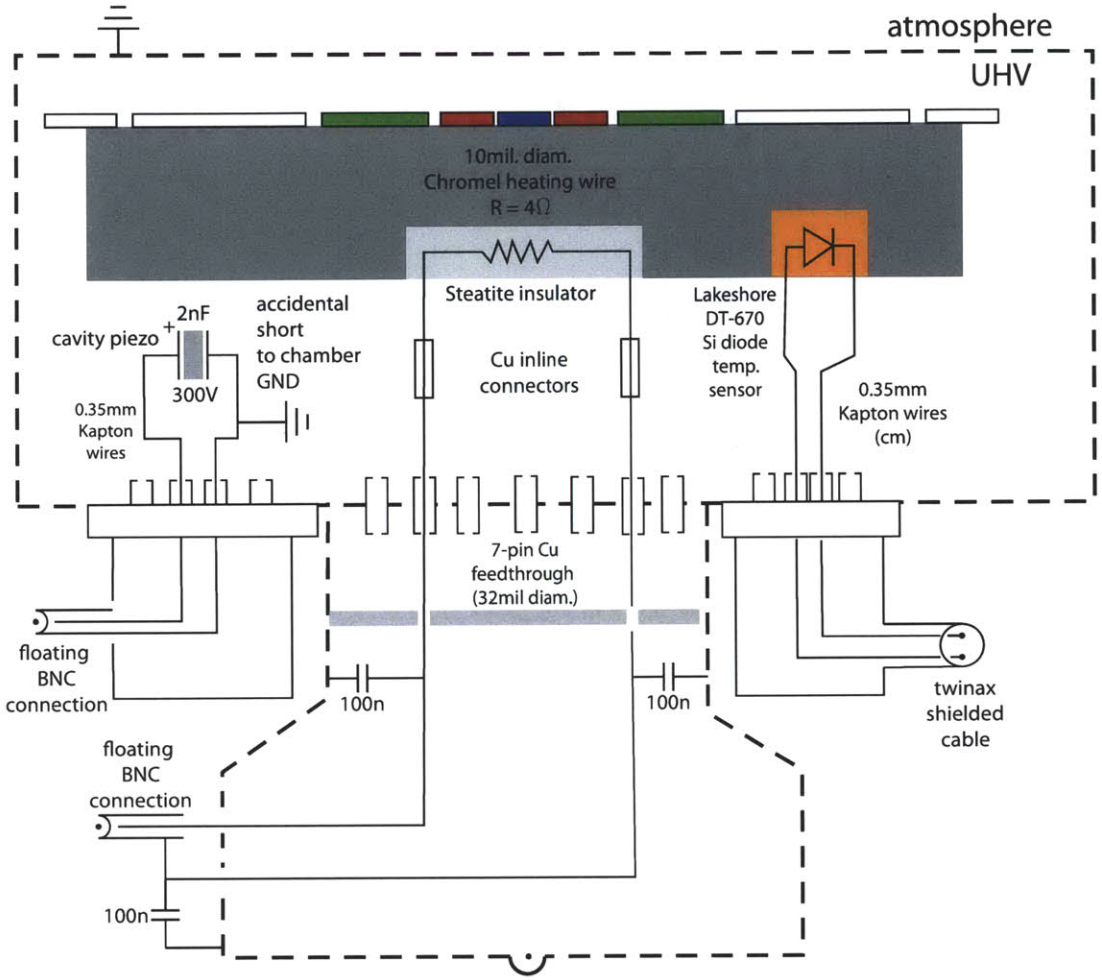

Figure 7-33: Electrical schematic of the system used to control the length of the optical resonator.

7.3.5 Loading of Ion Trap Array via MOT photoionization

To achieve the strongest collective coupling of ion chains to the resonator mode, dozens of individual traps, each on the scale of 100μm, need to be loaded with hundreds of ions. Since ions of different Yb isotopes do not couple to the resonator mode while occupying space in the traps, it is also desirable that the ion loading process be isotope-selective. Good isotope selectivity is especially important for loading the rarer isotopes such as $^{171}Yb^{+}$(14% natural abundance) which provides magnetic-field insensitive $F = 0$ and $F = 1$ ground-state hyperfine qubit states.

A method for high-efficiency isotope-selective loading of ions from a magneto-optical atom trap is described in Section 4.3 and in Appendix C. Building on this work, a vacuum system was designed to combine the ion trap/optical resonator assembly described in the previous section with a magneto-optical atom trap. Remarkably, this could be accomplished without sacrificing access to the trapped ions or affecting the optical resonator.

7.3.5.1 Yb Source

Operating a magneto-optical atom trap requires a relatively bright source of atoms. For atoms with low vapor pressures such as Yb, thermal ovens are typically used which achieve equilibrium between the metal vapor and the oven body and release the vapor towards the experimental region through a small opening.

To avoid degrading the vacuum in the experimental region by contaminants released from the heated oven, the effusive source is typically placed at a distance from the main experimental chamber with several stages of differential pumping. To counter the decay of the oven flux away from the source, cold-atom experiments commonly use large ovens in combination with a counter-propagating laser beam to slow down the atoms before capturing them in an atom trap. To compensate for the changing Doppler shift experienced by the slowing atoms, a spatially-varying magnetic field produced by a 'Zeeman slower' [PM82] is used. Although this Zeeman slower method has been successfully used for Yb [HTK+99], it presents several obstacles:

1. Due to high saturation intensity of the $^1S_0 - ^1P_1$ transition, high laser power is needed for slowing (>50 mW) which is not easily obtainable with laser diodes

2. The absolute efficiency of a Zeeman slower system is fairly low, necessitating a large oven and extensive differential pumping for maintaining ultrahigh vacuum in the experimental region.

3. In the typical counter-propagating configuration, the entrance vacuum window for the slowing beam is exposed to the Yb atom flux and needs to be heated to high temperature (>200°C) to avoid a buildup of Yb. A thin Yb film could also be used inside the vacuum chamber to stop the atom flux and reflect light inside the vacuum chamber, in which case the low reflectivity of Yb at 399nm doubles the power requirements for the slowing laser.

With typical lifetimes of trapped ions measured in minutes, ion traps allow a different approach: an effusive oven with a small thermal mass can be placed close to the experimental region and operated in pulsed mode. Due to its simplicity, this approach was adopted for the ion-resonator experiment presented in this thesis.

An Yb effusion oven is formed by a spot-welded pouch of Ta foil containing ≈ 2 g of Yb shavings as described in [Gri11]. The pouch is resistively heated to produce thermal Yb vapor which leaves through a ≈ 0.5 mm-diameter hole punched with a steel pin. The oven is held (33 ± 2) mm from the ion trap by four 1" long, 0.030" diameter 304 stainless steel wires passed through a MACOR retaining plate (Figure 7-36). With its favorable ratio of electrical to thermal conductivity, the steel doubles as a heat transport buffer.

To provide the electrical connection for heating the oven, the steel rods are spot-welded to 1/32" diameter Cu wires via of low-power two-pin electrical feedthrough (EFT0023032 from Kurt J. Lesker, PA). Since spot-welds between Cu and steel are unreliable, a thin Ta foil was used as a buffer between the two materials.

To shield the experimental setup from the direct heat flux of the oven, the oven body is covered with a cap made of welded pieces of 304 stainless steel anchored to a MACOR retaining plate. The MACOR plate is anchored to the vacuum chamber using a 5 degree-of-freedom assembly. Heat sinking of the oven is provided by two 1.4" long, 0.125" diameter molybdenum rods.

To direct the flux of contaminants outgassing from the heated oven away from the experimental region, the cavity formed by the MACOR plate and the steel cap is vented through a 0.35"-diameter opening in the MACOR plate. The oven flux exits through stainless steel cap via a 1.5 mm diameter opening located 3.5 mm - 4.5 mm from the Ta pouch. Further vacuum venting is provided through a 4mm gap in front of the oven cap.

The oven flux is collimated by a 1.9 mm$\times$2.5 mm rectangular groove cut into the chip holder described in Section 7.3.3.7. The collimation groove is capped on the top side with a baffle made of 0.17 mm thick 304 stainless sheet metal. Additional baffles

block all direct lines of sight from the oven cap opening to the surfaces of the optical resonator mirrors.

To protect the surface of the ion trap chip from the oven flux, the oven beam is directed at an angle of 12.7° relative to the chip surface (Figure 7-36) with one edge of the chip acting as a shadow baffle. At the design position of the oven opening, the chip edge blocks any direct oven flux at distances less than 390 μm from the trap surface. Additionally, the geometry of the precision-milled chip holder blocks all direct oven flux at distances less than 190 μm from the chip surface, ensuring good vacuum in the ion trapping region 135 μm above the trap surface.

The relative Yb flux as a function of oven current was measured via photoionization of Yb atoms using the two-step procedure described in Section 8.1. The ionized Yb atoms are detected using an avalanche ion detector (Magnum 5901 Channeltron from Burle Corporation, PA). The dependence of the detected ion flux on the oven current is shown on Figure 7-34. The detected ions are verified to be Yb by blocking the injecting beam into the 399 nm slave laser diode and observing a decrease in the detected ion counts to below 200/s. The sharp increase of Yb flux with the power dissipated by the oven is consistent with an Arrhenius behavior of the vapor pressure as a function of oven temperature[HD64].

The spatial profile of the oven flux was recorded by scanning a focused 399 nm laser beam resonant with the $^1S_0$-$^1P_1$ transition in Yb (Figure 7-35) across the experimental region. The excitation beam was pointed along the x-axis, directed to the center of the ion trap chip and scanned along the y-axis while recording the atom fluorescence with an imaging system pointed along the z-axis. The majority of the Yb oven flux is seen to be located $(2-5)$ mm above the ion traping region (located at $x = y = 0$) - a configuration suitable for operating a magneto-optical atom trap as described in Section 7.3.5.2.

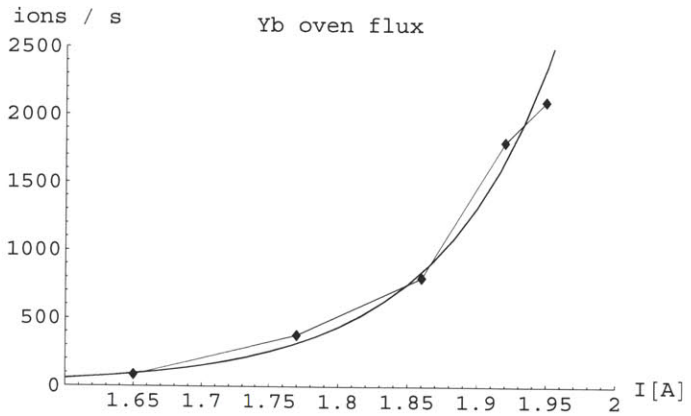

Figure 7-34: Yb atom flux (Φ) from the efusive oven measured by detection of Yb^+ ions following two-step photoionization as a function of the oven current I. The fit is to a linearized Arrhenius model $\Phi = Ae^{BI^2}$.

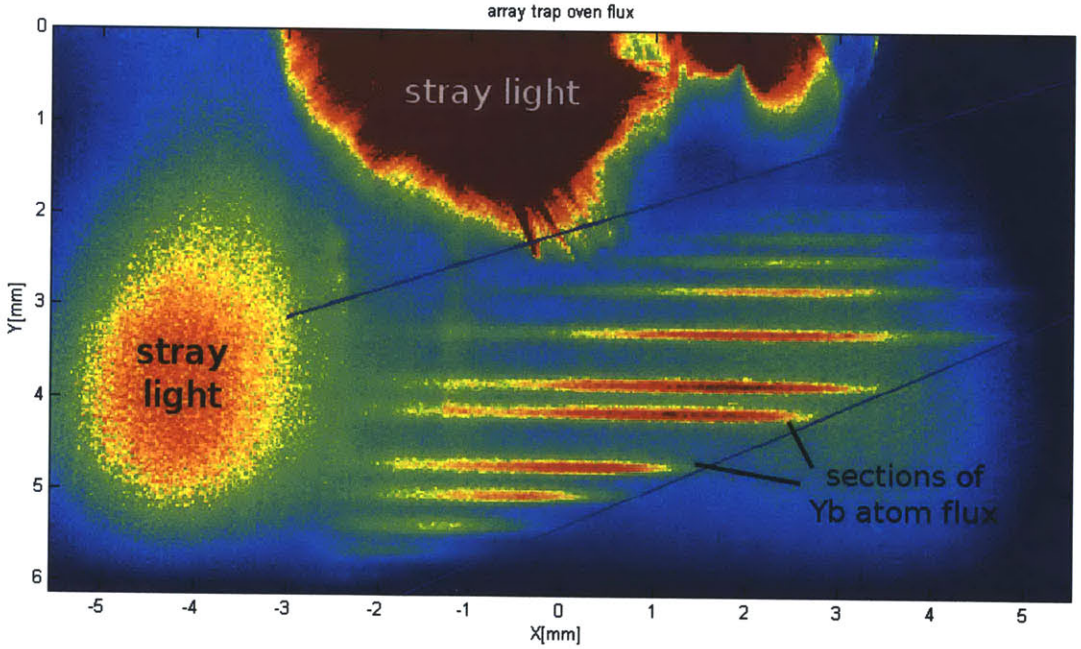

Figure 7-35: Yb atom flux from the effusive oven recorded via fluorescence of atoms excited via a focused $^1S_0 - ^1P_1$ 399 nm laser beam. The picture shown is the sum of pictures obtained at different excitation beam positions. The center of the ion trap chip corresponds to $x = y = 0$ with the z-axis of the chip pointing into the drawing. The thin straight lines are linear fits to the edges of the oven flux.

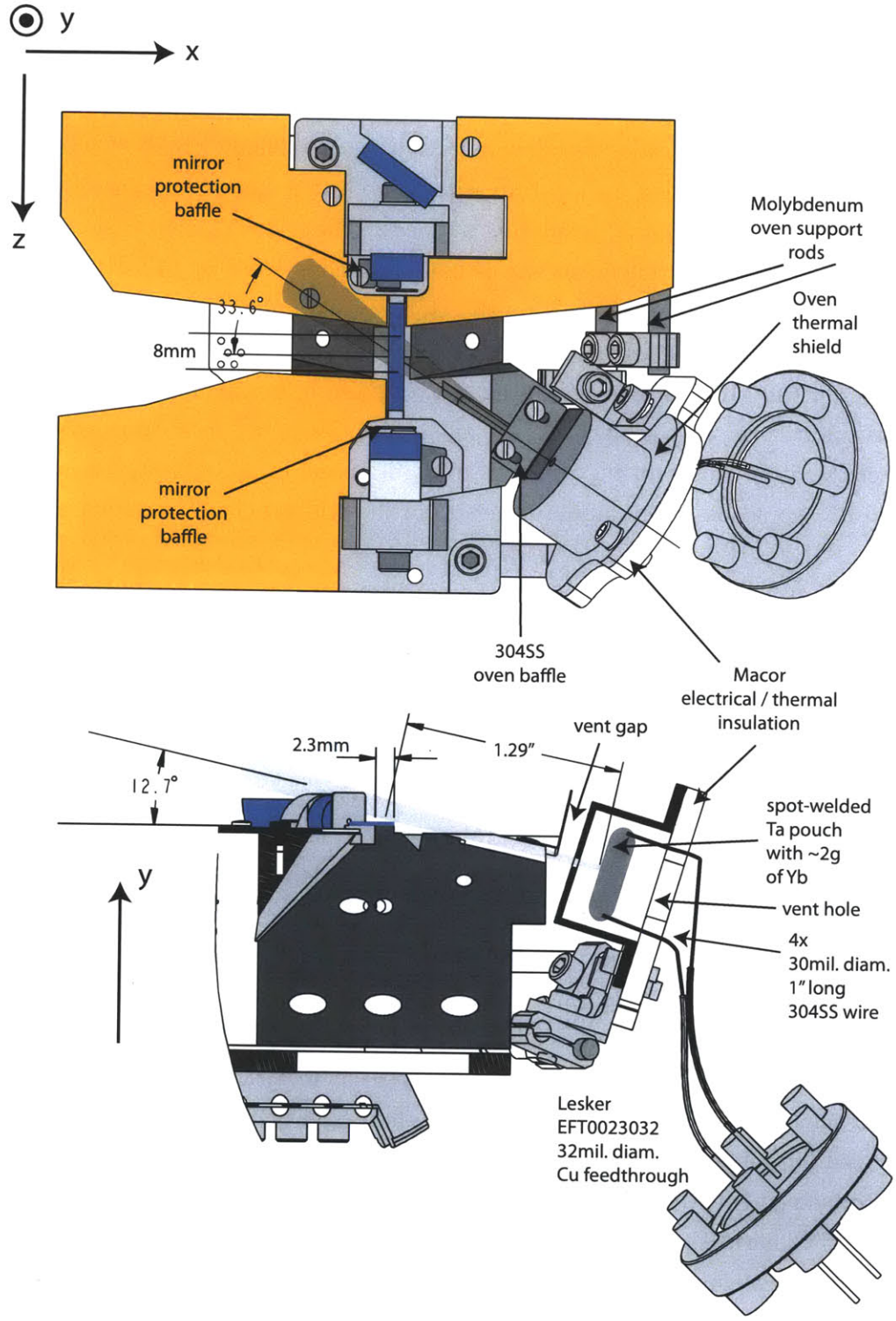

Figure 7-36: Design of the effusive Yb oven source: overview

7.3.5.2 Magneto-Optical Atom Trap

In cold atom experiments employing chip traps, a magneto-optical trap (MOT) is commonly formed close to the chip surface by retro-reflecting the MOT beams off the reflective chip. Unfortunately, the fabrication process chosen for producing our ion trap employs gold electrodes with low reflectivity at the 399nm Yb MOT wavelength. Additionally, illuminating an ion trap with blue light is known to cause buildup of stray charge on the residual insulating surfaces. These effects were observed in the ion-atom collision experiment and investigated in more detail by [HBHB10].

An alternative approach is to form the MOT several millimeters above the ion trap chip (Figure 7-37). The trapped atoms could then be transported to the ion trap by turning off the MOT beams and using a brief pulse of resonant light to launch the atoms towards the trap surface. At a launch velocities of ≈ 3 m/s, transverse expansion of the atom cloud during the time of flight at the Doppler-limited temperature of 680 μK would be comparable to the size of the original cloud as shown on Figure 7-40.

As the atoms transit the mode of the optical resonator, they could be ionized by a combination of 399 nm light and strong 370 nm light built up inside the resonator. With mW-scale input to our resonator with finese of 3,500, intracavity intensities of 10 kW/cm^2 can be reached; using the cross-section for ionization of the Yb $^1P_1$ state at 370 nm from Appendix C and assuming $^1P_1$ state fraction under excitation by 399 nm light of 1/3 , a Yb atom inside the resonator mode could then be ionized in < 50 μs. Comparing this to the $\sim$ 10 μs atom transit time through the resonator mode, ionization efficiencies of order 0.1 should be achievable.

The flux of MOT atoms in the ion trapping region is limited by the MOT atom number and its reloading rate. With sufficient laser power and at high oven fluxes, 10^5 Yb atoms could be cycled in $\sim$100ms. Accounting for the limited spatial overlap of a the MOT cloud with the resonator mode, > 100 cold, isotope-selected ions could be produced in the ion trapping region every second. With electron-recoil energies due to photoionization much smaller than the depth of the ion trap, most of the produced ions should be captured by the ion trap.

Producing a Yb MOT requires a considerable magnetic field gradient (> 30 G/cm, ideally 45 G/cm). To achieve such gradients, custom-wound magnetic field coils were placed around a compact multiport vacuum chamber (MCF600-SS-200408-A sphercal square from Kimball Physics, NH, Figure 7-38). The MOT coils are designed to maximize gradient while not occluding optical access to the ions (Figure 7-38).

With a constant current density J in both MOT coils, the predicted axial field

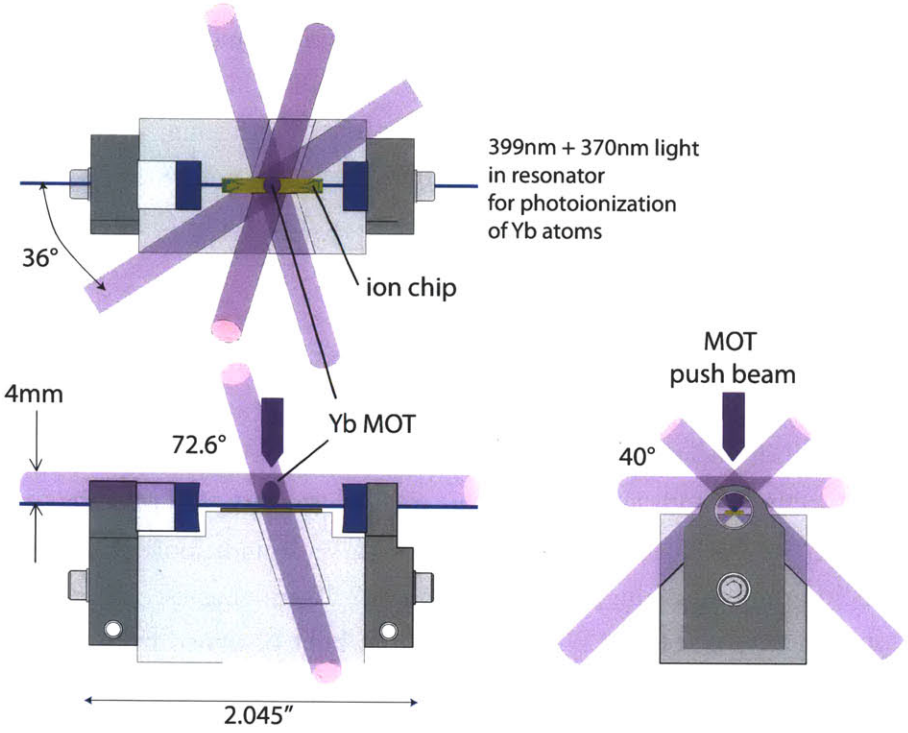

Figure 7-37: Geometry of Yb magneto-optical trap for loading of the ion trap array.

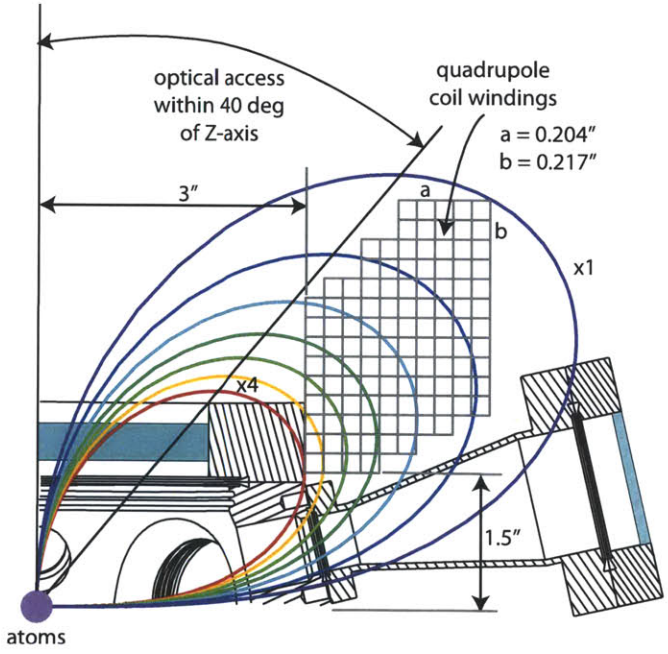

Figure 7-38: Design of the quadrupole field coils for the magneto-optical trap.

gradient at the atom location is $dB_z/dz = 2f\mu_0 J$ with $f = 0.114$.

To provide adequate cooling, the coils are wound using hollow oxygen-free Cu wire (.1875" × .1875" square cross-section with 1/16" diameter round inner bore). The coil tube was produced by Small Tube Products (Altoona, PA) and forwarded to S&W Wire Company (Cranberry TWP., PA) for insulation with a fiberglass resin, resulting in a .204" × .204" final wire cross-section. Including the gaps produced by the winding of the coils, the effective cross-section per turn is increased .204" × .217".

The coils are wound on a custom mandrel using a lathe and joined together using Cotronics Duralco NM 25-1 thermally conductive epoxy. A thermocouple is embedded into one of the coils to allow the implementation of a safety interlock to prevent overheating. A temperature rise of 2.4 K is measured using this thermocouple with with 43 A flowing through the coils cooled with water with 100 psi inlet pressure.

To operate the MOT, 46.8 A is sent through the quadrupole coils, producing a predicted field gradient at the MOT location of 47 G/cm. Laser cooling and trapping is accomplished with a total of 2.2 mW of 399nm light obtained from a 30 mW near-UV laser diode (NDHV310ACAE1 from Nichia Corporation, Japan). To compensate for the high saturation intensity of the $^1S_0$-$^1P_1$ transition in Yb ($I_s = 59.3$ mW/cm^2, [DBBN05]), the three MOT cooling beams are collimated with tight 2.1 mm-waists and recylcled by retro-reflecting them after passing through $\lambda/4$ waveplates. Accounting for losses in various optics, about 3.5mW of 399nm light enters the chamber and is incident on the atoms, resulting in an on-resonance saturation parameter $s \approx 0.8$.

The MOT is operated at point of maximal total atom fluorescence. At similar light intensity, this was previously determined (Section 4.2.3) to occur at laser detuning relative to resonance of $\delta \approx -\Gamma/2$ with $\Gamma = 2\pi \times 28.8$ MHz the natural linewidth of the $^1S_0 - ^1P_1$ transition in Yb [DBBN05]. Following (2.6), at this detuning each MOT atom can be expected to scatter $\Gamma_{sc} = 2.6 \times 10^7$ photons/s.

By recording the total fluorescence emitted by the MOT with a calibrated imaging setup, it is possible to obtain an estimate of the number of atoms in the MOT. The atom fluorescence is imaged through a 2.75" CF fused silica vacuum viewport (UKAEA) as shown on Figure 7-39. The image is recorded using an interline CCD camera (AVT F-146 Guppy from Allied Vision Technologies) with 4.65 μm pixels whose sensitivity was calibrated using a Gaussian 399nm laser beam with a known power. To avoid saturating the camera, the beam is passed through calibrated absorptive neutral density filters, obtaining 10.6 ± 0.5 photons / image count. An image of a MOT recorded using this setup is shown on Figure 7-40.

To determine the number of trapped atoms, images of the MOT were taken with

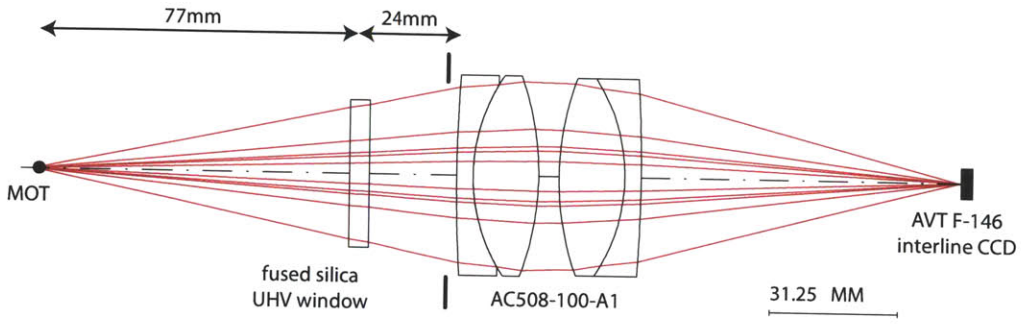

Figure 7-39: Setup for recording MOT fluorescence: The MOT is imaged through a 2.75" CF fused silica viewport using two back-to-back cemented achromatic doublets (AC508-100-A1 from Thorlabs) operating at infinite conjugate ratio. The 2"-diameter achromats are positioned 11.5cm from the ions and operate at or above $f/\# = 4.6$. The transmission of the achromats at the MOT wavelength of 399 nm was measured independently as 85%.

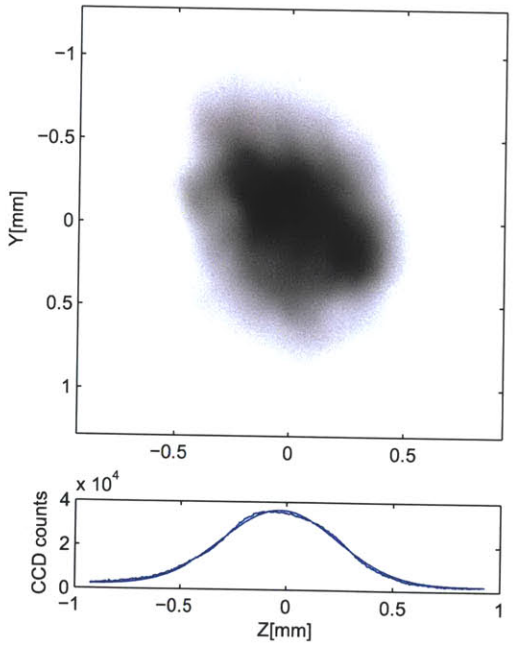

Figure 7-40: Image of $\approx 80 \times 10^3$ ^{172}Yb atoms in a MOT 2.6 mm above the ion chip surface. The fluorescence produced by laser cooling of atoms is collected with a $F/\# = 7.2$ imaging setup during and recorded on an interline CCD camera. The bottom panel shows the integrated pixel values together with a Gaussian fit yielding a r.m.s. diameter $w_{MOT} = (600 \pm 100)$ μm.

exposures of $(5-90)$ ms. To account for the effect of aberrations on the light gathering, the imaging system was apertured using fixed irises close to the conjugate plane (Figure 7-39). The results for $f/\# = 4.6-14.5$ are shown on Figure 7-41. Fitting the recorded atom fluorescence to the fraction of the solid angle subtended by the imaging setup for $f/\# > 7$, gives an estimate of the total MOT fluorescence of 2×10^{12} photons/s. Using the predicted fluorescence emitted by each atom of $\Gamma_{sc} = 2.6 \times 10^7$ photons/s, this yields an estimate of the total MOT atom number as $N_{MOT} \approx 8 \times 10^4$, accurate to within a factor of three, limited by uncertainties in light gathering, laser power and laser detuning (in that order).

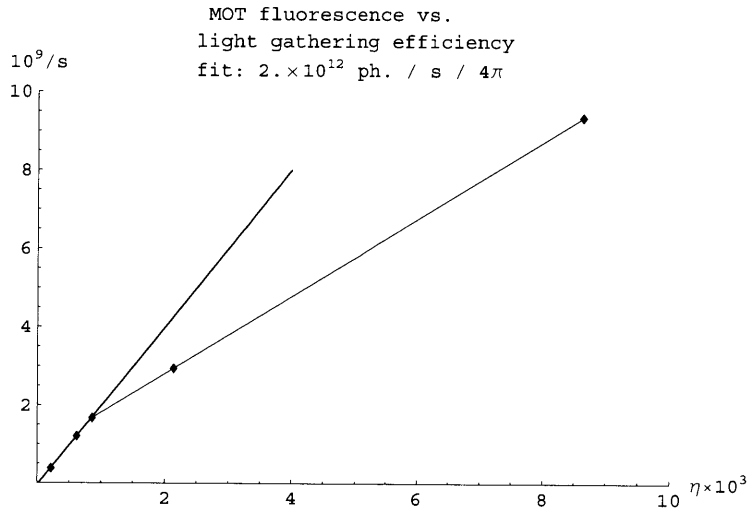

Figure 7-41: Gathered MOT fluorescence as a function of the fraction of the solid angle subtended by the imaging setup.

To produce Yb^+ ions, $P = 2.6$ mW of 370nm laser light is focused to a waist $w \ll w_{MOT}$ inside the MOT. As described in Appendix C, ion production by photoionization from the excited $^1P_1$ state is expected to scale linearily with the beam intensity and the number of atoms present inside the beam:

$$\frac{dN_{ion}}{dt} = p_e \frac{2P}{\pi w^2} \frac{\sigma_i}{hc/\lambda} \int e^{-2\left(x^2+y^2\right)/w^2} n\left(r\right) d^3r$$

with p_e is the $^1P_1$ state fraction, $\sigma_i \approx (2-8) \times 10^{-18}$ cm^2 is the ionization cross-section of the $^1P_1$ state of Yb determined in Appendix C and $n\left(r\right)$ is the MOT density. For a beam focused tightly close to the MOT center this simplifies to

$$\frac{dN_i}{dt} \approx p_e \frac{N_{MOT}}{(\pi/2)^{3/2}} \frac{\sigma_i}{w_{MOT}^2} \frac{P}{hc/\lambda} p_i$$

Under the experimental conditions described above, $p_e \approx 0.15$, yielding a predicted ion production rate on the order of 3×10^4 ions/s.

The produced ions were detected using a Channeltron ion detector (Magnum 5901 from Burle, PA) biased to -2 kV. With the 370 nm beam on, $(31 \pm 1) \times 10^3$ counts/s were detected above a background of 6×10^3 counts/s dominated by the ion pump. With the MOT beams detuned blue relative to resonance the detected ion flux drops to $(2 \pm 1) \times 10^3$ counts/s above the background, indicating that most of the produced ions originate from the cold MOT atoms.

The rough agreement between the predicted ion production rate and the observed Channeltron count rate also indicates that the Channeltron detection efficiency for ions produced close to the trap is of order unity.

Chapter 8

Ion Trap Array in an Optical Cavity: Demonstration

To demonstrate that the system presented in Chapter 7 can indeed be used as an ion-photon interface, it needs demonstrate a number of milestones.

First, Yb^+ ions need to be produced and loaded into the array of ion traps. Production of Yb^+ ions close to the center of the RF trap is demonstrated in Section 7.3.5 using two-stage ionization of thermal Yb atoms inside the experimental resonator. Surprisingly high loading rates were obtained without using the magneto-optical trap as called for in Section 7.3.5.

Trapping of the Yb^+ ions in the array trap is demonstrated in Section 8.2. By using the same 369.5 nm atom light inside the optical resonator that is used for photoionization to Doppler-cool the loaded ions, Section 8.2 also demonstrates an initial coupling of ions to the optical resonator.

To allow precise control over the ions' motion and reach maximal collective coupling, it is desireable that the ion loading process be isotope-selective. Loading of isotopically pure ion samples is demonstrated in Section 8.3 using a two-stage cross-beam resonant photoionization process.

To allow quantum manipulations of individual ion chains, it is desireable that the number of ions in each chain be fixed. Deterministic loading of the individual sub-traps in the array structure is demonstrated in Section 8.4 by taking advantage of the ion-ion Coulomb repulsion to suppress the fluctuations in the number of ions loaded into the each sub-trap.

Finally, the ions need to be coupled to the resonator. A quantitative evaluation of the coupling of one ion to the resonator mode is presented in Section 8.5. The measured coupling matches the value predicted from the resonator parameters, im-

plying a maximal coupling efficiency between a single Yb^+ ion and the resonator mode of $\eta = 2.1\%$. Methods to achieve higher coupling using collective effects will be discussed in Chapter 9.

8.1 Resonator-Aided Photoionization

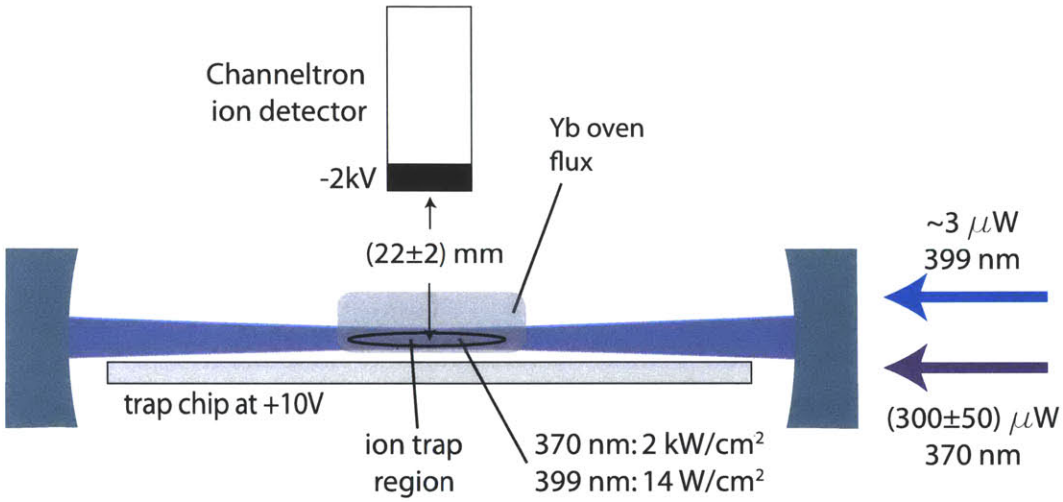

Figure 8-1: Production of Yb^+ ions via resonator-enhanced two-photon ionization of thermal atoms from an effusive oven

To demonstrate the initial operation of the ion trap array, it is sufficient to trap dozens of Yb ions with a natural isotope distribution. Although the MOT loading procedure described in Section 7.3.5.2 seemed complicated for this relatively simple task, a similar technique involving transport of atoms appeared necessary given that the ion trapping region was purposefully shielded from the direct oven flux.

Nonetheless, a high-finesse optical cavity resonant with both 370 nm and 399 nm light is a nearly optimal tool for photoionization of Yb^+ using the process described in Section 4.3. If, by chance, a significant flux of Yb atoms still existed in the ion trapping region, the ion trap could be efficiently loaded by building up the light needed for the two-step photoionization of Yb (Section 4.3) inside the resonator mode (Figure 8-1).

To explore this possibility, an external-cavity grating laser was stabilized within 50 MHz of the 399 nm $^1S_0$-$^1P_1$ transition in ^{172}Yb using the DAVLL method described in Section 4.1. The offset of the TEM_{00} mode of the resonant cavity relative to the

399 nm laser was measured via the Pound-Drever-Hall scheme and nulled by feedback to the piezo-electric transducer in the experimental resonator assembly.

With the measured resonator finesse at 399 nm of $\mathcal{F}_{399} = 310 \pm 30$, and the waist of the TEM_{00} mode of $w = 40$ μm, the ~ 2 μW of incident 399 nm light used for stabilizing the experimental resonator results in a the peak 399 nm light intensity in the TEM_{00} mode of the optical resonator of $I_{399} \approx 14$ W/cm^2. This corresponds to on-resonance atomic saturation parameter of $s_{399} = 210$ (accurate to within a factor of 2), which was sufficient to broaden the $^1S_0$-$^1P_1$ transition so as to allow significant ($p_e > 5\%$) excitation of the Doppler-broadened Yb atoms into the $^1P_1$ state.

Ionization from the excited $^1P_1$ state was accomplished by stabilizing a 370 nm external-cavity grating diode laser relative to the experimental resonator using the Pound-Drever-Hall method. At the time of this measurement, the resonator finesse at 370 nm was measured by the ringdown method [Gri11] as $\mathcal{F} = 5,900 \pm 500$, corresponding to a linewidth of 1 MHz. To allow stable locking of the 370 nm laser to this narrow cavity resonance, a high-frequency feedback loop to the laser diode drive current with ~ 200 kHz of bandwidth, was implemented.

With (300 ± 50) μW of incident 370 nm light, (4.5 ± 1.0) μW of light was transmitted through the resonator. Using the transmission coefficient specified by the mirror coating supplier (Section 7.3.2) yields an estimate of the peak intensity of the ionizing 370 nm inside the resonator as $I_{370} \approx 2.2$ kW/cm^2.

The ions produced by photoionization of Yb atoms were detected using a Channeltron detector (Magnum 5901 from Burle, Inc., PA). To improve the collection of ions from the region close to the trap surface, the ion trap electrodes were biased to +10 V (Figure 8-1).

With both 370 nm and 399 nm light present in the resonator and the oven running at 1.95 A, $\approx 10^3$ counts/s were detected by the Channeltron. A decrease of the detected counts to 1500/s when either of the two laser beams turned off indicates that the detected ions are indeed Yb^+. With the results from Section 7.3.5.2 indicating an order-unity Channeltron detection efficiency, this implies a production on the order of 10^3 Yb^+ ions/s inside the resonator mode.

Given that the oven design from Section 7.3.5.1 blocks a direct line of sight between the effusive source and the region at distances above the trap of less than 190 μm, the high production of Yb^+ ions within the resonator mode is somewhat surprising, One explanation is that Yb atoms are reflecting at a grazing incidence off the steel walls of the collimation groove in the chip holder 7.3.5.1. Such a reflection was observed in the earlier ion-atom collision experiment where Yb atoms impacting a Cu baffle were

reflected to coat the opposite wall of the vacuum chamber located approximately 1 cm away.

8.2 Initial Trap Loading

Owing to the alignment of the optical resonator mode with the ion trap described in Section 7.3.2, and the low energy of thermal atoms relative to the depth of the ion trap, the Yb^+ ions produced by resonator-aided photoionization in the previous section should be easily trapped in the ion trap array.

The trapping of ions is made easier by Doppler cooling on the 369.5nm $^2S_{1/2}$-$^2P_{1/2}$ transition as described in Section 4.1. Fortuitously, this can be accomplished using the same laser used for photoionization of Yb atoms from the $^1P_1$ state. At the high intensities ($I_{370} \approx 2.2$ kW/cm^2) used for photoionization of Yb atoms, the $^2S_{1/2}$-$^2P_{1/2}$ ion transition is heavily broadened by saturation, reaching widths on the order of $\Gamma' = 2\pi \times 1$ GHz. Nonetheless, Doppler cooling remains possible at larger detunings δ from the ion resonance ($\delta \sim \Gamma'/2 = 500$ MHz), with an increase in the corresponding Doppler-limited temperature as $T'_D \sim \hbar\Gamma'$.

To empty the $^2D_{3/2}$ state populated during laser cooling of Yb^+, approximately 500 μW of 935 nm laser light is sent through the resonator mirrors (largely transparent at this wavelength). The 935 nm light is directed along the resonator axis and focused to a 50 μm-waist located in the middle of the resonator.

The ion trap array is operated at 16.260 MHz with an RF voltage of $V_{RF,o} = (125 \pm 10)$V applied to the trap RF electrodes, together with a DC voltage of $V_Q \approx -4$ V.

Figure 8-2 shows Yb^+ ions loaded into the trap array and Doppler-cooled using the above setup.

Due to high laser power and high ion numbers ($\sim$ 1000) which result in RF-induced heating, the ions in Figure 8-2 remain above the Coulomb crystallization temperature. By reducing the ionization/cooling light intensity together with the detuning of the ion cooling light from the ion resonance, the trapped ions form a Coulomb crystal (Figure 8-3).

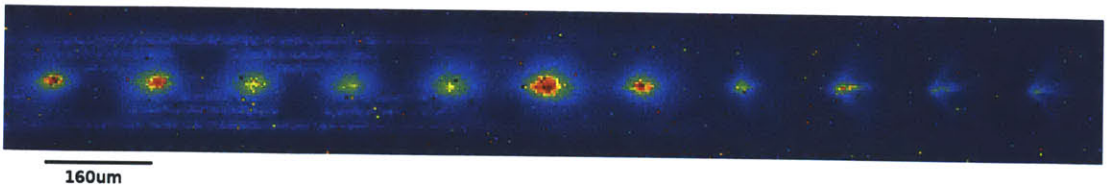

Figure 8-2: A Yb^+ ions produced by photoionization of thermal Yb, loaded into the ion trap array, and Doppler-cooled using 369.5 nm light in the TEM_{00} mode of the optical resonator. An additional 369.5 nm beam is illuminating the array electrode structure.

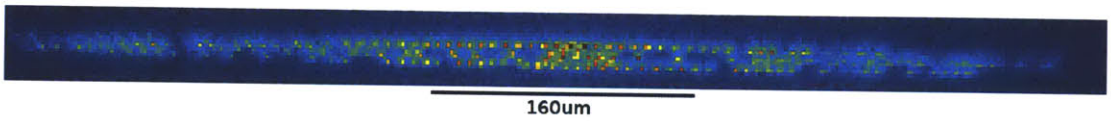

Figure 8-3: A Coulomb crystal of mixed Yb^+ isotopes trapped in the RF chip trap (no array potential applied).

8.3 Isotopic Purity

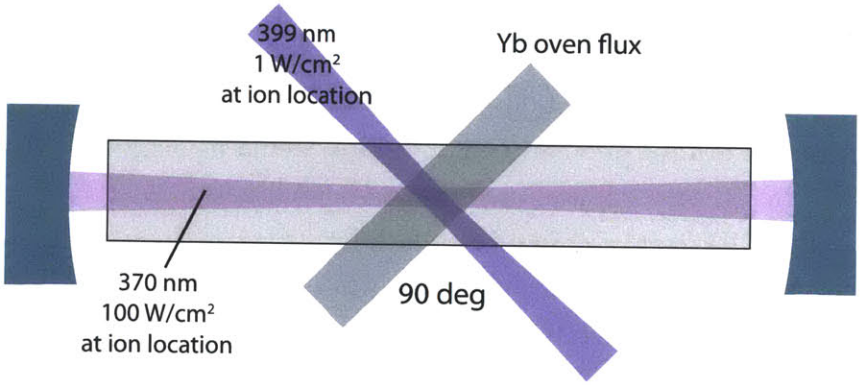

Figure 8-4: Setup for isotope-selective resonator-enhanced photoionization of Yb.

The isotope-selectivity of the trap loading method presented in the previous section is limited by the Doppler broadening of the thermal Yb atoms as well as the high intracavity intensity of the 399 nm light used for the resonant ionization step.

To improve the isotopic purity of the loaded ion samples, the 399 nm $S - P$ excitation light in the resonator was replaced with a 399 nm laser beam focused to a 90 μm $\times$ 1.1 mm-waist spot size at the location of the ion trap (Figure 8-4). By

directing the excitation beam in a direction perpendicular to the oven flux and using a decreased intensity of the 399 nm excitation light (up to 1 W/cm^2), most of the broadening can be removed, allowing the loading of isotopically pure ion chains, as shown on Figure 8-5.

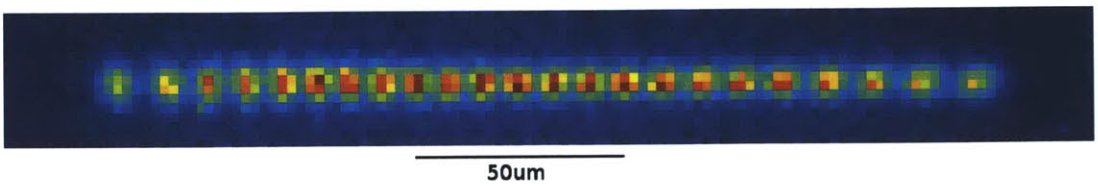

Figure 8-5: Isotopically pure chain of 22 $^{174}Yb^{+}$ ions held in the lithographic ion trap and laser-cooled via light stored in the optical resonator

8.4 Deterministic Loading of Ion Trap Array

For performing controlled quantum operations on the chains of ions stored in the sub-traps of the trap array, it is important that the properties of the loaded ion samples such as their vibrational frequencies, be consistent. For this, a fixed number of ions need to be loaded in each of the array sub-traps.

In neutral atom traps, atom-atom interactions have been used suppress the the fluctuations of the number of atoms loaded into trap arrays[WOS10]. Given the much stronger Coulomb interaction between ions, an even stronger suppression of fluctuations in the loading of an array of ion traps, would be expected. This was first demonstrated by [RBKD^{+}02] who used Coulomb repulsion to controlably split a pair of ions in a linear RF trap.

A similar control scheme was implemented in the current array trap. 22 $^{174}Yb^{+}$ ions were trapped in the RF trap (Figure 8-6). By applying only a weak axial confinement using the DC compensation electrodes, the ions were allowed to spread out between two sub-traps. Next, array potential was applied by ramping up the voltages applied to the three central sub-electrodes (Figure 7-6) from $V_c = V_i = V_0$ to $V_c = V_0 - 1.00V$, $V_i = V_0 + 0.78V$ over 111 ms. After splitting the ion chain in two, the potential ramp was reversed and the entire procedure repeated 48 times.

Histograms indicating the number of ions in each of the two sub-traps are shown on (Figure 8-6). Due to ion-ion repulsion, the variance of the number of ions in each of the two sub-traps is reduced more than 10$\times$ relative to that for uncorrelated atoms.

This loading method can be easily extended to semi-deterministically load a large

section of the trap array. The variation in the mean ion number at each site could be decreased by using the available DC electrodes to provide a box-like axial confinement so as to compress the initial ion chain and make its ion distribution less sensitive to small variations in the background DC potential.

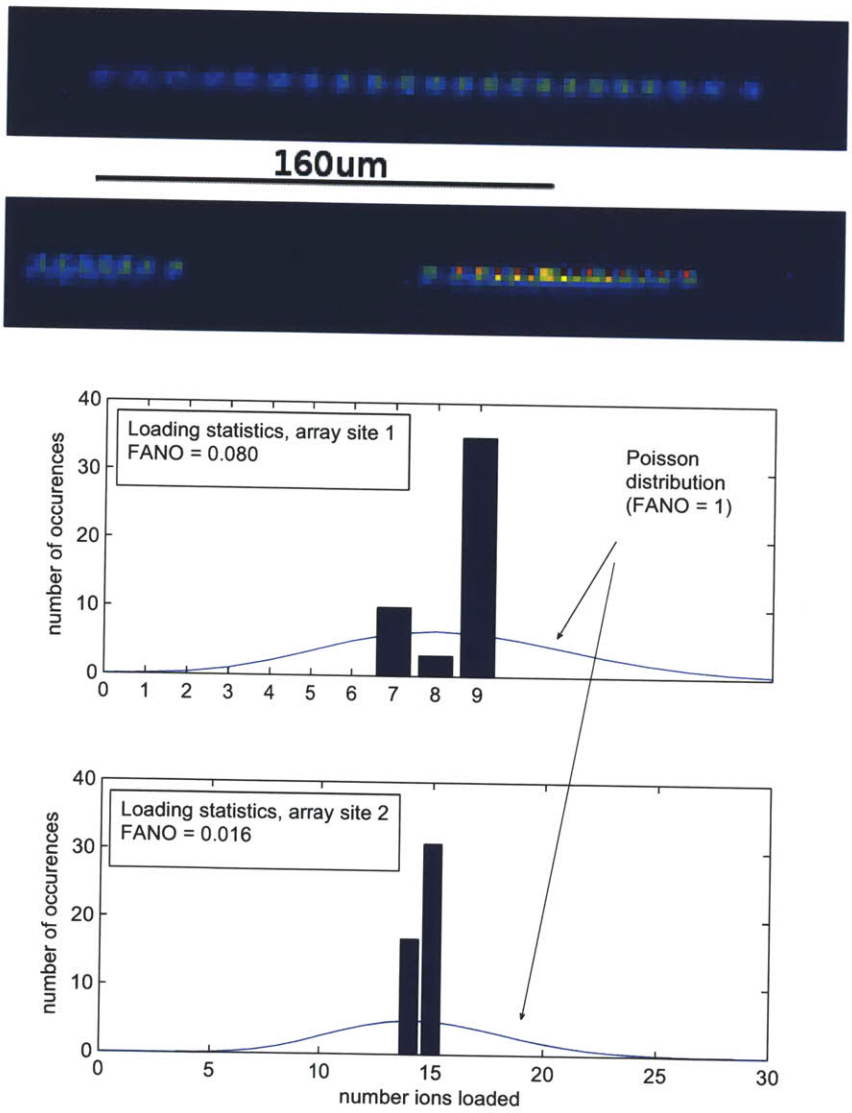

Figure 8-6: Controlled splitting of a chain of Yb ions by application of the array trap DC potential. The ratio of the variance of the number of ions loaded into each array sub-trap to that expected for a Poisson distribution with the same ion number is shown as the Fano parameter. Ion-ion repulsion results in a $> 10\times$ suppression of fluctuations in the number of ions loaded in each sub-trap.

8.5 Demonstration of Ion-Resonator Coupling

The main stated purpose of the present system is to couple ions to photons. In the limit of weak coupling relevant here, the ion-photon coupling efficiency introduced in Chapter 6 is equal to the ion-photon cooperativity i.e. the ratio of the number of photons emitted by the ions into the resonator mode to the number of photons emitted into free space.

The ion-atom cooperativity is experimentally evaluated in this section by using the optical resonator to collect the near-resonance fluorescence emitted by one trapped $^{174}Yb^{+}$ ion, as was previously done by [KLH+03] and [Lei09].

To observe the scattering of photons by the ion into the optical cavity, the laser which excites the ion has to be kept resonant with the cavity. The experimental setup used to accomplish this without introducing stray photons into the resonator mode is described in Section 8.5.1.

The results of the photon scattering measurement are presented and analyzed in Section 8.5.2. Accounting for the mechanisms which broaden the ion's fluorescence and decrease the rate of photon emission into the resonator, the measured ion-resonator agrees with the value predicted from the resonator parameters, implying a maximal coupling efficiency of a single ion to the resonator mode of 2.1%, limited by the resonator finesse.

8.5.1 Experimental Setup

The experimental setup for observing the coupling of ions stored in the ion trap array to the mode of the optical resonator is shown on Figure 8-7.

To load the ion trap, Yb atoms from the thermal oven are excited using a 399 nm laser beam resonant with the $^1S_0$ - $^1P_1$ transition in Yb, directed perpendicular to the oven flux as described in Section 7.3.5. Ionization from the Yb $^1P_1$ state is accomplished by shining approximately 200 μW of 370 nm light into the optical resonator, resonant with its TEM_{00} mode.

Either individual $^{174}Yb^{+}$ ions or small chains consisting of 1-20 $^{174}Yb^{+}$ ions are trapped inside the mode of the optical resonator and Doppler cooled with a 370 nm laser polarized parallel to the surface of the ion trap. To provide cooling of both transverse and axial vibrational modes of trapped ions, the Doppler cooling beam is directed at 80.7° relative to the resonator axis.

To reach the $^2S_{1/2} - ^2 P_{1/2}$ Doppler cooling transition at 369.5 nm, a Nichia NDU1113E 372 nm laser diode is placed in a Littrow external grating cavity and

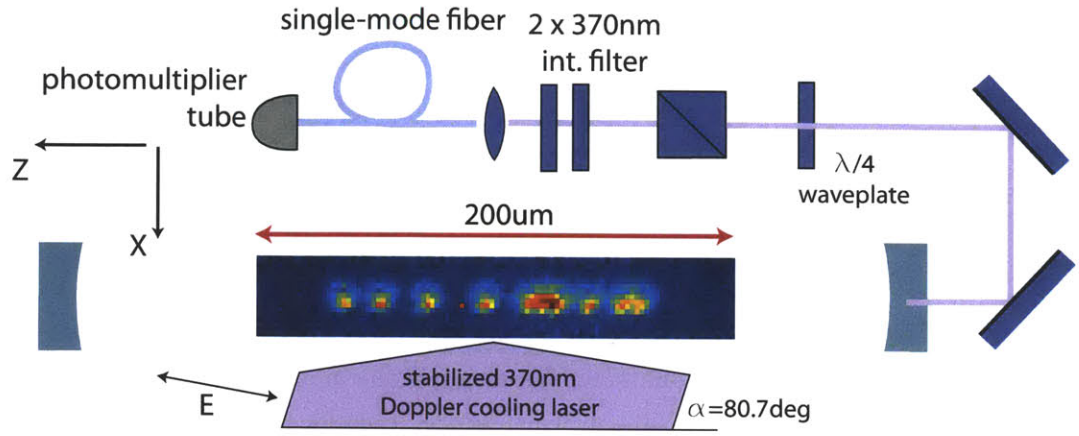

Figure 8-7: Experimental setup for observing coupling of ions to the optical resonator. A 370 nm laser is tuned to the red of the $^2S_{1/2} - ^2P_{1/2}$ transition in $^{174}Yb^+$ and used to cool a chain of $^{174}Yb^+$ ions placed inside the mode of a stabilized optical resonator. The resonator is stabilized relative to the laser and used to gather the light scattered by the ions. The gather light is polarization- and frequency-filtered, coupled to a single-mode fiber and recorded by a photon-counting photomultiplier.

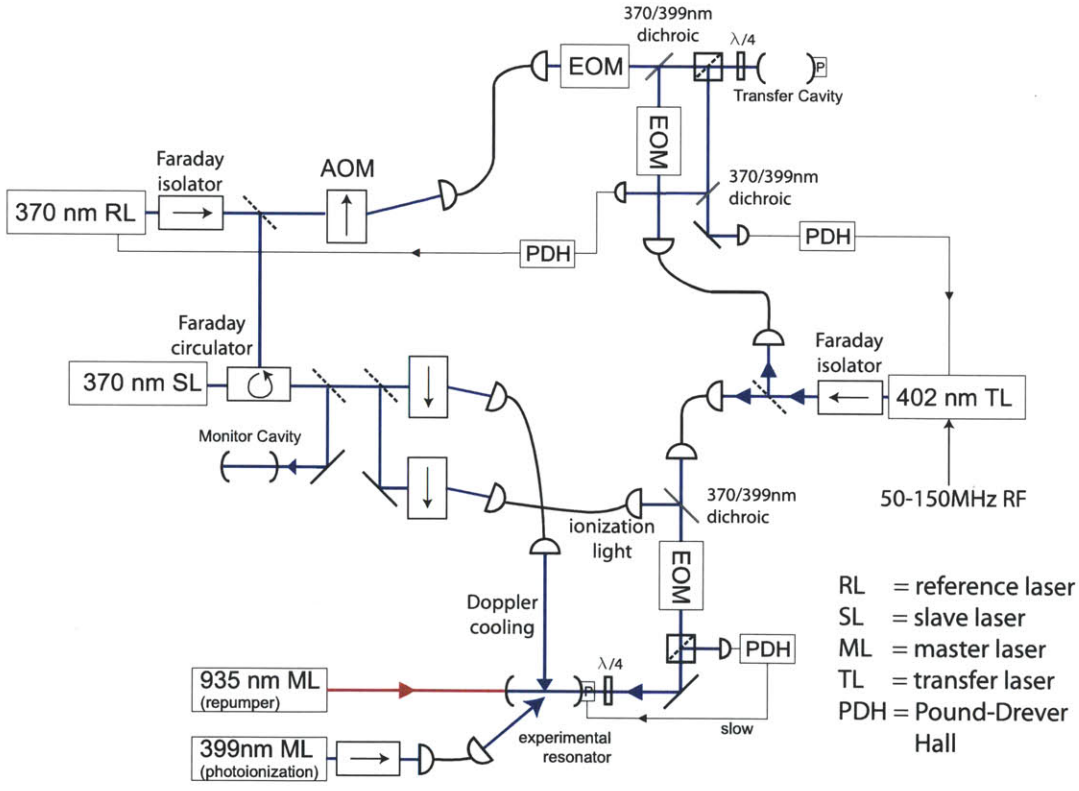

Figure 8-8: Laser setup used to cool and manipulate Yb^+ ions inside a stabilized optical resonator.

cooled to $-15°C$ in a hermetically sealed can (Appendix B). This reference laser is stabilized relative to an auxiliary Fabry-Perot resonator ("transfer cavity") using the Pound-Drever-Hall method (Figure 8-7). To provide sufficient light power for cooling longer ion chains, ≈ 500 μW of light from the reference laser is injected into a 'slave' 372nm laser diode (also cooled to $-15°C$ in a sealed can), causing the slave laser to phase-lock to the injected light. The optical injection lock is monitored with a confocal scanning Fabry-Perot cavity. After passing through an acousto-optic modulator (AOM) used for switching and intensity control, the output of the slave laser is coupled into a polarization-maintaining single-mode fiber. The fiber output of (750 ± 200) μW is focused to a 50 μm-waist at the ions' location.

To repump the $^{174}Yb^+$ ions from the metastable $^2D_{3/2}$ state (Figure 4-2), approximately 500 μW of 935 nm light produced by a stabilized external cavity diode laser is shined through the resonator mirrors (largely transparent at this wavelength) and focused to a 100 μm-waist at the ions' location.

The interaction of the ions with the resonator is observed by using the resonator to collect a part of the light scattered during the Doppler cooling of ions. The gathered photons are frequency-filtered using two interference filters, polarization-filtered in the σ^+/σ^- basis, spatially filtered using polarization-maintaining single-mode fiber and counted using a digital photomultiplier tube.

To stabilize the experimental resonator relative to the cooling laser without introducing stray 369.5 nm into the resonator mode, a scheme similar to the one previously used in the Vuletić group [Sim10], is employed (Figure 8-8). An auxiliary external grating cavity diode laser operating at 402 nm ("transfer laser") is stabilized relative to the transfer cavity using the Pound-Drever Hall scheme. The experimental cavity is stabilized relative to the transfer laser by feedback to a piezo transducer (also using the Pound-Drever-Hall scheme). To vary the detuning Δ of the TEM_{00} mode of the experimental cavity relative to the 370 nm Doppler cooling laser, the current fed into the transfer laser is modulated at $50-150$ MHz and the experimental cavity stabilized relative to the resulting red modulation sideband.

The stability of the experimental resonator relative to the Doppler cooling laser is evaluated by sending a weak ionization beam derived from the slave laser through the resonator and observing the transmission as a function of the laser-resonator detuning Δ (Figure 8-9). A Lorentzian fit to the transmission spectrum yields a full-width at half-maximum of (3.3 ± 0.6) MHz. The increase relative to the cavity linewidth of 1.8 MHz obtained by ringdown measurements (Section 7.3.2) can be explained by the laser linewidth together with instability of the transfer cavity system.

8.5.2 Photon Scattering into Resonator Mode

The photomultiplier signal recorded during the cooling of one ion at fixed laser detuning relative to the ion resonance is shown on Figure 8-10. As the frequency of the resonator TEM_{00} mode is scanned relative to the laser frequency, the resonator acts as a frequency analyzer for the fluorescence photons scattered by the ions.

The fluorescence spectrum shown on Figure 8-10 exhibits sidebands at the trap RF frequency of $\Omega/2\pi = 16.260$ MHz. These sidebands, originally observed in the fluorescence of an ion by [REB+00], can be explained by the effect of the ion's driven radial micromotion.

Viewed from the rest frame of an ion driven by the RF trap into sinusoidal micromotion with amplitude $\vec{A}$, the cooling laser acquires phase modulation as:

$$\vec{E}^L(t) = \mathrm{Re}\left(\vec{E}_0^L e^{i\omega_L t + iM\cos(\Omega t)}\right) \tag{8.1}$$

where ω_L is the laser frequency and $M = \vec{k}_L \cdot \vec{A}$ is the modulation index expressed in terms of the laser wavevector $\vec{k}_L$. Owing to the translational symmetry of the long ion trap chip, the dominant micromotion can be expected to be in the $x - y$ plane. Consequently, $\vec{k} \cdot \vec{A} \approx kA\cos\theta$, where $\theta = 80.7° - 90°$.

Equation (8.1) for the amplitude of the laser electric field as seen by the ion can be recast as a sum of sidebands with amplitudes given by the first-order Bessel functions $J_k(M)$:

$$\vec{E}^L(t) = \mathrm{Re}\left(\sum_{k=-\infty}^{\infty} \vec{E}_0^L J_k(M)\, e^{i\omega_L t + ik\Omega t}\right)$$

Since the resonator axis is perpendicular to the $x - y$ plane, the ions' emission into the resonator mode should remain unaffected by its micromotion and the ions' total emission will be equivalent to that from a stationary ion excited with a frequency-modulated laser beam with power spectrum given by

$$g(\omega) = \sum_{k=-\infty}^{\infty} \delta(\omega_L - k\Omega)\, J_m^2(M) \tag{8.2}$$

As described in Section 6.2.1, the coupling of an ion to a high-finesse resonator is limited to the $k = 0$ carrier component the micromotion spectrum, with the effective

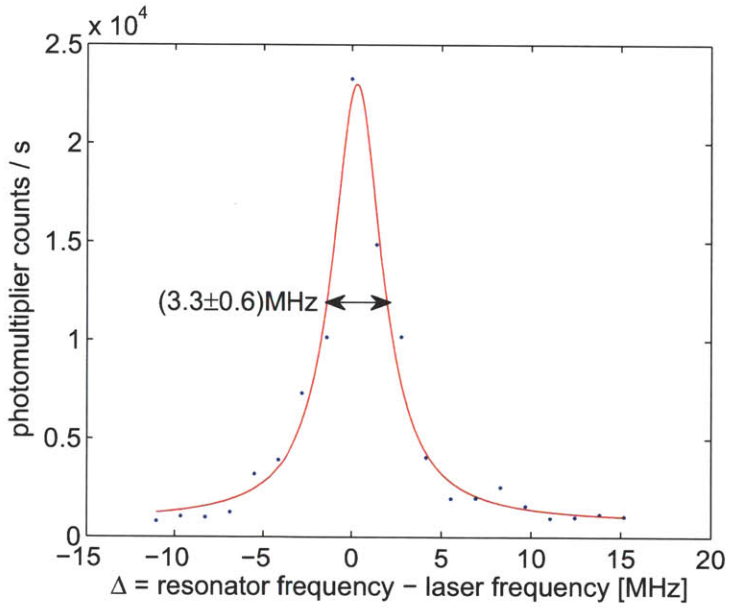

Figure 8-9: Transmission of a weak beam from the stabilized 370 nm probe laser through the experimental resonator.

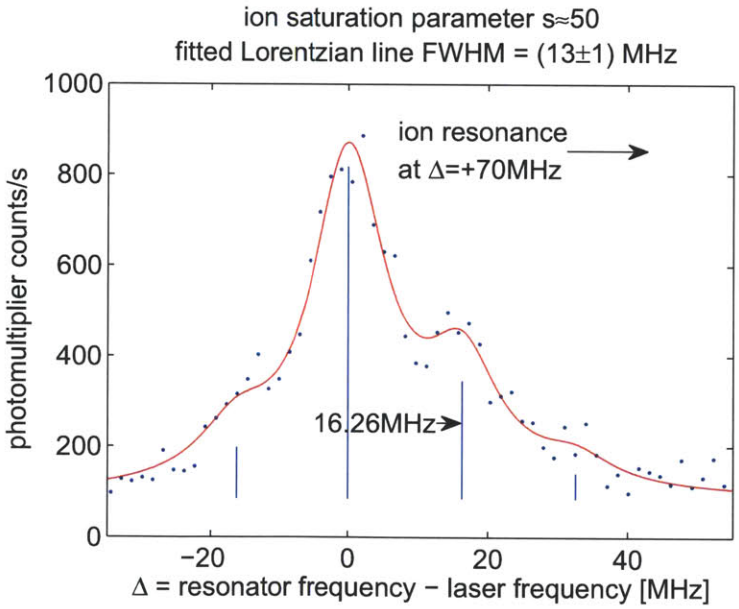

Figure 8-10: Spectrum of fluorescence from a single trapped ion collected via the TEM_{00} mode of the optical resonator. The x-axis shows the detuning of the resonator relative to the excitation laser which is detuned by $\delta \approx -70$ MHz to the red of the ion resonance. The fluorescence spectrum is fitted to a sum of homogeneously broadened Lorentzian peaks corresponding to a sum of homogeneously-broadened micromotion-induced sidebands.

cooperativity scaling as $J_0^2(M)$.

The sidebands in the fluorescence spectrum on Figure 8-10 are consistent with modulation index $M = (0.85 \pm 0.10)$ arising from RF-induced micromotion with amplitude $A = (50 \pm 5)$ nm perpendicular to the resonator axis. At the RF drive amplitudes used in our trap, such micromotion can arise from residual DC electric fields on the order of 20 V/m. Fields of this magnitude are commonly encountered in planar surface ion traps, especially as no careful effort was made to cancel them using the available DC compensation electrodes (in the present trap, a field of 15 V/m corresponds to a potential of 45 mV applied to the trap electrodes). Using the measurement described here as a sensitive tool to detect motional sidebands, it should be relatively straightforward to suppress the effective micromotion modulation index to $M < 0.4$, resulting in an effective ion-coupling of $> 90\%$ of the maximal value.

The asymmetry between the low- and high-frequency sidebands in the ion fluorescence spectrum can be explained by the effect of the laser detuning on the photon scattering rate. In terms of the detuning δ of the cooling laser relative to the ion resonance, the ratio of the photon scattering rates on the two first-order sidebands is given by (2.6) as:

$$\frac{\Gamma_{sc}(\delta+\Omega)}{\Gamma_{sc}(\delta-\Omega)} = \frac{(\Gamma'/2)^2 + (\delta-\Omega)^2}{(\Gamma'/2)^2 + (\delta+\Omega)^2}$$

where $\Gamma' = \sqrt{s+1}\Gamma$ is the saturation-broadened atomic linewidth with the saturation parameter s equal to the ratio of the laser intensity I_L and the saturation intensity $I_{sat} = \pi hc\Gamma/3\lambda^3 = 59.3$ mW/cm^2 of the $^2S_{1/2} - ^2P_{1/2}$ transition in Yb^+.

The ratio of the two first-order RF sidebands on Figure 8-10 of 2.3 ± 0.9, together with their known separation can be used to estimate the intensity of the Doppler cooling laser as seen by the ions as well as the detuning of this laser from the ion resonance. The broadening of the ion transition with increasing laser intensit bounds the cooling laser detuning and intensity as $|\delta| < 100$ MHz and $s < 100$. The observed ratio of sidebands is consistent with $s \approx 50$ and $\delta = -70$ MHz, corresponding to a total photon scattering rate from each ion of $\Gamma_{sc} \approx 3 \times 10^7$ photons/s.

In addition to acquiring sidebands due to RF micromotion, the ion's fluorescence spectrum is also broadened by inelastic scattering of laser photons. At high laser intensities used here, the inelastic components of the Mollow spectrum [Mol69] are predicted to be broadened to more than 30 MHz and hence appear as a low flat

background on the spectrum on Figure 8-10. The strength of the residual elastic component of the fluorescence spectrum is given by [Mol69] as:

$$g_{el} = \frac{(\Gamma/2)^2 + \delta^2}{(\Gamma'/2)^2 + \delta^2} = 0.6 \pm 0.2$$

This component is broadened from the original δ-function peak by inelastic scattering between the $m = -1/2$ and $m = +1/2$ ground-state Zeeman levels. The ratios of the different polarizations of scattered light and their spectral widths are summarized for the case of scattering between $J = 1/2$, $I = 0$ levels relevant to $^{174}Yb^+$ by [Ber08].

Just as for a classical emitter, the elastic component of the radiation scattered by the ion will be driven by the ion's dipole oscillating along the electric field of the incident light. With the polarization of the incident light aligned nearly parallel to the resonator axis, the emission of this radiation along the resonator axis will be weak. Instead, the light collected by the resonator can be expected to derive mostly from inelastic scattering on the σ^+ and σ^- Zeeman transitions.

The polarization filtering setup outside the optical resonator filters one of the two Zeeman components. With the incident light polarization nearly linear and without a strong magnetic field with Larmor frequency comparable to the photon scattering rate, the intensities of light scattered on the two σ-transitions - the one collected into the optical fiber and the one rejected - can be expected to be equal to within 20%.

When the ion is driven by linearily polarized π light, the $\sigma^{\pm}$ light will be scattered from its excited state in the form of wavepackets emitted at random times . The randomness of this emission process imparts the inelastic component of the fluorescence spectrum a linewidth on the order of the photon scattering rate. For the $J = 1/2$ - $J = 1/2$ transition studied here, a full analysis ([Ber08]) shows that the $\sigma^{\pm}$ inelastic components of the fluorescence will acquire a Lorentzian lineshape with full-width at half-maximum equal $\Gamma_{inel} = 2\Gamma_{sc}$.

Together with the laser-resonator Lorentzian linewidth from Figure 8-9, this inelastic broadening yields a total predicted width of each of the observed RF sidebands of 12.9 MHz, in agreement with the fit from Figure 8-10.

8.5.3 Estimate of Resonator Coupling

Based on the results from the previous section, Table 8.1 shows the budget for light collection from one ion.

maximal Yb^+ ion scattering rate	6×10^7 photons/s
finite laser intensity	0.5 ± 0.1
resonator's light gathering efficiency (η)	$(6.5 \pm 0.5) \times 10^{-2}$
branching ratio between ion's Zeeman states	1/3
resonator node/antinode average	0.5
two resonator outputs	0.5
elastic component of photon scattering	0.6 ± 0.2
spectral overlap with resonator mode	0.08 ± 0.02
fiber coupling efficiency	0.57 ± 0.02
photomultiplier quantum efficiency	0.19 ± 0.02
photomultiplier counts/s predicted	$(400 - 800)/s$
photomultiplier counts/s observed	$750/s$

Table 8.1: Summary of experimental photon collection by the resonator.

Given the linewidth of the $^2P_{1/2}$ state in $^{174}Yb^+$ of $\Gamma = 2\pi \times 19.6$ MHz [OHM+09], a fully saturated Yb^+ ion will emit $\Gamma/2 = 6 \times 10^7$ photons. At the laser intensity and detuning used in the present experiment, this total scattering rate is reduced as $\Gamma_{sc}/(\Gamma/2) = 0.5 \pm 0.1$.

At most a fraction $\eta_{max} = 24\mathcal{F}/\pi k^2 w^2$ of the scattered photons can be collected by the resonator. With the current value of the resonator finesse (Section 7.3.2) of $\mathcal{F} = 3600 \pm 300$, $\eta_{max} = 6 - 7\%$.

Without taking care to position the ion relative to the resonator's standing-wave mode, the ion's coupling is averaged between the nodes and antinodes of the standing wave, decreasing the photon collection by 50%. Another half of the collected photons is lost through the opposite port of the symmetric Fabry-Perot resonator.

When excited by linearly polarized light in the regime of weak magnetic field (Section 8.5.2), the scattered photons will be equally distributed between all three polarizations (σ^+, π and σ_-), only one of which will be collected by the resonator and filtered by the polarizer, corresponding to the branching ratio between the ion's Zeeman states of 1/3.

In the spectral domain, given the estimates for the detuning and intensity of the excitation light, the broad inelastic Mollow component is predicted to account for 0.4 ± 0.2 of the total ion fluorescence and will mostly not be collected by the narrow-band resonator. The gathering efficiency of the broadened elastic component shown on Figure 8-10 is determined by its spectral overlap integral with the 1.8 MHz wide Lorentzian cavity mode, evaluated as 0.08 ± 0.02.

In summary, accounting for the various loss and broadening mechanisms, the observed peak photomultiplier count rate of 750 counts/s is in good agreement with the predicted peak theoretical coupling efficiency of one ion to the resonator mode of $p_{coupling} \approx \eta \approx (6-7)\,\%$. In Yb^+, due to the branching ratio between the Zeeman and hyperfine levels, at most 2/3 of this couping can be realized in an experiment (e.g. for elastic scattering via an beam nearly parallel to the cavity operating with σ^+ polarization), corresponding to the maximal cooperativity in the present system of $\eta_{max} = (4.0-4.6)\%$.

It should be noted that the recorded number of photomultiplier counts is far smaller than the predicted rate $\eta_{max}\Gamma_{sc}$ of photon scattering into the resonator. A number of the factors that cause this difference, such as the presence of two resonator outputs, fiber coupling and PMT efficiencies, are external to the resonator. Consequently, although limiting for the rate at which information can be obtained from the ion-resonator system, they do not fundamentally limit the coupling of the ions to the resonator.

The same could not be said for the spectral overlap of the emitted photons with the cavity mode. This would clearly improve if the micromotion compensation was improved, laser power decreased, and proper (vertical) light polarization used to select the elastic scattering component.

An additional contribution to the linewidth of the ion's fluorescence, not seen at the level of this measurement, arises from the finite temperature of the ions. In scattering by ions at temperature T, the elastic scattering component will be Doppler-broadened in both absorption and emission, contributing a r.m.s. width to the elastic scattering component of

$$\Delta\nu_T = \sqrt{\frac{4k_BT}{m\lambda^2}} \tag{8.3}$$

which is comparable to the resonator linewidth (1.8 MHz) even at the Doppler limit of 470 μK for cooling Yb^+ on the $^2S_{1/2}$-$^2P_{1/2}$ transition. Lower ion temperatures could be reached by sub-Doppler cooling methods (Section 2.2.3) using Raman transition between ground hyperfine clock states in $^{171}Yb^+$.

Chapter 9

Ion Trap Array in an Optical Cavity: Perspectives

The hybrid ion trap array-resonator system presented in the previous chapters has a number of features desirable for quantum information processing, including:

1. relatively high coupling of a single ion to the mode of an optical resonator ($\eta \approx 6\%$)

2. deep ion confinement in traps with MHz-scale vibrational frequencies

3. ability to store > 100 ions in linear chains and couple them to the resonator with efficiencies similar to single ions

4. precise control over ion chains using DC potentials

5. ability to optically address single ions

6. availability of long-lived, magnetic-field insensitive, ground-state hyperfine qubit states

This chapter presents a number of directions for future work that take advantage of these features, as well as some limitations imposed by the effects of motional heating of ions.

9.1 Collective Ion-Resonator Coupling

A direct route to increasing the relatively modest coupling between a single ion the resonator mode is to employ collective effects as described in Section 6.3. To prepare superradiant W-states of the form (6.16), a read-write process similar to [ST07] can be implemented using Zeeman sublevels of $^{174}Yb^{+}$ (Figure 9-1).

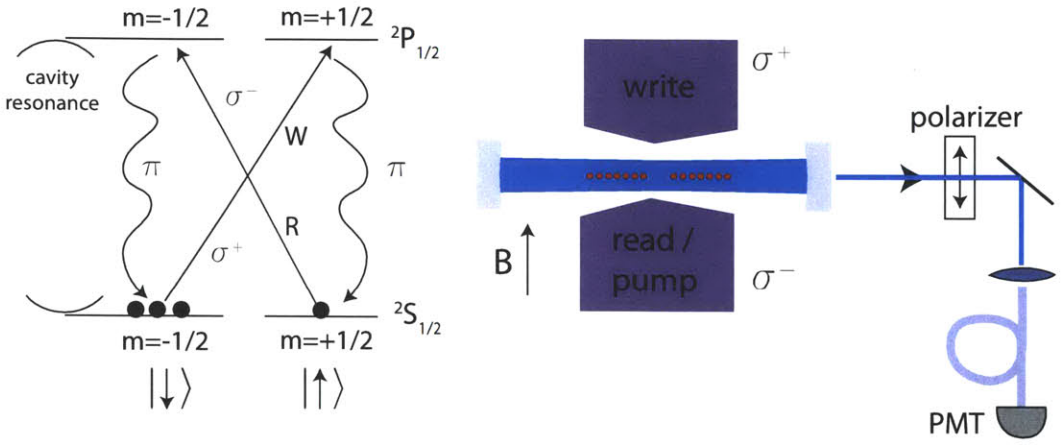

Figure 9-1: Collective read-write process for ions

Chains of ions are first pumped into the $m = -1/2$ $|\downarrow\rangle$ state by applying a σ^- polarized beam perpendicular to the resonator axis. A weak 'write' beam is applied to excite on average $p \ll 1$ atoms into the excited $^2P_{1/2}$, $m = +1/2$ $|\uparrow\rangle$ state. If, at this point, a π photon is detected using the photomultiplier tube, the ions' state is projected onto the W-state of the form (6.16) whose coupling to the resonator mode will be increased proportionally to the number of ions participating in the process.

To verify the enhanced emission of the resulting collective ion state into the cavity mode, a strong σ^- 'read' beam can be applied counterpropagating to the 'write' beam. In the limit of significant collective enhancement, the probability of receiving a 'read' photon conditioned on the detection of the write photon will be:

$$R_u = \frac{N\eta_{eff}}{N\eta_{eff}+1} \times \frac{1}{2} \times \eta_{op} \times \eta_{QE} \tag{9.1}$$

where η_{eff} is the mean effective cooperativity for the coupling of a single ion to the resonator mode, factor of $1/2$ accounts for the two resonator ports, η_{op} incorporates the optics and fiber losses and η_{QE} is the quantum efficiency of the photomultiplier detector.

In typical ion chains, the ions will be distributed nearly uniformly between nodes

and antinodes of the resonator field; including the polarization effects, one then has $\eta_{eff} \approx \eta/6 \approx 1\%$. To achieve efficient collective coupling corresponding to $N\eta_{eff} \sim 1$ in our system, based on the results from the previous section one would then need > 100 ions, either in one long chain or separated between ~ 10 sites of the linear trap array.

Being first-order sensitive to magnetic fields, the collective states prepared in the 'write' process in Figure 9-1 will be affected by both offsets and gradients of external magnetic fields, limiting their lifetimes. Lifetimes limited only by the ion heating effects (Section 9.4) should be possible by using $F = 0$ and $F = 1$, $m_F = 0$ ground hyperfine states in $^{171}Yb^+$ as shown on Figure 9-2 with identical effective cooperativity η_{eff}.

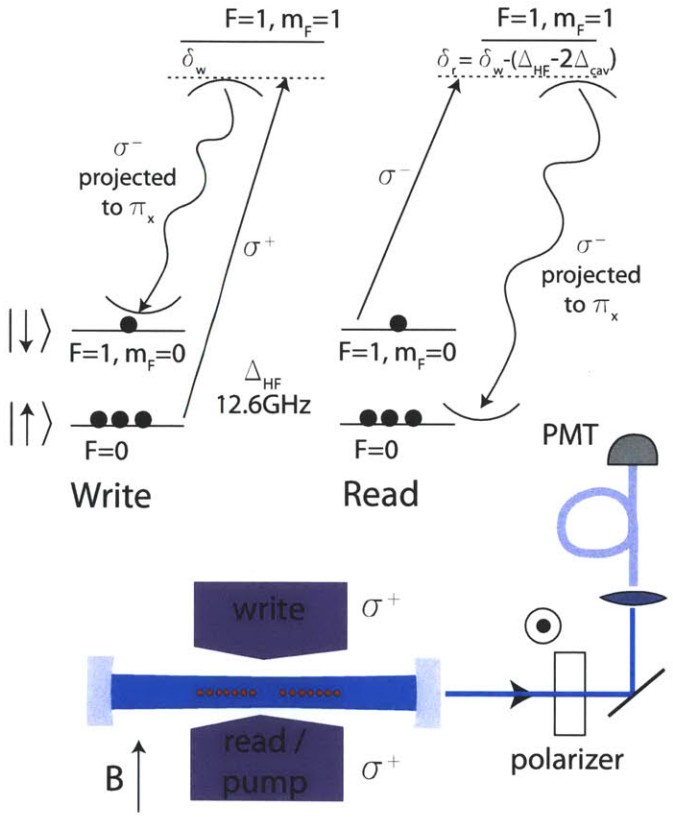

Figure 9-2: Collective read-write process between hyperfine states in $^{171}Yb^+$. Photon emissions into the reasonator during the read and write processes are on different longitudinal cavity modes with spacing $2\Delta_{cav}$ comparable to the hyperfine splitting of $\Delta_{HF} = 12.6$ GHz.

9.2 Probabilistic Ion Entanglement

Instead of addressing the entire ion ensemble, the 'write' beam from the previous section can be applied to two individual ions. If the intensity of the write beam is decreased to avoid coincident scattering of photons by the two ions, the detection of a photon scattered into the resonator will project the state of the ions' to

$$|W\rangle = \frac{1}{\sqrt{2}}[|\uparrow\downarrow\rangle + |\downarrow\uparrow\rangle]$$

creating heralded entanglement between two separated ions.

In contrast to the heralded two-photon entanglement schemes whose success probability scales as η^2 [MMO+07] for $\eta < 1$, the probability of scattering one photon into the cavity to create heralded entanglement scales as $R_u \sim \eta$, corresponding to the probability for *either* of the two ions to scatter one photon into the resonator (and not the free space photon modes).

Accounting for the branching ratio of the excited state (1/3), the existence of two cavity output ports (1/2), the expected fibere coupling efficiency ($\eta_{op} = 0.85$) and the photomultiplier efficiency ($\eta_{QE} = 0.19$), the present system promises entanglement probabilities on the order of 2×10^{-3} between ions stored in traps separated by mm-scale distances inside the mode of the optical resonator - 5 orders of magnitude higher than previously achieved using the two-photon scheme [MMO+07]!

9.3 Photon Storage

With their efficient coherent coupling to photons, collective W-states of the form (6.16) have been used in alkali atomic systems as a memory for photon states [TGS+09]. Unfortunately, such implementations suffer from decoherence due to the residual atomic motion: the coupling of a W-state to a given photon mode relies on the phase of the excitation of each atom relative to that of the photon at the same location; if the atoms are allowed to move freely on the scale of an optical wavelength (as in the early work with cold atoms by [ST07] and [CDLK08]), the required phase relationship is lost, limiting the lifetimes of collective states in atomic ensembles to less than 100 μs.

Motional decoherence can be avoided if the atoms are simply prevented from moving i.e. by placing them in a tight trap in which the mean atomic excursion is much smaller than an optical wavelength (the so-called Lamb-Dicke regime). This was demonstrated by [ZDJ+08] who used a optical lattice to extend the lifetime of a

photonic memory to more than 6ms.

Ultimately, the lifetimes of collective states of atoms in an optical latice were limited by lattice-induced AC Stark shifts and, more fundamentally, by heating due to spontaneous emission. As both of these effects are eliminated for ions confined in RF traps, lifetimes of photon states stored in Yb^+ ions in the current system could be significantly longer, limited mostly by the effect of the anomalous heating of ions, as analyzed in the following section.

9.4 Heating Effects

As outlined in the previous sections, motion of atoms will in general degrade the coupling of a collective atomic state to a particular mode. This chapter outlines the expected effects of the motion of trapped ions on their collective coupling to photons.

With $z_{i,w}$ the axial position of the j-th ion at the time of the write and $z_{j,r}$ the same position at the time of the read, the read efficiency will degrade as the overlap between the corresponding states:

$$R_u \sim \left| \sum_j \sin\left(kz_{j,w}\right) \sin\left(kz_{j,r}\right) / \sum_i \sin^2\left(kz_{j,w}\right) \right|^2$$

Since the vibrational frequencies of ion crystals are typically incommensurate, the motional dynamics of the ions will gradually randomize their positions. As the ion displacements relative to the initial positions become comparable to a wavelength, the recoded collective state is eroded and the coupling of the ion state to the resonator mode reverts to the coupling of a single emitter.

For $N \gg 1$ ions distributed uniformly between nodes and antinodes of the resonator mode, $\langle \cos\left(kz_{j,r} + kz_{j,w}\right) \rangle = 0$. In the Lamb-Dicke regime the read efficiency can then be written as:

$$R_u \approx \left[\sum_j \cos\left(k\Delta z_j\right) / N \right]^2 \approx \left(1 - \sum_j \frac{k^2 \left\langle \Delta z_j^2 \right\rangle}{2N} \right)^2$$

In an ion crystal, the displacement of the individual ions can be written as $\Delta z_j = \hat{z} \cdot \sum_l U_{jl} \Delta u_l$ where U_{jl} is an orthonormal matrix and Δu_l are the displacements of

the vibrational modes of the the crystal (Section 2.2). In ion chains such as those formed in our trap array, the transverse modes couple only weakly to the gradient of the resonator mode profile. In this case, one can focus on the longitudinal modes (labelled by the index l) to write:

$$\sum_j \langle \Delta z_j^2 \rangle = \sum_{l,j_1,j_2} U^T_{l,j_2} U_{l,j_1} \langle \Delta u_{j_2} \Delta u_{j_1} \rangle = \sum_l \langle \Delta u_l^2 \rangle$$

where the last line follows from the orthonormality of the mode matrix U_{jl}.

Each longitudinal mode of the chain behaves as an independent harmonic oscillator with frequency ω_l and mass equal to the ion mass m_i. Owing to the long-range of the Coulomb interaction, in short linear chains stored in harmonic traps, the longitudinal vibrational modes will be spaced nearly equally in frequency with characteristic mode spacing of roughly $\Delta\omega \approx 0.6\,\omega_{cm}$ where ω_{cm} is the frequency of the center-of-mass longitudinal mode [Ste97].

As outlined in Section 7.2.3 of Chapter 7, each array sub-trap can be expected to store at most $N = 30$ ions. Owing to the anharmonic sinusoidal potential of the trap array, the outermost ions in each trap will feel a decreased restoring force, corresponding to a lowering of some of the chains' vibrational modes. This perturbative effect can be approximated by lowering the mode spacing to $\Delta\omega \approx \omega_{cm}/2$.

The speed of the read-write process is limited by the resonator decay time ($\tau \approx 90$ ns). As the read-write times of hundreds of nanoseconds become comparable to the period of the ions' vibrational modes (~ 1 MHz), the relative ion displacements Δz_j can be expected to thermalize. For ions in thermal equilibrium at temperature T, one then obtains:

$$\sqrt{R_u} = 1 - \frac{k^2 k_B T}{2 m_i \omega_{cm}^2} \chi \tag{9.2}$$

where

$$\chi = \frac{4}{N} \sum_{l=1}^{N} \frac{1}{l^2}$$

is a numerical factor expressing the supression of displacements of higher vibrational modes of the ion chain arising from their higher frequencies relative to the center-of-mass mode.

Section 7.2.3 predicts the maximal number of ions in a chain at each trap array site as $N \approx 25$, achieved at an axial trap frequency of $\omega_{cm} \approx 2\pi \times 350$ kHz. In this

case, at the Doppler-limited ion temperature of $T_D = 470\ \mu$K, one obtains $R_u \approx 0.75$, corresponding to $< 25\%$ loss in fidelity of the collective ion state large times.

The above prediction was given assuming no ion heating during the photon storage time. Once technical noise sources are supressed, the dominant source of heating in the present array trap can be expected to be the fluctuating electric field $\vec{E}_{noise}$ arising from charge fluctuations on the trap surface [TKL+00]. The energy of one ion heated by the fluctuating field E_{noise} after time τ can be written following [TKL+00] as

$$\mathcal{E}_1(\tau) = \frac{e^2}{4m_i}\tau S_E(\omega_m) \tag{9.3}$$

where

$$S_E(\omega_m) = \frac{1}{2\pi}\int_{-\infty}^{\infty} e^{i\omega\tau}\vec{E}_{noise}(t)\cdot\vec{E}_{noise}(t+\tau)\,d\tau \tag{9.4}$$

is the temporal power spectral density of the fluctuating field $\vec{E}_{noise}$.

Neglecting any nonlinear coupling between vibrational modes, the heating of an ion chain reduces to the heating of the individual vibrational modes. A given mode l will experience an effective driving field E_l^{eff} equal to the projection of the fluctuating field along the ion displacements corresponding to this mode:

$$E_l^{eff}(\tau) = \sum_j U_{lj}\cdot\vec{E}_{noise}(\vec{r}_{0,j}, t) \tag{9.5}$$

Away from the surface, the Fourier components of the electric field produced by the fluctuating charges that are higher than $\approx 2\pi/h$, will decay away exponentially, leaving a fluctuating field with a spatial correlation length λ_c of at most $h/4 \approx 40\ \mu$m. Meanwhile, U_{lj} of the l-th axial motional mode will vary on a distance scale of L_c/l where $L_c \approx 100\ \mu$m is the length of the ion chain. Consequently, in a well-controlled system, only the first four modes of each ion chain can be expected to be strongly heated. In the limit of large time, the heating of these modes would each group of ≈ 6 ions uncorrelated with each other, preserving a collective enhancement in coupling to the resonator of at least a factor of 6.

Appendix A

Particle Dynamics in RF Traps

The existence of a conservative effective secular potential in a time-dependent RF trap may at first sight seem surprising. Intuitively, a time-dependent potential acting on a system of charged particles should cause heating and eventual deconfinement. Such RF-heating mechanisms are observed for large numbers of charges ras well as for few charges in non-harmonic traps.

To understand the limits of the secular potential approximation and gain insights into possible heating mechanisms, this appendix presents a more formal treatment of RF traps. These results will be especially important for understanding heating in ion-atom collisions as discussed in Section 3.1.

The existence of a secular potential in ion traps is closely related to the linearity of the relevant equations of motion. In general, this linearity will be violated due to particle-particle interactions and trap anharmonicities. Fortunately, past the phase transition of trapped ions to a Coulomb crystal, the ions are localized close to a fixed point in phase space. Close to this point, the system's Hamiltonian can be Taylor-expanded to second order, leading to linear evolution of the system appearing as a series of normal modes of the crystal.

The time periodicity of linear ion trap potentials mirrors the space-periodicity of the lattice potential in condensed matter systems or magnetic fields in strong focusing accelerators (the strong focusing principle was a big motivation for Paul's and Dehmelt's development of the RF traps). Just as the discrete space-translation symmetry of an electronic wavefunction in a crystal lattice gives rise to a conserved quasi-momentum k, the time-translation symmetry of a quadratic ion trap potential gives rise to a conserved secular Hamiltonian $\mathcal{H}$; as k exactly determines the evolution of an electron's wavefunction between points separated by a discrete number of lattice sites, $\mathcal{H}$ describes the ions' motion at times separated by an integer number of RF

periods. As the value of k is unchanged within a lattice period while the wavefunction follows the fine-scale excursions of the band function, $\mathcal{H}$ is conserved within an RF period while the ions follow RF-driven micromotion.

A.1 Floquet Theory

Formally, the dynamics of a classical time-periodic linear Hamiltonian system is described by the canonical Floquet theory century. The presentation here largely follows a recent review by [WP94]. The main results presented in this appendix will be an analytic form of $\mathcal{H}$ in terms of the original system Hamiltonian H. As noted before, the static form of $\mathcal{H}$ will exactly determine the secular motion of the system at times separated by an integer number of RF periods. Within each RF period, the ions will execute micromotion identified by the difference between the original coordinates/momenta and the action-angle variables of $\mathcal{H}$.

In any of the above cases, we can write the charges' Hamiltonian equations of motion as

$$\partial_t Y = \Omega_S \begin{pmatrix} \partial_r \\ \partial_p \end{pmatrix} H(t, r, p) \tag{A.1}$$

where $Y = (r, p)$ is a vector describing the system's location in phase space and

$$H_e = B(t)^T Y + \frac{1}{2} Y^T A(t) Y$$

is the effective quadratic Hamiltonian near the point O with

$$\begin{aligned} A(t) &= \begin{pmatrix} \frac{\partial^2 H}{\partial r^2} & \frac{\partial^2 H}{\partial r \partial p} \\ \frac{\partial^2 H}{\partial r \partial p} & \frac{\partial^2 H}{\partial p^2} \end{pmatrix}_O \\ B(t) &= \begin{pmatrix} \partial H/\partial r \\ \partial H/\partial p \end{pmatrix}_O \end{aligned}$$

Here,

$$\Omega_S = \begin{pmatrix} 0 & I \\ -I & 0 \end{pmatrix}$$

is the canonical 2-form encoding the structure of Hamilton's equations in phase space.

Ω_S is preserved by both the equations of motion and any other canonical transformations, a consequence of which is the preservation of phase space volume.

The single-particle equations of motion (A.1) will be linear as:

$$\partial_t Y = A(t) Y + B(t) \tag{A.2}$$

Any solution of (A.2) with initial conditions $Y(t = t_0) = Y_0$ can be written as $U(t_1, t_0) Y_0 + \Delta(t_1, t_0)$ where $U(t_1, t_0)$ is a linear operator satisfying

$$\begin{aligned} U(t_2, t_1) U(t_1, t_0) &= U(t_2, t_0) \\ U(t_0, t_0) &= I \end{aligned}$$

and $\Delta(t, t_0)$ is a particular solution corresponding to $Y(t_0) = 0$. Due to time-periodicity of A and B,

$$\begin{aligned} U(t_1 + T, t_0 + T) &= U(t_1, t_0) \\ \Delta(t_1 + T, t_0 + T) &= \Delta(t_1, t_0) \end{aligned}$$

Introducing the period-advance map $(U_{2\pi}, \Delta_{2\pi})$ starting at time t_0 by $U_{2\pi} = U(t_0 + T, t_0)$, $\Delta_{2\pi} = \Delta_{2\pi}^{(1)}(t_0) = \Delta(t_0 + T, t_0)$, we have for any initial conditions Y_0:

$$\begin{aligned} Y(t_0) &= Y_0 \\ Y(t_0 + (n+1)T) &= U_{2\pi} Y(t_0 + nT) + \Delta_{2\pi} \end{aligned}$$

or

$$\begin{aligned} Y(t_0 + nT) &= U_{2\pi}^n Y_0 + \Delta_{2\pi}^{(n)} \\ \Delta_{2\pi}^{(n+1)} &= U_{2\pi} \Delta_{2\pi}^{(n)} + \Delta_{2\pi} \end{aligned} \tag{A.3}$$

Just as the the lattice advance map determines the quasi-momentum of an electron, the RF period advance map will determine $\mathcal{H}$. Since

$$U(t_1, t_0) [U(t_0, t_1) Y_0 + \Delta(t_0, t_1)] + \Delta(t_1, t_0) \equiv Y_0$$

implies $U(t_1, t_0) = U^{-1}(t_0, t_1)$ and $U(t_1, t_0)\Delta(t_0, t_1) = -\Delta(t_1, t_0)$, the period advance map $(U_{2\pi}(t_1), \Delta_{2\pi}(t_1))$ starting at any other time t_1 will be:

$$U_{2\pi}(t_1) Y_0 + \Delta_{2\pi}(t_1) = U(t_1, t_0) U_{2\pi}(t_0) U(t_1, t_0)^{-1} Y_0 + U(t_1, t_0) \Delta_{2\pi}(t_0)$$

In other words, the period advance maps starting from different initial points during one RF period are related by the canonical linear transformation relating the phase space at these two points in time. As the time-evolution of the system follows the same linear transformation, the values of quantities such as $\mathcal{H}$ derived from the time-advance map will also be conserved *within* an RF period.

For large times $|t_1 - t_0|$, the behavior of the particle will be determined by the period-advance map $U_{2\pi}$ governed by $A(t)$ and the single-period displacement $\Delta_{2\pi}$ caused by $B(t)$. As any other matrix, $U_{2\pi}$ can be written in a Jordan block form as:

$$U_{2\pi} = \Lambda_J \begin{pmatrix} J_1 & 0 & 0 \\ 0 & \ldots & 0 \\ 0 & 0 & J_k \end{pmatrix} \Lambda_J^{-1}$$

where Λ is an invertible matrix and

$$J_i = \begin{pmatrix} \lambda_i & 1 & 0 \\ 0 & \ldots & 1 \\ 0 & 0 & \lambda_i \end{pmatrix}$$

are Jordan blocks with λ_i the eigenvalues of $U_{2\pi}$ which, for since $U_{2\pi}$ is real, will come in complex-conjugate pairs. Also, as noted before, phase space volume must be preserved by $U_{2\pi}$ so $\det U_{2\pi} = \prod_j \lambda_j^2 = \prod_j |\lambda|_j^2 = 1$.

We are especially interested in stable trapping of particles. This can only happen if $U_{2\pi}^n$ remains bounded. Since

$$J_i^n = \begin{pmatrix} \lambda_i^n & n & 0 \\ 0 & \ldots & n \\ 0 & 0 & \lambda_i^n \end{pmatrix}$$

all Jordan blocks must be of dimension one and for all eigenvalues λ_i, $|\lambda_i| < 1$. Since $\prod_j |\lambda_j| = 1$, all eigenvalues must be of unit magnitude i.e. $\lambda_j = e^{i\phi_j}$. In this case, one can easily show that:

$$
\begin{aligned}
U_{2\pi} &= \Lambda \tilde{U}_{2\pi} \Lambda^{-1} \\
\tilde{U}_{2\pi} &= \begin{pmatrix} R(-\phi_1) & 0 & 0 \\ 0 & \ldots & 0 \\ 0 & 0 & R(-\phi_k) \end{pmatrix}
\end{aligned}
$$

where

$$
R(\phi_j) = \begin{pmatrix} \cos\phi_j & \sin\phi_j \\ -\sin\phi_j & \cos\phi_j \end{pmatrix}
$$

are 2×2 rotation matrices acting in the corresponding $\lambda_j - \bar{\lambda}_j$ subspaces.

In the basis described by Λ, we may also write the single-period displacements as:

$$
\begin{aligned}
\tilde{\Delta}_{2\pi}^{(n)} &= \begin{pmatrix} \Delta_1^{(n)} & \ldots & \Delta_k^{(n)} \end{pmatrix}^T \\
\tilde{\Delta}_j^{(n+1)} &= R(-\phi_j)\, \Delta_j^{(n)} + \Delta_j
\end{aligned}
$$

The total displacements $\tilde{\Delta}_i^{(n)}$ can be computed as

$$
\begin{aligned}
\tilde{\Delta}_j^{(n)} &= R(-n\phi) \sum_{j=0}^{n-1} R(j\phi)\, \tilde{\Delta}_i \\
&= R(-n\phi)\, [I - R(n\phi)]\, [I - R(\phi)]^{-1}\, \tilde{\Delta}_i
\end{aligned}
$$

One sees that if $U_{2\pi}^n$ is bounded, so is $\Delta^{(n)}$. In other words, fixed forces acting near the point O will in general not affect the stability of the system trajectories.

The above lends itself to a simple physical view. Viewed stroboscopically every RF period, the particle's motion consists of secular dynamics described by $U_{2\pi}^n$ together with a fixed, bounded shifts described by $\Delta^{(n)}$. Relative to $\Delta^{(n)}$, in phase-space coordinates determined by Λ, stable secular motion takes the form of independent rotations in the $V_{Xi} - V_{Yi}$ planes by angles $-\phi_i$ - analogous to the dynamics of three independent harmonic oscillators with angular frequencies $\omega_i = \phi_i / T$.

The harmonic oscillator analogy can be made more explicit by finding a canonical transformation E from (r, p) to new phase space coordinates $(X_i,\ P_i)$ such that in the new coordinates, $U_{2\pi}$ appears as the evolution by time T under a Hamiltonian

$\mathcal{H}_u$ corresponding to the above three harmonic oscillators. A procedure to do this is described in [WP94]. For completeness, we briefly summarize it here.

We looking for basis E such that in this basis $U_{2\pi}$ takes the form of the evolution harmonic oscillators given by $\tilde{U}_{2\pi}$ with the corresponding canonical form

$$\begin{aligned}\Omega_S' &= E^T \Omega_S E = \begin{pmatrix} \Omega_S^{2\times 2} & 0 & 0 \\ 0 & \dots & 0 \\ 0 & 0 & \Omega_S^{2\times 2} \end{pmatrix} \\ \Omega_S^{2\times 2} &= \begin{pmatrix} 0 & 1 \\ -1 & 0 \end{pmatrix}\end{aligned}$$

Since $U_{2\pi}$ is canonical, we must have $U_{2\pi}^T \Omega_S U_{2\pi} = \Omega_S$ or

$$\begin{aligned}\left(\Lambda \tilde{U}_{2\pi} \Lambda^{-1}\right)^T \Omega_S \Lambda \tilde{U}_{2\pi} \Lambda^{-1} &= \Omega_S \\ \tilde{U}_{2\pi}^T \left(\Lambda^T \Omega_S \Lambda\right) \tilde{U}_{2\pi} &= \left(\Lambda^T \Omega_S \Lambda\right)\end{aligned}$$

Since $\tilde{U}_{2\pi}$ is orthogonal, we conclude that $\Lambda^T \Omega_S \Lambda$ must commute with it. The only antisymmetric 2×2 matrices that commute with rotations $R(-\phi_j)$ are proportional to $\Omega_{2\times 2}$ so we must have:

$$\Lambda^T \Omega_S \Lambda = \begin{pmatrix} d_1 \Omega_{2\times 2} & 0 & 0 \\ 0 & \dots & 0 \\ 0 & 0 & d_k \Omega_{2\times 2} \end{pmatrix}$$

The basis E can then be constructed as:

$$\begin{aligned}D &= \begin{pmatrix} d_1^{-1/2} I_{2\times 2} & 0 & 0 \\ 0 & \dots & 0 \\ 0 & 0 & d_k^{-1/2} I_{2\times 2} \end{pmatrix} \\ E &= \begin{pmatrix} X_1 & P_1 & X_2 & P_2 & X_3 & P_3 \end{pmatrix} = \Lambda D\end{aligned}$$

Indeed:

$$E \tilde{U}_{2\pi} E^{-1} = \Lambda D \tilde{U}_{2\pi} D^{-1} \Lambda^{-1} = \Lambda \tilde{U}_{2\pi} \Lambda^{-1} = U_{2\pi}$$

and

$$\begin{aligned} E^T \Omega_S E &= D\left(\Lambda^T \Omega_S \Lambda\right) D = \left(\Lambda^T \Omega_S \Lambda\right) D^2 \\ &= \left(\Lambda^T \Omega_S \Lambda\right) \left(-\Omega_{S'} \Lambda^T \Omega_S \Lambda\right)^{-1} \\ &= \left(-\Omega_{S'}\right)^{-1} = \Omega_{S'} \end{aligned}$$

To produce $\tilde{U}_{2\pi}$, the effective secular Hamiltonian in the E-basis must be $\frac{1}{2} Y^T D_\omega Y$ with

$$D_\omega = \begin{pmatrix} \omega_1 I_{2\times 2} & 0 & 0 \\ 0 & \ldots & 0 \\ 0 & 0 & \omega_k I_{2\times 2} \end{pmatrix}$$

In $X - P$ coordinates, this becomes:

$$\begin{aligned} \mathcal{H}_u\left(O, t_0\right) &= \frac{1}{2} Y^T \mathcal{H}_Q Y \\ \mathcal{H}_Q &= \left(E^{-1}\right)^T D_\omega E^{-1} \\ &= \left(\Lambda^{-1}\right)^T D_\omega \left(-\Omega_{S'} \Lambda^T \Omega_S \Lambda\right) \Lambda^{-1} \qquad \text{(A.4)} \\ &= \\ &= -\left(\Lambda^{-1}\right)^T D_\omega \Omega_{S'} \Lambda^T \Omega_S \qquad \text{(A.5)} \end{aligned}$$

The Hamiltonian $\mathcal{H}_u$ does not describe the shifts $\Delta^{(n)}$. We can put these back by adding a term of the form $v^T Y$ to $\mathcal{H}_u$. Then, one must have

$$\Delta_{2\pi} = \int_0^{2\pi/\Omega} d\tau \, \exp\left[\tau \Omega_S \mathcal{H}_Q\right] \Omega_S v$$

After some computation, we finally get:

$$v = \Omega_S \left[I - U_{2\pi}\right]^{-1} \Omega_S \mathcal{H}_Q \Delta_{2\pi} \qquad \text{(A.6)}$$

for the effective secular Hamiltonian

$$\mathcal{H}\left(O, t_0\right) = \mathcal{H}_u\left(O, t_0\right) + v\left(O, t_0\right)^T Y$$

The $\mathcal{H}(O,\, t_0)$ above was derived in the case of stable long-term trajectories. An effective secular Hamiltonian can also be derived when the long-term system trajectory is unstable by replacing the rotations $R(-\phi_i)$ on the diagonal of $\tilde{U}_{2\pi}$ with the more general real Jordan blocks [WP94].

In summary, when viewed at times $t_n = t_0 + nT$ separated by an integer number of RF periods, the dynamics of a set of charges in an RF trap close to a fixed phase-space point O can be described by an equivalent secular continuous-time evolution under an effective conserved quadratic Hamiltonian $\mathcal{H}$. In action-angle coordinates of $\mathcal{H}$, the system's evolution proceeds a the evolution of a series of harmonic oscillators. The relation between these coordinates and the original coordinates/momenta (r, p) changes periodically during one RF period and can be identified as the system's micromotion.

In general, over time, the system may evolve away from O and the expansion used to produce $\mathcal{H}(O,\, t_0)$ may cease to be valid. However, if the evolution is slow relative to both the RF period and the secular evolution described by $\mathcal{H}$, we can simply recompute $\mathcal{H}$ relative to the current point in phase space at each time slice t_n. Under the same assumptions, the resulting secular evolution will be well-approximated by a single secular Hamiltonian for the whole phase space determined as $\mathcal{H}(Y,\, t_0)$ where $Y = (q, p)$. A particular case of this argument is the derivation of the secular potential in Section 2.1.

A.2 Single-Particle Trapping

At distances much smaller than the RF free-space wavelength, the total electric field in a harmonic trap can be described as $E = -\nabla(\Phi_{RF} + \Phi_{DC})$ where

$$\begin{aligned}
\Phi_{RF}(t) &= -r \cdot E_0 \cos(\Omega t) + \frac{1}{2} r^T g_c r \cos(\Omega t) + \frac{1}{2} r^T g_s r \sin(\Omega t) \\
\Phi_{DC} &= -r \cdot E_{DC}^0 + \frac{1}{2} r^T g_{DC} r
\end{aligned}$$

For a single particle in the trap, the total Hamiltonian is

$$H = \frac{p^2}{2m} + Q(\Phi_{RF} + \Phi_{DC})$$

As described in the previous section, the overall secular dynamics of the particle

will be determined by the evolution over a single RF-period. To describe this evolution, it is useful to cast H into a more convenient form by a canonical transformation $t \to 2t/\Omega$, $H \to 2H/\Omega$, $p \to p\sqrt{m\Omega/2}$, $r \to r/\sqrt{m\Omega/2}$, after which we can write

$$\begin{aligned} H &= \frac{p^2}{2} - \left(ec + e^{DC}\right) \cdot r + \frac{1}{2} r^T \left[2q_c c + 2q_s s + a_{DC}\right] r^T \\ c = \cos 2t \quad &, \quad s = \sin 2t \\ q_{c,s} = \frac{2Qg_{c,s}}{m\Omega^2} \quad &, \quad a_{DC} = \frac{4Qg_{DC}}{m\Omega^2} \\ e = \frac{2QE_0}{\sqrt{m\Omega^3}} \quad &, \quad e_{DC} = \frac{2QE^0_{DC}}{\sqrt{m\Omega^3}} \end{aligned}$$

The parameters q_c, q_s and a characterize the deviation of a single RF period map $U_{2\pi}$ from free particle propagation while e and e_{DC} characterize the drift during a single RF period $\Delta_{2\pi}$. Since the equations of motion are linear, the drift will scale linearly with e and e_{DC} without any qualitative change in the particle dynamics.

The magnitude of q_c, q_s and a will determine the non-perturbative nature of $U_{2\pi}$. In their small limit, we expect to obtain the effective secular potential from Section (Paul traps). $U_{2\pi}$ can then be expanded perturbatively as:

$$\begin{aligned} U_{2\pi} &\approx U_0(T) + \int_0^T d\tau_1 \int_0^{\tau_1} d\tau_2 \\ &\times U_0(T-\tau_1) V(\tau_1) U_0(\tau_1-\tau_2) V(\tau_2) U_0(\tau_2) \\ &+ \int_0^T U_0(T-\tau) V(\tau) U_0(\tau) d\tau \end{aligned}$$

where

$$U_0(t) = \begin{pmatrix} 1 & t \\ 0 & 1 \end{pmatrix}$$

describes free particle propagation and

$$V(t) = \Omega_S \begin{pmatrix} 2q_c c + 2q_s s + a_{DC} & 0 \\ 0 & 0 \end{pmatrix}$$

describes the effect of the added potentials. After some computation and keeping only the leading terms in q_c, q_s and a:

$$U_{2\pi} \approx I + T \begin{pmatrix} -q_s & 1+q_c \\ -\frac{a}{2} - \frac{q_c^2}{2} - \frac{3q_s^2}{2} & q_s \end{pmatrix}$$

After a canonical coordinate change $(r, p) \to \left(r,\, p + \frac{q_s}{2} r - \frac{q_c q_s}{4} r\right)$ we get to leading order:

$$U_{2\pi} \approx I + T\Omega_S \begin{pmatrix} \frac{a}{2} + \frac{q_c^2}{2} + \frac{q_s^2}{2} & 0 \\ 0 & 1+q_c \end{pmatrix}$$

To the same leading order, this is equivalent to the evolution under an effective Hamiltonian

$$\mathcal{H}_e \approx \frac{1}{4} r^T \left(a + q_c^2 + q_s^2\right) r + \frac{1+q_c}{2} \left(p + \frac{q_s}{2} r\right)^2$$

Since we did not make use of (A.5), the above is valid even for unstable traps.

In the limit of small q_c, q_s and a, the main effect of the offset electric fields e_{DC} and e can be obtained by taking the average over one RF cycle. The offset RF field e then averages to zero while the offset DC field produces a constant force e_{DC}. Corrections to this will scale as q_c, q_s and a. Neglecting these terms, the offset fields can be added to the effective Hamiltonian to obtain

$$\mathcal{H} = -e^T r + \frac{1}{4} r^T \left(a + q_c^2 + q_s^2\right) r + \frac{1}{2} \left(p + \frac{q_s}{2} r\right)^T (I + q_c) \left(p + \frac{q_s}{2} r\right)$$

or, in the original units

$$\begin{aligned} \mathcal{H} &= V(r) + \frac{1}{2m} \left(p + \frac{Q g_s}{\Omega} r\right)^T (I + q_c) \left(p + \frac{Q g_s}{\Omega} r\right) \\ V(r) &= -Q E_{DC}^{0T} r + \frac{Q}{2} r^T g_{DC} r + r^T \frac{Q^2 \left(g_c^2 + g_s^2\right)}{4 m \Omega^2} r \end{aligned}$$

As expected, $V(r)$ matches the secular potential introduced in Section 2.1. The momentum terms are offset from that of a free particle by $p_{mm} = -Q g_s r / \Omega^2$, which is precisely the momentum $m v_{mm}$ carried by the micromotion

$$v_{mm} = -\frac{Q g_s r}{m\Omega} \cos(\Omega t) + \frac{Q g_c r}{m\Omega} \sin(\Omega t)$$

driven by the field $E = g_s r \cos \Omega t + g_s r \sin \Omega t$ at time $t = 0$.

Another effect apparent from the momentum term in $\mathcal{H}$ is a rescaling of the mass of the particle by $(I + q_c)^{-1}$. Being one order higher in the q's, the effect of this on the

secular frequencies should be compared to further terms in a perturbative expansion. Using (A.6) one may see that corrections to slow external forces will also scale with $q_{c,s}$. One may then show that to lowest order, the response to a slow force will be rescaled in time by $1 + q_c$.

Appendix B

Blue-Violet Diode Lasers for Ion Trapping

The strong transitions in alkali and alkali earth-like ions, including the main Doppler-cooling transition, are all in the blue and UV spectral regions. To access these wavelengths, dye or titanium-sapphire lasers have traditionally been used, often followed by frequency-doubling [WDW78, KBBG90, RRG$^+$00, NHTD78]. These systems have been expensive, complex and often unreliable.

The development of room-temperature continuous-wave GaN diode lasers by Nakamura et al. at the Nichia Corporation [NSN$^+$96] promised a cheap, flexible and reliable light source for cooling and manipulation of atoms and ions in the blue and near-UV frequency range. Soon after Nichia offered the first commercial blue laser diode (NLHV500A) in October 1999, it ws employed for Doppler cooling of Ca^+ [HUW00]. By 2004, Nichia was offering diodes in the 370 nm - 380 nm, 390 nm - 425 nm and 440 nm - 465 nm spectral ranges, enabling direct Doppler cooling of Yb [PY03] and promising cooling of Yb^+ and Sr^+.

Before the these new diodes could be used in a new atomic physics experiment, it was necessary to have assurance of their lifetime and future availability. Commercial interest in blue laser diodes is strongly driven by the HDDVD and Blu-Ray high-density optical disk standards put forth in 2002. Both standards specified the use of violet laser diodes with wavelengths near 405 nm with the Blu-Ray standard also requiring laser wavelengths above 400nm in order to avoid degradation of the disc polymer [Ass10]. In 2002, Sanyo Electric Co. offered 405 nm laser diodes and, after licensing agreements with Nichia, Sony and Sharp followed suit in 2002 and 2008 respectively [Cor02, Cor08]. However, the availability of diodes outside the 400 nm - 410 nm Blu-Ray band has been poor - to date, no commercial manufacturer except

Nichia is offering such diodes. Moreover, as Nichia focused on volume production, their wavelength spread close to 400nm decreased, resulting in a dearth of diodes suitable for cooling Ca^+ and Yb at 398nm and Sr^+ at 422 nm.

Due to their use in biology for fluorescence excitation and flow cytometry, the availability of the 371 nm - 373 nm Nichia diodes useful for cooling and manipulation of Yb has been considerably better with continued improvements in slope efficiency and output power. In the next sections, we will present a number of features of these diodes as well as the steps we took to make them suitable in atomic physics experiments.

B.1 Nichia Diode Lasers for Cooling and Trapping of Yb and Yb^+

A scanning electron microscope of a NDHU110APAE2 373nm InGaAlN laser diode from Nicha used for cooling Yb^+ in this thesis is shown on Figure B-1.

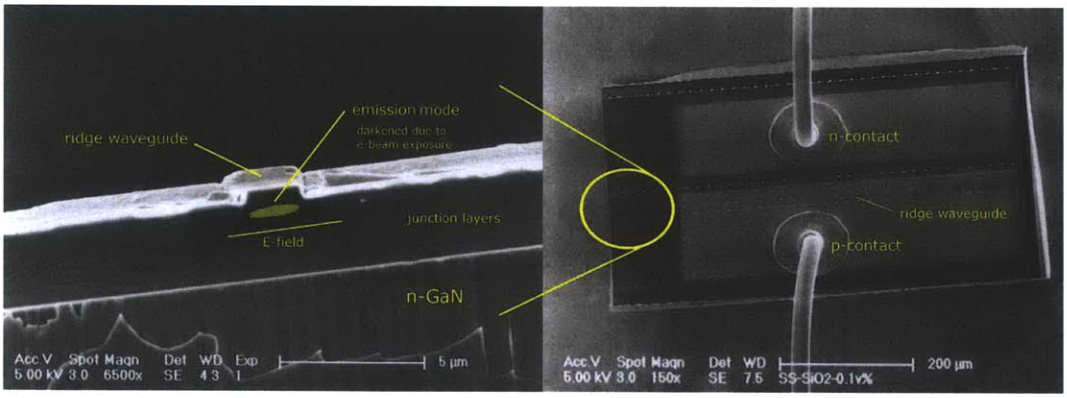

Figure B-1: Scanning electron microscope image of the NDHU110APAE2 InGaAlN Fabry-Perot ridge waveguide laser diode from Nichia Corporation

An overview of the structure of GaN laser diodes can be found in [SF97]. n-type GaN is grown by molecular beam epitaxy (MBE) on a sapphire substrate. A part of the grown n-type GaN is metalized with gold and wire-bonded to the cathode contact. On the remaining part of the n-layer surface, the n-p junction layers are sequentially grown by the same method. Radiative recombination rate is enhanced by confining carriers passing through the junction in multiple quantum wells with low defect density.

To couple the carrier emission to a particular laser mode, the active region including the quantum wells, is enclosed in an optical TE ridge waveguide. One end of the waveguide is tapered to provide high reflectivity while the other is sharply cleaved to form the emission plane. The length of the waveguide in the Nichia devices can be estimated from Figure B-1 as $L = (610 \pm 30)$ μm. Using the AlGaN refractive index at 370 nm ($n_o \approx 2.6$, [TMK+01]), this predicts the spacing between the neighboring longitudinal laser modes of $c/(2n_oL) = 95$ GHz. The discrepancy with the experimental value of (50 ± 10)GHz can be explained by the loading from transverse waveguide confinement and the injected carriers.

The cleaved 350 μm $\times$ 650 μm laser wafer is attached to a gold-plated 5.6mm TO18 package with the tapered end of the waveguide pointed towards a Si monitoring photodiode. Using the Nichia datasheet specification of $100\mu A$ photodiode current for 10mW of optical output and a typical 50% Si photodiode quantum efficiency at 373nm, one can determine the output coupling of the rear facet to be less than 10% of the front output coupling and so negligible for the laser operation as described in the following sections.

Connections to both the anode and the cathode pads of the device are made with 1mm long 30 μm-diameter gold wire bonds. The effect of the inductance of these wire bonds on the current modulation behavior of the diode will be discussed in a later section.

Finally, the entire device is hermetically sealed with a protective cap containing a 250 μm-thick fused silica AR-coated window.

B.1.1 Mode Profile

The small size of the emission region leads to a fast divergence of the output mode of the laser diode. To produce a useful beam, we collimate the diode output using the C671TME-A collimator from Thorlabs based on the Lightpath 352671 molded ECO-550 glass aspheric lens designed for collimation of 405nm diodes. We measured >90% transmission of 370nm light through this optic. In spite of reports (Streed, private comm.) of optical damage to the ECO-550 glass due to exposure to 370nm light from the 20mW Nichia laser diodes (max. light intensity of $5W/cm^2$), we have not yet observed this effect.

The laser diode mode after collimation with the C671TME-A collimator is shown along the fast and slow axes on Figures B-2 and B-3, respectively. Right after the col-

limator, the intensity profile of the diode mode is approximately Gaussian with waists $w_{fast} = (1560 \pm 30)$ μm in the fast plane perpendicular to the light polarization and $w_{slow} = (660 \pm 20)$ μm in the slow plane parallel to the light polarization. Defining the numerical aperture (NA) of the laser diode mode as the sine of the angle at which the intensity drops to $1/e^2$ of the maximum, a ray-tracing model of the C671TME-A collimator gives $\mathrm{NA}_{fast} = 0.376 \pm 0.008$ and $\mathrm{NA}_{slow} = 0.160 \pm 0.005$.

The intensity plot after the collimating lens does not give information about the phase of the laser diode wavefront. Due to the symmetry of the ridge waveguide structure (Figure B-1), the laser diode mode is even. Assuming waveguide and that the emission point is located on the lens axis, the phase ϕ of the laser wavefront at the collimator output, at distance ρ from the system axis can then be parametrized as:

$$\phi(\rho) = \frac{k\rho^2}{2R} + 2\pi \sum_{k=2}^{\infty} A_{2k} \left(\frac{\rho}{w}\right)^k \tag{B.1}$$

where R is the radius of curvature of the wavefront, $w = \sqrt{w_{slow} w_{fast}}$ is the mean beam waist and A_{2k} are unitless parameters quantifying deviation of the wavefront from a Gaussian beam normalized to waves of deviation one beam waist away from the optical axis. For weak aberrations and near-collimated output, we may consider only A_4, describing the spherical aberration of the wavefront. We may also expect A_4 to be independent of the lens position which, to first order, will only affect the beam curvature R.

The beam curvature R and the spherical aberration coefficient A_4 can be determined by measuring the beam profile of the collimated beam after various propagation lengths. Figure B-2 shows a comparison of the above simple model with various values of A_4 with the measured beam profiles. The red curves show good qualitative agreement with the model while the disagreement in the shape of the blue curves and green curves allows us to put a firm bound on the amount of spherical aberration along the fast axis as $0 < A_4 < 0.2$.

A similar procedure can be carried out along the slow axis with results shown on Figure B-3. The measured profiles agree well with the propagation of a non-aberrated Gaussian beam (green curves) and qualitatively disagree with the spherical aberration observed along the fast axis (red curves).

Since the collimating lens is axially symmetric, we ascribe the spherical aberration present along the fast axis to the laser diode mode and not to the collimating lens. This is confirmed by observing a very similar mode propagation along the fast axis

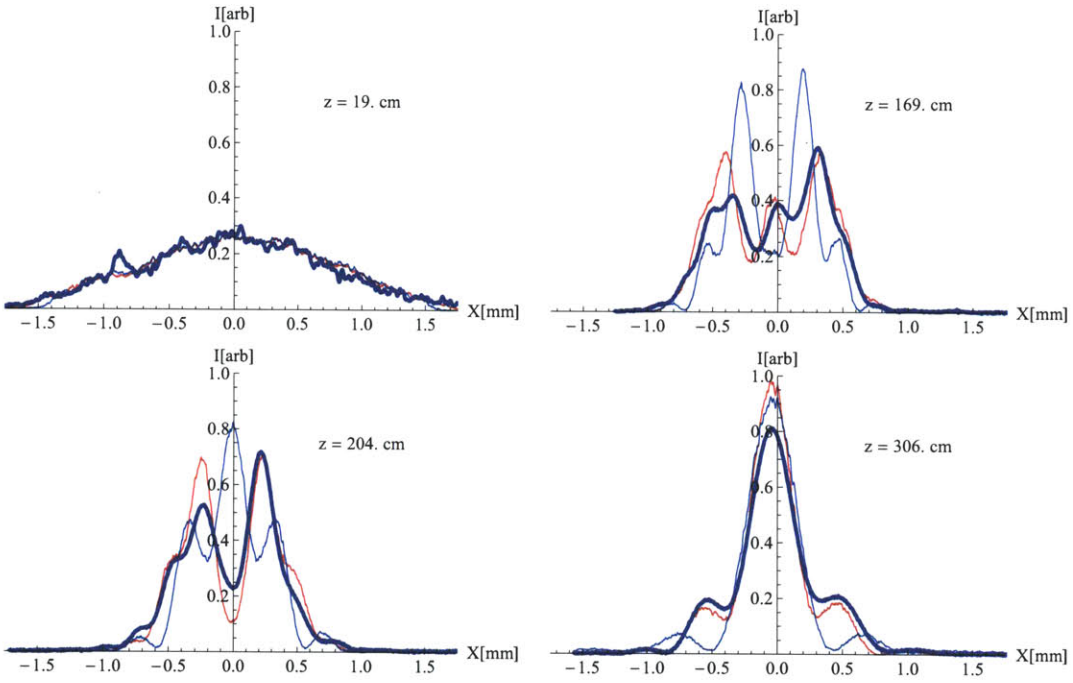

Figure B-2: Black curves: Measured beam profiles of a collimated NDHU110APAE2 Nichia laser diode along the fast axis as function of distance to the collimator. Colored curves: Beam profiles computed based on the intensity profile at the collimator output and phase ϕ given by Eq. B.1 – green: $R = -11$ m, $A_4 = 0$, red: $R = -11$ m, $A_4 = +0.11$, blue: $R = -11$ m, $A_4 = +0.20$

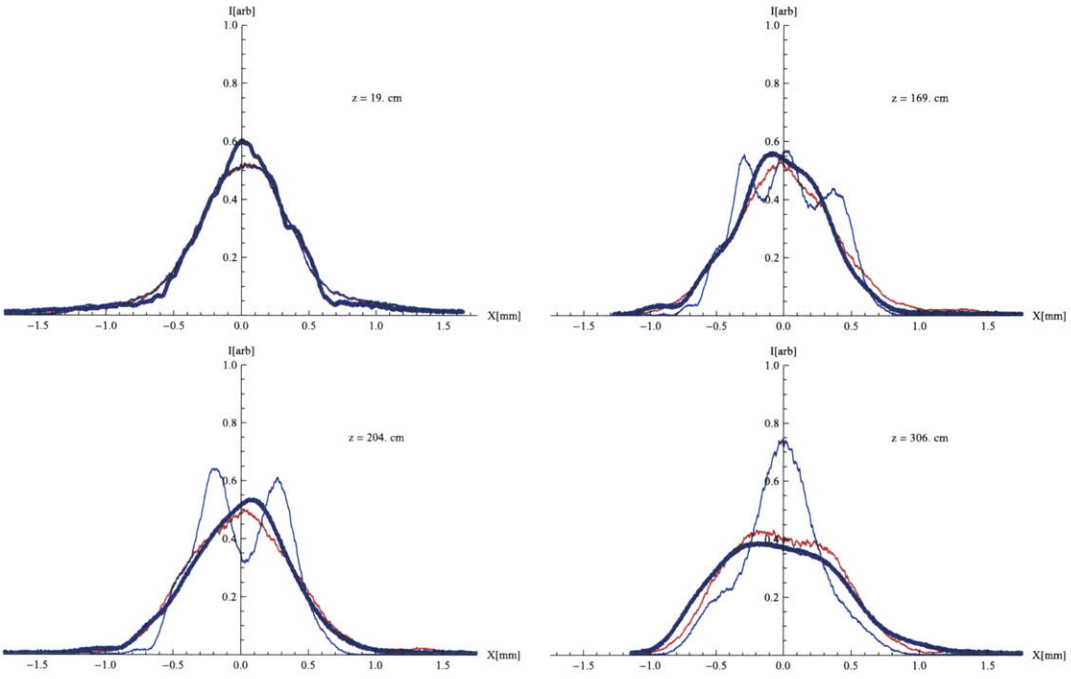

Figure B-3: Black curves: Measured beam profiles of a collimated NDHU110APAE2 Nichia laser diode along the slow axis as function of distance to the collimator. Colored curves: Beam profiles computed based on the intensity profile at the collimator output and phase ϕ given by Eq. B.1 – green: $R = -11$ m, $A_4 = 0$, red: $R = -11$ m, $A_4 = +0.11$

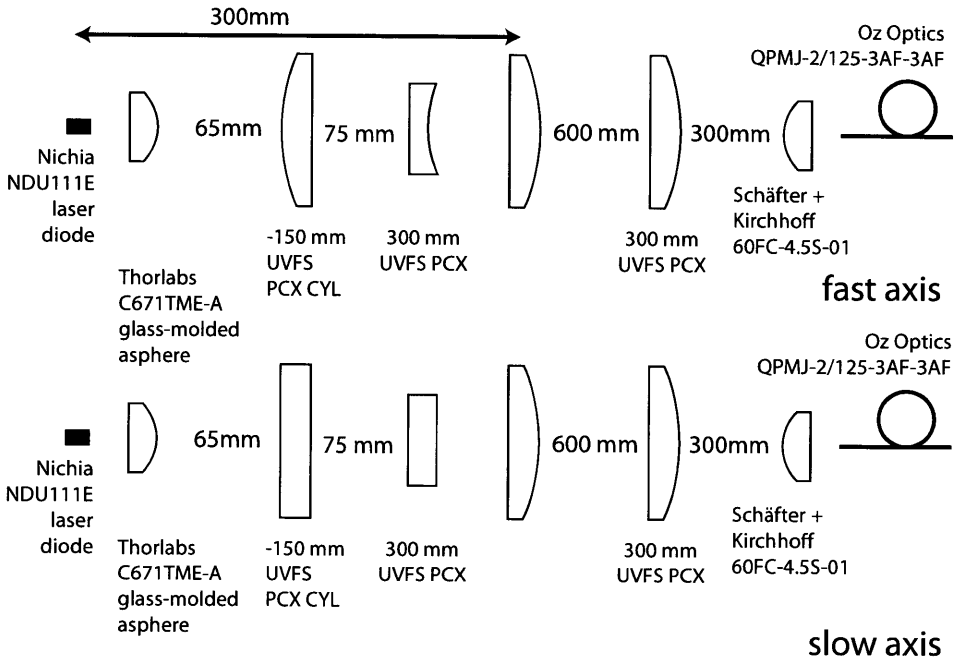

Figure B-4: $4f$ imaging setup for efficient coupling of output from a Nichia NDU111E near-UV laser diode into a 2 μm-core bowtie single-mode polarization maintaining fiber

when using a NA0.6 microscope objective to collimate the beam. The sign of the observed spherical aberration along the fast axis corresponds to the marginal portions of the beam wavefront appearing to originate from a point shifted closer to the lens surface.

B.1.2 Fiber Coupling

Due to high saturation intensities of the strong near-UV atomic transitions ($\sim$50 mW/cm^2) and a low output power of the near-UV laser diodes ($\leq$20 mW), the efficient coupling of their emission into a single-mode optical fiber becomes important. However, achieving good coupling in the presence of astigmatism and spherical aberration in of the diode mode can be difficult.

A solution using $4f$ Fourier imaging to achieve 55% coupling efficiency (including losses) into a 4 m long, 2 μm-core polarization-maintaining bowtie fiber (QPMJ-2/125-3AF3AF from Oz Optics, Canada) is shown on Figure B-4.

B.1.3 Gain Profile

The emission profile of the shortest-wavelength laser diodes available at the start of this thesis is shown on Figure B-5. The red curve was obtained at a low drive current where the effects of stimulated emission are small and the emission profile is expected to match the gain of the laser medium. As the drive current is increased (green curve), the buildup of photons in the laser cavity causes increased stimulated emission near the gain peak, narrowing the emission profile until, at threshold, a single mode at the gain peak is singled out as the lasing mode (blue curve).

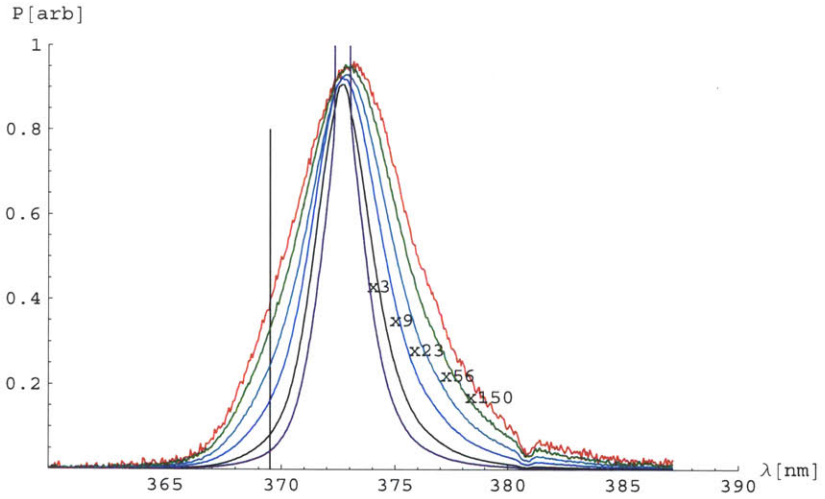

Figure B-5: Emission profiles of a room-temperature 373nm Nichia laser diode at various injected currents I relative to the threshold current I_{th}. Red curve: $I = 0.2\, I_{th}$, black curve: $I = 0.9\, I_{th}$, purple curve: $I = 1.1\, I_{th}$. The laser threshold current was $I_{th} = 45$ mA. The vertical line denotes the target wavelength of 369.5 nm. We thank Andrew Benedick and prof. Franz Kärtner's group for giving us access to an Ando AQ6315E optical spectrum analyzer for this measurement.

To tune the laser wavelength to the 369.5 nm Doppler cooling transition in Yb^+ (vertical black line on Figure B-5), the peak of the gain profile seen by the laser cavity photons needed to be shifted. One way to do this was to provide external feedback to the laser by a frequency-selective element such as a diffraction grating [RWE+95] (Figure B-6).

Together with the front facet of the diode, the grating acts as a reflector with effective reflection coefficient

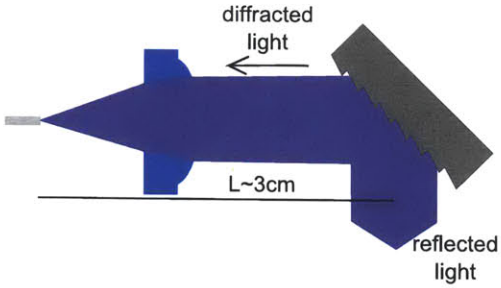

Figure B-6: A diffraction grating in Littrow configuration used to narrow the emission and tune the wavelength of a diode laser

$$\begin{aligned} r'(\lambda) &= r + t^2\left(r_g\sqrt{\eta}e^{i\phi} - r_g^2\eta e^{2i\phi}r + r_g^3\eta^{3/2}e^{3i\phi}r^2 + ...\right) \\ &= r + \frac{t^2\sqrt{\eta}r_g(\lambda)e^{i\phi}}{1 + rr_g(\lambda)\sqrt{\eta}e^{i\phi}} \end{aligned}$$

where r and t are the laser output facet reflection and transmission coefficients, $r_g(\lambda)$ is the grating reflection coefficient, η is the efficiency of coupling light back into the laser waveguide mode, and $\phi = 2\pi L/\lambda$ is the round-trip phase from the laser front facet to the grating. The presence of the grating alters the round-trip gain of the laser cavity from $g_{medium}|r|^2$ to $g_{medium}|r'(\lambda)|^2$, allowing one to compensate for the shape of the gain curve and tune the emission wavelength of the laser.

On a fine frequency scale of order $c/(2L) \sim 5$ GHz, the wavelength-selectivity of the grating assembly derives from the dependence of the grating cavity round trip phase ϕ on the light frequency. The use of this effect for obtaining stable single-frequency operation as well as modulating laser diodes will be described later.

On a larger scale, the frequency selectivity derives from the dependence of the angle of the diffracted light on wavelength:

$$\frac{\Delta\theta}{\Delta\lambda} = \frac{1}{\sqrt{4d^2 - \lambda^2}}$$

together with the overlap of the reflected light with the collimated laser mode:

$$\int_{-\infty}^{\infty} \frac{1}{\sqrt{2\pi}w/2} e^{-2x^2/w^2} e^{ik\Delta\theta x} dx = \exp\left\{-\frac{k^2w^2\Delta\lambda^2}{8(4d^2 - \lambda^2)}\right\} \tag{B.2}$$

with d the grating line spacing. Assuming that the reflectivity of the front diode facet comes mostly from the index mismatch between the waveguide and air so that $r \approx (n_o - 1)/(n_o + 1) \approx 0.45$, $t \approx 2\sqrt{n_0}/(n_0 + 1) \approx 0.9$ and using a high-reflectivity

grating ($r_g \approx \sqrt{0.6}$) together with good mode-matching ($\eta \sim 0.5$), one may expect an increase in the reflectivity seen by the laser medium from 20% to 65% with with a Gaussian full-width at half-maximum of less than 0.2 nm. The resulting threefold enhancement of the effective gain at the target wavelength would be enough to shift the total gain maximum and laser emission to the 369.5 nm Doppler cooling wavelength.

To test this, a 2400 lines/mm holographic grating with 52% diffraction efficiency for our laser polarization (electric field parallel to grating lines) was used in a Littrow configuration with a Nichia NDHU110APAE2 373nm laser diode. The lowest wavelength achievable in this fashion was 371.2 nm. We suspect that these poor results are due to low backcoupling efficiency and a higher front facet reflectivity.

The reflectivity of the front facet can be decreased by coating the waveguide output with a $\lambda/4$ thick layer of an appropriate low-loss index-matching material ($n = \sqrt{n_o n_{air}}$). In an ideal case, the reflectivity of the laser cavity is entirely determined by the grating as $r' = \sqrt{\eta} r_g e^{i\phi}$, allowing wavelength tuning across most of the gain region.

To test this method with GaN devices, we coated 6 Nichia NDHU110APAE2 laser diodes with an anti-reflective Al_2O_3 layer in an e-beam evaporator. The diode TO18 packages were opened and the diodes put into the evaporator chamber. The threshold current of the diodes was monitored during evaporation and the coating thickness adjusted to maximize threshold, indicating a minimum in the reflectivity of the front facet.

Upon subsequent testing in air, three diodes exhibited an electrical short. Of the remaining three diodes, two showed laser threshold with an external grating. However, over two months of operation, the threshold current of both diodes increased until no laser emission could be obtained.

B.1.4 Temperature Tuning

Another method for tuning the emission of laser diodes is by changing the temperature of the gain medium. The free emission wavelength of a Nichia 373nm laser diode as it is cooled to -25 °C is shown on Figure B-8. The corresponding threshold current is shown on Figure B-10.

An undesired effect observed during the cooling of the GaN diodes was an increase in the operating voltage (Figure B-9), possibly due to an increased contact resistance of the diode. Fortunately, any increase in the device heat load is largely compensated by the expected decrease in threshold current with temperature (Figure B-10).

B.1.5 Microwave modulation

One method to perform multi-qubit operations on Yb^+ is to employ Raman transitions between the ground $F = 0$ and $F = 1$ hyperfine states separated by 12.6 GHz. To preserve coherence during the ion operations, it is neccessary that the two Raman beams be phase coherent. One way of achieving this would be to generate 6.3 GHz-sidebands on the same laser beam by direct current modulation of a laser diode. To this end, we investigated the current modulation response of Nichia laser diodes.

A Nichia 373nm NDHU110APAE3 laser diode (newer model of NDHU110APAE2) was plugged into a TO18 socket (Thorlabs S7060R) which was soldered directly to the pin of a SMA microwave bulkhead connector. External feedback to the diode was provided from a Thorlabs GH13-3600U 3600 lines/mm holographic grating located 5.5 cm from the diode and providing 15% diffraction efficiency in Littrow configuration for laser polarization parallel to the grating lines.

The diode assembly was connected via a 50 Ω SMA cable to a high-speed bias tee (ZX85-12G+ from Minicircuits, NY). The DC input of the bias tee was driven with a low-noise DC-100 kHz current source while the microwave port of the bias tee was connected to one port of a 60 MHz - 40 GHz network analyzer. The second port of the network analyzer was used to monitor amplitude modulation of the laser diode using a high-speed photodiode (Hamamatsu G4175) biased via a 15 GHz microwave bias tee (from Picosecond Pulse Labs, CO) and fed into a high-speed RF amplifier (LPA-10-10 amplifier from RF Bay, Inc.).

The total laser diode modulation (both amplitude and phase) was simultaneously monitored using a confocal, scanning Fabry-Perot resonator with finesse $\mathcal{F} \sim 100$. Comparing the modulation sidebands observed on the Fabry-Perot to the photodiode signal and assuming that the ratio of frequency and amplitude modulation does not change between 100 MHz and 3 GHz, we obtain the modulation response shown on Figure B-7.

The rapid decrease in the modulation response above 700 MHz of $\approx$ 60 dB/decade makes direct modulation of the Nichia laser diodes at 6.3 GHz unlikely. However, the required modulation has been achieved by using the enhancement of the grating cavity, here seen at 2.5 GHz. By using a shorter cavity, required modulation at 6.3 GHz has been achieved.

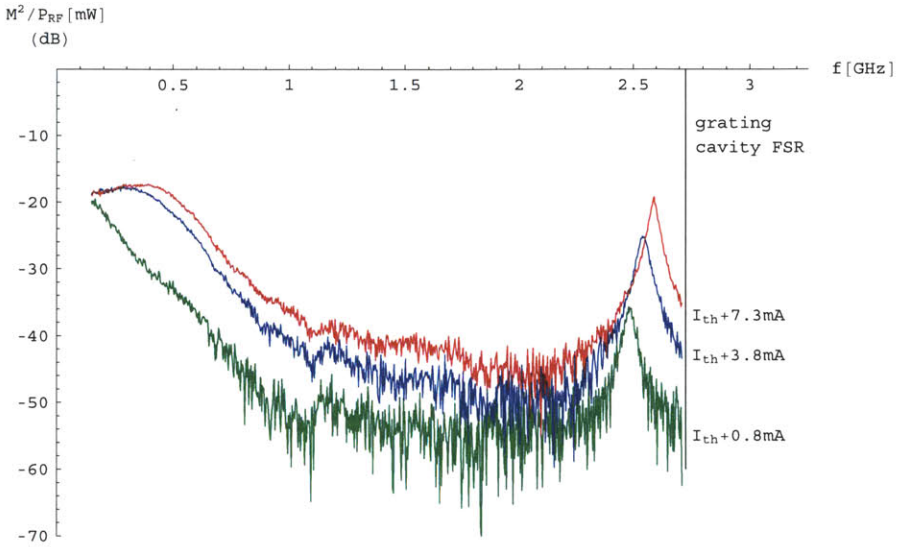

Figure B-7: The square of the modulation index of a NDHU110APAE3 diode in external grating feedback configuration relative to the incident RF power in the $50\,\Omega$ feed line. The grating cavity length is (5.5 ± 0.2) cm and the grating reflectivity 15% for laser polarization parallel to the grating lines.

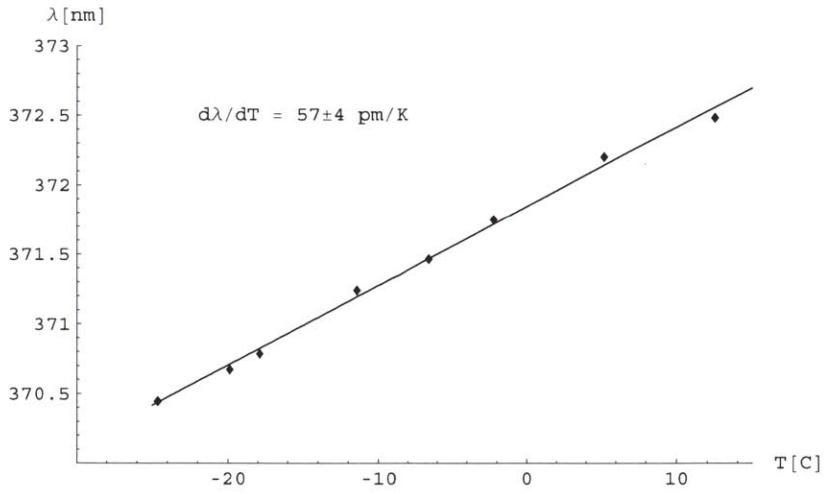

Figure B-8: Temperature dependence of the emission wavelength of a free-running 373nm Nichia NDHU110APAE2 laser diode. The diode is held clamped in an aluminum Thorlabs LM9F mount whose temeprature is monitored using a negative temperature coefficient (NTC) resistor placed in a hole drilled in the LM9F mount and thermally contacted using thermally conductive paste.

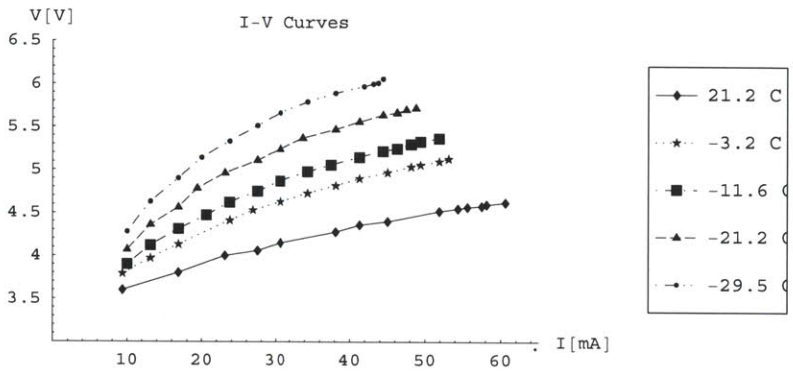

Figure B-9: Current-voltage curves of a Nichia NDHU110APAE2 373nm laser diode depending on temperature

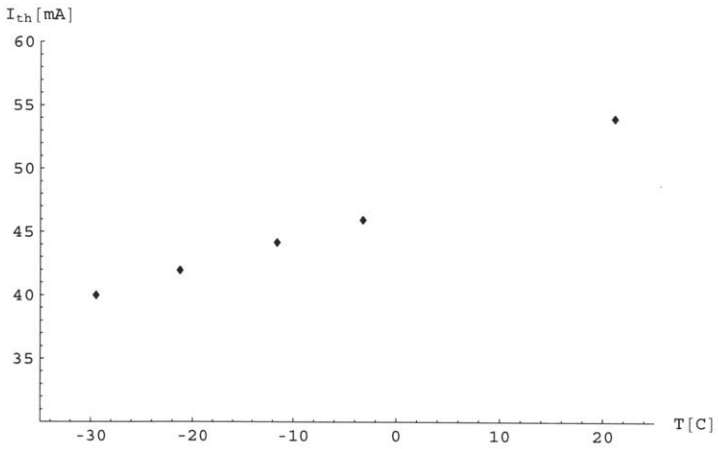

Figure B-10: Temperature dependence of the threshold current of a free-running 373 nm Nichia NDHU110APAE2 laser diode

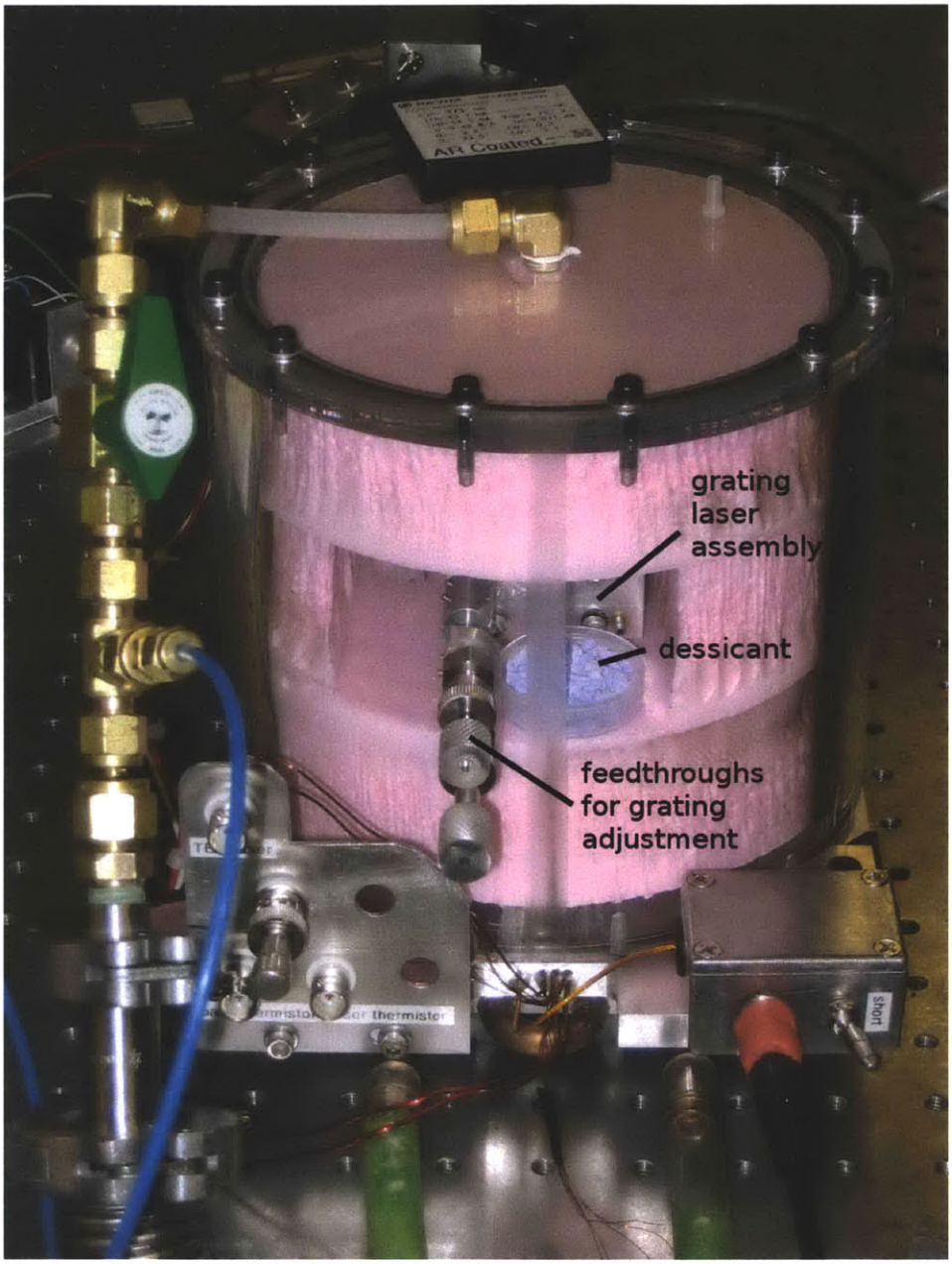

Figure B-11: A grating grating laser based on a Nichia 373nm laser diode operating at $-30°C$. The entire grating laser assembly is cooled between $-15°C$ and $-30°C$ using a two-stage thermo-electric cooler. The system is insulated with Dow Corning InsulPink insulation and sealed in a moisture-tight container containing dessicant.

Appendix C

Reprint of "Bright Source of Cold Ions for Surface Electrode Traps"

This appendix contains a reprint of [CGC+07]: Marko Cetina, Andrew Grier, Jonathan Campbell, Isaac Chuang, and Vladan Vuletić, *Bright source of cold ions for surface electrode traps,* Phys. Rev. A **76,** 041401(R) (2007).

PHYSICAL REVIEW A **76**, 041401(R) (2007)

Bright source of cold ions for surface-electrode traps

Marko Cetina, Andrew Grier, Jonathan Campbell, Isaac Chuang, and Vladan Vuletić
Department of Physics, MIT-Harvard Center for Ultracold Atoms, and Research Laboratory of Electronics, Massachusetts Institute of Technology, Cambridge, Massachusetts 02139, USA
(Received 1 February 2007; published 24 October 2007)

We produce large numbers of low-energy ions by photoionization of laser-cooled atoms inside a surface-electrode-based Paul trap. The isotope-selective trap's loading rate of 4×10^5 Yb^+ ions/s exceeds that attained by photoionization (electron-impact ionization) of an atomic beam by three (six) orders of magnitude. Traps as shallow as 0.13 eV are easily loaded with this technique. The ions are confined in the same spatial region as the laser-cooled atoms, which will allow the experimental investigation of interactions between cold ions and cold atoms or Bose-Einstein condensates.

DOI: 10.1103/PhysRevA.76.041401 PACS number(s): 32.80.Pj, 03.67.Lx, 32.80.Fb, 34.70.+e

Among the many candidate systems for large-scale quantum-information processing, trapped ions currently offer unmatched coherence and control properties [1]. The basic building blocks of a processor, such as quantum gates [2], subspaces with reduced decoherence [3], quantum teleportation [4,5], and entanglement of up to eight ions [6,7] have already been demonstrated. Nevertheless, since a logical qubit will likely have to be encoded simultaneously in several ions for error correction [8,9], even a few-qubit system will require substantially more complex trap structures than currently in use. Versatile trapping geometries can be realized with surface-electrode Paul traps, where electrodes residing on a surface create three-dimensional confining potentials above it [10]. Such surface traps allow good optical access to the ions and can be fabricated using simpler lithographic techniques than three-dimensional traps [11–13].

While the prospect of scalable quantum computing has been the main motivation for developing surface-electrode traps, it is likely that this emerging technology will have a number of other important, and perhaps more immediate, applications. Porras and Cirac have proposed using dense lattices of ion traps, where neighboring ions interact via the Coulomb force, for quantum simulation [14]. A lattice with a larger period, to avoid ion-ion interactions altogether, could allow the parallel operation of many single-ion optical clocks [15], thereby significantly boosting the signal-to-noise ratio. The increased optical access provided by planar traps could be used to couple an array of ion traps to an optical resonator and efficiently map the stored quantum information onto photons [16]. Since the surface-electrode arrangement allows one to displace the trap minimum freely in all directions, ions can be easily moved through an ensemble of cold neutral atoms for investigations of cold-ion–atom-collisions [17–19], as proposed by Smith *et al.* [20]. One could even implant a single ion inside a Bose-Einstein condensate [21].

Compared to standard Paul traps [11–13], the open geometry of surface-electrode traps restricts the trap depth and increases the susceptibility to stray electric fields, making trap loading and compensation more difficult. Nevertheless, successful loading from a thermal atomic beam has recently been demonstrated using both photoionization [22] and electron-impact ionization aided by buffer gas cooling [23]. Photoionization, first demonstrated in Ref. [24], is superior in that it provides faster, isotope-selective loading [22,25–27]. However, the loading rate R for microfabricated traps remains relatively low ($R<1$ s^{-1} [11]), while charge-exchange collisions make it difficult to prepare large, isotopically pure samples even in macroscopic traps with $R\sim100$ s^{-1} [26].

In this Rapid Communication, we demonstrate that large numbers of low-energy ions can be produced by photoionization of a laser-cooled, isotopically pure atomic sample, providing a robust and virtually fail-safe technique to load shallow or initially poorly compensated surface ion traps. We achieve a loading rate of 4×10^5 Yb ions per second into a $U_0=0.4$ eV deep printed-circuit ion trap, several orders of magnitude larger than with any other method demonstrated so far, and have directly loaded traps as shallow as $U_0=0.13$ eV. The trapping efficiency for the generated low-energy ions is of order unity. We also realize a system where ions are confined in the same spatial region as laser-cooled atoms [20], allowing for future experimental studies of cold ion-atom collisions [17–19].

Efficient photoionization of Yb atoms is accomplished with a single photon from the excited $^1P_1$ state that is populated during laser cooling, which lies 3.11 eV (corresponding to a 394 nm photon) below the ionization continuum. Due to momentum and energy conservation, most of the ionization photon's excess energy is transferred to the electron. Therefore, when we ionize atoms at rest even with 3.36 eV (369 nm) photons (the ion cooling light), the calculated kinetic energy of the ions amounts to only 8 mK (0.7 μeV). Previously, excitation of cold atoms to high-lying Rydberg states has been used to generate and study cold but untrapped plasmas in the 1 K temperature range [32].

The ion trap is a commercial printed circuit on a vacuum-compatible substrate (Rogers 4350) with low radiofrequency (rf) loss. The three 1-mm-wide, 17.5-μm-thick copper rf electrodes are spaced by 1-mm-wide slits (Fig. 1), whose inner surfaces are metallized to avoid charge buildup. Twelve dc electrodes placed outside the rf electrodes provide trapping in the axial direction and permit cancellation of stray electric fields. In addition, the rf electrodes can be dc biased to apply a vertical electric field. All dielectric surfaces outside the dc electrodes have been removed with the exception of a 500-μm-wide strip supporting the dc electrodes.

The ratio between the rf voltages V_c and V_o applied to the

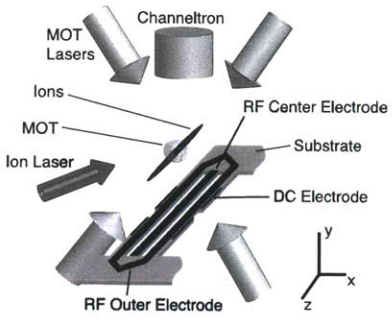

FIG. 1. Setup for loading a surface-electrode ion trap by in-trap photoionization of laser-cooled atoms. A ^{172}Yb or ^{174}Yb magneto-optical trap (MOT) is formed 4 mm above the trap surface. Cold Yb^+ ions are produced inside the Paul trap by single-photon excitation from the excited $^1P_1$ atomic state.

center and outer electrodes, respectively, determines the trap height above the surface. For $V_c/V_o=-0.63$, the rf node is located 3.6(1) mm above the surface. At a rf frequency of 850 kHz $V_o=540$ V yields a secular trap potential with a predicted depth of $U_0=0.16$ eV (Fig. 2) and a calculated (measured) secular frequency of 100 kHz (90 kHz). The trap can be deepened by applying a static bias voltage $V_{dc}<0$ to all rf electrodes [23] and unbiased after loading (Fig. 2). This enables us to load traps with depths as small as $U_0=0.13$ eV.

All Yb and Yb^+ cooling, detection, and photoionization light is derived from near-uv external-cavity diode lasers. A master-slave laser system consisting of an external-cavity grating laser and an injected slave laser using violet laser diodes (Nichia) delivers 10 mW in three pairs of 3.4-mm-diameter beams for a magneto-optical trap (MOT) operating on the $^1S_0\rightarrow{}^1P_1$ transition at 399 nm [28]. The MOT, located 4 mm above the substrate, is loaded with ^{171}Yb, ^{172}Yb, ^{173}Yb, ^{174}Yb, or ^{176}Yb atoms from an atomic beam produced by a nearby small oven, and typically contains 5×10^5 Yb atoms at an estimated temperature of a few millikelvins.

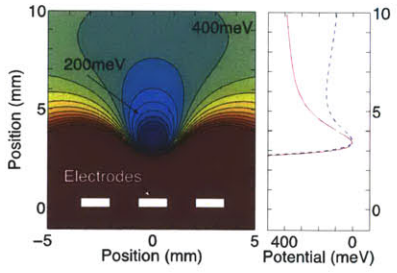

FIG. 2. (Color online) Left: Trapping pseudopotential for rf amplitudes of $V_o=540$ V and $V_c=-340$ V applied to the outer and center electrodes together with a dc bias of −1.25 V applied to all electrodes. The contours are spaced by 50 meV. Right: The dc-unbiased trap (dashed blue curve) exhibits less micromotion heating but is significantly shallower than the dc-biased trap (solid red curve).

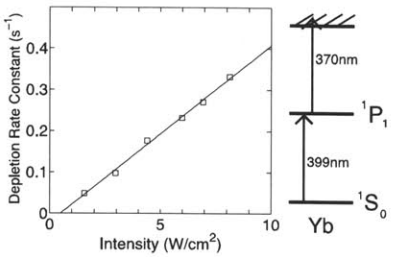

FIG. 3. Linear dependence of the loss rate constant of a ^{174}Yb MOT (rms width of 300 μm) on 370 nm beam peak intensity ($w=43$ μm), indicating that photoionization is accomplished with a single 370 nm photon from the $^1P_1$ state that is populated during laser cooling with 399 nm light.

Photoionization from the excited $^1P_1$ state populated during laser cooling is accomplished using either the ion cooling laser at 370 nm with a power of 750 μW and intensity of 500 mW/cm^2, or a focused uv-light-emitting diode at 385±15 nm with a power of 8.7 mW and intensity of 125 mW/cm^2 at the MOT position. Efficient ionization is manifest as a 30% decrease in MOT atom number due to an increase in the MOT decay rate constant by $\Gamma=0.3$ s^{-1}. The generated ions are also detected directly with a Burle Magnum 5901 Channeltron avalanche detector located 4 cm above the MOT. The uv-light-induced MOT loss depends linearly on uv laser intensity (Fig. 3), indicating that the ionization process involves a single 370 nm photon. We have also confirmed that the dominant ionization proceeds from the $^1P_1$ state: when we apply on-off modulation to both the 399 nm MOT light and the 370 nm uv light out of phase, such that the uv light interacts only with ground-state atoms, we observe a more than 13-fold decrease in ionization compared to that for in-phase modulation. From the observed loss rate in combination with an estimated saturation $s=0.6-2$ of the $^1S_0\rightarrow{}^1P_1$ MOT transition, we determine a cross section $\sigma=4\times10^{-18}$ cm^2 for ionization of ^{174}Yb with 370 nm light from the excited $^1P_1$ state, accurate to within a factor of 2.

The photoionization typically produces 4×10^5 cold ions per second near the minimum of the pseudopotential. Given this bright source of cold ions, trapping is easily accomplished even without ion laser cooling. We have thus trapped $^{171}Yb^+$, $^{172}Yb^+$, $^{173}Yb^+$, $^{174}Yb^+$, and $^{176}Yb^+$ ions simply by changing the MOT frequency to prepare the corresponding atomic isotopes. When searching for an initial signal with a poorly compensated trap, or to measure trap loading rates, we detect the ions after a short trapping time with the Channeltron. Since the detector electric field overwhelms the pseudopotential, we turn on the Channeltron in 1 μs using a Pockels cell driver, fast compared to the 3.3 μs flight time of the ions. Figure 4 shows the loading rate for photoionization of ^{172}Yb atoms from the MOT and from the atomic beam for the compensated trap with a depth of $U_0=0.4$ eV shown in Fig. 2. The loading rates of $^{171}Yb^+$, $^{173}Yb^+$, $^{174}Yb^+$, and $^{176}Yb^+$ relative to $^{172}Yb^+$ are 0.32, 0.03, 0.65, and 1.36, respectively, matching the observed MOT fluorescences. The absolute calibration of ion number in Fig. 4 has been accom-

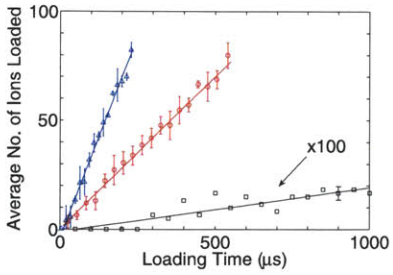

FIG. 4. (Color online) Number of trapped ^{172}Yb ions for photoionization loading with the uv LED from an atomic beam (black squares), with a uv LED from a MOT (red circles), and from a MOT with both uv LED and a 370 nm laser (blue triangles). The fitted rates are $R=200$, 1.4×10^5, and 3.8×10^5 s^{-1}, respectively.

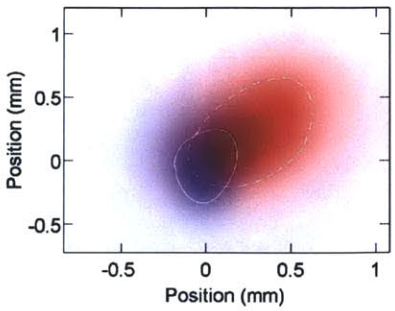

FIG. 5. (Color online) Spatially overlapping ion and atom clouds. The false color image shows a trapped ^{172}Yb$^+$ ensemble containing 10^2-10^3 ions (blue cloud, lower left), placed inside a magneto-optical trap containing 5×10^5 neutral ^{172}Yb atoms (red cloud, upper right). The solid and dashed lines indicate the half-maximum contour for the ions and atoms, respectively.

plished by comparing the Channeltron signal to the fluorescence from a known number of ions, as described below. The *loading* rate from the MOT, $R=4\times10^5$ s^{-1}, is three orders of magnitude higher than that from the beam alone, compared to a ratio of only 4 in the ion *production* rates measured without a trap. Thus ions that were produced from laser-cooled atoms are 200 times more likely to be trapped than ions produced from the atomic beam. We ascribe this difference to the much higher MOT atomic density near the ion-trap minimum, and to the lower energy of the produced ions. As the MOT is isotopically pure, our observations of a 10^3 loading rate ratio between MOT and atomic beam imply an additional factor of 10^3 in isotope selectivity beyond the 400:1 isotope selectivity resulting from spectrally selective photoionization of an atomic beam [26].

From other work comparing electron-impact ionization and photoionization loading [25,26], we conclude that our loading rate is 10^6–10^7 times higher than that achieved with electron-impact ionization, 10^6 times higher than demonstrated for other surface-electrode or microfabricated traps [11,22,23], and 10^3-10^4 higher than in any previous experiment. By comparing the typical observed loss rate from the MOT (10^5 s^{-1}) to the typical ion-trap loading rate (2×10^5 s^{-1}) under similar conditions, we conclude that our trapping efficiency for the generated ions is comparable to unity. Near-unity efficiency may help suppress anomalous ion heating that has been linked to electrode exposure to the atomic beam during the loading process [13]. The large loading rate will also be beneficial for applications that require a large, isotopically pure sample in a microfabricated trap, such as quantum simulation with an ion lattice [14].

The trapped ions are cooled and observed via fluorescence using an external-cavity grating laser [29]. To reach the target wavelength of 369.525 nm with a 372 nm laser diode (Nichia), we cool the diode to temperatures between −10 and −20 °C. The laser provides 750 μW of power into a 600-μm-diameter beam at the trap, and for initial cooling is typically tuned 150 MHz below the $^2S_{1/2}\rightarrow{}^2P_{1/2}$ transition. An external-cavity repumper laser operating at 935 nm is also necessary to empty the long-lived $^2D_{3/2}$ state on the $^2D_{3/2}\rightarrow{}^2D[3/2]_{1/2}$ transition [30]. With cooling, ^{172}Yb$^+$ ion lifetimes in excess of 10 min were observed, limited by either laser drift or collisions with the atomic beam, compared to 5 s without laser cooling. Laser cooling of ^{174}Yb$^+$ has also been observed, while cooling of the odd isotope ^{171}Yb$^+$ would require an additional laser frequency for hyperfine repumping. The uv light scattered by the ions is collected with an aspheric lens (numerical aperture=0.4) placed inside the vacuum chamber and optimized for light gathering. The collected light passes through an interference filter and is evenly split between a charge-coupled device camera and a photomultiplier, obtaining a maximum count rate of 5000 s^{-1} per ion.

To calibrate the Channeltron detector, we first cool a small cloud of typically 100 ^{172}Yb$^+$ ions to below the gas-liquid transition temperature, as identified by a small drop and subsequent strong rise in fluorescence as the laser is scanned from the long-wavelength side towards resonance [31,33]. By comparing the homogenously broadened fluorescence of the cold cloud to that of a single trapped ion, we determine the absolute number of ions loaded and subsequently measure the Channeltron signal for the same cloud.

The optical observation of the trapped ions allows us to determine the trap position and optimize the overlap with the neutral-atom cloud. Figure 5 shows that for the optimal loading position of the trap, the pseudopotential minimum, adjusted vertically via the amplitude ratio of the rf voltages, is located inside the neutral-atom cloud. We have thus achieved simultaneous trapping of cold ions and neutral atoms in the same spatial region, which will allow the experimental investigation of cold-ion–atom collisions [17,18,20] and charge transport [19]. To study collisions beyond the current Doppler limit, the ions could be sideband cooled while the atoms could be loaded into an optical lattice [34]. The latter would also eliminate residual ion-trap loading due to MOT self-ionization.

In conclusion, we discuss a possible application of our loading technique to quantum simulation or many-ion optical clocks with signal-to-noise ratio superior to that of single-ion schemes. We consider a 100×100 array of weakly coupled single-ion traps, to be loaded with a single isotope. At the loading rates $R<1$ s^{-1} typical of atomic-beam photoioniza-

tion loading for microfabricated traps [11], this array would take many hours to load, during which time charge-exchange collisions with the atomic beam would replace the isotope of interest with undesired ions. To address these problems, we propose a nested electrode design, where large outer electrodes provide initial trapping in the MOT region, as demonstrated in this paper, and smaller inner electrodes define the array of traps near the chip surface. A sample loaded into the larger trap can then be transferred adiabatically into the array by varying the rf voltages supplied to the different electrodes. With the technique demonstrated here, we expect to load such an array with $1:10^4$ isotope purity in less than 1 s.

We would like to thank Brendan Shields and Ken Brown for assistance. This work was supported in part by the NSF Center for Ultracold Atoms.

[1] P. Zoller *et al.*, Eur. Phys. J. B **36**, 204 (2005).
[2] C. Monroe, D. M. Meekhof, B. E. King, W. M. Itano, and D. J. Wineland, Phys. Rev. Lett. **75**, 4714 (1995).
[3] D. Kielpinski, V. Meyer, M. A. Rowe, C. A. Sackett, W. M. Itano, C. Monroe, and D. J. Wineland, Science **291**, 1013 (2001).
[4] M. D. Barrett *et al.*, Nature (London) **429**, 737 (2004).
[5] M. Riebe *et al.*, Nature (London) **429**, 734 (2004).
[6] D. Leibfried *et al.*, Nature (London) **438**, 639 (2005).
[7] H. Haeffner *et al.*, Nature (London) **438**, 643 (2005).
[8] P. W. Shor, Phys. Rev. A **52**, R2493 (1995).
[9] A. M. Steane, Phys. Rev. Lett. **77**, 793 (1996).
[10] J. Chiaverini *et al.*, Quantum Inf. Comput. **5**, 419 (2005).
[11] D. Stick, W. Hensinger, S. Olmschenk, M. Madsen, K. Schwab, and C. Monroe, Nat. Phys. **2**, 36 (2006).
[12] B. DeMarco *et al.*, Quantum Inf. Comput. **5**, 419 (2005).
[13] L. Deslauriers, S. Olmschenk, D. Stick, W. K. Hensinger, J. Sterk, and C. Monroe, Phys. Rev. Lett. **97**, 103007 (2006).
[14] D. Porras and J. I. Cirac, Phys. Rev. Lett. **93**, 263602 (2004).
[15] W. H. Oskay *et al.*, Phys. Rev. Lett. **97**, 020801 (2006).
[16] M. Keller, B. Lange, K. Hayasaka, W. Lange, and H. Walther, Nature (London) **431**, 1075 (2004).
[17] R. Côté and A. Dalgarno, Phys. Rev. A **62**, 012709 (2000).
[18] O. Makarov, R. Côté, H. Michels, and W. W. Smith, Phys. Rev. A **67**, 042705 (2003).
[19] R. Côté, Phys. Rev. Lett. **85**, 5316 (2000).
[20] W. W. Smith, O. P. Makarov, and J. Lin, J. Mod. Opt. **52**, 2253 (2005).
[21] R. Côté, V. Kharchenko, and M. Lukin, Phys. Rev. Lett. **89**, 093001 (2002).
[22] S. Seidelin *et al.*, Phys. Rev. Lett. **96**, 253003 (2006).
[23] K. R. Brown *et al.*, Phys. Rev. A **75**, 015401 (2007).
[24] N. Kjaergaard *et al.*, Appl. Phys. B: Lasers Opt. **71**, 207 (2000).
[25] C. Balzer, A. Braun, T. Hannemann, C. Paape, M. Ettler, W. Neuhauser, and C. Wunderlich, Phys. Rev. A **73**, 041407(R) (2006).
[26] D. M. Lucas *et al.*, Phys. Rev. A **69**, 012711 (2004).
[27] M. Keller, B. Lange, and K. Hayasaka, J. Phys. B **36**, 613 (2003).
[28] C. Y. Park and T. H. Yoon, Phys. Rev. A **68**, 055401 (2003).
[29] D. Kielpinski, M. Cetina, J. A. Cox, and F. X. Kärtner, Opt. Lett. **31**, 757 (2005).
[30] A. S. Bell, P. Gill, H. A. Klein, A. P. Levick, C. Tamm, and D. Schnier, Phys. Rev. A **44**, R20 (1991).
[31] F. Diedrich, E. Peik, J. Chen, W. Quint, and H. Walther, Phys. Rev. Lett. **59**, 2931 (1987).
[32] Y. C. Chen *et al.*, Phys. Rev. Lett. **93**, 265003 (2004).
[33] L. Hornekaer and M. Drewsen, Phys. Rev. A **66**, 013412 (2002).
[34] Y. Takasu *et al.*, Phys. Rev. Lett. **91**, 040404 (2003).

Appendix D

Reprint of "Observation of Cold Collisions Between Trapped Ions and Trapped Atoms"

This appendix contains a reprint of [GCOV09]: Andrew T. Grier, Marko Cetina, Feđa Oručević, and Vladan Vuletić, *Observation of cold collisions between trapped ions and trapped atoms*, Phys. Rev. Lett. **102**, 223201 (2009).

Observation of Cold Collisions between Trapped Ions and Trapped Atoms

Andrew T. Grier, Marko Cetina, Fedja Oručević, and Vladan Vuletić
Department of Physics, MIT-Harvard Center for Ultracold Atoms, and Research Laboratory of Electronics, Massachusetts Institute of Technology, Cambridge, Massachusetts 02139, USA
(Received 26 August 2008; published 4 June 2009)

We study cold collisions between trapped ions and trapped atoms in the semiclassical (Langevin) regime. Using Yb^+ ions confined in a Paul trap and Yb atoms in a magneto-optical trap, we investigate charge-exchange collisions of several isotopes over three decades of collision energies down to 3 μeV ($k_B \times 35$ mK). The minimum measured rate coefficient of 6×10^{-10} cm^3 s^{-1} is in good agreement with that derived from a Langevin model for an atomic polarizability of 143 a.u.

DOI: 10.1103/PhysRevLett.102.223201 PACS numbers: 34.70.+e, 31.15.ap, 32.10.Hq

Studies of cold collisions between trapped neutral atoms have revealed a plethora of fascinating quantum phenomena, including Wigner threshold laws [1], magnetically tunable Feshbach resonances [2], controlled molecule formation [3], and the suppression of individual scattering channels [4]. Collisions between trapped ions, on the other hand, are featureless since the strong long-range repulsive Coulomb interaction prevents the ions from approaching each other. Collisions between ions and neutral atoms [5–8] fall into an intermediate regime where an attractive long-range r^{-4} potential leads to semiclassical behavior for a wide range of collision energies, but where quantum phenomena dominate at very low energies. Cold ion-atom collisions have been proposed as a means to implement quantum gates [9], to cool atoms [7,10] or molecules [11,12] lacking closed optical transitions, to bind small Bose-Einstein condensates to an ion [13], or to demonstrate novel charge-transport dynamics [14].

As a function of collision energy, charge-exchange and momentum-transfer ion-atom collisions exhibit three distinct regimes [6,7]: a high-energy classical (hot) regime with a logarithmic dependence of cross section σ on energy E, a wide semiclassical Langevin (cold) regime with a power-law dependence $\sigma(E) \propto E^{-1/2}$ [5,6], and a quantum (ultracold) regime where contributions from individual partial waves can be distinguished. However, given the large forces on ions produced by small stray electric fields, it has been difficult to reach experimentally even the semiclassical regime. References [15,16], studying charge exchange at $E \sim 100$ meV, report the only observations of Langevin-type ion-atom collisions. In ion-molecule systems, experimental signatures of Langevin collisions have been seen at high temperature [17–19], and recently also at 1 K (80 μeV) [20]. In all previous work, at most one of the collision partners was trapped.

In this Letter, we study collisions between independently trapped, laser-cooled ions and atoms down to unprecedented low energy (3 μeV) in the semiclassical collision regime. Using a double-trap system [21], we investigate resonant charge-exchange collisions for different $Yb^+ + Yb$ isotope combinations and find agreement with the Langevin model to within a factor of 2 over three decades of energy [5,6]. The highest energy, 4 meV = $k_B \times 45$ K, corresponds to the transition to the classical regime [22,23], while at the lowest energy, 3 μeV = $k_B \times$ 35 mK, where approximately 40 partial waves contribute to the cross section, isotope shifts should become relevant. The lower limit on collision energy is set by our ability to detect and minimize the micromotion of a single ion in the Paul trap.

The long-range interaction potential between a singly charged ion and a neutral atom is the energy of the induced atomic dipole in the ion's electric field, given by $V(r) = -C_4/(2r^4)$, where $C_4 = \alpha q^2/(4\pi\epsilon_0)^2$ is proportional to the atomic polarizability α, and q is the electron charge. For a given collision energy E in the center-of-mass frame, there exists a critical impact parameter $b_c = (2C_4/E)^{1/4}$ that separates two types of collisions: those with impact parameter $b < b_c$ that result in inward-spiraling orbits of radius approaching zero, and those with $b > b_c$ that never cross the angular-momentum barrier [5,24].

For collisions of an ion with its parent atom, a semiclassical resonant charge-exchange cross section σ_{ce} can be simply derived, provided that b_c is large compared to the range of the molecular potential. For collisions with $b > b_c$, the electron should remain bound to the incoming atom. For close-range collisions with $b < b_c$, the electron in the resonant process $A^+ + A \rightarrow A + A^+$ is equally likely to exit attached to either nucleus, resulting in either a charge-exchange collision or an elastic collision. It follows that the resonant charge-exchange cross section is $\sigma_{ce} = \sigma_L/2$, where $\sigma_L = \pi b_c^2$ is the Langevin cross section. The corresponding semiclassical rate coefficient $K_{ce} = \sigma_{ce} v = \pi\sqrt{C_4/\mu}$, where v is the relative velocity and μ the reduced mass, is independent of energy.

At high energies this model becomes invalid when b_c becomes so small that charge exchange outside the centrifugal barrier starts to play a role; for Yb, this occurs at energies $E \gtrsim 10$ meV = $k_B \times 120$ K [6,22,23]. At very

low energies, the semiclassical Langevin model ceases to be valid when the s-wave scattering limit is reached, which happens near $E_s \sim \hbar^4/(2\mu^2 C_4) = 4$ peV $= k_B \times 50$ nK. Quantum simulations [6] of this system [22] confirm the semiclassical Langevin model in the indicated energy range. For collisions between different isotopes, the Langevin expression should be modified at low collision energies comparable to the small difference in binding energy of the electron to the two nuclei, i.e., the isotope shift of the ionization potential. In this case, we expect endoenergetic charge-exchange collisions to be suppressed [25,26].

We use a magneto-optical trap (MOT) in combination with a Paul trap, as originally proposed by Smith [11]. The setup, shown in Fig. 1, is described in detail elsewhere [21]. In the present work, ^{172}Yb, ^{174}Yb, or ^{171}Yb atoms are selectively loaded from an atomic beam into a MOT by tuning the laser frequency near the $^1S_0 \rightarrow {}^1P_1$ transition at $\lambda_a = 398.8$ nm. Typically, the MOT is operated at a 75 G/cm magnetic-field gradient and contains 3×10^5 atoms at a peak density of 2×10^8 cm^{-3} and a temperature of 700 μK as determined by a time-of-flight measurement.

Cold ions are produced by nonresonant photoionization from the excited $^1P_1$ state of the MOT with 370-nm light from a semiconductor laser [21]. The ion trap is a surface-electrode Paul trap printed on a vacuum-compatible substrate [21], and is typically operated at 1.4 MHz to create a 0.3 eV deep pseudopotential trap 3.6 mm above the trap surface with a secular frequency of 67 kHz. Ion trap populations can be adjusted between a single and 10^4 ions by varying the trap loading time.

Two beams from the same 370 nm laser used for photoionization provide Doppler cooling of the ions on the $^2S_{1/2} \rightarrow {}^2P_{1/2}$ transition along all three principal trap axes. Ions that decay to a metastable D state are repumped [27] using a laser operating at 935 nm [21]. We detect the ion population by monitoring trap fluorescence at 370 nm with a photomultiplier tube. A single cold, trapped ion produces 5 kcounts/s.

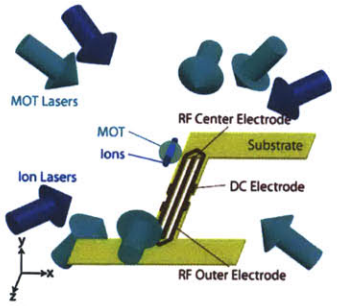

FIG. 1 (color online). Setup for trapping neutral (MOT) and singly charged (surface planar Paul trap) Yb in the same spatial volume. Stray dc field compensation and trapping along $\hat{z}$ for the Paul trap is provided by dc electrodes. The traps are imaged along both the (1,0,1) and (0,1,1) axes.

Collisions that change only the particles' energy and momentum are difficult to observe in our setup due to the continuous laser cooling. On the other hand, charge-exchange collisions between different isotopes $^{\alpha}\mathrm{Yb}^+ + {}^{\beta}\mathrm{Yb} \rightarrow {}^{\alpha}\mathrm{Yb} + {}^{\beta}\mathrm{Yb}^+$ are easy to observe using isotope-selective ion fluorescence: we first load the ion trap from the MOT with isotope $^{\alpha}\mathrm{Yb}^+$, change the MOT isotope to $^{\beta}$Yb by adjusting the frequency of the 399-nm laser, and then monitor the decay of the $^{\alpha}\mathrm{Yb}^+$ ion population through the decay of the 370-nm fluorescence. In order to prevent photoionization and direct loading of the ion trap with $^{\beta}\mathrm{Yb}^+$, we modulate the MOT and ion light out of phase to ensure that the MOT contains no excited atoms when the 370-nm light is present. Without the MOT, the ion trap loss is exponential with a typical lifetime $\tau_0 = 400$ s for ion crystals (Fig. 2, circles), presumably due to collisions with background gas atoms. In the presence of the MOT, τ is substantially shortened, with a shorter lifetime for higher MOT density. Simple exponential decay over a decade in ion number indicates that the loss involves a single ion, rather than collisions between ions. We also measure the trap fluorescence for identical ion and MOT isotopes. In the latter case, we observe a small initial decay, likely due to heating by collisions interrupting the ions' micromotion, but no exponential loss (Fig. 2, inset). This confirms that the measured trap loss for different ion and MOT isotopes is indeed due to charge-exchange collisions, and not caused by heating from ion-atom collisions that interrupt the ion's micromotion [28].

To accurately determine the charge-exchange rate coefficient, we vary the atomic density at the ion trap location by moving the MOT with a magnetic bias field. We determine the local atomic density at the ions' location by

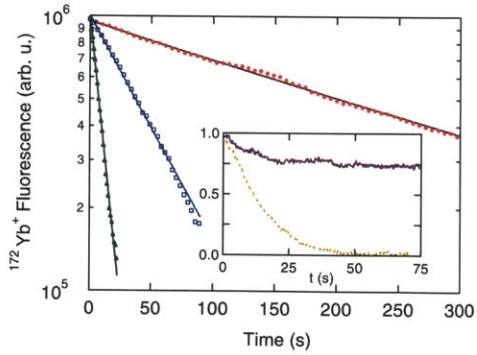

FIG. 2 (color online). Typical $^{172}\mathrm{Yb}^+$ ion-crystal fluorescence decay and exponential fits for no (circles), moderate (squares), and high (triangles) ^{174}Yb atomic density at the ion trap site. Inset: $^{172}\mathrm{Yb}^+$ (dashed line) and $^{174}\mathrm{Yb}^+$ (solid line) population evolution in the presence of ^{174}Yb. Both traces are normalized by the same peak value.

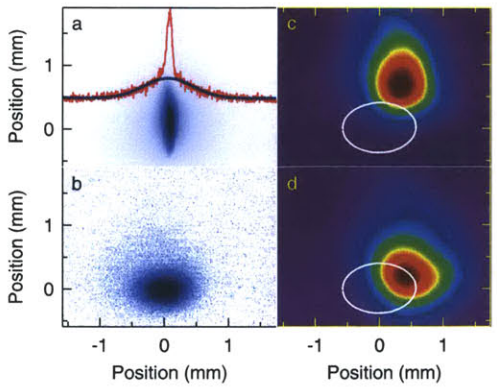

FIG. 3 (color online). (a) (1,0,1) camera image of the ion crystal (blue or dark gray) and cross-section showing highly non-Gaussian shape of crystal (red or gray). (b) (0,1,1) camera image of the ion crystal. (c) Typical low-overlap setting between MOT (colored or shaded contours) and $1/e^2$ contour of ions (white). (d) Same as (c) but for a higher overlap setting.

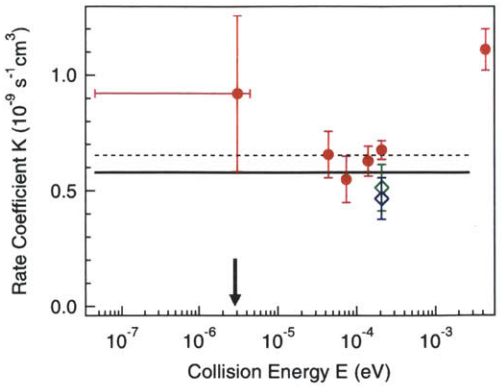

FIG. 4 (color online). Charge-exchange rate coefficient K with statistical uncertainty as a function of average collision energy E in the center-of-mass frame. Circles, green (or light gray) diamonds, and blue (or dark gray) diamonds represent $^{172}Yb^+ + {}^{174}Yb$, $^{172}Yb^+ + {}^{171}Yb$, and $^{174}Yb^+ + {}^{172}Yb$, respectively. The solid line indicates the theoretical Langevin rate coefficient K_{ce} [22], the dashed line assumes a contribution from the P-state polarizability [31] (see text). The black arrow indicates the ionization isotope shift between ^{174}Yb and ^{172}Yb.

taking images of both the MOT cloud and the ions on charge-coupled device (CCD) cameras along two different directions (see Fig. 3), with the total atom number calibrated by means of an absorption measurement. We then calculate the average atomic density experienced by the ions $\langle n \rangle = \int p(\mathbf{r}) n(\mathbf{r}) d\mathbf{r}$, where $p(\mathbf{r})$ is the normalized ion distribution and $n(\mathbf{r})$ is the local atomic density. The inelastic rate coefficient K is obtained by a linear fit of the observed ion decay rate constant $\Gamma = 1/\tau$ vs $\langle n \rangle$.

We note that the ions' kinetic energy is determined by their micromotion throughout the rf cycle [29]. Any ion displacement from the zero of the oscillating electric field, be it due to ion-crystal size or a dc electric field, results in micromotion whose energy easily exceeds that of the thermal motion in the secular potential of the Paul trap. To investigate the dependence of the rate coefficient K on average center-of-mass collision energy E, we vary the latter by loading different numbers of ions into the trap or by intentionally offsetting the ion crystal from the zero of the rf quadrupole field with a dc electric field.

The rate coefficient $K(E)$ is shown in Fig. 4. In the region $E \gtrsim 30$ μeV we calculate E from the observed Doppler broadening of the ion fluorescence. For well-compensated traps containing small crystals or single ions, where the Doppler broadening is smaller than the natural linewidth, we determine E from the observed correlation between rf drive signal and ion fluorescence [29]. For all energies investigated here, the atoms' contribution to the collision energy is negligible.

The data point at the lowest energy $E = 3.1$ μeV, being an average of 22 single-ion measurements, has large uncertainty in K. It also has large energy uncertainty because the micromotion is sufficiently well compensated for the fluorescence correlation signal to be dominated by noise. The other data points show observable Doppler broadening and were measured with up to a few thousand ions, resulting in smaller statistical uncertainties. We estimate systematic uncertainties to be a factor of 2 in K due to the difficulty of absolute MOT density calibration, and $\pm 50\%$ in E, due to the nonthermal energy distribution of the micromotion.

The *ab initio* calculated value for the polarizability $\alpha_S = 143$ a.u. $= \epsilon_0 \times 2.66 \times 10^{-28}$ m^3 [22] for the atomic $^1S_0$ ground state yields $K_{ce} = 5.8 \times 10^{-10}$ cm^3 s^{-1} for ground-state collisions (Fig. 4 solid line). Our experimentally measured value of $K = 6 \times 10^{-10}$ cm^3 s^{-1} in the semiclassical region around $E \sim 100$ μeV is thus in good agreement with the Langevin model. The measured K at the highest average collision energy $E = 4$ meV, close to the transition to the classical scattering region, is somewhat larger than the classical prediction [22,23]. Given the rapid Doppler cooling of the ions, the discrepancy is probably not due to collision-induced heating and trap loss. Rather, we speculate that it may be caused by averaging our nonthermal (micromotion) energy distribution over an oscillating cross section in the transition region [30]. Doubly excited collisions $Yb^{+*} + Yb^*$ cannot occur as the excitation light for ions and atoms is modulated out of phase. For $Yb^{+*} + Yb$ collisions, the Langevin cross section, depending only on the ion's charge and the atom's polarizability, is unchanged, and the charge-exchange process remains resonant, yielding the same value of σ_{ce}. $Yb^+ + Yb^*$ collisions cannot contribute for our collision energies since the atomic transition is tuned out of resonance with the MOT

light at an ion-atom distance $R_0 \approx 30$ nm, larger than $b_c = 2$–12 nm, and modeling of collision trajectories shows that the time required to move between $r = R_0$ and $r = b_c$ exceeds several excited-state lifetimes. For illustration, we have indicated in Fig. 4 the small change in K_{ce} if $Yb^+ + Yb^*$ collisions with $\alpha_P = 500$ a.u. for the $^1P_1$ state [31] were to contribute at our measured MOT excited-state fraction.

The theoretical value $K_{ce} = \sigma_L v/2$, corresponding to equal binding probability of the electron to the two nuclei, should apply when the collision energy far exceeds the isotope shift of the ionization potential. The latter can be estimated from spectroscopic data of a transition to a state with low electron probability density at the nucleus, such as $4f^{14}6s^2 \rightarrow 4f^{14}6s10d$ [32]. It follows that the $^{172}Yb^+ + {}^{174}Yb \rightarrow {}^{172}Yb + {}^{174}Yb^+$ reaction should be exothermic and release $\Delta E = 2.9\ \mu eV = h \times 0.7$ GHz. At the substantially larger collision energy $E = 0.21$ meV $\gg \Delta E$ we have investigated various isotope combinations, $^{172}Yb^+ + {}^{174}Yb$, $^{174}Yb^+ + {}^{172}Yb$, and $^{174}Yb^+ + {}^{171}Yb$, and find that they all display the same K (Fig. 4). We speculate that the data point $^{172}Yb^+ + {}^{174}Yb \rightarrow {}^{172}Yb + {}^{174}Yb^+$ at the lowest energy $E = 3.1\ \mu eV$, corresponding to exothermic collisions with $E \approx \Delta E$, may exhibit an increased rate coefficient compared to K_{ce}.

While it may be impossible to compensate stray fields well enough to reach the s-wave scattering limit $E_s = 4$ peV [6,22], Feshbach and other collision resonances may be observable well above E_s [8]. All the Yb isotopes used here have been cooled to quantum degeneracy in an optical dipole trap [33,34], which would allow the investigation of collision processes between an ion and a Bose-Einstein condensate or Fermi gas. Alternatively, to avoid the large resonant charge-exchange cross section observed here, a different species such as Rb could be used for sympathetic cooling of ions [7,10], or for studying ion impurities in a Bose-Einstein condensate [13].

We would like to thank T. Pruttivarasin for technical assistance and D. DeMille, D. Leibfried, A. Dalgarno, P. Zhang, R. Côté, W. Smith, and I. Chuang for suggestions and stimulating discussions. This work was supported by the NSF and the NSF Center for Ultracold Atoms.

[1] T. Köhler, K. Goral, and P. S. Julienne, Rev. Mod. Phys. **78**, 1311 (2006).
[2] S. Inouye, M. R. Andrews, J. Stenger, H.-J. Miesner, D. M. Stamper-Kurn, and W. Ketterle, Nature (London) **392**, 151 (1998).
[3] E. A. Donley, N. R. Claussen, S. T. Thompson, and C. E. Wieman, Nature (London) **417**, 529 (2002).
[4] B. DeMarco, J. L. Bohn, J. P. Burke, Jr., M. Holland, and D. S. Jin, Phys. Rev. Lett. **82**, 4208 (1999).
[5] P. Langevin, Ann. Chim. Phys. **5**, 245 (1905).
[6] R. Côté and A. Dalgarno, Phys. Rev. A **62**, 012709 (2000).
[7] O. P. Makarov, R. Côté, H. Michels, and W. W. Smith, Phys. Rev. A **67**, 042705 (2003).
[8] Z. Idziaszek, T. Calarco, P. S. Julienne, and A. Simoni, Phys. Rev. A **79**, 010702(R) (2009).
[9] Z. Idziaszek, T. Calarco, and P. Zoller, Phys. Rev. A **76**, 033409 (2007).
[10] Y. Moriwaki, M. Tachikawa, Y. Maeno, and T. Shimizu, Jpn. J. Appl. Phys. **31**, L1640 (1992).
[11] W. W. Smith, O. P. Makarov, and J. Lin, J. Mod. Opt. **52**, 2253 (2005).
[12] K. Mølhave and M. Drewsen, Phys. Rev. A **62**, 011401(R) (2000).
[13] R. Côté, V. Kharchenko, and M. D. Lukin, Phys. Rev. Lett. **89**, 093001 (2002).
[14] R. Côté, Phys. Rev. Lett. **85**, 5316 (2000).
[15] H. A. Schuessler, C. H. Holder, Jr., and C.-S. O, Phys. Rev. A **28**, 1817 (1983).
[16] O. Hadjar, D. Ascenzi, D. Bassi, P. Franceschi, M. Sabidò, and P. Tosi, Chem. Phys. Lett. **400**, 476 (2004).
[17] T. Speck, T. I. Mostefaoui, D. Travers, and B. R. Rowe, Int. J. Mass Spectrom. **208**, 73 (2001).
[18] V. H. S. Kwong, D. Chen, and Z. Fang, Astrophys. J. **536**, 954 (2000).
[19] K. Motohashi, T. Takahashi, N. Takahashi, and S. Tsurubuchi, J. Phys. B **38**, 3339 (2005).
[20] S. Willitsch, M. T. Bell, A. D. Gingell, S. R. Procter, and T. P. Softley, Phys. Rev. Lett. **100**, 043203 (2008).
[21] M. Cetina, A. Grier, J. Campbell, I. Chuang, and V. Vuletić, Phys. Rev. A **76**, 041401(R) (2007).
[22] P. Zhang and A. Dalgarno, J. Phys. Chem. A **111**, 12471 (2007).
[23] A. Dalgarno and P. Zhang (private communication).
[24] G. Gioumousis and D. P. Stevenson, J. Chem. Phys. **29**, 294 (1958).
[25] E. Bodo, P. Zhang, and A. Dalgarno, New J. Phys. **10**, 033024 (2008).
[26] B. D. Esry, H. R. Sadeghpour, E. Wells, and I. Ben-Itzhak, J. Phys. B **33**, 5329 (2000).
[27] A. S. Bell, P. Gill, H. A. Klein, A. P. Levick, C. Tamm, and D. Schnier, Phys. Rev. A **44**, R20 (1991).
[28] F. G. Major and H. G. Dehmelt, Phys. Rev. **170**, 91 (1968).
[29] D. J. Berkeland, J. D. Miller, J. C. Bergquist, W. M. Itano, and D. J. Wineland, J. Appl. Phys. **83**, 5025 (1998).
[30] A. Dalgarno, M. R. C. McDowell, and A. Williams, Phil. Trans. R. Soc. A **250**, 411 (1958).
[31] S. G. Porsev, Y. G. Rakhlina, and M. G. Kozlov, Phys. Rev. A **60**, 2781 (1999).
[32] C. S. Kischkel, M. Baumann, and E. Kümmel, J. Phys. B **25**, 4447 (1992).
[33] Y. Takasu, K. Maki, K. Komori, T. Takano, K. Honda, M. Kumakura, T. Yabuzaki, and Y. Takahashi, Phys. Rev. Lett. **91**, 040404 (2003).
[34] T. Fukuhara, Y. Takasu, M. Kumakura, and Y. Takahashi, Phys. Rev. Lett. **98**, 030401 (2007).

Bibliography

[ABLM81] S. Andreev, V. Balykin, V. Letokhov, and V. Minogin. Radiative slowing and reduction of the energy spread of a beam of sodium atoms to 1.5 K in an oppositely directed laser beam. *Pis'ma Zh. Eksp. Teor. Fiz.*, 34(463), 1981.

[ADD+06] A. André, D. DeMille, J. M. Doyle, M. D. Lukin, S. E. Maxwell, P. Rabl, R. J. Schoelkopf, and P. Zoller. A coherent all-electrical interface between polar molecules and mesoscopic superconducting resonators. *Nature Physics*, 2(9):636–642, August 2006.

[ADW+06] Takao Aoki, Barak Dayan, E. Wilcut, W. P. Bowen, A. S. Parkins, T. J. Kippenberg, K. J. Vahala, and H. J. Kimble. Observation of strong coupling between one atom and a monolithic microresonator. *Nature*, 443(7112):671–4, October 2006.

[Ass10] Blu-ray Disc Association. Blu-ray Disc Format White Paper, 2010.

[ATK08] Tomoya Akatsuka, Masao Takamoto, and Hidetoshi Katori. Optical lattice clocks with non-interacting bosons and fermions. *Nature Physics*, 4(12):954–959, October 2008.

[AUW+10] J. M. Amini, H. Uys, J. H. Wesenberg, S. Seidelin, J. Britton, J. J. Bollinger, D. Leibfried, C. Ospelkaus, a P. VanDevender, and D. J. Wineland. Toward scalable ion traps for quantum information processing. *New Journal of Physics*, 12(3):033031, March 2010.

[BB84] C. H. Bennett and Gilles Brassard. Quantum cryptography: Public key distribution and coin tossing. *International Conference on Computers, Systems & Signal Processing*, 1984.

[BBM+07] A. Boozer, A. Boca, R. Miller, T. Northup, and H. Kimble. Reversible State Transfer between Light and a Single Trapped Atom. *Physical Review Letters*, 98(19):1–4, May 2007.

[BCK+08] Lev S. Bishop, J. M. Chow, Jens Koch, A. A. Houck, M. H. Devoret, E. Thuneberg, S. M. Girvin, and R. J. Schoelkopf. Nonlinear response of the vacuum Rabi resonance. *Nature Physics*, 5(2):105–109, December 2008.

[Ber08] Paul Berman. Light scattering. *Contemporary Physics*, 49(5):313–330, September 2008.

[BGBE10] Kristian Baumann, Christine Guerlin, Ferdinand Brennecke, and Tilman Esslinger. Dicke quantum phase transition with a superfluid gas in an optical cavity. *Nature*, 464(7293):1301–6, April 2010.

[BGK+91] A. S. Bell, P. Gill, H. A. Klein, A. P. Levick, Chr. Tamm, and D. Schnier. Laser cooling of trapped ytterbium ions using a four-level optical-excitation scheme. *Physical Review A*, 44:R20, 1991.

[BHIW91] J. J. Bollinger, D. J. Heinzen, W. M. Itano, and D. J. Wineland. A 303-MHz Frequency Standard Based on Trapped Be^+ Ions. *IEEE Trans. Instr. Meas.*, 40(126), 1991.

[BHL+05] K.-A. Brickman, P. Haljan, P. Lee, M. Acton, L. Deslauriers, and C. Monroe. Implementation of Grover's quantum search algorithm in a scalable system. *Physical Review A*, 72(5):23–26, November 2005.

[BKRB08] Jan Benhelm, Gerhard Kirchmair, Christian F. Roos, and Rainer Blatt. Towards fault-tolerant quantum computing with trapped ions. *Nature Physics*, 4(6):463–466, April 2008.

[Bla98] Eric Black. Notes on the pound-drever-hall technique. *Technical Note LIGO-T980045-00-D*, 4(617):16–98, 1998.

[BLB+09] J. Britton, D. Leibfried, J. a. Beall, R. B. Blakestad, J. H. Wesenberg, and D. J. Wineland. Scalable arrays of rf Paul traps in degenerate Si. *Applied Physics Letters*, 95(17):173102, 2009.

[Blo08] Immanuel Bloch. Quantum coherence and entanglement with ultracold atoms in optical lattices. *Nature*, 453(7198):1016–22, June 2008.

[BMB+98] D. J. Berkeland, J. D. Miller, J. C. Bergquist, W. M. Itano, and D. J. Wineland. Minimization of ion micromotion in a Paul trap. *Journal of Applied Physics*, 83(10):5025, 1998.

[BOC+11] K. R. Brown, C. Ospelkaus, Y. Colombe, a. C. Wilson, D. Leibfried, and D. J. Wineland. Coupled quantized mechanical oscillators. *Nature*, 471(7337):196–199, February 2011.

[BOV+09] R. Blakestad, C. Ospelkaus, A. VanDevender, J. Amini, J. Britton, D. Leibfried, and D. Wineland. High-Fidelity Transport of Trapped-Ion Qubits through an X-Junction Trap Array. *Physical Review Letters*, 102(15):1–4, April 2009.

[BPG93] R. W. Berends, E. H. Pinnington, and B. Guo. Beam-laser lifetime measurements for four resonance levels of Yb II. *Journal of Physics B:*, 701, 1993.

[BPT+10] W. S. Bakr, A. Peng, M. E. Tai, R. Ma, J. Simon, J. I. Gillen, S. Fölling, L. Pollet, and M. Greiner. Probing the Superfluid-to-Mott-Insulator Transition at the Single-Atom Level. *Science (New York, N.Y.)*, 547(2010), June 2010.

[BRD+03] A. Banerjee, U. D. Rapol, D. Das, A. Krishna, and V. Natarajan. Precise measurements of UV atomic lines : Hyperfine structure and isotope shifts in the 398.8 nm line of Yb. *Europhysics Letters*, 63, 2003.

[Cam06] Jonathan A. Campbell. *Surface Trap for Ytterbium Ions.* Master's thesis, Massachusetts Institute of Technology, 2006.

[CBBJ05] J. Chiaverini, R. B. Blakestad, J. Britton, and J. D. Jost. Surface-electrode architecture for ion-trap quantum information processing. *Quantum Information and Computation*, 5(6):419–439, 2005.

[CBL+05] J. Chiaverini, J. Britton, D. Leibfried, E. Knill, M. D. Barrett, R. B. Blakestad, W. M. Itano, J. D. Jost, C. Langer, R. Ozeri, T. Schaetz, and D. J. Wineland. Implementation of the semiclassical quantum Fourier transform in a scalable system. *Science (New York, N.Y.)*, 308(5724):997–1000, May 2005.

[CCR00] R. CCRCMFLXoté. From classical mobility to hopping conductivity: charge hopping in an ultracold gas. *Physical Review Letters*, 85(25):5316–9, December 2000.

[CD00] R. CCRCMFLXoté and a. Dalgarno. Ultracold atom-ion collisions. *Physical Review A*, 62(1):4–9, June 2000.

[CDLK08] K S Choi, H Deng, J Laurat, and H J Kimble. Mapping photonic entanglement into and out of a quantum memory. *Nature*, 452(7183):67–71, March 2008.

[CGC+07] Marko Cetina, Andrew Grier, Jonathan Campbell, Isaac Chuang, and Vladan Vuletić. Bright source of cold ions for surface-electrode traps. *Physical Review A*, 76(4):1–4, October 2007.

[CGT+06] L. Childress, M. V. Gurudev Dutt, J. M. Taylor, A. S. Zibrov, F. Jelezko, J. Wrachtrup, P. R. Hemmer, and M. D. Lukin. Coherent dynamics of coupled electron and nuclear spin qubits in diamond. *Science (New York, N.Y.)*, 314(5797):281–5, October 2006.

[Chu36] Alonzo Church. An unsolvable problem of elementary number theory. *American Journal of Mathematics*, 58(2):345–363, 1936.

[CKL02] R. CCRCMFLXoté, V. Kharchenko, and M. Lukin. Mesoscopic Molecular Ions in Bose-Einstein Condensates. *Physical Review Letters*, 89(9), August 2002.

[CLH+98] K. L. Corwin, Z. T. Lu, C. F. Hand, R. J. Epstein, and C. E. Wieman. Frequency-stabilized diode laser with the Zeeman shift in an atomic vapor. *Applied Optics*, 37(15):3295–3298, May 1998.

[CLS+04] J. Chiaverini, D. Leibfried, T. Schaetz, M. D. Barrett, R. B. Blakestad, J. Britton, W. M. Itano, J. D. Jost, E. Knill, C. Langer, R. Ozeri, and D. J. Wineland. Realization of quantum error correction. *Nature*, 432(7017):602–5, December 2004.

[Cor02] Nichia Corporation. Nichia and Sony Announce Joint Development & Technology Alliance for Production of Blue-Violet Laser Diodes, 2002.

[Cor08] Nichia Corporation. Nichia and Sharp Enter into LED and Laser Diode Patent Cross-Licensing Agreement, 2008.

[Cro05] Andrew W. Cross. *Synthesis and Evaluation of Fault-Tolerant Quantum Computing Architectures.* PhD thesis, Massachusetts Institute of Technology, 2005.

[CW08] John Clarke and Frank K. Wilhelm. Superconducting quantum bits. *Nature*, 453(7198):1031–42, June 2008.

[CZ95] J. I. Cirac and P. Zoller. Quantum computations with cold trapped ions. *Physical Review Letters*, 1995.

[DBBN05] Dipankar Das, Sachin Barthwal, Ayan Banerjee, and Vasant Natarajan. Absolute frequency measurements in Yb with 0.08ppb uncertainty: Isotope shifts and hyperfine structure in the 399-nm $^1S_0$-$^1P_1$ line. *Physical Review A*, 72(3):1–7, September 2005.

[DBIW89] F. Diedrich, J. C. Bergquist, W. M. Itano, and D. J. Wineland. Laser cooling to the zero-point energy of motion. *Physical Review Letters*, 62(4):403–406, 1989.

[DCJ+07] M. V. Gurudev Dutt, L. Childress, L. Jiang, E. Togan, J. Maze, F. Jelezko, A. S. Zibrov, P. R. Hemmer, and M. D. Lukin. Quantum register based on individual electronic and nuclear spin qubits in diamond. *Science (New York, N.Y.)*, 316(5829):1312–6, June 2007.

[Deh68] H. G. Dehmelt. Radiofrequency Spectroscopy of Stored Ions I: Storage*. *Advances in Atomic and Molecular Physics*, 1968.

[Den09] Johannes Hecker Denschlag. An ion in a sea of ultracold atoms. 2009.

[Deu85] D. Deutsch. Quantum Theory, the Church-Turing Principle and the Universal Quantum Computer. *Proceedings of the Royal Society A: Mathematical, Physical and Engineering Sciences*, 400(1818):97–117, July 1985.

[DeV09] Ralph DeVoe. Power-Law Distributions for a Trapped Ion Interacting with a Classical Buffer Gas. *Physical Review Letters*, 102(6):1–4, February 2009.

[Dic54] R. H. Dicke. Coherence in Spontaneous Radiation Processes. *Physical Review*, 1954.

[DIC10] Hauke Doerk, Zbigniew Idziaszek, and Tommaso Calarco. Atom-ion quantum gate. *Physical Review A*, 81(1):1–13, January 2010.

[DiV00] David P. DiVincenzo. The Physical Implementation of Quantum Computation. *Fortschritte der Physik*, 48(9-11):771–783, September 2000.

[DMW58] A. Dalgarno, M. R. C. McDowell, and A. Williams. The Mobilities of Ions in Unlike Gases. *Philosophical Transactions of the Royal Society A: Mathematical, Physical and Engineering Sciences*, 250(982):411–425, April 1958.

[DOS+06] L. Deslauriers, S. Olmschenk, D. Stick, W. K. Hensinger, J. Sterk, and C. Monroe. Scaling and Suppression of Anomalous Quantum Decoherence in Ion Traps. *Physical Review Letters*, page 48109, January 2006.

[DPC+87] F. Diedrich, E. Peik, JM Chen, W. Quint, and H. Walther. Observation of a phase transition of stored laser-cooled ions. *Physical Review Letters*, 59(26):2931–2934, 1987.

[DRB+10] François Dubin, Carlos Russo, Helena G. Barros, Andreas Stute, Christoph Becher, Piet O. Schmidt, and Rainer Blatt. Quantum to classical transition in a single-ion laser. *Nature Physics*, 6(5):350–353, March 2010.

[Dub93] D. H. E Dubin. Theory of structural phase transitions in a trapped Coulomb crystal. *Physical Review Letters*, 71(17), 1993.

[Ear42] Samuel Earnshaw. On the Nature of the Molecular Forces which Regulate the Constitution of the Luminiferous Ether. *Trans. Camb. Phil. Soc.*, 7:97–112, 1842.

[Eke91] A. K. Ekert. Quantum cryptography based on Bell's theorem. *Physical Review Letters*, 1991.

[FEF+08] Ilya Fushman, Dirk Englund, Andrei Faraon, Nick Stoltz, Pierre Petroff, and Jelena Vučković. Controlled phase shifts with a single quantum dot. *Science (New York, N.Y.)*, 320(5877):769–72, May 2008.

[Fey82] Richard P. Feynman. Simulating physics with computers. *International Journal of Theoretical Physics*, 21(6-7):467–488, June 1982.

[GCOV09] Andrew Grier, Marko Cetina, Fedja Oručević, and Vladan Vuletić. Observation of Cold Collisions between Trapped Ions and Trapped Atoms. *Physical Review Letters*, 102(22):1–4, June 2009.

[GKH+01] G. R. Guthöhrlein, M. Keller, Kazuhiro Hayasaka, Walther Lange, and Herbert Walther. A single ion as a nanoscopic probe of an optical field. *Nature*, 414(6859):49–51, November 2001.

[GMW+09] Alpha Gaëtan, Yevhen Miroshnychenko, Tatjana Wilk, Amodsen Chotia, Matthieu Viteau, Daniel Comparat, Pierre Pillet, Antoine Browaeys, and Philippe Grangier. Observation of collective excitation of two individual atoms in the Rydberg blockade regime. *Nature Physics*, 5(2):115–118, January 2009.

[Gri11] Andrew T. Grier. *Interaction of Trapped Ions with Trapped Atoms.* PhD thesis, Massachusetts Institute of Technology, 2011.

[GRL+03] Stephan Gulde, Mark Riebe, Gavin P T Lancaster, Christoph Becher, Jürgen Eschner, Hartmut Häffner, Ferdinand Schmidt-Kaler, Isaac L. Chuang, and Rainer Blatt. Implementation of the Deutsch-Jozsa algorithm on an ion-trap quantum computer. *Nature*, 421(6918):48–50, January 2003.

[Gro96] Lov K. Grover. A fast quantum mechanical algorithm for database search. *Proceedings of the twenty-eighth annual ACM symposium on Theory of computing - STOC '96*, pages 212–219, 1996.

[GT07] Nicolas Gisin and Rob Thew. Quantum communication. *Nature Photonics*, 1(3):165–171, March 2007.

[HBHB10] M. Harlander, M. Brownnutt, W. Hänsel, and R. Blatt. Trapped-ion probing of light-induced charging effects on dielectrics. *New Journal of Physics*, 12(9):093035, September 2010.

[HBO+05] C. Hoyt, Z. Barber, C. Oates, T. Fortier, S. Diddams, and L. Hollberg. Observation and Absolute Frequency Measurements of the $^1S_0$-$^3P_0$ Optical Clock Transition in Neutral Ytterbium. *Physical Review Letters*, 95(8):1–4, August 2005.

[HD64] C. E. Habermann and A. H. Daane. Vapor Pressures of the Rare-Earth Metals. *The Journal of Chemical Physics*, 41(9):2818, 1964.

[HDM+09] Peter F. Herskind, Aurélien Dantan, Joan P. Marler, Magnus Albert, and Michael Drewsen. Realization of collective strong coupling with ion Coulomb crystals in an optical cavity. *Nature Physics*, 5(7):494–498, June 2009.

[HKD+09] A. A. Houck, Jens Koch, M. H. Devoret, S. M. Girvin, and R. J. Schoelkopf. Life after charge noise: recent results with transmon qubits. *Quantum Information Processing*, 8(2-3):105–115, February 2009.

[Hol52] T. Holstein. Mobilities of positive ions in their parent gases. *The Journal of Physical Chemistry*, 56(7):832–836, 1952.

[HOS+06] W. K. Hensinger, S. Olmschenk, D. Stick, D. Hucul, M. Yeo, M. Acton, L. Deslauriers, C. Monroe, and J. Rabchuk. T-junction ion trap array for two-dimensional ion shuttling, storage, and manipulation. *Applied Physics Letters*, 88(3):034101, 2006.

[HTK+99] K. Honda, Y. Takahashi, T. Kuwamoto, M. Fujimoto, K. Toyoda, K. Ishikawa, and T. Yabuzaki. Magneto-optical trapping of Yb atoms and a limit on the branching ratio of the $^1P_1$ state. *Physical Review A*, 59(2):R934–R937, February 1999.

[HUW00] Kazuhiro Hayasaka, Shinji Urabe, and Masayoshi Watanabe. Laser Cooling of Ca+ with an Extended-Cavity Ultraviolet Diode Laser. *Japanese Journal of Applied Physics*, 39:L687–L689, 2000.

[ICZ07] Zbigniew Idziaszek, Tommaso Calarco, and Peter Zoller. Controlled collisions of a single atom and an ion guided by movable trapping potentials. *Physical Review A*, 76(3):1–16, September 2007.

[KBBG90] H. A. Klein, A. S. Bell, G. P. Barwood, and P. Gill. Laser cooling of trapped Yb^+. *Applied Physics B: Lasers and Optics*, 50(1):13–17, 1990.

[KBT+06] F. H. L. Koppens, C. Buizert, K. J. Tielrooij, I. T. Vink, K. C. Nowack, T. Meunier, L. P. Kouwenhoven, and L. M. K. Vandersypen. Driven coherent oscillations of a single electron spin in a quantum dot. *Nature*, 442(7104):766–71, August 2006.

[KCCK06] D. Kielpinski, M. Cetina, J. A. Cox, and F. X. Kärtner. Laser cooling of trapped ytterbium ions with an ultraviolet diode laser. *Optics letters*, 31(6):757–9, March 2006.

[KHTY99] T. Kuwamoto, K. Honda, Y. Takahashi, and T. Yabuzaki. Magneto-optical trapping of Yb atoms using an intercombination transition. *Physical Review A*, 60(2):R745–R748, August 1999.

[Kim08] H. J. Kimble. The quantum internet. *Nature*, 453(7198):1023–30, June 2008.

[KLH+03] M. Keller, B. Lange, K. Hayasaka, W. Lange, and H. Walther. Deterministic coupling of single ions to an optical cavity. *Applied Physics B: Lasers and Optics*, 76(2):125–128, February 2003.

[KLH+04] Matthias Keller, Birgit Lange, Kazuhiro Hayasaka, Wolfgang Lange, and Herbert Walther. Continuous generation of single photons with controlled waveform in an ion-trap cavity system. *Nature*, 431(28):1075–1078, 2004.

[KMW02] D. Kielpinski, C. Monroe, and D. J. Wineland. Architecture for a large-scale ion-trap quantum computer. *Nature*, 417(6890):709–11, June 2002.

[Lab08] Jaroslaw Labaziewicz. *High Fidelity Quantum Gates with Ions in Cryogenic Microfabricated Ion Traps.* PhD thesis, Massachusetts Institute of Technology, 2008.

[Lan05] Paul Langevin. Une formule fondamentale de théorie cinétique. *Annales des Chimie et des Physique*, 5:245, 1905.

[LBSM00] T. Loftus, J. Bochinski, R. Shivitz, and T. Mossberg. Power-dependent loss from an ytterbium magneto-optic trap. *Physical Review A*, 61(5):1–4, April 2000.

[LD98] Daniel Loss and David P. DiVincenzo. Quantum computation with quantum dots. *Physical Review A*, 57(1):120–126, January 1998.

[Lei09] D.R. Leibrandt. *Integrated chips and optical cavities for trapped ion quantum information processing.* PhD thesis, Massachusetts Institute of Technology, 2009.

[LFDF09] Elena Litvinova, Hans Feldmeier, Jacek Dobaczewski, and Victor Flambaum. Nuclear structure of lowest Th229 states and time-dependent fundamental constants. *Physical Review C*, 79(6):1–12, June 2009.

[LGA+08] Jaroslaw Labaziewicz, Yufei Ge, Paul Antohi, David Leibrandt, Kenneth Brown, and Isaac Chuang. Suppression of Heating Rates in Cryogenic Surface-Electrode Ion Traps. *Physical Review Letters*, 100(1):1–4, January 2008.

[LGL+08] Jaroslaw Labaziewicz, Yufei Ge, David Leibrandt, Shannon Wang, Ruth Shewmon, and Isaac Chuang. Temperature Dependence of Electric Field Noise above Gold Surfaces. *Physical Review Letters*, 101(18):1–4, October 2008.

[LHLBH89] H. Lehmitz, J. Hattendorf-Ledwoch, R. Blatt, and H. Harde. Population trapping in excited Yb ions. *Physical Review Letters*, 62(18):2108–2111, 1989.

[LLC+09] DR Leibrandt, J Labaziewicz, RJ Clark, IL Chuang, RJ Epstein, C Ospelkaus, JH Wesenberg, JJ Bollinger, D Leibfried, DJ Wineland, and Others. Demonstration of a scalable, multiplexed ion trap for quantum information processing, 2009.

[LLC+11] L. Lamata, D. R. Leibrandt, I. L. Chuang, J. I. Cirac, M. D. Lukin, V. Vuletic, and S. F. Yelin. Ion crystal transducer for strong coupling between single ions and single photons. *Arxiv preprint arXiv:1102.4141*, pages 3–6, 2011.

[LWGS05] V. Letchumanan, M. Wilson, P. Gill, and A. Sinclair. Lifetime Measurement of the Metastable 4d $^2D_{5/2}$ State in $^{88}Sr^+$ Using a Single Trapped Ion. *Physical Review A*, 72(1):1–8, July 2005.

[LZC+08] A. D. Ludlow, T. Zelevinsky, G. K. Campbell, S. Blatt, M. M. Boyd, M. H. G. de Miranda, M. J. Martin, J. W. Thomsen, S. M. Foreman, Jun Ye, T. M. Fortier, J. E. Stalnaker, S. A. Diddams, Y. Le Coq, Z. W. Barber, N. Poli, N. D. Lemke, K. M. Beck, and C. W. Oates. Sr lattice clock at 1 x 10^{-16} fractional uncertainty by remote optical evaluation with a Ca clock. *Science (New York, N.Y.)*, 319(5871):1805–8, March 2008.

[Mai] R. J. Mailloux. *Phased Array Antenna Handbook*. Artech House, Boston, 1994 edition.

[MCMS03] Oleg Makarov, R. CCRCMFLXoté, H. Michels, and W. Smith. Radiative Charge-Transfer Lifetime of the Excited State of $NaCa^+$. *Physical Review A*, 67(4):1–5, April 2003.

[MD68] F. G. Major and H. G. Dehmelt. Exchange-collision technique for the rf spectroscopy of stored ions. *Physical Review*, 170(1):91–107, 1968.

[MKB+02] A. Mundt, A. Kreuter, C. Becher, D. Leibfried, J. Eschner, F. Schmidt-Kaler, and R. Blatt. Coupling a Single Atomic Quantum Bit to a High Finesse Optical Cavity. *Physical Review Letters*, 89(10):1–4, August 2002.

[MLN+99] S. Mannervik, J. Lidberg, L-O Norlin, P. Royen, A. Schmitt, W. Shi, and X. Tordoir. Lifetime Measurement of the Metastable 4d $^2D_{3/2}$ Level in Sr^+ by Optical Pumping of a Stored Ion Beam. *Physical Review Letters*, 83(4):698–701, July 1999.

[MlSr99] Klaus Mø lmer and Anders Sø rensen. Multiparticle Entanglement of Hot Trapped Ions. *Physical Review Letters*, 82(9):1835–1838, March 1999.

[MMK+95] C. Monroe, DM Meekhof, BE King, WM Itano, and DJ Wineland. Demonstration of a fundamental quantum logic gate. *Physical Review Letters*, 75(25):4714–4717, 1995.

[MMO+07] P. Maunz, D. L. Moehring, S. Olmschenk, K. C. Younge, D. N. Matsukevich, and C. Monroe. Quantum interference of photon pairs from two remote trapped atomic ions. *Nature Physics*, 3(8):538–541, June 2007.

[MNB+05] R Miller, T E Northup, K M Birnbaum, a Boca, a D Boozer, and H J Kimble. Trapped atoms in cavity QED: coupling quantized light and matter. *Journal of Physics B: Atomic, Molecular and Optical Physics*, 38(9):S551–S565, May 2005.

[MNS+11] James McLoughlin, Altaf Nizamani, James Siverns, Robin Sterling, Marcus Hughes, Bjoern Lekitsch, Björn Stein, Seb Weidt, and Winfried Hensinger. Versatile ytterbium ion trap experiment for operation of scalable ion-trap chips with motional heating and transition-frequency measurements. *Physical Review A*, 83(1):1–9, January 2011.

[Mol69] B. R. Mollow. Power spectrum of light scattered by two-level systems. *Physical Review*, 188(5), 1969.

[MSB+11] Thomas Monz, Philipp Schindler, Julio Barreiro, Michael Chwalla, Daniel Nigg, William Coish, Maximilian Harlander, Wolfgang Hänsel, Markus Hennrich, and Rainer Blatt. 14-Qubit Entanglement: Creation and Coherence. *Physical Review Letters*, 106(13):1–4, March 2011.

[MSW+08] A. Myerson, D. Szwer, S. Webster, D. Allcock, M. Curtis, G. Imreh, J. Sherman, D. Stacey, A. Steane, and D. Lucas. High-Fidelity Readout of Trapped-Ion Qubits. *Physical Review Letters*, 100(20):2–5, May 2008.

[MTMS92] Y. Moriwaki, M. Tachikawa, Y. Maeno, and T. Shimizu. Collision cooling of ions stored in quadrupole radio-frequency trap. *Japanese Journal of Applied Physics*, 31:1640–1640, 1992.

[NC04] Michael A. Nielsen and Isaac L. Chuang. *Quantum Computation and Quantum Information*. Cambridge University Press, Cambridge, 2004.

[NHTD78] W. Neuhauser, M. Hohenstatt, P. Toschek, and H. Dehmelt. Optical-sideband cooling of visible atom cloud confined in parabolic well. *Physical Review Letters*, 41(4):233–236, 1978.

[NSN+96] S. Nakamura, M. Senoh, S. Nagahama, N. Iwasa, T. Yamada, T. Matsushita, H. Kiyoku, and Y. Sugimoto. InGaN-based multi-quantum-well-structure laser diodes. *Japanese Journal of Applied Physics*, 35(1B):L74–L76, 1996.

[OHM+09] S. Olmschenk, D. Hayes, D. Matsukevich, P. Maunz, D. Moehring, K. Younge, and C. Monroe. Measurement of the lifetime of the $6p^2P_{1/2}$ level of Yb^+. *Physical Review A*, 80(2):1–5, August 2009.

[OYM+07] S. Olmschenk, K. Younge, D. Moehring, D. Matsukevich, P. Maunz, and C. Monroe. Manipulation and detection of a trapped Yb^+ hyperfine qubit. *Physical Review A*, 76(5):1–9, November 2007.

[PC04a] D. Porras and J. Cirac. Bose-Einstein Condensation and Strong-Correlation Behavior of Phonons in Ion Traps. *Physical Review Letters*, 93(26):1–4, December 2004.

[PC04b] D. Porras and J. I. Cirac. Effective Quantum Spin Systems with Trapped Ions. *Physical Review Letters*, 92(20):1–4, May 2004.

[PJT+05] J. R. Petta, A. C. Johnson, J. M. Taylor, E. A. Laird, A. Yacoby, M. D. Lukin, C. M. Marcus, M. P. Hanson, and A. C. Gossard. Coherent manipulation of coupled electron spins in semiconductor quantum dots. *Science (New York, N.Y.)*, 309(5744):2180–4, September 2005.

[PM82] W.D. Phillips and H. Metcalf. Laser deceleration of an atomic beam. *Physical Review Letters*, 48(9):596–599, 1982.

[PS53] Wolfgang Paul and H. Steinwedel. Ein neues Massenspektrometer ohne Magnetfeld. *Zeitschrift für Naturforschung A*, 8(7):448–450, 1953.

[Pur46] E. M. Purcell. Spontaneous emission probabilities at radio frequencies. *Physical Review*, 69(681):681, 1946.

[PY03] Chang Park and Tai Yoon. Efficient magneto-optical trapping of Yb atoms with a violet laser diode. *Physical Review A*, 68(5):2–5, November 2003.

[RBKD+02] M. A. Rowe, A. Ben-Kish, B. DeMarco, D. Leibfried, V. Meyer, J. Beall, J. Britton, J. Hughes, W. M. Itano, B. Jelenkovic, C. Langer, T. Rosenband, and D. J. Wineland. Transport of quantum states and separation of ions in a dual RF ion trap. *Quantum Information and Computation*, 2(4):257–271, 2002.

[REB+00] C Raab, J Eschner, J Bolle, H Oberst, F Schmidt-Kaler, and R Blatt. Motional sidebands and direct measurement of the cooling rate in the resonance fluorescence of a single trapped ion. *Physical review letters*, 85(3):538–41, July 2000.

[RHS+08] T. Rosenband, D. B. Hume, P. O. Schmidt, C. W. Chou, A. Brusch, L. Lorini, W. H. Oskay, R. E. Drullinger, T. M. Fortier, J. E. Stalnaker, S. A. Diddams, W. C. Swann, N. R. Newbury, W. M. Itano, D. J. Wineland, and J. C. Bergquist. Frequency ratio of Al^+ and Hg^+ single-ion optical clocks; metrology at the 17th decimal place. *Science (New York, N.Y.)*, 319(5871):1808–12, March 2008.

[RRG+00] C. Roos, H. Rohde, S. Gulde, A.B. Mundt, G. Reymond, M. Lederbauer, J. Eschner, F. Schmidt-Kaler, D. Leibfried, and R. Blatt. Towards quantum information with trapped calcium ions. *2000 IEEE International Symposium on Circuits and Systems. Emerging Technologies for the 21st Century. Proceedings (IEEE Cat No.00CH36353)*, page 240, 2000.

[RSH+07] T. Rosenband, P. Schmidt, D. Hume, W. M. Itano, T. Fortier, J. Stalnaker, K. Kim, S. Diddams, J. Koelemeij, J. Bergquist, and D. J. Wineland. Observation of the $^1S_0$-$^3P_0$ Clock Transition in $^{27}Al^+$. *Physical Review Letters*, 98(22):1–4, May 2007.

[RTB+00] M. Roberts, P. Taylor, G. P. Barwood, W. R. C. Rowley, and P. Gill. Observation of the $^2S_{1/2}$-$^2F_{7/2}$ electric octupole transition in a single $^{171}Yb^+$ ion. *Physical Review A*, 62(2):1–4, July 2000.

[RWE+95] L. Ricci, M. Weidemüller, T. Esslinger, A. Hemmerich, C. Zimmermann, V. Vuletić, W. König, and T. W. Hänsch. A compact grating-stabilized diode laser system for atomic physics. *Optics Communications*, 117(5-6):541–549, 1995.

[SCH+06] T. Steinmetz, Y. Colombe, D. Hunger, T. W. Hänch, A. Balocchi, R. J. Warburton, and J. Reichel. Stable fiber-based Fabry-Perot cavity. *Applied Physics Letters*, 89(11):111110, 2006.

[SCR+06] S. Seidelin, J. Chiaverini, R. Reichle, J. J. Bollinger, D. Leibfried, J. Britton, J. H. Wesenberg, R. B. Blakestad, R. J. Epstein, D. B. Hume, J. D. Jost, C. Langer, R. Ozeri, N. Shiga, and D. J. Wineland. A microfabricated surface-electrode ion trap for scalable quantum information processing. *Physical Review Letters*, 96:253003, January 2006.

[SEHS10] Ch. Schneider, M. Enderlein, T. Huber, and T. Schaetz. Optical Trapping of an Ion. *Nature Photonics*, 4:772–775, 2010.

[SF97] S. Pearton S. Nakamura and G. Fasol. *The Blue Laser Diode.* Springer, Heidelberg, first edit edition, 1997.

[SHD10] Stefan Schmid, Arne Härter, and Johannes Denschlag. Dynamics of a Cold Trapped Ion in a Bose-Einstein Condensate. *Physical Review Letters*, 105(13):1–4, September 2010.

[SHG+10] L. Slodička, G. Hétet, S. Gerber, M. Hennrich, and R. Blatt. Electromagnetically Induced Transparency from a Single Atom in Free Space. *Physical Review Letters*, 105(15):1–4, October 2010.

[Shi06] Brendan John Shields. Loading a Planar RF Paul Trap From a Cold Yb^+ Source, 2006.

[Sho95] Peter W. Shor. Scheme for Reducing Decoherence in Quantum Memory. *Physical Review A*, 52(4):R2493, 1995.

[SHO+05] D. Stick, W. K. Hensinger, S. Olmschenk, M. J. Madsen, K. Schwab, and C. Monroe. Ion trap in a semiconductor chip. *Nature Physics*, 2(1):36–39, December 2005.

[Sim10] Jonathan Simon. *Cavity QED with Atomic Ensembles.* PhD thesis, Harvard University, 2010.

[SJF00] E. Smalbrugge, B. Jacobs, and S. Falcone. Electroplating of Gold using a Sulfite-based Electrolyte. *Symp. IEEE/LEOS*, 2000.

[SKHR+03] Ferdinand Schmidt-Kaler, Hartmut Häffner, Mark Riebe, Stephan Gulde, Gavin P. T. Lancaster, Thomas Deuschle, Christoph Becher, Christian F. Roos, Jürgen Eschner, and Rainer Blatt. Realization of the Cirac-Zoller controlled-NOT quantum gate. *Nature*, 422(6930):408–11, March 2003.

[SLAH94] Peter W Shor, T Bell Labs, Mountain Ave, and Murray Hill. Algorithms for Quantum Computation : Discrete Log and Factoring Extended Abstract 1 Introduction. In *Proceedings of the 35th Annual Symposium on the Foundations of Computer Science*, page 124, 1994.

[SML05] Winthrop W. Smith, Oleg P. Makarov, and Jian Lin. Cold ion-neutral collisions in a hybrid trap. *Journal of Modern Optics*, 52(16):2253–2260, November 2005.

[SNJ+11] Erik Streed, Benjamin Norton, Andreas Jechow, Till Weinhold, and David Kielpinski. Imaging of Trapped Ions with a Microfabricated Optic for Quantum Information Processing. *Physical Review Letters*, 106(1):2–5, January 2011.

[SPZSK08] Stephan A. Schulz, Ulrich Poschinger, Frank Ziesel, and Ferdinand Schmidt-Kaler. Sideband cooling and coherent dynamics in a microchip multi-segmented ion trap. *New Journal of Physics*, 10(4):045007, April 2008.

[SSLV10] Monika H. Schleier-Smith, Ian D. Leroux, and Vladan Vuletić. States of an Ensemble of Two-Level Atoms with Reduced Quantum Uncertainty. *Physical Review Letters*, 104(7):1–4, February 2010.

[ST07] Jonathan Simon and Haruka Tanji. Interfacing Collective Atomic Excitations and Single Photons. *Physical Review Letters*, 98(18):2–5, May 2007.

[Ste86] Stig Stenholm. The semiclassical theory of laser cooling. *Reviews of Modern Physics*, 58:699–739, 1986.

[Ste96] A. Steane. Multiple-Particle Interference and Quantum Error Correction. *Proceedings of the Royal Society A: Mathematical, Physical and Engineering Sciences*, 452(1954):2551–2577, November 1996.

[Ste97] A. Steane. The ion trap quantum information processor. *Applied Physics B: Lasers and Optics*, 64(6):623–643, 1997.

[SW98] Charles H. Bennett Shor and Peter W. Quantum Information Theory. *IEEE Transactions on Information Theory*, 44(6):2724–2742, August 1998.

[TCA+08] Meng Khoon Tey, Zilong Chen, Syed Abdullah Aljunid, Brenda Chng, Florian Huber, Gleb Maslennikov, and Christian Kurtsiefer. Strong interaction between light and a single trapped atom without the need for a cavity. *Nature Physics*, 4(12):924–927, October 2008.

[TGS+09] Haruka Tanji, Saikat Ghosh, Jonathan Simon, Benjamin Bloom, and Vladan Vuletić. Heralded Single-Magnon Quantum Memory for Photon Polarization States. *Physical Review Letters*, 103(4):1–4, July 2009.

[TKL+00] Q. A. Turchette, B. E. King, D. Leibfried, D. M. Meekhof, C. J. Myatt, M. a. Rowe, C. A. Sackett, C. S. Wood, W. M. Itano, C. Monroe, and D. J. Wineland. Heating of trapped ions from the quantum ground state. *Physical Review A*, 61(6):1–8, May 2000.

[TMK+01] U. Tisch, B. Meyler, O. Katz, E. Finkman, and J. Salzman. Dependence of the refractive index of AlGaN on temperature and composition at elevated temperatures. *Journal of Applied Physics*, 89(5):2676, 2001.

[TRGK+97] P. Taylor, M. Roberts, S. Gateva-Kostova, R. Clarke, G. Barwood, W. Rowley, and P. Gill. Investigation of the $^2S_{1/2}$-$^2D_{5/2}$ clock transition in a single ytterbium ion. *Physical Review A*, 56(4):2699–2704, October 1997.

[Tur36] A. M. Turing. On computable numbers, with an application to the Entscheidungsproblem. *Proceedings of the London Mathematical Society*, 42:230, 1936.

[UJH+09] E. Urban, T. a. Johnson, T. Henage, L. Isenhower, D. D. Yavuz, T. G. Walker, and M. Saffman. Observation of Rydberg blockade between twoÂ atoms. *Nature Physics*, 5(2):110–114, January 2009.

[UTSM+07] R. Ursin, F. Tiefenbacher, T. Schmitt-Manderbach, H. Weier, T. Scheidl, M. Lindenthal, B. Blauensteiner, T. Jennewein, J. Perdigues, P. Trojek, B. Ömer, M. Fürst, M. Meyenburg, J. Rarity, Z. Sodnik, C. Barbieri, H. Weinfurter, and A. Zeilinger. Entanglement-based quantum communication over 144km. *Nature Physics*, 3(7):481–486, June 2007.

[WBI+87] D. J. Wineland, J. C. Bergquist, W. M. Itano, J. J. Bollinger, and C. H. Manney. Atomic-ion Coulomb clusters in an ion trap. *Physical Review Letters*, 59(26):2935–2938, 1987.

[WDW78] D. J. Wineland, R. E. Drullinger, and F. L. Walls. Radiation-pressure cooling of bound resonant absorbers. *Physical Review Letters*, 40(25):1639–1642, 1978.

[Wes08] J. Wesenberg. Electrostatics of surface-electrode ion traps. *Physical Review A*, 78(6):1–12, December 2008.

[WES+11] Christof Weitenberg, Manuel Endres, Jacob F. Sherson, Marc Cheneau, Peter Schauß, Takeshi Fukuhara, Immanuel Bloch, and Stefan Kuhr. Single-spin addressing in an atomic Mott insulator. *Nature*, 471(7338):319–324, March 2011.

[WHA+09] H. Wang, M. Hofheinz, M. Ansmann, R. Bialczak, Erik Lucero, M. Neeley, A. O'Connell, D. Sank, M. Weides, J. Wenner, A. Cleland, and John Martinis. Decoherence Dynamics of Complex Photon States in a Superconducting Circuit. *Physical Review Letters*, 103(20):1–4, November 2009.

[WMI+97] D. J. Wineland, C. Monroe, W. M Itano, D. Leibfried, B. E. King, and D. M. Meekhof. Experimental issues in coherent quantum-state manipulation of trapped atomic ions. *Journal of Research of the National Inst. of Standards and Technology*, 103(3), 1997.

[WOS10] S. Whitlock, C. F. Ockeloen, and R. J. C. Spreeuw. Sub-Poissonian Atom-Number Fluctuations by Three-Body Loss in Mesoscopic Ensembles. *Physical Review Letters*, 104(12):24–27, March 2010.

[WP94] W. E. Wiesel and D. J. Pohlen. Canonical Floquet theory. *Celestial Mechanics and Dynamical Astronomy*, 58(1):81–96, 1994.

[WPGH05] F. Werner, O. Parcollet, a. Georges, and S. Hassan. Interaction-Induced Adiabatic Cooling and Antiferromagnetism of Cold Fermions in Optical Lattices. *Physical Review Letters*, 95(5):1–4, July 2005.

[WSB+04] A. Wallraff, D. I. Schuster, A. Blais, L. Frunzio, J. Majer, S. Kumar, S. M. Girvin, and R. J. Schoelkopf. Strong coupling of a single photon to a superconducting qubit using circuit quantum electrodynamics. *Nature*, 431(September):0–5, 2004.

[WW30] V. Weisskopf and E. Wigner. Die Streuung des Lichts an angeregten Atomen. *1Zeitschrift für Physik*, 930.

[Yab87] Eli Yablonovitch. Inhibited spontaneous emission in solid-state physics and electronics. *Physical Review Letters*, 58(20):2059–2062, 1987.

[YM00] N. Yu and L. Maleki. Lifetime measurements of the $4f^{14}5d$ metastable states in single ytterbium ions. *Physical Review A*, 61(2):12–15, January 2000.

[ZD07] Peng Zhang and Alexander Dalgarno. Static dipole polarizability of ytterbium. *The journal of physical chemistry. A*, 111(49):12471–6, December 2007.

[ZDC09] Peng Zhang, Alex Dalgarno, and Robin CCRCMFLXoté. Scattering of Yb and Yb^+. *Physical Review A*, 80(3):1–4, September 2009.

[ZDJ+08] R. Zhao, Y. O. Dudin, S. D. Jenkins, C. J. Campbell, D. N. Matsukevich, T. a. B. Kennedy, and A. Kuzmich. Long-lived quantum memory. *Nature Physics*, 5(2):100–104, December 2008.

[ZPR+10] Christoph Zipkes, Stefan Palzer, Lothar Ratschbacher, Carlo Sias, and Michael Köhl. Cold Heteronuclear Atom-Ion Collisions. *Physical Review Letters*, 105(13):1–4, September 2010.

[ZPSK10] Christoph Zipkes, Stefan Palzer, Carlo Sias, and Michael Köhl. A trapped single ion inside a Bose-Einstein condensate. *Nature*, 464(7287):388–91, March 2010.

[ZRSK11] Christoph Zipkes, Lothar Ratschbacher, Carlo Sias, and Michael Köhl. Kinetics of a single trapped ion in an ultracold buffer gas. *New Journal of Physics*, 13(5):053020, May 2011.